Contributions to Image Processing in the Perspective of Medical Applications: From CAD to Embedded Systems for In Situ Diagnosis

Aymeric Histace

University of Cergy-Pontoise **Doctoral School SI**

Contributions to Image Processing in the Perspective of Medical Applications: From CAD to Embedded Systems for In Situ Diagnosis

THESIS

publically presented and defended the 28th of November 2014

for the obtention of the

"Habilitation à diriger des recherches"

by

Aymeric HISTACE

Members of the jury

President:	Le président
Reviewers:	Prof. D. Friboulet (INSA Lyon, CREATIS) Prof. M. Garreau (Université de Rennes 1, LTSI) Prof. N. Vincent (Université de Paris 5, LIPADE)
Supervisors:	Prof. F. Précioso (Université de Nice/Sophia, I3S) Prof. O. Romain (Université de Cergy-Pontoise, ETIS)
Examiners:	Prof. A. Lundervold (University of Bergen, Neuroinformatics and Image Analysis Lab.) Prof. M. Paindavoine (Université de Bourgogne, LEAD) Prof. N. Noury (Université Claude Bernard, Lyon 1, INL)

Équipes Traitement de l'Information et Systèmes (ETIS) — UMR CNRS 8051

My PhD thesis was dedicated to my parents, and sister.
This manuscript is dedicated to my wife Sabrina, and children, Zoé, Léo and Tom, the three musketeers, for their unconditional love, patience and comprehension.

Summary

Introduction

Motivation and Objective

For the last decade, Medical Image Analysis for Computer-Aided-Diagnosis (CAD) has been the central motivation of my research activity. With the constant increase of the imaging capabilities of medical devices and the huge amount of produced digital information, physicians are in real need for semi-automatic image processing tools making possible fast, precise and robust analysis, including restoration, segmentation, pattern detection and recognition, quantitative analysis, etc.

In this particular application area, from an image processing angle, my research work has mainly focused for the last 8 years on two main tracks:

1. The study of the variational approach framework for image restoration and segmentation which common point is the formalization of the related optimization problem under the form of a Partial Differential Equation (PDE).
2. The development of embeddable pattern detection and recognition methods for real-time in situ diagnostic.

Objective of this document is twofold:

- First to demonstrate my abilities, through the experience of the last 8 years, to coordinate original research activities (scientific animation, publications, fundings, etc.) that would lead to the continuation of some existing projects but also to the emergence of new ones in my field of expertise but not only.
- Second to show that I am able to jointly assume the activities of a Lecturer/Researcher through my investment into the everyday-life of a University.

Context

I was hired as an Associate Professor at University of Cergy-Pontoise, ETIS lab, in September 2006 to join the Imagery, Communication, Information (ICI) team and most precisely to develop a research activity in image restoration and segmentation with a particular application to Computer-Aided-Diagnosis. On this basis, I started a research work with Dr. Frédéric Precioso from the Multimedia Indexing (MIDI) team of ETIS on parametric-region-based active contour and maintained two national collaborations with David Rousseau (at that time Associate Professor at the University of Angers) on the study of the Stochastic Resonance effect in non-linear-Partial-Differential-Equation-based image restoration approaches, and a second one with Prof Michel Ménard from University of La Rochelle on Oriented PDE for image enhancement. These different activities led me to join the UK funded project ECSON[1] (see Chapter 1)

[1] Engineering and Computational Sciences for Oncology Network

at the beginning of 2008 on the invitation of Prof. David Burton from the Liverpool John Moore University and Prof. Bogdan Matuszewski from the University of Central Lancashire (Preston) to develop new collaborations on active-contour segmentation for Computer-Aided-Diagnosis in Oncology.

At the end of 2008, this new research group was officially presented to the lab and, taking profit of the expertise session of ETIS lab by French Research Agency (AERES) at the same period, it was agreed on the creation of a research activity inside ICI team with a particular focus on Computer-Aided-Diagnosis (CAD): the SIMBAD (Medical and Biomedical Image Segmentation for Computer-Aided-Diagnosis) activity was officially born.

As said before, main aim of this research activity was (and still is) to propose original signal and image processing algorithms to help physicians in their daily pratique. With the constant increase of the imaging capabilities of medical devices and the huge amount of produced digital information, they are in real need for semi-automatic image processing tools making possible fast, precise and robust analysis, including restoration, segmentation, pattern detection and recognition, quantitative analysis, etc. In this particular context, with the collaboration of Dr. Frédéric Precioso, we decided to focus the scientific research work on variational approach for image processing, area in which both of us already had a good experience.

From this starting point, several projects were funded first locally ("Bonus Quota Recherche", ENSEA, Preston project, 2009), then at an international level with our integration as partner in the already mentioned ECSON project funded by EPSRC[2] with Prof. Bogdan Matuszewski (University of Central Lancashire, ADSIP Research Centre) as principal investigator. This collaboration with Prof. Matuszewski allows us to publish first papers during the year 2009 (1 journal paper, and 5 conferences) mainly focused on medical image segmentation using active contour approach.

In parallel, the collaborations with Prof. Michel Ménard and David Rousseau on PDE (Partial Differential Equation)-based image restoration led to joint publications (2 journal papers and 3 conferences in the last 6 years) also contribute to strengthen the fundaments of the SIMBAD activity.

In September 2010, the first PhD funding was accorded to the SIMBAD activity (Leila Meziou) as well as a new local funding (project BIOMICMAC, ENSEA, UCP) ; We were again invited to join as partner, the TeRaFs[3] project funded by EPSRC by the University of Central Lancashire, and more publications overcame from these different collaborations.

In parallel to these activities, starting from mid-2011, I have been involved by Prof. Patrick Duvault in the cosupervising of the Clément Fouquet's PhD work (50%). This PhD, funded by a CIFRE agreement between ETIS end the TRAPIL company) aims at proposing a complete image processing scheme for the early detection and recognition of structural defaults in pipelines using ultrasonic images.

In September 2011, with arrival of Prof. Olivier Romain in ASTRE team of ETIS, a collaborative activity between ICI and ASTRE team, centered on "Embedded Systems for Wireless Health Monitoring", was created with a particular application for in situ diagnosis of colorectal cancer using wireless videocapsule.

Finally, to this day, after nearly 6 years of existence, the SIMBAD activity has published in total 7 journal papers and around 30 international and national conference papers (see the full publication list in Annex), Leila Meziou successfully defended her PhD the 28th of November 2013, Cément Fouquet will defend his PhD work the 13th of June 2014, and a new PhD focusing

[2]Engineering and Physical Sciences Research Council
[3]Technology in Radiotherapy Feasibility Study

on early diagnosis of colorectal pathologies based on videocapsule image analysis will start in September 2014 with Prof. Olivier Romain as cosupervisor. I am also involved in several projects dedicated mainly to Computer-Aided-Diagnosis and in situ diagnosis.

Layout of the document

The following sections aims at presenting main contributions of "my" research work all along the last 8 years in the particular scientific framework of PDE-based approaches mainly and more recently in embedded image processing.

The document is divided into 2 parts:

1. The first one is composed of two chapters focusing respectively on my extended CV[4], and a summary of my research activities.

   The CV brings information on my research activities from a kind of "administrative" point of view (supervising, fundings, administrative responsibilities inside ETIS lab, etc.), but also details on my teaching activities and administrative responsibilities at the Institute of Technology of Cergy-Pontoise where I have been deeply involved for the last 8 years.

   Chapter 2 is an extended summary of the main research activities I have been involved in, following my PhD work (2001-2004). This chapter only gives a synthetic overview of the contributions brought to the different issues addressed in image processing. Reader should refer to Part 2 for a detailed description.

2. Part 2 focuses on a detailed presentation of the main research activities I have been interested in since 2006 and proposed a full description of the related scientific contributions.

More details on Part 2 are given below:

- Chapter 3 focuses on the scientific contributions to PDE-based image restoration. The main starting idea is to show that the former work of Perona-Malik in that area is still of real interest when considering original diffusive functions like the double-well function proposed or the Stochastic Resonance phenomenon, also known as a constructive action of noise in a nonlinear process.

  The different scientific aspects of this Chapter were developed in collaboration with Prof. Michel Ménard (L3i, University of La Rochelle) and Prof. David Rousseau (CREATIS, University of Lyon 1).

- Chapter 4 focuses on image segmentation using active contour technics. The scientific aspect of this chapter is situated in the same area than Chapter 3, since we still are considering PDE-based approaches and more precisely, variationnal approaches. Nevertheless, the constituting PDE are somehow different in the particular context of active contour segmentation.

  Two main contributions are presented: first of all, a general framework for shape prior constrains in active contour segmentation is introduced, and second, contributions to statistical-region-based approaches are proposed. In the latter case, we focus our attention on the proposal of statistical-region-based descriptor: a fractional entropy inspired from Rényi's one, and a study of a particular divergence family called the alpha-divergence.

[4]The first version of this Chapter was written in March 2014. I updated the current version in October 2014 to take into account the most up-to-date elements

The work on shape constraints was jointly developed with Prof. Bogdan Matuszewski (ADSIP Research Center, University of Central Lancashire, UK), Dr Yan Zhang (Post-Doc student at ADSIP), and Prof. Frédéric Precioso formerly Associate Professor at ETIS.

The fractional entropy descriptor was studied during the MSc internship of Mickael Garnier. The alpha-divergence contribution was studied during the PhD of Dr Leila Meziou (2010-2013) for which I was cosupervisor (70%) with Prof. Frédéric Precioso.

- Chapter 5 is dedicated to a more recent research activity related to "Embedded Systems for Health" in which I have been involved for more than 2 years now with Prof. Olivier Romain (Head of ASTRE team of ETIS).

  This Chapter is quite different from Chapters 3 and 4, since the global framework is definitely more constrained in terms of technology capabilities (energy, small amount of memory, real-time process...) when comparing with classic Computer-Aided-Diagnosis area. From an applicative point of view, this Chapter focuses on a particular project named "Cyclope" which objective is to design and develop a new generation of wireless videocapsule for early diagnosis of colorectal cancer (polyp detection and identification) and more generally for detection and recognition of gastrointestinal abnormal structures.

  This project is developed in collaboration with Prof. Bertrand Granado (LIP6, University Pierre et Marie Curie), Prof. Xavier Dray and Prof Philippe Marteau (Gastroenterologists (PU-PH), Hôpital Lariboisière, APHP). Part of the presented study was made during the MSc internship of Juan-Silva Quintero in the second half of 2012.

Part 2 does not include a general conclusion. I chose on purpose not to dedicate a particular section to this, but in every Chapter it is composed of, a "Conclusion and Perspectives" section is proposed so that to give concrete elements to discuss on for each contribution.

Finally, this document ends with a section focusing on the future works I want to concentrate on. Both scientific and concrete elements (fundings!) are brought in this section.

If scientific aspects of Chapter 3 and 4 were developed not necessarily from an application-oriented point of view, but with the idea of proposing approaches that fit to a wide area of Image Processing, Chapter 5, in comparison is more application-oriented and is at the interface of several scientific areas that need to "collaborate" (electronics, medicine, signal and image processing, industrial valorization) to be efficient.

How to read this document

My objective in the writing of this document is to provide to the reader a self sufficient manuscript with no need to go for some of my joint publications to have the full detailed on the proposed methods. With that objective in mind and in the same time to facilitate the reading, I put an effort to make each Chapter of Part 2 "independent" that is to say that they can be read on their own, depending on the reader's interests.

I finally conclude this introduction by specifying that if applications to medical image analysis and CAD are not necessarily proposed for each of the contributions presented in this document, this particular application area remains the main and most important motivation of my research activities.

Part I

Overview

Chapter 1

Curriculum Vitae

1.1 Administrative data

First names:	Aymeric, René, Pierre, André
Last name:	Histace
Date and place of birth:	4th of September 1977, Lyon, France
Marital status:	PACS, 3 children
Current position:	"Maître de Conférences" (Associate Professor), University of Cergy-Pontoise, France
Teaching activities:	Institute of Technology (IUT), University of Cergy-Pontoise, Electrical Engineering and Industrial Informatics department (GEII), 4 Mail Gay-Lussac, 95000 Cergy-Pontoise
Research activities:	ETIS Lab, UMR 8051, ENSEA, University of Cergy-Pontoise, CNRS, 6 av. du Ponceau, 95014, Cergy-Pontoise
Phone:	+33(0)1 34 25 68 34
Webpage:	aymeric.histace.free.fr
Email:	aymeric.histace@u-cergy.fr

1.2 Diploma, Qualification and Others

2013: Obtaining of the **"Prime d'Excellence Scientifique (PES)"**

2005: Obtaining of the **"Qualification" in 61st section of the French CNU**

2004: **"Doctorat" (PhD) from the University of Angers**, defended the 19th of November 2004

Speciality	Signal and Image Processing
Title	Segmentation and tracking of structures in image sequences: application to tagged cardiac MRI analysis.
Supervising	Prof. Bertrand Vigouroux and Dr Christine Cavaro-Ménard
Jury members	Prof. Francoise Prêteux (reviewer), Prof. Pierre Bonton (reviewer) Dr Nicolas Rougon, Prof. Michel Ménard, Prof. Jean-Louis Ferrier, Prof. Jean-Jacques Lejeune, Prof. Nicole Vincent (Jury President)
Mention	"Très honorable avec les félicitations du jury"

2001: **Master of Science** from the University of Angers

Speciality	Signal and Image in Medecine and Biology (SIBM)
Title	Quantitative Evaluation of Wavelet Compression degradations on Numerical Chest Radiographies.
Mention	"Bien"

2001: **"Diplôme d'ingénieur" (Master of Engineering)** from EIGSI-La Rochelle

1995-1998: **Preparatory school for the "Grandes Écoles"** (CPGE), Physics and Chemistry

1.3 Professional Experience

2006-...: **"Maître de Conférences" (Associate Professor)**
at the University of Cergy-Pontoise, France, with ETIS laboratory (UMR CNRS 8051)

2004-2006: **"ATER" (Assistant Professor)**
at the University of Angers, France,
with LISA laboratory (Laboratoire en Ingénierie des Systèmes Automatisés)

2001-2004: **PhD student** (funded by French government) and **"Moniteur"** (Contractual Lecturer),
University of Angers, France, LISA laboratory

1.4 Teaching Activities

1.4.1 Teaching

As an Associate Professor, my obligations are of 192 hours of teaching per year at the University of Cergy-Pontoise, and more precisely at the Institute of Technology (GEII department). Nevertheless due to an important teaching workload in that kind of particular structures (numbers of students and related labs), I usually teach about 100 extra hours a year since I have been hired in 2006. Tab. 1.1 shows an illustration of my usual year of teaching and Tab. 1.2 shows the total amount of teaching hours per year starting in 2006.

My teaching activities are in "Electrical Engineering and Energy" and "Control Theory" mainly, plus some extra hours for advanced lectures in Image Processing (MSc Student with speciality "Systèmes Intelligents et Communicants") and Signal Processing (School of Engineering of Cergy-Pontoise, ENSEA).

As it can be noticed, a major part of my teaching is not closely related to my research activities and does not facilitate a joint profit between my teaching activities and my research ones. Nevertheless, as for other colleagues I have met who are in the same situation, this particularity can be managed and can even be seen as a way to draw connections for students between the technological and the research "worlds" that, too often, seems somehow unreachable to them.

A Focus on Some Particular Teaching Activities

- From 2006 to 2008, I was deeply involved in the updating of the labs of the "Electrical Engineering and Energy" classes with the complete rewriting of the related "student" supports. This includes labs on the fundamental theorems of electricity, labs on components such as diode, transistor, operational amplifiers, on the basis of boolean algebra for digital electronic, and fundaments of power electronics (components and inverters).
- From 2006, I have been in charge of the "Electrical Engineering" classes of the L3 IFS ("Railway Infrastructures and Signaling") of the Institute of Technology (co-habilitated with the French SNCF since 2006). Mainly, I built from scratch a complete set of lectures, tutorials and labs on the fundaments of electrotechnics, including topics as engines technologies, inverters, and national rules for electric installation (NFC 15-100). I gave a particular attention to the specificity of the students coming from very different areas (Electronics, Electrotechnics, but also, Industrial Maintaining and Automatism).

- About the "Control Theory" classes (2nd-year students, L2) at the Institute of Technology, I have been in charge for the last 5 years of the coordination of the module. This includes the constant updating of the related lectures, tutorials and labs and in 2013, the complete renewal of the scientific content in the context of the national reform of the French "Baccalauréat": A complete electronic updated support of all the lectures can be downloaded by students on a dedicated webpage[5] (as a major part of my teaching).

- About the MSc lectures at the University of Cergy-Pontoise, in 2011, I was in charge of the complete updating of the Image Processing lectures following Prof. Sylvie Philipp-Foliguet's retirement: I took this opportunity to propose some particular lectures on variational approach in image processing (PDE-based image restoration approaches and active contour segmentation). Moreover, since 2012, I am also in charge of the "Statistical Learning part 2" lectures of the MSc MADoCs[6] (Binary Decision Tree and extension to Random Forest, Boosting-based approaches) from which I am also co-head with Prof. Chalmond.

Students	**Classes**	**Lectures +Tutorials**	**Labs (h)**
IUT 1st year (L1)	Electrical Engineering and Energy	60	24
IUT 2nd year (L2)	Electrical Engineering and Energy		24
IUT 2nd year (L2)	Control Theory (Analog)	28	32
IUT 2nd Year (A), (L2)	Control Theory (Analog and Digital)	54	40
IUT Prof. Licence (L3)	Electrical Engineering and Energy	30	
ENSEA 3rd year (M2)	Signal Processing for ECG	6	
MSc SIC (M2)	Image Processing	16	
MSc SIC and MADOCS (M2)	Data Learning	6	
Total (h)		**190**	**96**

Table 1.1: Example of my usual teaching year since 2006 as an Associate Professor at the University of Cergy-Pontoise. "(A)" highlights the fact that the students are apprentices, i.e. in contract with a company.

1.4.2 Administrative Responsibilities

Since my arrival at the University of Cergy-Pontoise, I have been deeply involved in the administrative life of the GEII department of the Institute of Technology, and more recently in the organization of the Master classes. A list and a short description of the different tasks I have assumed until now is given below.

[5] aymeric.histace.free.fr
[6] https://sites.google.com/site/mastermadocinfo/

Year	Lect. and Tut. (h)	Labs (h)	Total (h)
2013-2014	190	96	**286**
2012-2013	180	92	**272**
2011-2012	187	93	**280**
2010-2011	176	104	**280**
2009-2010	172	123	**295**
2008-2009	154	132	**286**
2007-2008	133	175	**308**
2006-2007	119	204	**323**

Table 1.2: Total of teaching hours per year.

2012-...: **Co-Head of the MSc MADoCs** of the University of Cergy-Pontoise ("Méthodes pour l'Analyse des Données ComplexeS") with Prof. Bernard Chalmond
Teaching program, teaching coordination, research projects

2011-2014: **In charge of the "Image and Multimedia Indexing" speciality** of the MSc SIC ("Systèmes Intelligents et Communicants") of the University of Cergy-Pontoise
Teaching program, teaching coordination, internship management

2008-2014: **In charge of the coordination of the apprenticeship students**
Institute of Technology of Cergy-Pontoise, GEII dpt
Contacts with companies, Contracts, financial negociation and agreement, Student recruitment and placement.

2008-2011: **In charge of the teaching coordination of the 2nd year students in apprenticeship**,
Intitute of Technology of Cergy-Pontoise, GEII Dpt
Teaching program, teaching coordination, jury, mark management

2007-2008: **In charge of the teaching coordination of the *Licence professionnelle* "Instrumentation et Mesure"**
(Instrumentation and Sensors)
Institute of Technology of Cergy-Pontoise
Teaching program, teaching coordination, jury, mark management, internship placement

To these administrative responsibilities must be added the regular follow-up of students of the GEII dpt during their internship or apprenticeship period. Follow-up that includes the participation to the final oral presentation, one or two visit(s) where the internship takes place and finally the reading of the different activity reports. I usually follow 2 classic students and 4 or 5 apprentices a year.

1.5 Research Activities

1.5.1 Extended Abstract

For the last 10 years, Medical Image Analysis for Computer-Aided-Diagnosis has been the central motivation of my research activity. With the constant increase of the imaging capabilities of medical devices and the huge amount of produced digital information, physicians are in real need for semi-automatic image processing tools making possible fast, precise and robust analysis, including restoration, segmentation, pattern detection and recognition, quantitative analysis, etc.

Type of publications	**Total**
Articles in peer-reviewed journal	**8**
Invited conference	**1**
International conferences	**27**
National conferences	**5**
Book chapters	**3**
Book and proceedings editor	**2**

Table 1.3: Publications in Brief

In this particular application area, my research work has mainly focused for the last 8 years on two main tracks:

1. The study of the variational approach framework for image restoration and segmentation which common point is the formalization of the related optimization problem under the form of a Partial Differential Equation (PDE).

   The main scientific contributions of these research activities have been since 2006:

   - In image restoration:
     - The study of the stochastic resonance phenomenon in non-linear PDE for image restoration.
     - The study of double-well potential functions for Gradient-Oriented-PDE in image restoration.
   - In image segmentation:
     - Active contour segmentation approach with learning-based shape prior information.
     - Alpha-divergence-based active contour image segmentation.
     - Fractional-entropy-based active contour image segmentation.

   These contributions have until now found applications in MR image analysis, as well as standard X-Radiography, Confocal Microscopy and Videoendoscopy image analysis.

2. The development of embeddable pattern detection and recognition methods based on statistical learning process for real-time in situ diagnostic.

   The main scientific contributions of these research activities have been:

- The proposal of a complete embeddable image processing scheme for in situ polyp detection in Wireless Capsule Endoscopy for colorectal cancer diagnosis.
- A real-time computer-aided-analysis method for non-destructive inspection of pipelines using ultrasonic images (detection and recognition of defect signatures).

Tab. 1.3 shows the summary of the related publications during the last 8 years.

1.5.2 Collaborations and Projects

The different research activities described above were and still are funded by several research projects in the context of local, national and international collaborations. Details about these collaborations and related projects are given in following sections.

1.5.2.1 Collaborations

International

2008-...:	UCLan	ADSIP Research Centre, University of Central Lancashire, Preston, UK Prof. Bogdan Matuszewski **Computer Vision and Image Processing**
2008-...:	LJMU	GERI, Liverpool John Moore University, Liverpool, UK Prof. David Burton, Dr Mark Murphy **Computer Vision and Image Processing, Cellular Biology**
2012-...	UB	Image Processing Group, Universitat de Barcelona, Spain Dr. Lluis Garrido **Computer Vision and Image Processing, Optimisation**

At an international level, the collaboration with UCLan is one of my most active with the joint publications of 4 peer-reviewed journal articles (including JMIV and IJCARS), 11 peer-reviewed international conferences, a "Best Student Paper Award" at the MIUA 2012 Conference and 3 student exchanges since 2009.

National

2008-...	Reims	CHU de Reims, Maison-Blanche Hospital Dr. Christophe Portefaix **Image Processing, Medical Image analysis**
2008-...	L3i	L3i lab, University of La Rochelle Prof. Michel Ménard, Prof. Arnaud Revel **Image Processing**
2010-...:	CREATIS	Creatis lab, University of Lyon Prof. David Rousseau **Signal Processing, Information Theory**
2011-...:	I3S	I3S lab, University de Nice Prof. Frédéric Precioso **Computer Vision, Image Processing, Machine Learning**
2012-...:	IRIT	IRIT lab, University of Toulouse Dr. Benoît Gaudou **Multi Agent System**
2008-2010:	LISA	LISA, University of Angers Dr. Christine Cavaro-Ménard, Dr David Rousseau **Image Processing, Medical Image Analysis, Information Theory**

Local

2011-...	ERR	ERRMECE lab, University of Cergy Prof. Franck Carreiras **Cellular Biology**
2011-...	Larib	Lariboisière Hospital, Gastroenterology dpt Prof. Xavier Dray (PUPH), Prof. Philippe Marteau (PUPH) **Videoendoscopy, Medical Image Analysis**
2011-...	LIP6	LIP6 Lab, SYEL team, Paris 6 Prof. Bertrand Granado, Prof. Patrick Garda, Dr. Andréa Pinna **Embedded Systems, Digital Electronic, Signal Processing**

1.5.2.2 Projects

In this section, a summary of past and ongoing projects (2009-2013) related to the research activities and collaborations detailed above is given Tab. 1.4.

In the framework of the collaborations with the University of Central Lancashire and the Universitat de Barcelona, Prof. Bogdan Matuszewski (UCLan) and Dr Lluis Garrido (UB) benefited from a 1-month invitation as "Professeur invité" at ETIS lab, respectively in 2011 and 2014.

Name	Years	Type of funding	Collaboration	Role	Budget
ECSON	2007-2009	EPSRC (UK)	UCLan, LJMH	Partner	154k£
TeRaFs	2009-2011	EPSRC (UK)	UCLan, LJMH	Partner	200k£
Preston	2009-2011	BQR ENSEA	UCLan, LISA, Reims, L3i	**Leader**	5k€
BIOMICMAC	2010-2012	BQR ENSEA, UCP	UCLan, LJMH, ERR	**Leader**	10k€
GEODIFF	2011-2012	CNRS (PEPS)	IRIT, L3i	**Leader**	15k€
Cyclope	2011-2013	BQR ENSEA	LIP6, Larib	**Co-Leader**	9k€
3DCell	2012-2013	BQR ENSEA	UB, UCLan, ERR, LJMU	Leader	5k€
FibroSES	2012-2014	CNRS (PEPS)	LIP6, ERR	Partner	80k€
SmartEEG	2013-2016	FUI 15	LIP6, Larib, +Private Companies	Partner	2M€

Table 1.4: Research projects and related collaborations

Glossary

3DCell:	3D Modeling of cell shape for characterization of cancerous morphological changes in laser confocal microscopy images
BQR:	"Bonus Quota Recherche"
BIOMICMAC:	Predictive Oncology from Cells to Organs
ECSON:	Engineering and Computational Science for Oncology Network
EPSRC:	Engineering and Physical Sciences Research Council
FibroSES:	Fibrosis phenomenon in embedded systems for wireless health monitoring
GEODIFF:	Joint SMA-PDE Modeling of Complex Diffusion Process
SmartEEG:	Signal and Video Analysis for Smart Electroencephalogram acquisition
TeRaFs:	Technology in Radiotherapy Feasibility
UCP:	University of Cergy-Pontoise

1.5.3 Supervising activities

1.5.3.1 In brief (2009-2013)

Type of supervising	Total (%)	Number of students
PhD	**170%**	3
MSc	**400%**	7

Table 1.5: Supervising activity in brief

1.5.3.2 PhD Students

Defended PhD (2)

Student:	Leila Ikram MEZIOU
Date:	2010-2013 (Defended the 28th of November 2013)
Title:	Alpha-divergence based active contour segmentation: application to medical and biomedical image segmentation
Jury:	Prof. D. Rousseau (CREATIS, Univ. of Lyon, Reviewer), Prof. S. Ruan (LITIS, Univ. of Rouen, Reviewer), Prof. N.Vincent (LIPADE, Univ. of Paris 5, Chairman ("Présidente"))
Supervising:	A. Histace 70%, Prof. F. Precioso 20%, Prof. M. Nguyen-Verger 10%
Funding:	PhD funding from University of Cergy-Pontoise
Current situation:	R&D Engineer (Image Processing) with Altran (Cardental company)

Student:	Clément FOUQUET
Date:	2011-2014 (Defended the 13th of June 2014)
Title:	Automatic analysis of ultrasonic images for pipeline oil inspection: detection and recognition of defect signatures
Jury:	Prof. F. Precioso (I3S, University of Nice, Reviewer) Prof. M. Paindavoine (LEAD, University of Bourgogne, Reviewer) Prof. Olivier Alata (H. Curien Lab, University of St Etienne, Chairman)
Supervising:	A. Histace 50%, Prof. P. Duvaut 50%
Funding:	"CIFRE" agreement with TRAPIL company
Current situation:	R&D Engineer in Computer-Vision with TRAPIL company

On Going PhD (1)

Student:	Quentin Angermann
Date:	2014-2017
Title:	Smart Videocapsule for Early Detection and Recognition of Colorectal Pathologies
Supervising:	A. Histace 50%, Prof. 0. Romain 50%
Funding:	PhD funding from University of Cergy-Pontoise

1.5.3.3 MSc Students

Graduate Students

- Gaurav Pardeschi, April 2014-September 2014, "Embedded Impedance Spectroscopy for Wireless Monitoring of Fibrosis Phenomenon", Supervising: Mehdi Terosiet 33%, A. Histace 33%, Prof. O. Romain 33%.
- Samy Mouzay, April 2014-September 2014, "FPGA-Embedding of detection and recognition algorithms for application to in situ diagnosis of colorectal cancer in videocoloscopy", Supervising: A. Histace 50%, Prof. O. Romain 50%.
- Chakib Azib, April 2013-September 2013, "FPGA-Embedding of the Circular Hough Transform for real-time use", Supervising: A. Histace 50%, Prof. O. Romain 50%, Current situation: PhD student in China (Chen Zen).

- Augustin Izart, April 2013-September 2013, "FPGA-Embedding of the Cooccurrence matrix for real-time texture analysis: Application to polyp detection in Videocolonoscopy", Supervising: A. Histace 50% , Prof. O. Romain 50% , Current situation: Research Engineer (LIP6, Univ. Paris 6).
- Juan Silva, April 2012-September 2012, "Boosting-based approach for robust detection and recognition of polyps in videocapsule images", Supervising: A. Histace 70%, Prof. O. Romain 30% , Current situation: Development Engineer with SIRA Company, Franconville, France.
- Mickael Garnier, April 2011-September 2011, "Fractional-entropy for confocal microscopy image segmentation using active contour", Supervising: A. Histace 100%, Current situation: PhD student (LIPADE, Paris 5).
- Marine Breuilly, April 2009-September 2009, "Histogram-based active contour segmentation using Wasserstein Distance: Application to medical image segmentation", Supervising: A. Histace 50%, Prof. B. Matuszewski 50% (Univ. Central Lancashire, Preston, UK), Current situation: PhD from University of Nice, France (INRIA, AESCLEPIOS team).

1.5.3.4 Others

Plus these supervising activities:

- I am unofficially involved as "Image Processing" consultant in the PhD Thesis of Fabien Pottier (Labex PATRIMA, 2013-2016) on the "Iconographic Analysis of the Codex Borbonicus", supervisors: Prof. B. Lavédrine (CRCC-Paris), Prof. Olivier Romain (ETIS, UCP), Prof. F. Goublard (LPPI, UCP).
- I was unofficially involved in the Post-Doc supervising of Yan Zhang (University of Central Lancashire, supervisor : Prof. B. Matuszewski, 2009) which aim was to investigate new active-contour-based image segmentation methods with prior knowledge for medical image data analysis. Dr Yan Zhang had a one-month invitation at ETIS lab during his Post-Doc position.
- I was unofficially involved in the supervising of Elizabeth Bonnefoye's MSc internship (University of Central Lancashire, Supervisor: Prof. B. Matuszewski, April-August 2012) which aim was to develop an original approach for MRI cardiac segmentation and quantitative evaluation of the Right Ventricle function.
- I regularly take in charge 1 or 2 MSc students (SIC and MADOCS) per year for their "Initiation Research Project" (about 150 hours of work), on topics closely related to the ongoing research activities.

1.5.4 Related Activities

1.5.4.1 Scientific Event Organizations

In Tab. 1.6 a list of the Scientific events I have been involved in is given.

- The "Bionic Man" event is a thematic cycle that will take place all along 2014 at the University of Cergy-Pontoise. It will take form of a series of seminars from international keynote speakers, workshop sessions, dedicated labs etc. These different events will be

Event	Year	Type of event	Location	Role
Biomaterial and Smart Devices	2014	2-day Workshop	University of Cergy	Organization and Scientific Committees
Bionic Man	2014	1-year thematic school	University of Cergy	Organization Committee
GEODIFF	2013	1-day Workshop	Barcelona (Spain)	Organizer and Chairman
ICIP	2011	1-day Special Session	Bruxelles (Belgium)	Organization Committee
SocPar	2010	Conference	Cergy (France)	Local Organization Committee
ECSMIO	2010	1-day Special Session	Angers (France)	Organization Committee

Table 1.6: Organizations of Scientific events I have been involved in.

open to PhD students, MSc students mainly and will focus on the translational joint research work between cellulars biology, electronics, signal and image processing for health monitoring. This event is coordinated by Prof. Emmanuel Pauthe from the University of Cergy-Pontoise.

- Workshop GEODIFF was focused on "Joint MAS-PDE modeling of complex diffusion proces", and was organized in conjunction with international conference VISIGRAPP 2013. This event gathered researchers from 4 universities (Lyon, La Rochelle, Cergy-Pontoise and Toulouse) ans was organized under the banner of GEODIFF project (funded by CNRS, see Tab. 1.4)

- ICIP Special Session was entitled "Analysis of Microscopy and Reconstructive Images for applications in Medicine and Biology" and was organized under the banner of TeRaFs project (Tab. 1.4) by Prof. Bogdan Matuszewski from University of Central Lancashire.

- SocPar is an international yearly conference focusing on Soft Computing and Pattern Recognition. The 2010 conference was organized in Cergy by ETIS lab and chaired by Prof. Dominique Laurent.

- The ECSMIO Special Session (Engineering and Computational Sciences for Medical Imaging in Oncology) was chaired by Prof. Bogdan Matuszewski under the banner of ECSON project.

1.5.4.2 Scientific Animation

- Since 2008, I am in charge of the scientific animation of the SIMBAD activity (Biomedical and Image Segmentation for Computer-Aided Diagnosis) in the ICI (Imagery, Communication, Information) team of ETIS lab.

- Since september 2013, I co-animate with Prof. Olivier Romain the "Embedded System for Wireless Health Monitoring" working group (joint group between ICI and ASTRE teams of ETIS).

- Since October 2014, I am head of the 'Embedded System for Wireless Health Monitoring", scientific axis of ASTRE team.

1.5.4.3 GDR ("Groupement de Recherche") Seminars

- "Alpha-Divergence-Based Active Contour: Application to Medical Image Analysis ", Telecom Paristech, "Statistical and Variational Approaches for Medical Image Analysis', Paris, France, 7 June 2013.

- "Cyclope : Embedded Detection and Recognition of Polyps for Early Diagnosis of Colorectal Cancer Using Wireless Videocapsule", University of Grenoble, INPG, "Capteur en Traitement du Signal et de l'Image", Grenoble, France, 27 September 2012.

1.5.4.4 External Seminars

- "Histogram-based segmentation with extremization of alpha-divergences: application to medical and biomedical image segmentation", University of Central Lancashire, Preston, UK, 11 April 2012.

- "Boosting from the medical image analysis perspective", University of Central Lancashire, Preston, UK, 14 October 2010.

- "Active contours: from basics to recent advances in medical image segmentation", University of Central Lancashire, Preston, 27 April 2009, Under the Banner of the IET.

1.5.4.5 PhD Jury

- The 24th November 2014, I will be external examiner in the PhD jury of Mickael Garnier, Descartes University (Paris 5), Title: "Descriptive Modelings of spatial relations for CAD in Biomedical Images".

- The 13th June 2014, I will be local examiner (as co-superviser) in the PhD jury of Clément Fouquet, University of Cergy-Pontoise (see "supervising activities" section for details).

- The 28th November 2013, I was local examiner (as co-superviser) in the PhD jury of Leila I. Meziou, University of Cergy-Pontoise (see "supervising activities" section for details).

- The 16th November 2012, I was external examiner in the PhD jury of Xiao W. Zhao, University of La Rochelle, Title: "Target Detection and Localization through walls using UWB technology".

1.5.4.6 Awards

- The conference paper entitled "Fractional Entropy Based Active Contour Segmentation of Cell Nuclei in Actin-Tagged Confocal Microscopy Images" and presented at the 2012 Medical Image Understanding and Analysis conference (MIUA), received the **"Best Student Paper"** award.

- Quentin Angermann obtained the 3rd best student poster-award during the "Biomaterials and Smart Devices" Workshop in 2014 (Cergy, France), for his work on smart videocapsules for early diagnosis of colorectal cancer.

1.5.4.7 Reviewer and Chairman Activity

I regularly review papers for the following scientific journals: IEEE Transactions on Image Processing (2011-...), Journal of Digital Imaging (Springer, 2012-...), Pattern Analysis and Applications (Springer, 2012-...), Biomedical Signal Processing and Control (Elsevier, 2012-...), Pattern Recognition Letters (Elsevier, 2009-...), Journal of Visual Communications and Image Representations (Elsevier, 2006-...), Journal of Electronic Imaging (SPIE, 2005-...)

- In 2014, I was Chairman of a session on Image Processing at the "Biomaterials and Smart Devices" Workshop (Cergy, France, 27-28 March).
- In 2014, I was Chairman of a session on Biomedical Signal Processing at the International Conference BIOSIGNALS (Angers, France, 6 March).
- In 2013, I was Chairman of the GEODIFF Workshop, in conjunction with the international conference VISIGRAPP (Barcelona, Spain, February).
- In 2012, I was Chairman of a session focusing on Motion tracking and Stereovision at the international conference VISAPP (Rome, Italy, Session 4, 25 February).
- In 2007, I was Chairman of a session focusing on Vision for Robotic at the international conference ICINCO (Angers, France).

1.5.4.8 Councils and Commissions

- Since September 2014, I am member of the "Commission de Choix" of the Institute of Technology (Cergy-Pontoise), representing GEII dpt. This commission is in charge of the recruitment strategy of the Institute.
- Since September 2012, I am an elected member of the Laboratory Council of ETIS.
- In 2014, I was external member of two commissions for the recruitment of two "Maître de Conférence" (Associate Professor) positions ("Comité de Sélection"). The first one at the University of Angers for LARIS lab (formerly, LISA lab), and second one at the University of Rouen (LITIS lab).
- In 2011, I was local member of a commission for the recruitment of a "Maître de Conférence" (Associate Professor) position at the Institute of Technology of Cergy-Pontoise.

Chapter 2

Summary of My Research Activities (2006-2014)

2.1 Introduction

For the last 8 years, Medical Image Analysis for Computer-Aided-Diagnosis has been the central motivation of my research activity. With the constant increase of the imaging capabilities of medical devices and the huge amount of produced digital information, physicians are in real need for semi-automatic image processing tools making possible fast, precise and robust analysis, including restoration, segmentation, pattern detection and recognition, quantitative analysis, etc.

In this particular application area, my research work has mainly focused for the last 8 years on two main tracks:

1. The study of the variational approach framework for image restoration and segmentation which common point is the formalization of the related optimization problem under the form of a Partial Differential Equation (PDE).

   The main scientific contributions of these research activities have been since 2006:

   - In image restoration:
     - The study of the stochastic resonance phenomenon in non-linear PDE for image restoration.
     - The study of double-well potential functions for Gradient-Oriented-PDE in image restoration.
   - In image segmentation:
     - Active contour segmentation approach with learning-based shape prior information.
     - Alpha-divergence-based active contour image segmentation.
     - Fractional-entropy-based active contour image segmentation.

   These contributions have until now found applications in MR image analysis, as well as standard X-Radiography, Confocal Microscopy and Videoendoscopy image analysis.

2. The development of embeddable pattern detection and recognition methods based on statistical learning process for real-time in situ diagnostic.

The main scientific contribution of these research activities have been the proposal of complete embeddable image processing schemes for the in situ early detection and recognition of colorectal pathologies (cancer, Chrone's disease, ulcers) using Wireless Capsule Endoscopy images

In the following sections, I give a synthetic overview of each of these contributions, starting with a recall on my PhD work in order to explain the "origins" of my current scientific activities.

2.2 Recalls on my PhD work

During 2001-2004, I worked on a CAD problematic related to the quantitative assessment of the cardiac function using Tagged Magnetic Resonance Imaging technique (Tagged MRI). Technically speaking, the classic SPAMM (Space Modulation of Magnetization) acquisition protocol [Zerhouni *et al.*, 1988] used for the tagging of MRI data, displays a deformable 45-degrees oriented dark grid which describes the contraction of myocardium (Fig. 2.1) on the images of temporal Short-Axis (SA) sequences. This is the temporal tracking of this grid that can enable radiologists to evaluate the local intramyocardial displacement.

Figure 2.1: SA tagged MRI of the Left Ventricle (LV) extracted from a sequence acquired between end-diastole and end-systole.

Tagged cardiac images present peculiar characteristics which make the analysis difficult. More precisely, images are of low contrast compared with classic MRI, and their resolution is only of approximately one centimeter.

The main contribution of my PhD work was to propose a complete restoration and segmentation scheme making possible direct segmentation and tracking of the myocardial boundaries (for Left Ventricle area delineation) and of the grid of tags for the local quantification of the LV contraction.

This 3-years research activity familiarized me with the "variationnal approaches" framework of image processing since the complete proposed method included a directional restoration step (enhancement of the grid of tags) and a gradient-based active contour segmentation approach for LV boundaries delineation. In both case, the "solution" of the addressed issue (segmentation, restoration) can be formalized as the optimization (minimization in most cases) of a particular energy, and then, using Euler-Lagrange optimization techniques, to the iterative solving of the corresponding Partial Differential Equation (PDE).

In the 2005-2006 period, as an Assistant Professor (ATER) in the same lab, I was able to valorize in terms of publications part of my PhD work that was not yet published, and in 2006, I started to work with David Rousseau (at this time in the same lab) on nonlinear PDE for image denoising.

PDE-based approaches, because of their abilities to encompass a wide area of applications in Image Processing, remain of great interest and still are a challenging problem to address. This theoretical framework was the starting point for the SIMBAD research activities at my arrival in ETIS.

2.3 PDE-Based Approaches in Image Processing

Compared with other approaches, the variational PDE method has remarkable advantages in both theory and computation. First, it allows one to directly handle and process visually important geometric features such as gradients, tangents, curvatures, and level sets. It can also effectively simulate several visually meaningful dynamic processes, such as linear and nonlinear diffusions and the information transport mechanism. Second, in terms of computation, it can profoundly benefit from the existing wealth of literature on numerical analysis and computational PDE.

The first point was for me the most interesting one because of the very wide possible applications in CAD: In a first period of 2 years (2006-2008), I concentrated on non-linear-based image restoration approaches in the context of two collaborations already mentioned (David Rousseau (Angers, France), Prof. Michel Ménard (La Rochelle, France)). Jointly, in 2008, I then started an internal collaboration with Frédéric Precioso (MIDI team of ETIS) on active-contour-based segmentation and mainly on the possibility of integrating into the segmentation process the particular statistics of the region to segment (distribution law) and some external constraints like shape. Those two objectives were mainly motivated by the fact that for medical image devices, the corrupting noise can be in most cases, modeled (parametrically or not) and that the "shape" and/or the topology of an organ or a tumor is of primary interest to develop efficient CAD tools for clinicians.

In the two following subsections a synthesis on the work achieved on those two particular objectives is proposed.

2.3.1 Nonlinear PDE for image restoration

In the particular field of image restoration, nonlinear or anisotropic regularization PDE's are of primary interest. The benefit of PDE-based regularization methods lies in their ability to smooth data in a nonlinear way, allowing the preservation of important image features (contours, corners or other discontinuities). In the particular domain of scalar image restoration, the introduction of the Perona–Malik process [Perona and Malik, 1990] in 1990 as triggered a large interest since then.

In the original Perona-Malik process the observable noisy image ψ_0 is restored by considering the solution of the partial differential equation given by

$$\frac{\partial \psi}{\partial t} = div(g(\|\nabla\psi\|)\nabla\psi), \qquad \psi(x, y, t = 0) = \psi_0 \ , \tag{2.1}$$

where the anisotropy of this diffusion process is governed by $g(\cdot)$ a nonlinear decreasing function of the norm of the gradient $\nabla\psi$.

The starting point of these investigations was to demonstrate that the former PDE proposed by PM is still of real interest by the possibility offered to take benefits of the nonlinearity of Eq. (2.1).

2.3.1.1 Double Well Function for Gradient Intensity Selectivity

A first contribution was to introduce as a diffusive function in the PM's PDE a double-well function of the form:

$$c_{DW}(u) = 1 - \phi(u) \ , \tag{2.2}$$

with

$$\phi(u) = \int_0^u v(\alpha - v)(v - 1)dv \ , \tag{2.3}$$

instead of the classic function g so defined as:

$$g(u) = e^{-\frac{u^2}{k^2}} \ , \tag{2.4}$$

It is recognized that usual Perona-Malik's PDE presents instability problems. More precisely, as shown in [Catté *et al.*, 1992], sometimes noise can be enhanced instead of being removed (detailed reasons can found in Chapter 3): we showed in this study, that the DW function proposed had interesting stability properties related to the fact that its first derivative has sufficiently small variations to not produce the same effect as with the formerly introduced PM's function.

We also showed that the α parameter of the DW function permits here to tune the intensity of the gradient to be preserved from the diffusive effect of the PM's PDE.

Practically speaking, tests were carried out on different type of images, from synthetic ones, to natural ones, including medical data.

Examples of results are shown Fig. 2.2 and Fig. 2.3.

Related publications:[7] [A.3.27, A.3.32, A.3.33, A.4.1]

2.3.1.2 Useful Noise Effect for Nonlinear-PDE-Based Image Restoration

A second contribution to the particular field of PDE-based image restoration approach was the study of the Stochastic Resonance Effect due to the purposely injection of a controlled amount of noise "into" the non linearity of PM's PDE.

As paradoxical as it may seem, noise can play a constructive role in the domain of nonlinear information processing. Originally introduced to describe the mechanism of a constructive action of a white Gaussian noise in the transmission of a sinusoid by a nonlinear dynamic system governed by a double well potential, the phenomenon of stochastic resonance has experienced large varieties of extensions with variations concerning the type of noise, the type of information carrying signal or the type of nonlinear system interacting with the signal-noise mixture.

First of all, we proposed to study a possible SR phenomenon with the PM's PDE by simply injecting a controlled amount of noise into the nonlinearity governed by g of Eq. (2.1). Corresponding PDE is then given by:

$$\frac{\partial \psi}{\partial t} = div(g_\eta(\|\nabla\psi\|)\nabla\psi) \ , \tag{2.5}$$

which is of a form similar to Eq. (2.1) except for the nonlinear function $g_\eta(\cdot)$ which is given by

$$g_\eta(u) = g(u + \eta(x, y)) \ , \tag{2.6}$$

[7] All the references given in this Chapter refer to the Annex A of the document.

(a) (b)

(c) (d)

Figure 2.2: (a) Original image “lena" and (b) its corrupted version ψ_0 . Corrupting noise is a white Gaussian one of mean zero and standard deviation $\sigma = 0.1$. (c) Restored image with usual Perona-Malik's approach, (d) Restored image with proposed approach.

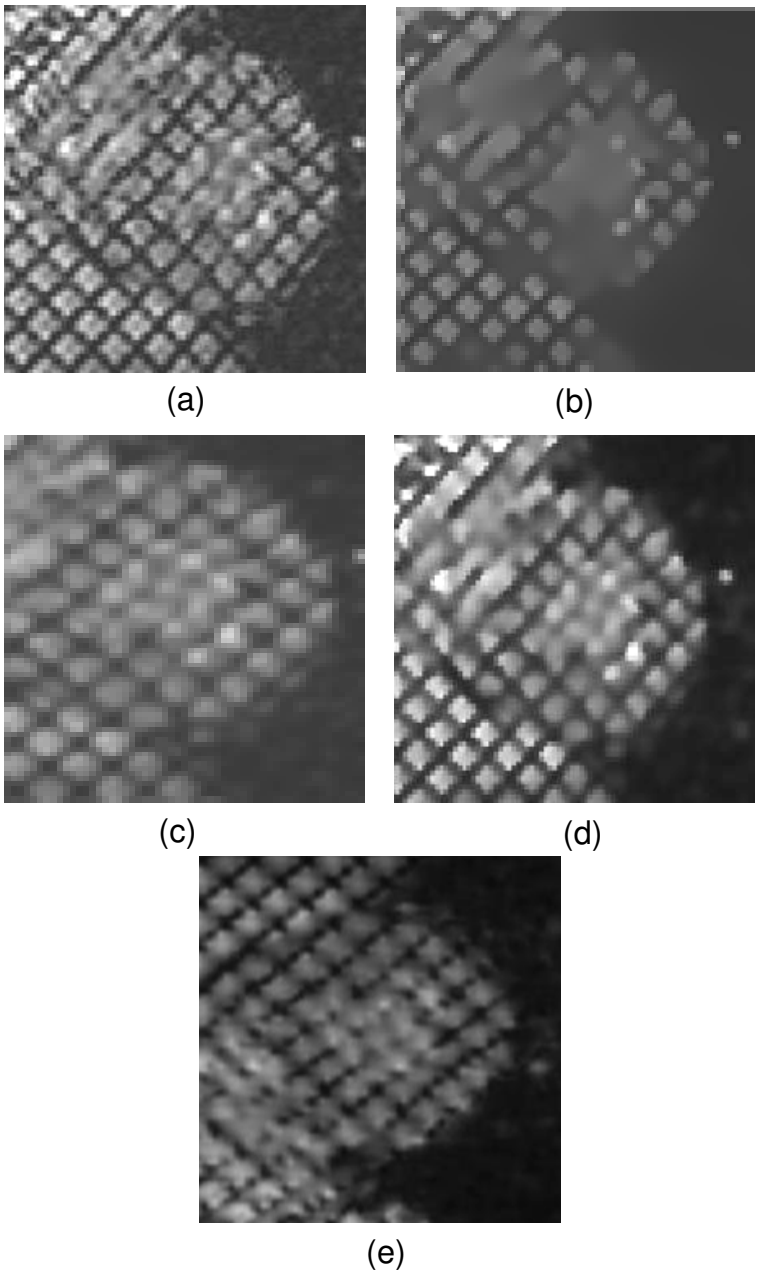

Figure 2.3: Tagged MRI restoration: (a) Original image, (b) PM's approach, (c) Weickert's approach, (d) PM's approach with $c(.) = c_{DW}(.)$, (e) Result obtained with the proposed approach). "Optimal" visual results for each methods are shown.

where η is a noise assumed independent and identically distributed with probability density function $f_\eta(u)$ and rms amplitude σ_η. The noise η, which is distinct from the native noise component to be removed, is a purposely added noise applied to influence the operation of $g(\cdot)$.

Thanks to this particular PDE, we first demonstrate as a proof of concept that the purposely injection of noise could lead to very interesting restoration results in the particular case of "salt and pepper" corrupting noise on the original image. These results were then extended to other couplings of corrupting noise, including additive and multiplicative couplings (Gaussian and Speckle noise). For illustration, the image "cameraman" (see image (d) in Fig. 2.4), is chosen as reference for the original image ψ_{ori}. Noisy versions of this original image are presented as the observable images ψ_0 of our restoration task in Fig. 2.4 for various image–noise coupling.

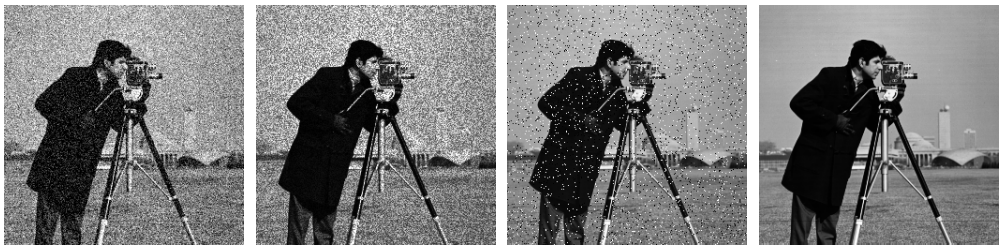

(a) (b) (c) (d)

Figure 2.4: The original image ψ_{ori} cameraman (d) corrupted by three different native noises ξ: (a) additive zero-mean Gaussian noise with $\psi_0 = \psi_{ori} + \xi$, (b) multiplicative Gaussian noise of mean unity with $\psi_0 = \psi_{ori} + \xi.\psi_{ori}$, (c) impulsive noise.The rms amplitude of these noises are separately adjusted in order to have each of the images (a,b,c) characterized by the same normalized crosscovariance (given in Eq. (3.19)) with the original image equal to 0.87.

A visual appreciation of the performance of the stochastic version of Perona–Malik process of Eq. (2.6) and the original Perona–Malik process of Eq. (2.1) is shown in Fig. 2.5.

To complete these different studies, made from an experimental point of view until this moment, we finally theoretically showed the existence of the SR effect in this particular case of application by considering a simple set of parameters for function g (a simple threshold function) in order to be able to derive the SR equivalent function as proposed in [Chapeau-Blondeau, 2000]. This study was also conducted considering a simplified objective: the restoration of a step function corrupted by a Zero-Mean Gaussian noise. This way, we succeeded in showing that the SR phenomenon from the nonlinear-PDE-based restoration approach could be seen as a novel instance of a purposely injection of noise in the case of image restoration. More precisely, the purposely injection of noise was demonstrated to act like an inner retuning of the k parameter of the usual PM's diffusive function, making possible preservation of the gradient information that was not possible for a bad tuning of this value. Fig. 2.6 shows results obtained for the edge restoration task.

Moreover, as for all SR phenomena, the beneficial effect is probabilistic and for a given tuning of k value Fig.2.7 shows the probability of denoising with preservation of the contour gradient information.

Related publications: [A.1.4, A.1.8, A.3.22, A.3.34]

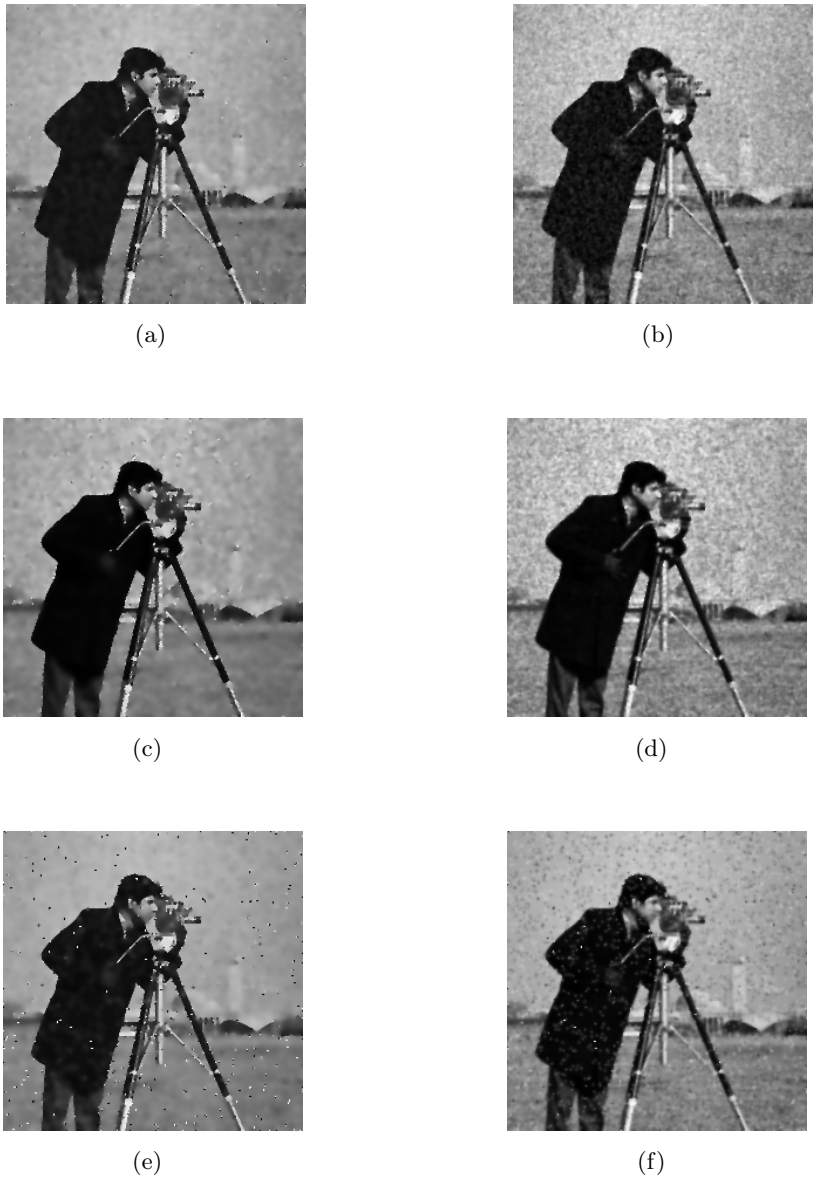

(a) (b)

(c) (d)

(e) (f)

Figure 2.5: Visual comparison of the performance of the original restoration Perona–Malik process and the corresponding stochastic version. The left column shows the results obtained with usual Perona-Malik restoration process and the right column with our stochastic version of the Perona–Malik process. Each image is obtained with the iteration number n corresponding to the highest value of the normalized crosscovariance. The top (a,b), middle (c,d) and bottom (e,f) lines are respectively standing for the additive, multiplicative and impulsive noise component described in Fig. 3.17.

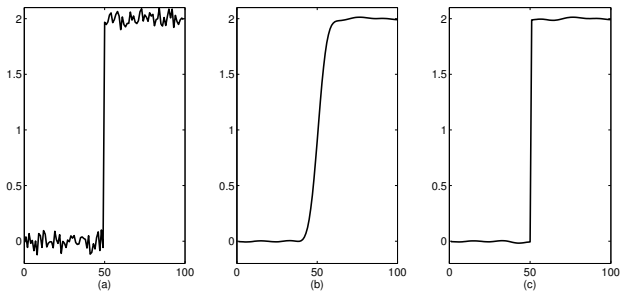

Figure 2.6: (a) Noisy step ψ_0, (b) Perona-Malik restoration of ψ_0 (50 iterations), (c) Stochastic Perona-Malik restoration of ψ_0 (50 iterations and $\sigma_\eta = 0.3$. Injection of η noise makes possible to obtain a better restoration of the noisy step regarding the fact that noise is suppressed and step discontinuity is preserved.

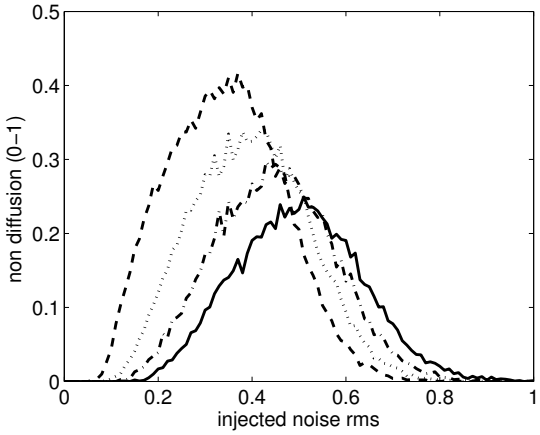

Figure 2.7: Ratio of non-diffused steps function of rms amplitude σ_η. N is fixed to 1000. Dashed line stands for $k = 0.65$, dotted one for $k = 0.7$, dash-dotted one for $k = 0.75$ and solid one for $k = 0.8$. For each value of k, the non-diffusion ratio is maximum for a non zero amount of purposely injected noise, which demonstrates the existence of a SR phenomenon.

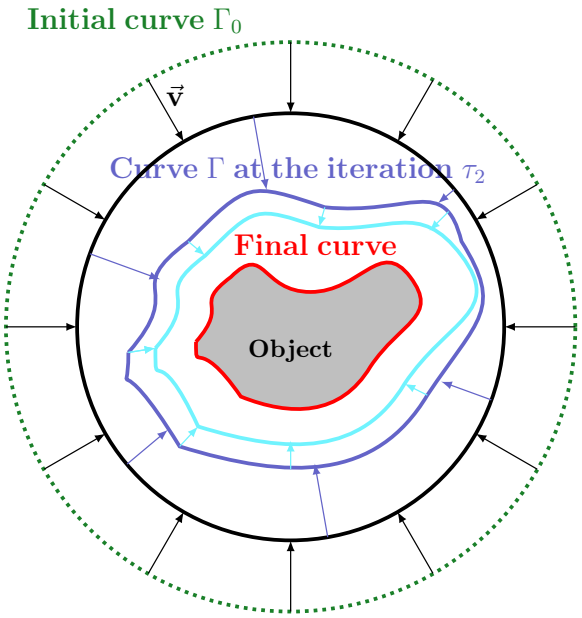

Figure 2.8: Illustration of active contour segmentation: $\Gamma = \Gamma(p, \tau)$ denotes the coordinate of the point p of the curve at iteration τ of the segmentation process.

2.3.2 Active-Contour-Based Segmentation

Differently from the application to image restoration, in the context of active contour segmentation, the iterative optimization process of a given energy is applied so as to deform an initial curve towards the boundaries of a targeted object. (see Fig. 2.8 for illustration). The PDE that steers the evolution of the curve comes from the minimization of a particular energy defined in order to take into account the characteristics of the segmentation task (noise, shape, texture, etc.). Formerly introduced in [Kass *et al.*, 1988], active contour has been a very active center for research in segmentation since then. In the following sections, two contributions to this particular field of image segmentation are synthetically introduced.

2.3.2.1 Shape Constraints

In late 2008, we began with Dr Precioso and Dr Matuszewski from University of Central Lancashire a collaboration on active-contour-based image segmentation for CAD. Under the banner of ECSON project (2007-2009) (following then by TERAFS project (2009-2011)), we focused our attention on shape constraint embedding into a variationnal framework with objective to be able to statistically learn this shape constraint from a database, which tends to be adapted to the particular case of medical image analysis (lot of examples coming from different patients).

This collaboration took form of several visits, the welcoming of Dr Yan Zhang (Post-Doc Student) for a one-month period in 2009 and two MSc internships in ADSIP research Center (in 2009 and 2012).

Scientifically speaking, the proposed segmentation framework can be seen as constrained contour evolution, with the evolution driven by an iterative optimization of the posterior probability model that combines a prior shape probability and an image likelihood function linked with a coupling prior imposing constraints on the contour evolution in the image domain.

The prior shape probability function is estimated using Parzen window method, on the training shape samples given in the estimated beforehand shape space. The likelihood function is constructed from conditional image probability distribution, with the image modeled to have regions of approximately constant intensities. The coupling distribution is defined as the prior distribution on the image likelihood function which imposes feasible shapes changes based on the current shape parametrization in the shape space.

In a variational approach framework, corresponding energy to minimize can be written the following way:

$$E(\boldsymbol{\lambda}_r) = E_{prior}(\boldsymbol{\lambda}_r) + E_{image}(\boldsymbol{\lambda}_r) \tag{2.7}$$

where the shape prior term is defined as:

$$E_{prior}(\boldsymbol{\lambda}_r) = -\ln\left(\sum_{i=1}^{N_s} \mathcal{N}(\boldsymbol{\lambda}_r; \boldsymbol{\lambda}_{r,i}, \sigma^2)\right) \tag{2.8}$$

and is built based on the shape samples Ω_i used for the shape learning step in the Legendre moment space ($\boldsymbol{\lambda}_r$). The image term is defined as:

$$E_{image}(\boldsymbol{\lambda}_r) = E_{cv}(\Omega, \mu_\Omega, \mu_{\Omega^c}|I)|_{\Omega=\Omega(\boldsymbol{\lambda}_r)} \tag{2.9}$$

where optimization of E_{cv} is constraint to shapes Ω from the estimated shape space $\Omega = \Omega(\boldsymbol{\lambda}_r)$ where $\Omega(\boldsymbol{\lambda}_r)$ denotes a shape from the shape space represented by the Legendre moments .

The resulting constrained optimization problem is solved using combinations of level set active contour evolution in the image space and steepest descent iterations in the shape space. The decoupling of the optimization processes into image and shape spaces provides an extremely flexible optimization framework for general statistical shape based active contour where evolution function, statistical model, shape representation all become configurable.

The experimental results, obtained on synthetic and natural images, demonstrated very strong resilience of the proposed method to the random as well as structural noise present in the image (see Fig. 2.9 for illustration of a shape training set and Fig. 2.10 for illustration of obtained results for different scenarios of strong corrupting noise).

This activity is still in progress with main objective to use the proposed method in a CAD context (Prostate Cancer in our case).

Related publications: [A.1.2, A.3.20, A.3.24]

2.3.2.2 Statistical-Region-Based Active Contour

In 2009, through the internship of Marine Breuilly, we also began to focus our attention on statistical-region-based active contour. This particular family of region-based active contour, introduced by [Aubert *et al.*, 2003] proposes to compare the probability density function (PDF) of inner and outer region delimited by the active curve and to use the "distance" between those two PDF to steer the evolution of the curve towards the boundaries of the targeted object.

That kind of approaches is of great interest for medical image segmentation where the PDF of the "object" and the background of the image can be very different from classic Gaussian distributions for instance (Rayleigh, Poisson, Mixture of Gaussians, etc.).

In terms of related energy to optimize, two options are possible:

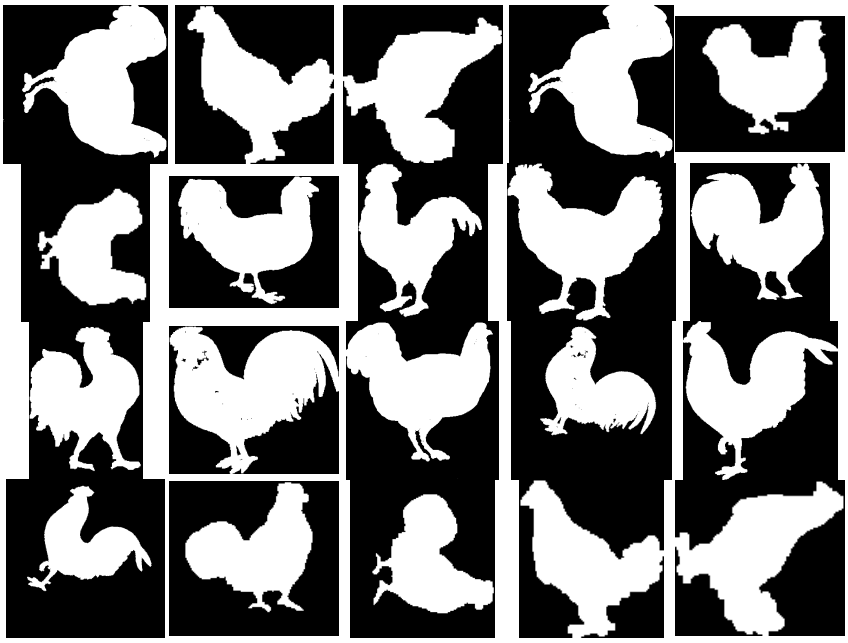

Figure 2.9: The chicken image set.

- In the first case, the energy is defined so as to compete inner and outer regions of the active curve using an entropy measurement as the descriptors related to the PDF of considered regions ; Shannon's entropy is usually considered [Herbulot *et al.*, 2006].

- An other option is to define the energy as a divergence between the PDF of inner and outer regions so as to a maximization process of this similarity measure leads to the object to segment. In this case the Kullback-Leibler divergence remains the most used [Lecellier *et al.*, 2010].

Alpha-Divergence Family

The PhD work of Leila Meziou (2010-2013) focused on the second option. Most precisely, we proposed to use as a similarity measure between PDF a particular family of divergence called the alpha-divergence. The contribution of this work is twofold: First, in the framework of the divergence maximization between non-parametrically-estimated PDF, we propose to derive the corresponding PDE, and second, we particularize to the case of alpha-divergence family, a flexible statistical similarity measure between PDF whose inner metric can be adapted to the statistics of the data.

More precisely, we proposed a joint-PDE process where the distance between the PDF and the metric of the alpha-divergence are optimized in turn. Most precisely, the joint optimization of the divergence and α parameter is obtained by the following PDE systems:

$$\begin{cases} \dfrac{\partial \alpha}{\partial \tau} = & -\partial_{\alpha} D_{\alpha}(p_{in}, p_{out}, \alpha) \\ \dfrac{\partial \Gamma}{\partial \tau} = & -\partial_{p_{in}, p_{out}} D_{\alpha}(p_{in}, p_{out}, \alpha). \end{cases} \tag{2.10}$$

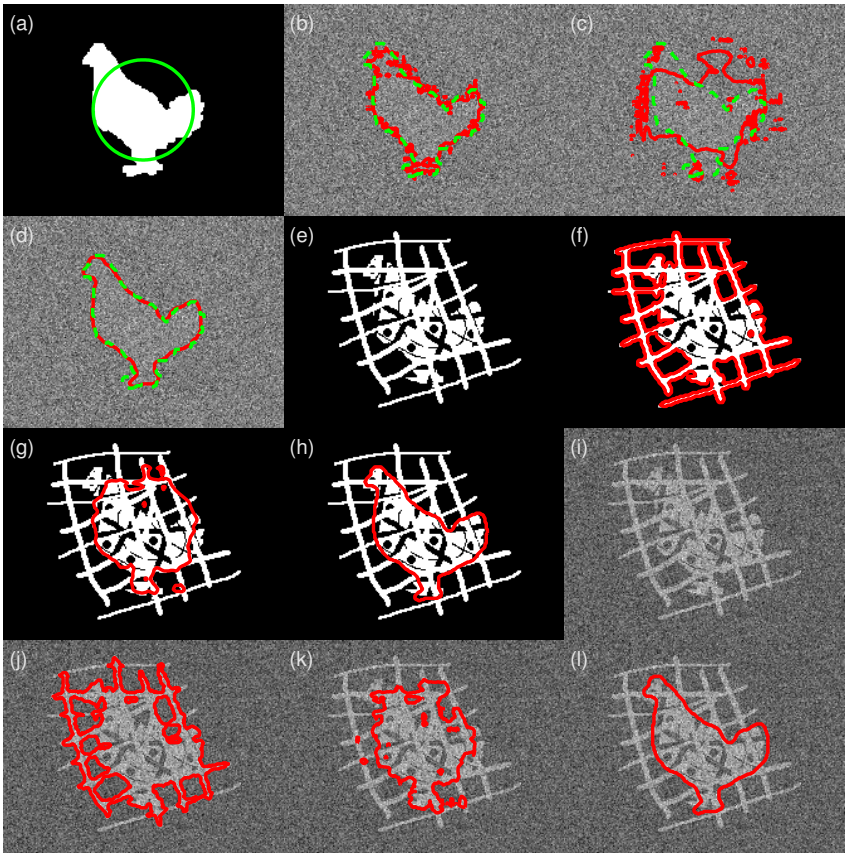

Figure 2.10: Results for a set of experiments using different chicken's silhouette image. The segmentation results are shown as red solid curves, whereas the desired results are shown as green dash lines. (a) Original noise-free test image with initial active contour shown as a circle at the center of the image; (b) Segmentation of the test image with severe Gaussian noise using Chan-Vese method; (c) Segmentation of the same test image as in (b) using the multi-reference method proposed by Foulonneau *et al.*; (d) Segmentation of the same test image as in (b) using the proposed method; (e) Test image with structural noise; (f) Segmentation of (e) using Chan-Vese model; (g) Segmentation of (e) using the multi-reference method; (h) Segmentation of (e) using the proposed method; (i) Test image with hybrid noise; (j) Segmentation of (i) using Chan-Vese method; (k) Segmentation of (i) using the multi-reference method; (l) Segmentation of (i) using the proposed method.

where $D_\alpha(p_{in}, p_{out}, \alpha)$ is the alpha-divergence between the inner (p_{in}) and outer (p_{out}) PDF, defined by:

$$D_\alpha(p_{in} \| p_{out}, \Omega) = \int_{\chi^m} \varphi_\alpha(p_{in}, p_{out}, \lambda)\, d\lambda \tag{2.11}$$

with $\varphi_\alpha(p_{in}, p_{out}, \lambda) =$

$$\begin{cases} \dfrac{\alpha p_{in} + (1-\alpha) p_{out} - {p_{in}}^{\alpha} {p_{out}}^{1-\alpha}}{\alpha(1-\alpha)} , & \alpha \in \mathbb{R} \setminus \{0,1\} \\ p_{out}\ log\left(\dfrac{p_{out}}{p_{in}}\right) + p_{in} - p_{out} , & \alpha = 0 \\ p_{in}\ log\left(\dfrac{p_{in}}{p_{out}}\right) - p_{in} + p_{out} , & \alpha = 1 \end{cases} \tag{2.12}$$

It can be noticed here that at the limits α tends to 1 and 0, the corresponding divergence is the classic KL divergence (L'Hôpital Theorem): A complete study about the mathematical properties of alpha-divergences can be found in [Beirami *et al.*, 2008], but more than KL particular case, let us highlight that for specific values of α, some aforementioned standard distances can also be connected to alpha-divergences. For instance: $D_2(\Omega) = \frac{1}{2} D_{\chi^2}(\Omega)$, $D_{\frac{1}{2}}(\Omega) = 2 D_{Hellinger}(\Omega)$. This makes alpha-divergence a generic distance estimation, with multiple tuning possibilities via α parameter and as a consequence, a very flexible measure.

A major issue of the proposed joint-optimization strategy of Eq. (2.10) is the initialization of α : More precisely, two initialization strategies can be considered.

- A first one, $\alpha_0 \gg 1$ or $\ll 1$, avoids possible falling into local minimum as the joint optimization process starts. Nevertheless, because being far from the Shannon case where $\alpha = 1$, such initialization need prior information on the statistics of the data to be efficient.
- The second one, $\alpha \to 1$, proposes to take as a starting point the most general divergence as defined by Shannon, corresponding to the maximization of p_{in}, with respect to p_{out} to fit with the usual active contour segmentation framework.

We naturally chose the second strategy that fit the most to the considered segmentation task, for which no prior is given on the inner and outer PDFs and we showed that this approach overcomes some drawbacks of the classic Kullback-Leibler divergence that can stick into a local optimum: In that particular case, alpha-parameter optimization makes possible to avoid such situation and to finally reach the expected segmentation.

This approach demonstrated to reach some very interesting results for various type of images including synthetic, natural and medical ones. In the latter case, we more particularly showed results obtained on X-Ray radiographies (see Figs 2.11, 2.12, 2.13 and Fig. 2.14 for illustrations).

Related publications: [A.1.3, A.3.1, A.3.14, A.3.15, A.3.16, A.3.17, A.3.18, A.3.19, A.3.21, A.6.1]

A Fractional Entropy Descriptor

Jointly with the work on alpha-divergence, we also turned our attention on the possibility

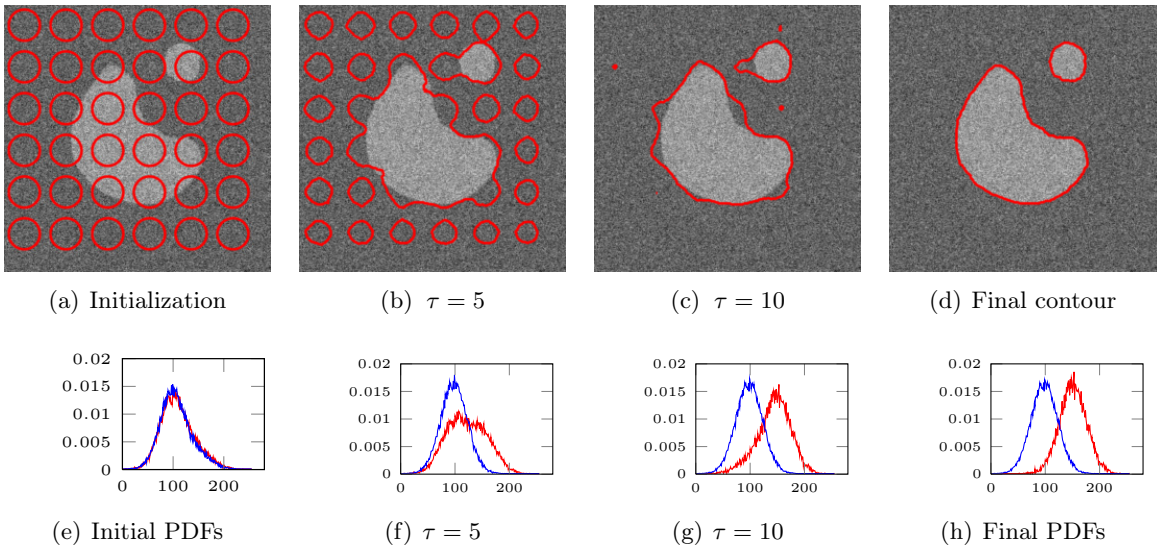

(a) Initialization (b) $\tau = 5$ (c) $\tau = 10$ (d) Final contour

(e) Initial PDFs (f) $\tau = 5$ (g) $\tau = 10$ (h) Final PDFs

Figure 2.11: Some steps of the active contour Γ and related PDFs (p_{in} (red) and p_{out} (blue)) evolutions for the Gaussian noise with PSNR$= 10dB$.

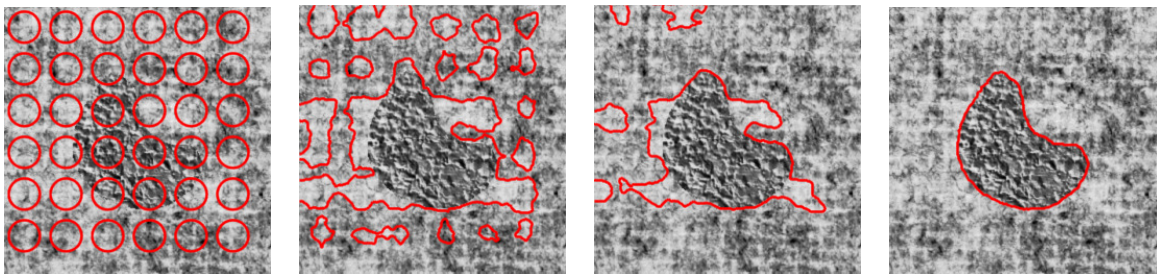

(a) Initialization (b) $\tau = 5$, KL (c) $\tau = 50$ (d) Final contour

Figure 2.12: Some steps of the active contour evolution for segmentation of proposed textured image with joint optimization of α parameter.

to use a Rényi-like entropy computed on the PDF of object and background, into a region competition strategy. Main idea was to overcome classic limitations of Shannon Entropy that does not lead to satisfying segmentation results in the particular case of a very important amount of corrupting noise. Rényi's entropy is concave and shows an additional parameter α which can be used to make it more or less sensitive to the shape of PDF.

This relaxation property is the starting point of the following study. Unfortunately, Rényi's entropy as expressed is part of the non-integral entropy family that can not be easily associated to a region-based criterion in a classic active contour based segmentation. Nevertheless, taking benefits of the possible sensibility tuning of the Rényi's entropy using α parameter, we proposed to define a fractional entropy measure adapted to the framework of statistical region-based active contour segmentation. This entropic descriptor H is defined in the usual way on subregion Ω_i of the image by:

$$H(\Omega_i) = \int_{\Omega_i} \varphi\left(p(\mathbf{I}(\mathbf{x}), \Omega_i)\right) \, d\mathbf{x} \, , \tag{2.13}$$

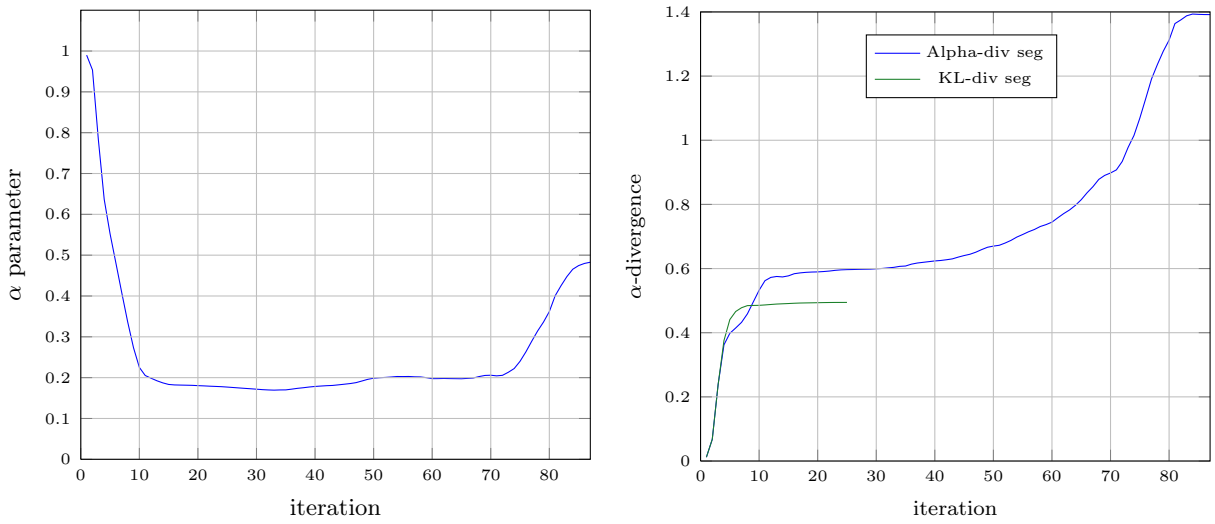

Figure 2.13: Segmentation of a texture image with optimization : Evolution of α parameter and the related divergence during segmentation process. On the right, it can be noticed with the green curve that the KL divergence sticks in a local optimum that does not correspond to the satisfying segmentation.

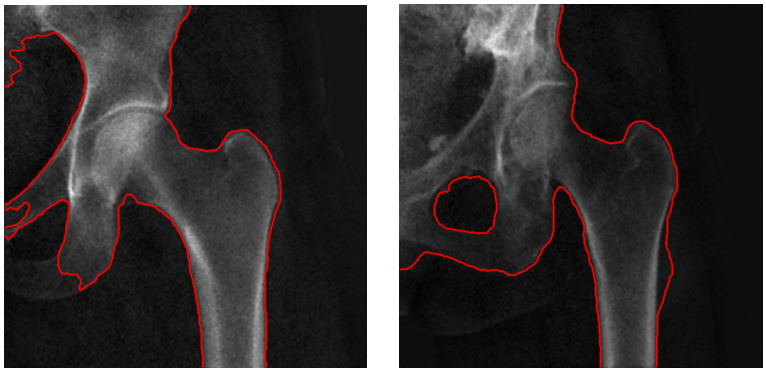

Figure 2.14: Segmentation of X-Ray images using proposed joint optimization of α and related divergence.

with $p(\mathbf{I}(\mathbf{x}), \Omega_i)$ is the PDF of the luminance $\mathbf{I}(\mathbf{x})$ of the pixels of region Ω_i, and φ function and its derivative are given by:

$$\varphi(r) = \varphi_\alpha(r) = -log\,(r^\alpha) \quad \text{and} \quad \varphi'_\alpha(r) = -\frac{\alpha}{r}\,. \tag{2.14}$$

with $\alpha \in [0, 1]$.

In the particular context of TERAFS project and the MSc internship of Mickael Garnier (2012), we carried out experiments on the segmentation of cellular structure in actin tagged-confocal microscopy images. Main objective was to segment the nucleus of each different cell in order to extract shape and texture features for further investigations on effect of a radiation insult (radiotherapy). It turned out that the proposed entropy descriptor was robust even to strong amount of Poisson noise and was able to lead to very satisfying segmentation results as

illustrated in Fig. 2.15 in a level-set framework. This work received the "Best student paper award" of the "Medical Image Understanding and Analysis (MIUA)" 2012, and an extended version of the conference paper was published in 2013 in the "Annals of the British Machine Vision Association".

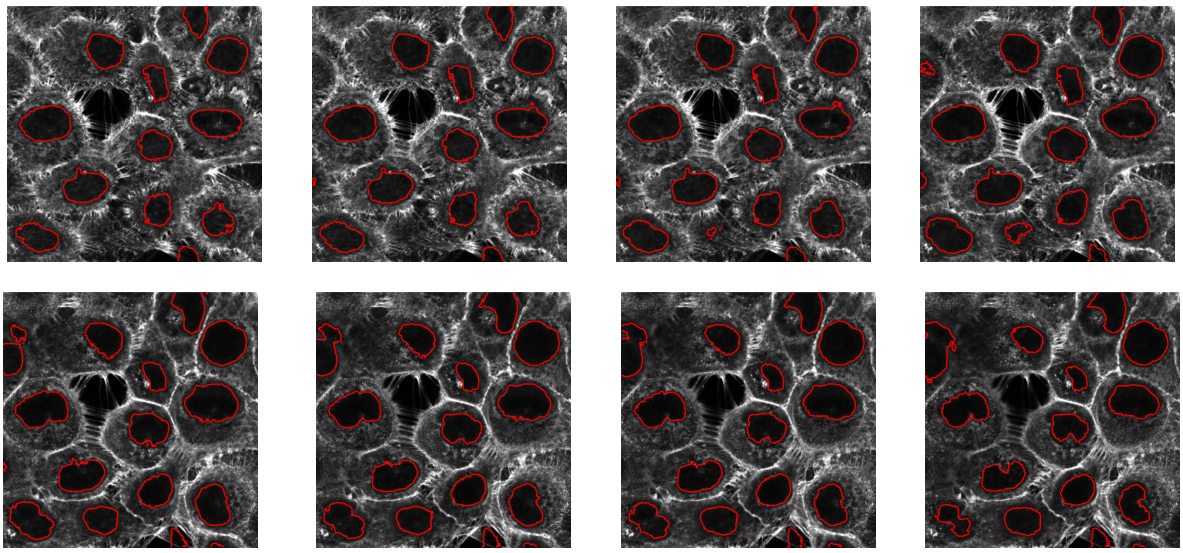

Figure 2.15: Segmentation of nuclei made on different slices of a typical stack of images obtained with laser confocal microscopy. In each case, the segmentation is initialized by a set of small circles regularly dispatched all over the image.

Related publications: [A.1.3, A.3.13 ("Best Student Paper Award")]

2.4 Embeddable Image Processing Tools for Real-Time In Situ Diagnosis

In parallel to the work described above on PDE-based approaches in image processing with application to CAD, I started in 2011 a new collaboration with Prof. Olivier Romain, Head of ASTRE Team of ETIS. Starting point of this joint work is the "Cyclope" project which objective is to propose a new generation of videocapsules with abnormal structure detection/recognition capabilities for early diagnosis of gastrointestinal pathologies.

This collaboration took first the form of a feasibility study on the possibility to use the work achieved during the Leila Meziou's PhD on alpha-divergence on images extracted from a video taken by the videocapsule during its travel along the intestinal tract. This first study help me to be aware of the new constraints the method had to take into account: low energy consumption, low complexity, real-time use. As a consequence, in the following of this first work, we focused our attention on the possibility to provide a full processing scheme for polyp detection and in accordance with the previous constraints.

In the framework of the MSc internship of Juan Silva (2012), we then proposed an entire detection chain that combines geometric and textural features for polyp characterization: If the first geometric step remains simple with the use of the Hough transform, the texture features computed from co-occurrence matrices are integrated within a boosting-based approach making

possible to achieve good classification performance (around 90% of sensibility for 5% False Positive rate). At last, the complete developed detection/classification scheme is in accordance with a hardware implementation which is of primary importance for possible in situ application using WCE. An overview of the global processing scheme is shown in Fig. 2.16 and some examples of detection/recognition are illustrated Fig. 2.17.

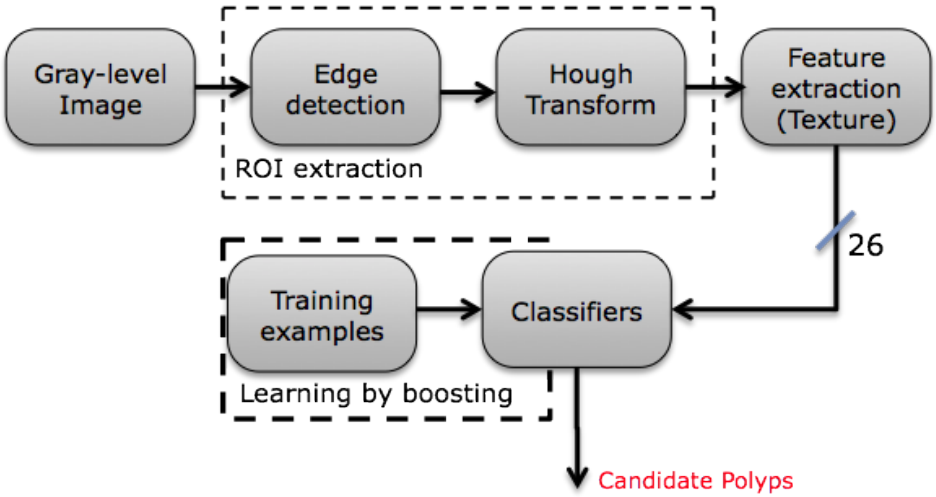

Figure 2.16: Proposed scheme for the detection of polyps within videoendoscopy images.

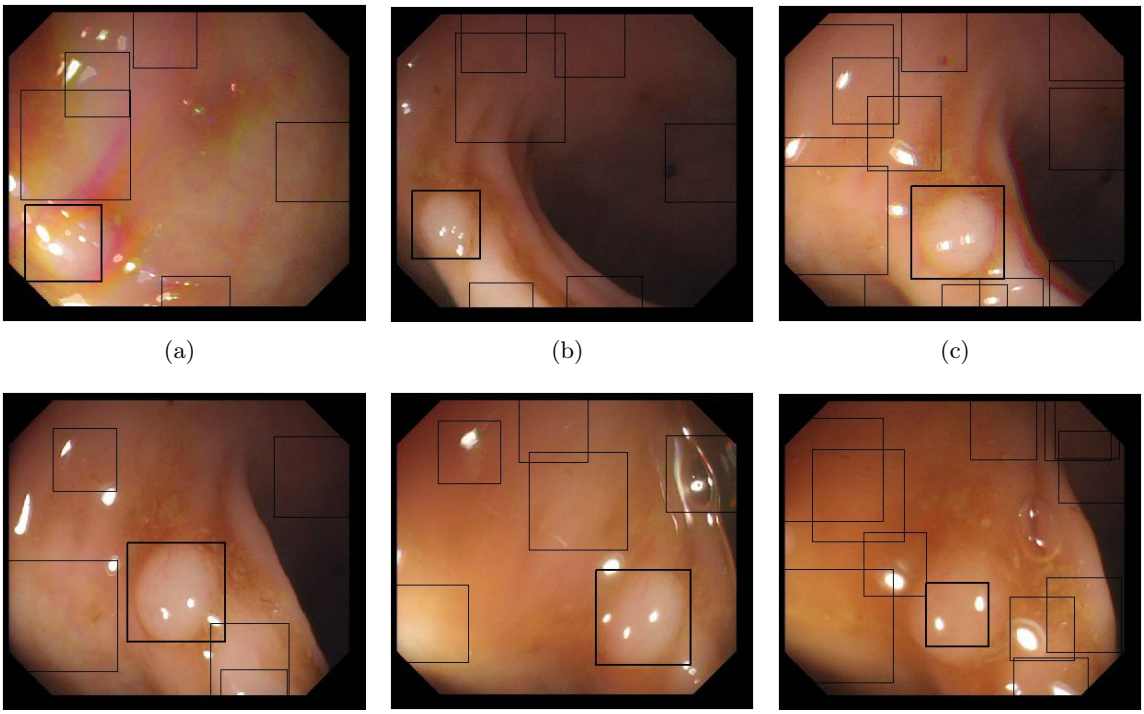

Figure 2.17: Detection examples

In terms of the performance detection mentioned above, a comparison with one of the most recent state-of-the-art paper [Bernal *et al.*, 2012] was proposed and showed some very interesting results as it can be noticed in Fig. 2.18.

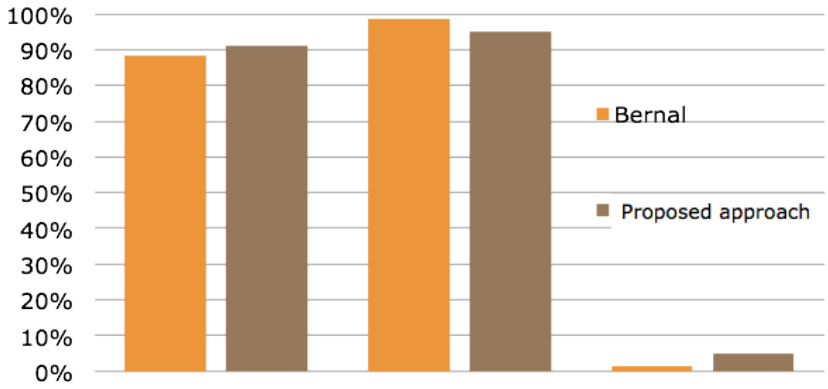

Figure 2.18: Comparison between the method exposed by Bernal *et al.*and the attentional boosting based classification method proposed: from left to right: Sensitivity, Specificity and FPR

Most precisely, considering the classic sensibility, sensitivity and False Positive Rate parameter (FPR), it can be seen that the proposed method is quite competitive.

This work was followed in 2013 by two new MSc internships (Chakib Azib and Augustin Izard) which aim was to practically embed into a FPGA device the algorithms proposed. Currently, a new MSc Student is now working on the practical FPGA embedding of the overall processing scheme in order to provide a first demonstrator that could be used before end of 2014 in a clinical environment.

Related publications: [A.1.1, A.2.1, A.3.5, A.3.7, A.3.8, A.3.9, A.3.10, A.3.14]

2.5 GEODIFF and TRAPIL Project

In addition to the research activities presented here, the work on PDE and Embedded Detection/Recognition algorithms have known kind of extensions in the form of two projects: the GEODIFF (2011-2012) and the TRAPIL projects (2012-2014). This two projects are not included in the second Part of this manuscript, since they are somehow at a too early stage (GEODIFF) for some of the obtained results, and/or developed in collaboration with a private company (TRAPIL). Nevertheless, general information about these two projects are given below.

2.5.1 GEODIFF

Main idea of GEODIFF project is to propose original modelling tools of complex diffusion processes that can lead to a better understanding of some usual natural phenomena like spreading of a disease, forest wildfire or plant growing for instance. That kind of complex diffusion process can be modelled at different scales (micro and macro) using both variationnal approaches or Multi-Agent-Systems (MAS) commonly used within the image analysis and understanding community (with applications to image segmentation, restoration, inpainting): If variationnal approaches are well suited to continuous description of processes like diffusion (macro scale),

MAS brings a different angle, as the whole process is based on some local heuristics leading the behaviour of the agents (in a micro scale) representing part of the whole process. In this latter case, the phenomenon is hard to model by a continuous physical equation.

Formerly, this project was funded by CNRS (PEPS Rupture 2011 Call) and involved ETIS lab and L3i Lab (University of La Rochelle) in the global framework of our long existing collaboration in the area of PDE-based image restoration approach.

Our main contribution to this project was to propose a joint PDE-SMA modelling of a particular pest-insect behavior (the bark beetle) that permits to take into account both the social interaction of the colonies and the physical phenomena related to molecules diffusion that steer the population to move to an other source of food. Main objective is to be able to have a better forecast of the population movement within a forest in order to optimally preserved the resources from devastation (which is currently happening in USA). Since late 2012, this project now include the IRIT lab form he University of Toulouse (Benoit Gaudou) and simulation platform including nonlinear diffusion capabilities has been developed under the GAMMA environment.

Related publications: [A.3.11, A.5.1]

2.5.2 TRAPIL: "Embedded Pipeline Inspection"

Going back to a more traditional image processing, the "TRAPIL: Embedded Pipeline Inspection" project is born from a collaboration with TRAPIL Company (Poissy, France) in 2010 which main activity is to design ultrasonic pipeline inspection devices for non destructive detection and recognition of defect signatures like corrosion for instance. Main challenge is to provide efficient image processing algorithm that would help the analyst (in charge of the psychovisual analysis of the kilometers of data coming from a single inspection) in his daily task.

This collaboration has taken form of a CIFRE PhD for the last 3 years (Clément Fouquet) that is to be defended in June 2014. A complete scheme for the analysis of the ultrasonic data has been proposed, including weld detection, defect signatures detection and recognition using random forest algorithm.

This project was an opportunity to work on a project with very concrete expectations from the companies, since the system has been now partly deployed in the related department, and will be soon entirely functional for a routine use.

Related publications: [A.3.2, A.3.8]

Part II

Research Activities in Details

Chapter 3

Contribution to PDE-Based Approaches for Image Restoration

This Chapter focuses on the scientific contributions to PDE-based image restoration. The main starting idea is to show that the former work of Perona-Malik in that area is still of real interest when considering original diffusive functions like the double-well function proposed or the Stochastic Resonance phenomenon, also known as a constructive action of noise in a nonlinear process.

The different scientific aspects of this Chapter were developed in collaboration with Prof. Michel Ménard (L3i, University of La Rochelle) and Prof. David Rousseau (CREATIS, University of Lyon 1).

In the particular field of image restoration, nonlinear or anisotropic regularization PDE's are of primary interest. The benefit of PDE-based regularization methods lies in their ability to smooth data in a nonlinear way, allowing the preservation of important image features (contours, corners or other discontinuities). In the particular domain of scalar image restoration, the introduction of the Perona–Malik process [Perona and Malik, 1990] in 1990 as triggered a large interest since then:[Alvarez *et al.*, 1992; Catté *et al.*, 1992; Geman and Reynolds, 1992; Nitzberg and Shiota, 1992; Whitaker and Pizer, 1993; Weickert, 1995; Deriche and Faugeras, 1996; Weickert, 1998; Terebes *et al.*, 2002; Tshumperlé and Deriche, 2002; Tschumperle and Deriche, 2005; El Hamidi *et al.*, 2009; Histace and Rousseau, 2010; Guidotti *et al.*, 2013] for a selected list of papers.

In the particular field of medical image processing, PDE based approach for denoising are very promising tools, but generally needs to be adapted to the imaging context (PET, CT, Cone-beam CT, MRI, etc.) since noise can be of very different types (Gaussian, Poisson, Rayleigh). In [Histace *et al.*, 2009], we showed that, considering a particular general parameterizable PDE, it was possible to integrate selectivity regarding the gradient directions to diffuse or not within the considered image. Qualitative and quantitative results were also presented on a particular medical application: enhancement of tagged cardiac MRI.

In the same track, the two following sections introduced two different non-linear PDE inspired by the work of Perona and Malik (PM). More precisely, in a first study, we show that a double-well diffusive function can bring stability and interesting selectivity properties to the classic PM PDE, and in a second one, we investigate the possible benefit effect of a purposely injection of noise in the non-linear process of PM, phenomenon also known as Stochastic Resonance effect.

3.1 Nonlinear PDE-Based Image Restoration Using Double-Well Function for Gradient Selectivity

In the following, we propose a complementary PDE to the one presented in [Histace *et al.*, 2009] which enables integration of selectivity regarding the intensity of the gradient to restore and which makes the preservation of thin structures from the diffusive effect possible. More precisely, we propose to make this selectivity possible thanks to the integration of a double-well potential diffusion function within the classic Perona-Malik's PDE [Perona and Malik, 1990]. That kind of approaches can be of interesting benefits for medical image restoration and particularly for MRI enhancement, since even thin structures can be of primary importance to establish the most appropriate diagnosis.

Our aims and motivation for such a study are mainly to show that, firstly, such a choice can lead to a stable PDE-based approach for scalar image denoising that can overpass classic approach of Perona-Malik's from which it is derived and which presents instability problems as formerly shown in [Catté *et al.*, 1992]. Secondly, we also want to show that this integration leads to a selective PDE-based approach that overcomes classic mean curvature or tensor driven diffusion problems, which in the particular case of directional diffusion are not suitable (see [Histace *et al.*, 2005] and [Terebes *et al.*, 2002]) because they tend to smooth transitions between patterns.

In this section, we propose to tackle a known problem of us: enhancement of tagged cardiac MRI. Such a choice is guided by the fact that we have already worked on that particular MR imaging sequence and that qualitative results have already been computed for comparison. Moreover, this particular sequence of acquisition can be of primary importance for the follow-up of cardiovascular pathologies [Petitjean and Dacher, 2011] and totally fits the problem we want

to address: preservation of thin structures within the enhanced data.

3.1.1 PDE-Based Regularization Approach: A General Framework

In [Deriche and Faugeras, 1996], authors propose a global scheme for PDE-based restoration approaches. More precisely, if we denote $\psi(\mathbf{r},t) : \mathbb{R}^2 \times \mathbb{R}^+ \rightarrow \mathbb{R}$ the time intensity function of a corrupted image $\psi_0 = \psi(\mathbf{r},0)$, the corresponding regularization problem of ψ_0 is equivalent to the minimization problem described by the following PDE:

$$\frac{\partial \psi}{\partial t} = c_\xi(\|\nabla\psi\|)\frac{\partial^2\psi}{\partial\xi^2} + c_\eta(\|\nabla\psi\|)\frac{\partial^2\psi}{\partial\eta^2} \quad , \tag{3.1}$$

where $\eta = \nabla\psi/\|\nabla\psi\|$, $\xi \perp \eta$ and c_ξ and c_η are two weighting functions (also called diffusive functions). This PDE can be interpreted as the superposition of two monodimensional heat equations, respectively oriented in the orthogonal direction of the gradient and in the tangential direction: It is characterized by an anisotropic diffusive effect in the privileged directions ξ and η allowing a non-linear denoising of scalar image. An illustration of the moving vector basis associated to a given is shown Fig. 3.1

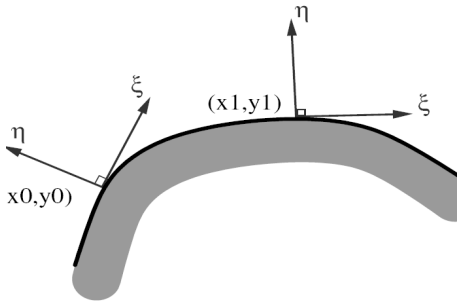

Figure 3.1: An image contour and its moving vector basis (ξ, η). Taken from [Tschumperlé and Deriche, 2002].

Eq. (3.1) is of primary importance, for all classic methods can be expressed in that global scheme: For instance, if we consider the former anisotropic diffusive equation of Perona-Malik's [Perona and Malik, 1990] given by

$$\frac{\partial \psi}{\partial t} = div\left(c(\|\nabla\psi\|)\nabla\psi\right) \ , \tag{3.2}$$

with $\psi(\mathbf{r},0) = \psi_0$ and $c(.)$ a monotonic decreasing function, it is possible to express it in the global scheme of Eq. (3.1) with

$$\begin{cases} c_\xi = c(\|\nabla\psi\|) \\ c_\eta = c'(\|\nabla\psi\|).|\nabla\psi| + c(\|\nabla\psi\|) \end{cases} \tag{3.3}$$

Formulation of Eq. (3.1) is also interested, for it makes stability study of classic proposed methods possible. More precisely, a stable PDE-based method for denoising will be characterized by a weighting function c_η positive for all values of $\|\nabla\psi\|$ as formerly shown in [Catté *et al.*, 1992].

What we proposed here is a prospective study for the integration of a double well potential as a diffusive function $c(.)$ in Eq. (3.2).

3.1.2 Tagged Cardiac MRI

Mainly, to help cardiologists to establish a pre surgery scheme for reperfusion of myocardial tissue after an infarction, a study of the myocardial local viability is necessary: Whereas classic cardiac MRI does not make the study of the local contraction of the myocardium possible, tagged cardiac MRI allows this local estimation. More precisely, the classic SPAMM (Space Modulation of Magnetization) acquisition protocol [Zerhouni *et al.*, 1988] used for the tagging of MRI data, displays a deformable 45-degrees oriented dark grid which describes the contraction of myocardium (Fig. 3.2) on the images of temporal Short-Axis (SA) sequences. This is the temporal tracking of this grid that can enable radiologists to evaluate the local intramyocardial displacement.

Figure 3.2: SA tagged MRI of the Left Ventricle (LV) extracted from a sequence acquired between end-diastole and end-systole.

Tagged cardiac images present peculiar characteristics which make the analysis difficult. More precisely, images are of low contrast compared with classic MRI, and their resolution is only of approximately one centimeter. Numerous studies were carried out concerning the analysis of the deformations of the grid of tag on SA sequences (see [Petitjean *et al.*, 2005; Axel *et al.*, 2007] for a complete overview) but all have in common the necessary enhancement of tagged cardiac images.

Classically, diffusive restoration approaches like the Perona-Malik's former one [Perona and Malik, 1990], perform a non-linear smoothing of the data by taking into consideration the local value of the gradient intensity. This makes the enhancement of the boundaries of the image possible. Nevertheless, as one can notice on Fig. 3.3, due to the fact that norms of the gradient levels of tagged MRI are very noisy, and then unadapted to usual restoration approaches, it is necessary to develop a method that integrates within diffusion process more than only this usual parameter: for instance, calculation and integration of the direction of local gradients of the grid could be of primary interest.

This can be achieved by considering some variations of the usual restoration approaches like, for example, a variant of the Perona-Malik's process [Perona and Malik, 1990] given by

$$\frac{\partial \psi}{\partial t} = div(c(||\mathbf{A}.\nabla\psi||)\nabla\psi) \; . \tag{3.4}$$

with $c(u) = e^{-\frac{u^2}{k^2}}$ and $\mathbf{A}$ is a vector field defining the particular direction(s) to preserve from the diffusion process (in this particular medical application, the gradient direction of the grid). k represents here a soft threshold driving the decrease of $c(.)$. In both cases, the directional weighting of the diffusion process is driven by the scalar product between the norm of the local

(a) (b)

Figure 3.3: (a) Original Image, (b) Norm of the corresponding gradients. As one can notice, the grid of tags does not allow us to obtain a good gradient attractor for a good tracking of the grid.

gradient and **A**. As a consequence when local gradient and **A** are parallel, there is no diffusion, for $c(||\mathbf{A}.\nabla\psi||) = 0$, whereas all other directions are diffused: the grid of tags is enhanced.

Nevertheless, because of instability problems (see section 4 for more details) of PM's approach, it appears that process of Eq. (3.4) does not lead to interesting results. Moreover, the usual $c(.)$ function does not allow to integrate within the iterative restoration scheme selectivity regarding the preservation of particular gradient levels. However, such a selectivity would be of significant benefits since value of the tags' gradient can be easily identified [Denney, 1999].

To overpass the drawbacks of Eq. (3.4) , we propose to define $c(.)$ as a double well potential function. This particular function will make integration of gradient level selectivity possible as well as the obtaining of a stable PDE.

3.1.3 Double Well Potential and Related PDE

3.1.3.1 Diffusive Function

The double well potential considered here is defined by the following function:

$$\phi(u) = \int_0^u v(\alpha - v)(v - 1)dv \ . \tag{3.5}$$

Some graphical representations of Eq. (3.5) for different values of α are proposed Fig. 3.4.(a). The roots of the corresponding non linear force (i.e. $f(u) = u(\alpha - u)(u - 1)$) 0, and 1 corresponds to the local positions of the minima of the potential, whereas the root α represents the position of the potential maximum. The non linearity threshold α defines the potential barrier between the potential minimum with the highest energy and the potential maximum.

This function has to be compared with the usual Perona-Malik's function $c_{PM}(.)$ given by:

$$c_{PM}(u) = e^{-\frac{u^2}{k^2}} \ , \tag{3.6}$$

with k a soft threshold defining selectivity of $c_{PM}(.)$ regarding values of image gradients. Fig. 3.5 shows graphical representations of $c_{PM}(.)$ defined by Eq. (3.6) for different values of k.

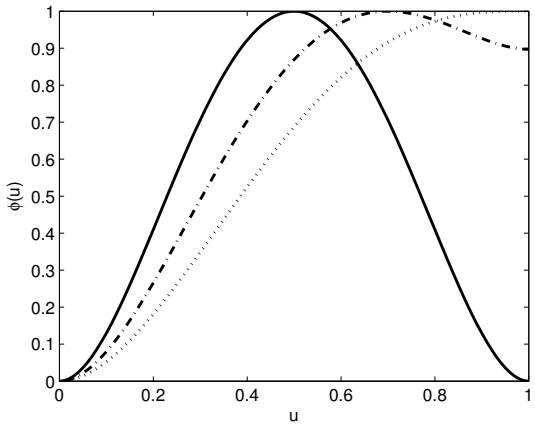

Figure 3.4: plots of double well potential $\phi(.)$ of Eq. (3.5) for different values of $\alpha \in [0.5, 1]$. Solid lines stand for $\alpha = 0.5$, dash-dotted lines for $\alpha = 0.7$ and dotted lines for $\alpha = 1$.

As one can notice on Fig. 3.5.(a), for $\|\nabla\psi\| \to 0$, $c_{PM}(\|\nabla\psi\|) \to 1$, whereas for $\|\nabla\psi\| \to 1$, $c_{PM}(\|\nabla\psi\|) \to 0$. As a consequence, boundaries within images which are on a threshold, function of k, are preserved from the smoothing effect of Eq. (3.2). Regarding Fig. 3.4, in order to preserve this major property with integration of Eq. (3.5) as a diffusive function in Eq. (3.2), it is necessary to define this diffusive function as follows:

$$c_{DW}(u) = 1 - \phi(u) \ . \tag{3.7}$$

Graphical representations of c_{DW} are proposed in Fig. 3.6.

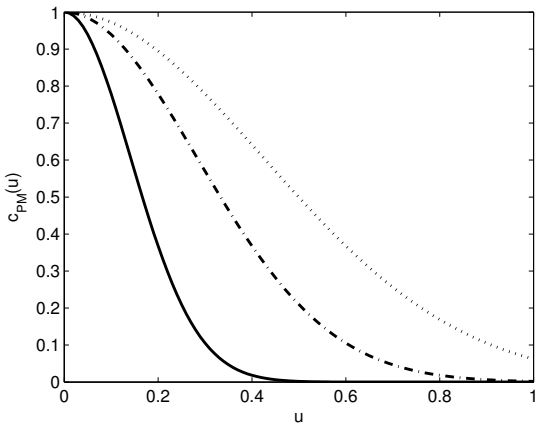

Figure 3.5: Plots of function $c_{PM}(.)$ of Eq. (3.6) for different values of k. Solid lines stand for $k = 0.2$, dash-dotted lines for $k = 0.4$, and dotted lines for $k = 0.6$.

One can notice on Fig. 3.4 that $\phi(.)$ has been normalized. As a consequence, we are able to ensure that $0 \leq c_{DW}(u) \leq 1$ for all values of u like usual PM's function of Eq. (3.2). Global variations of c_{DW} can be compared to those of c_{PM} for $\alpha = 0$ and $\alpha = 1$. For $0 \leq \alpha < 1$, since c_{DW} is issued from a double well potential, selectivity of Eq. (3.2) is more important and

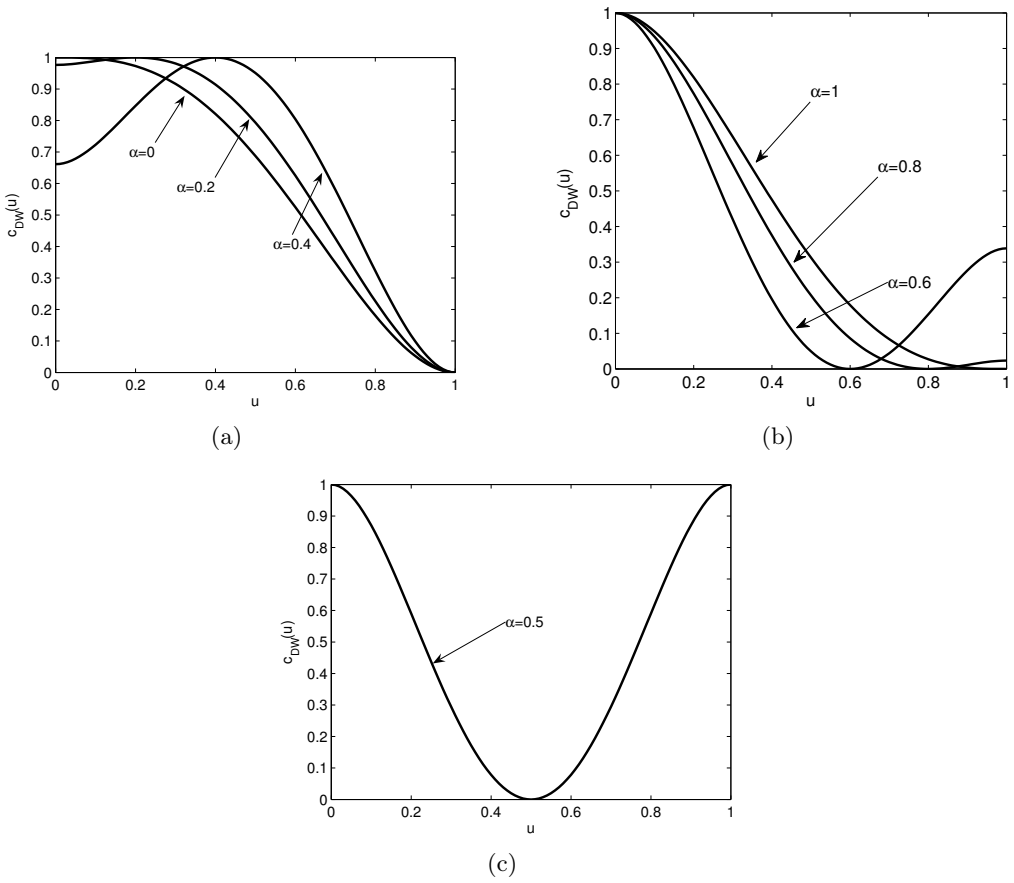

(a) (b)

(c)

Figure 3.6: Plots of function $c_{DW}(.)$ of Eq. (3.5) for different values of α: (a) $0 < \alpha < 0.5$, (b) $0.5 < \alpha < 1$, and (c) $\alpha = 0.5$.

centered on a particular gradient value function of α. For instance, for $\alpha = 0.5$, only gradients of value 0.5 are totally preserved from the diffusive effect that can be interpreted as an integration of gradient level selectivity within the restoration process.

Moreover, we are now going to show, that integration of c_{DW} as diffusive function leads to interesting stability property of corresponding PDE.

3.1.3.2 Study of Stability

It is recognized that usual Perona-Malik's PDE presents instability problems. More precisely, as shown in [Catté *et al.*, 1992], sometimes noise can be enhanced instead of being removed. This can be explained considering Eq. (3.3). If we consider $c_{PM}(.)$ function, it appears that corresponding c_η function of Eq. (3.3), in the global scheme of Eq. (3.1), can sometimes takes negative values (see Fig. 3.7.(a) for illustrations). This leads to local instabilities of the Perona-Malik's PDE which degrades the processed image instead of denoising it.

Now, if we calculate mathematical expression of c_η with $c(.) = c_{DW}(.)$ of Eq. (3.7), one can obtain that:

$$c_\eta(\|\nabla\psi\|) = c'_{DW}(\|\nabla\psi\|).|\nabla\psi| + c_{DW}(\|\nabla\psi\|)\ , \tag{3.8}$$

that can be written:

$$c_\eta(\|\nabla\psi\|) = \|\nabla\psi\|(\alpha - \|\nabla\psi\|)(\|\nabla\psi\| - 1).|\nabla\psi|$$

$$+1 - \frac{\|\nabla\psi\|^3}{3}(\alpha + 1) + \frac{\|\nabla\psi\|^2}{2}(\alpha + \frac{\|\nabla\psi\|^2}{2}). \tag{3.9}$$

Considering Eq. (3.9), if we plot this function, one can notice that corresponding c_η function never takes negative values (see Fig. 3.7.(b) for illustrations): Diffusive process remains stable for all gradient values of processed image which is of primary importance.

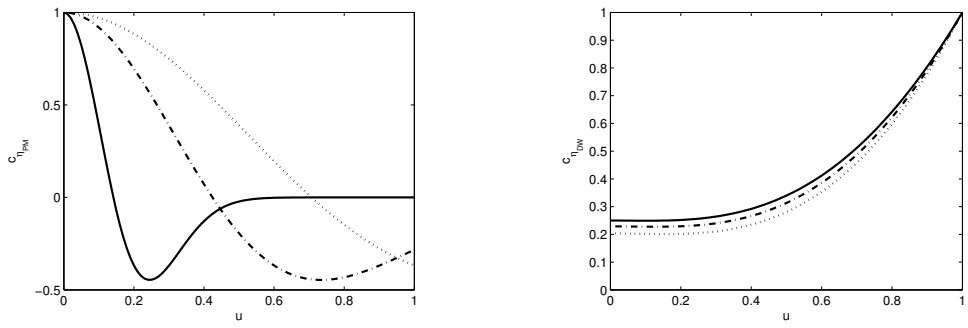

(a) (b)

Figure 3.7: Plots of function $c_{\eta_{PM}}$ and $c_{\eta_{DW}}$ for different values of k and α. Solid lines stand for $k = 0.2$ and $\alpha = 0.5$, dash-dotted lines for $k = 0.4$ and $\alpha = 0.7$ and dotted lines for $k = 0.6$ and $\alpha = 1$.

3.1.4 Experimental Results

We propose in this section to make a visual and quantitative comparison between usual Perona-Malik's PDE of Eq. (3.2) with diffusive function $c(.) = c_{PM}(.)$ of Eq. (3.6), and proposed derived PDE with $c(.) = c_{DW}(.)$ of Eq. (3.7) as diffusive function.

For practical numerical implementations, the process of Eq. (3.2) is sampled with a time step τ. The restored images $\psi(t_n)$ are calculated at discrete instant $t_n = n\tau$ with n the number of iterations.

3.1.4.1 Synthetic Images

The first proposed image is the binary image of Fig. 3.8.(a) corrupted by a white gaussian noise of mean zero and standard deviation σ.

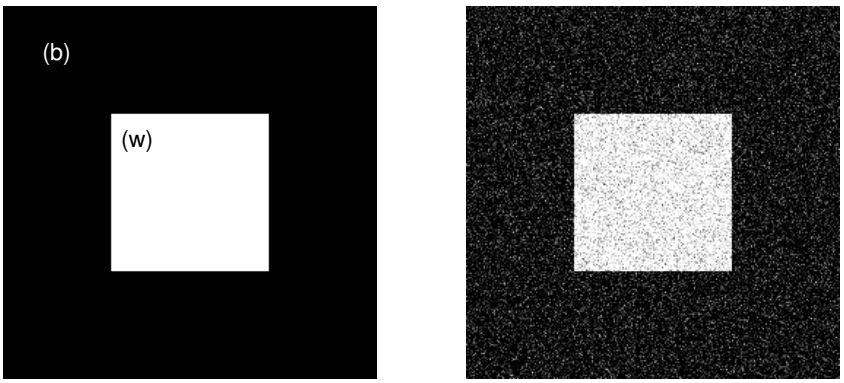

(a) (b)

Figure 3.8: (a) Original synthetic image and (b) its corrupted version ψ_0 . Corrupting noise is a white Gaussian one of mean zero and standard deviation $\sigma = 0.05$.

Considering binary nature of non corrupted image (Fig. 3.8.(a)), quantification of the denoising effect of Eq. (3.2) with $c(.) = c_{PM}(.)$ and $c(.) = c_{DW}(.)$, will be estimated with Fisher's index given by

$$I_{Fisher} = \frac{(m_w - m_b)^2}{\sigma_w^2 + \sigma_b^2} \ , \tag{3.10}$$

with $m_{w,b}$ the average value of the pixels of the restored image $\psi(t_n)$ being originally in the white (w) or black (b) part of original image (Fig. 3.8.(a)) and $\sigma_{w,b}$ the corresponding standard deviation. One can notice that $I_{Fisher} \to \infty$ for original non corrupted image of Fig. 3.8.(a).

Because aim of this study is to show potentiality of the described restoration method, only optimal results for both compared approaches are presented Fig. 3.9: Values of k and α parameters are empirically chosen and strategy for optimal choice is not describe here.

As one can notice on Fig. 3.9, both visually and quantitatively, restoration of binary image of Fig. 3.8.(a) is better with the diffusive function of Eq. (3.5). More precisely, stability property of the double well function prevents restoration process from possible enhancement of corrupting Gaussian noise. Homogenous areas of Fig. 3.9.(b) does not visually shows oscillations, nor corners of the white square as in Fig. 3.9.(a). This visual impression is confirmed by variations of Fisher's index in Fig. 3.9.(c) that reaches a level third times more important than with usual approach of Perona-Malik's. At last, one can also notice that this higher maximum is obtained faster than with usual approach: only one hundred iterations is needed for proposed approach

(a) (b)

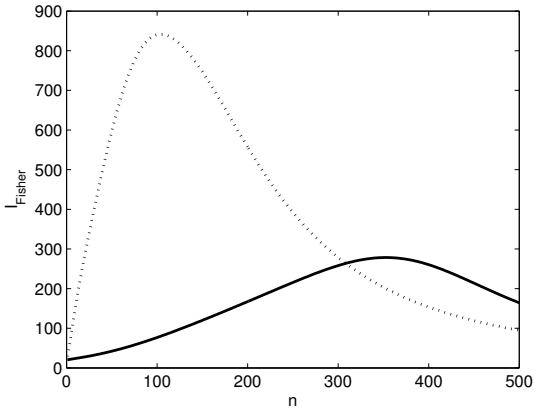

(c)

Figure 3.9: (a) Restored image with $c(.) = c_{PM}(.)$ (usual Perona-Malik's approach), (b) Restored image with $c(.) = c_{DW}(.)$ (proposed approach), (c) Fisher index function of iteration number n, solid lines stands for usual Perona-Malik's approach, dotted line stands for proposed method. k is equal to 0.4, α is equal to 0.5 (these values have been empirically tuned).

of Eq. (3.5) compare to the nearly four hundred iterations of the usual approach of Eq. (3.6). The value of α parameter corresponding to best results is 0.5: this is not surprising, for it is also the value of the gradient intensity characterizing the boundaries of the with square. As a consequence, this experiment also confirmed the possible gradient intensity selectivity of the proposed approach interpreted as a directional diffusion process.

We shall now experiment the proposed approach in the context of restoration of real scalar images.

3.1.4.2 Lena... Of Course

We propose to compare both our proposed method with PM's approach on the usual "lena" image. For our purpose, this latter has been corrupted by a white gaussian noise of mean zero and standard deviation σ (see Fig. 3.10).

(a) (b)

Figure 3.10: (a) Original image "lena" and (b) its corrupted version ψ_0 . Corrupting noise is a white Gaussian one of mean zero and standard deviation $\sigma = 0.1$.

Considering nature of non corrupted image (Fig. 3.10.(a)), quantification of the denoising effect of Eq. (3.2) with $c(.) = c_{PM}(.)$ and $c(.) = c_{DW}(.)$, will be estimated with a usual PSNR measurement.

Once again, because aim of this work is to show potentiality of the described restoration method, only optimal results for both compared approaches are presented Figs. 3.11 and 3.12.

One can notice on Figs. 3.11 and 3.12 that both visually and quantitatively, it is possible to find a value of α that can outperform results of optimal usual PM's approach. Although the number of iterations corresponding to the optimal restoration results is, this time, more important with the proposed approach than with PM's approach, quantitatively speaking PSNR is around 2dB higher and visually speaking, boundaries on Fig. 3.11.(b) are preserved in a better way from the diffusion effect.

3.1.4.3 Tagged Cardiac MRI Enhancement

We now focus this study on tagged cardiac MRI enhancement.

What we propose here is to compare enhancement results obtained with: (a) the usual PM's approach, (b) the usual Weickert's approach [Weickert, 1995] (Edge Enhancing Diffusion-EED),

(a) (b)

Figure 3.11: (a) Restored image with $c(.) = c_{PM}(.)$ (usual Perona-Malik's approach), (b) Restored image with $c(.) = c_{DW}(.)$ (proposed approach). The red circles highlight some regions of interest where the preservation of edges are better than with Perona-Malik's approach. k is equal to 1 for PM's restoration approach, α is equal to 0.8 for proposed approach (these values have been empirically tuned).

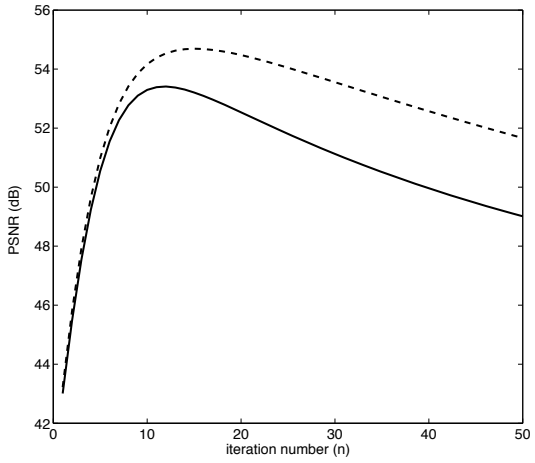

Figure 3.12: PSNR function of iteration number n, solid lines stands for usual Perona-Malik's approach, dotted line stands for proposed method. k is equal to 0.5, α is equal to 0.2 (these values have been empirically tuned to obtained the best denoising effects). These two curves have been computed by calculation of the mean results obtained for one hundred different realizations of the gaussian corrupting noise.

(c) with PM's approach integrating $c_{DW}(.)$ function, and (d) with the following PDE:

$$\frac{\partial \psi}{\partial t} = div(c_{DW}(||\mathbf{A}.\nabla\psi||)\nabla\psi) \ . \tag{3.11}$$

c_{DW} function is set in order to preserve the gradient level of the tag from diffusion.

To obtain restoration results with Eq. (3.11) only one direction of the grid has been taken into account thanks a judicious computation of $\mathbf{A}$. More precisely, each local a priori direction of the corresponding gradient has been estimated thanks to a frequential analysis of processed image (see [Histace *et al.*, 2009] for full detailed of the method). In order to compute a precise estimation of $\mathbf{A}$ from the frequential analysis, we propose to directly use the method of Rao [Rao and Jain, 1992] and Terebes [Terebes *et al.*, 2002]. Parameter α of the double well potential is set empirically to 0.5 [Denney, 1999]. As a consequence, each a priori gradient direction computed from the frequential analysis is preserved from diffusion effect thanks to $\mathbf{A}$, and $c_{DW}(.)$ function makes the enhancement of the tag possible by preserving the gradient level of tags from diffusion.

As one can notice, the grid enhancement performed thanks to the usual PM's approach (Fig. 3.13.(b)) presents strong instabilities. As a consequence, the resulting enhanced grid is corrupted and presents no real interest for the tracking of the grid. Considering now the usual Weickert's EED (Fig. 3.13.(c), one can clearly notice that the method fails in enhancing the tag pattern. This is mainly due to the fact that the poor quality of the tagged MR images makes the computation of the local structure tensor difficult. Fig. 3.13.(d) shows results obtained with usual PM's approach but with $c(.) = c_{DW}(.)$. The first consequence of such a choice for $c(.)$ function is the absence of stability problems within the iterative enhancing resulting process. As one can see, visually speaking the grid is enhanced and the corresponding boundaries are preserved from the diffusion effect. If such a result is of real interest, enhancement effect can be outperformed by considering Eq. (3.11). This time, result shown Fig. 3.13.(e) clearly demonstrates the possibility of enhancing the tag patterns by selecting (i) a particular direction, locally computed thanks to a frequential analysis, and (ii) a particular gradient-level characterizing the boundaries of the tags.

3.1.5 Conclusion and Perspectives

In this work, we have proposed an alternative diffusive function for restoration of scalar images within the framework of PDE-based restoration approaches. The proposed diffusive function allows integrating prior knowledge on the gradient level to restore thanks parameter α of Eq. (3.7) and remains always stable on the contrary of usual PM's approach. Proposed method also remains fast and easy to compute. Quantitatively speaking, better restoration results have been obtained, but this point must be now discussed. Since α parameter finally corresponds to integration of prior information about gradient level to preserve from the diffusion process, it would be interesting to make a adaptive local use of the proposed approach more than a global use.

If interesting visual and quantitative results have been obtained on "lena" image thanks to a global use of the proposed PDE, we have also shown that a local tuning of this parameter in terms of particular localization within the processed image could lead to more interesting results than usual approaches on a particular medical application: enhancement of tagged cardiac MR images. Strategy of this local tuning and more precisely about the local calculation of gradient intensity to preserve still to be now completely automatized. For instance, In the framework of tagged cardiac MRI, it could be of primary interest for the method to be able to adapt the value

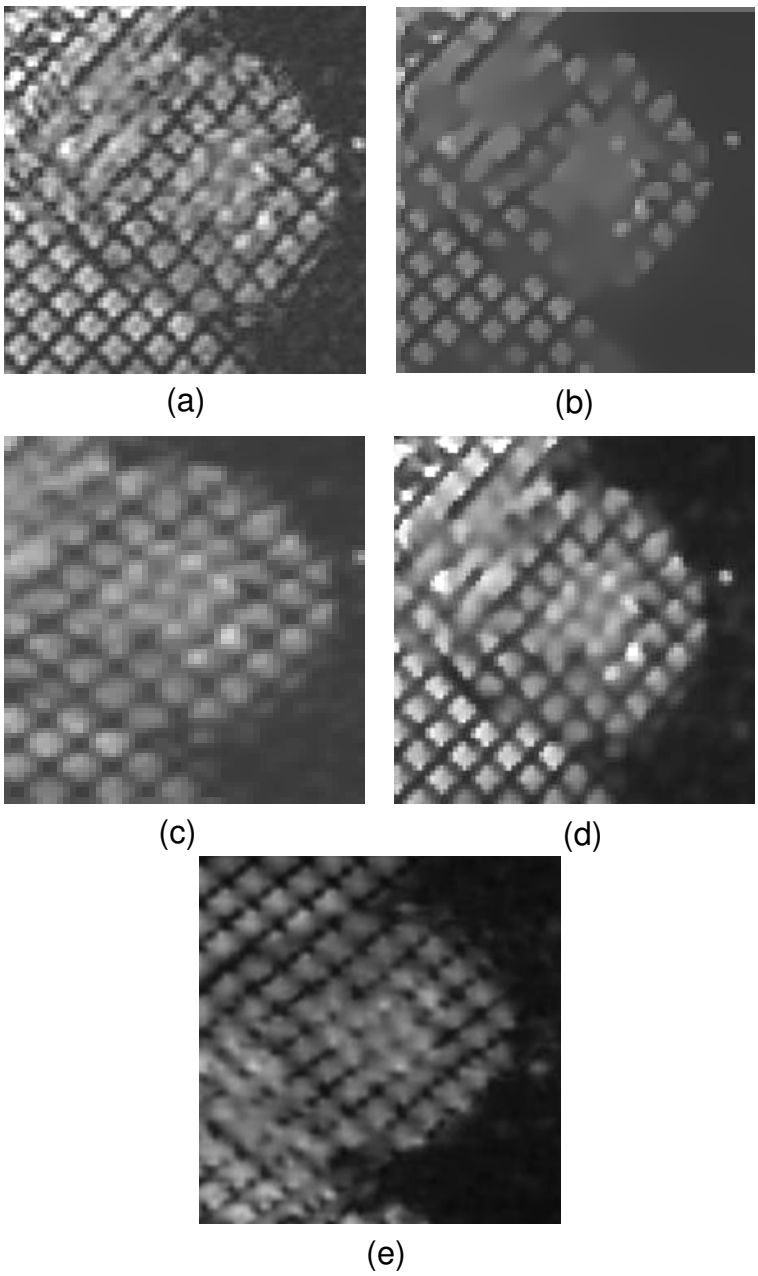

Figure 3.13: Tagged MRI restoration: (a) Original image, (b) PM's approach, (c) Weickert's approach, (d) PM's approach with $c(.) = c_{DW}(.)$, (e) Result obtained with Eq. (3.11). "Optimal" visual results for each methods are shown.

of α to the fading of the tags due to the non persistency of the magnetization corresponding to the grid (see Fig. 3.2). More precisely, the fact that this fading phenomenon can be analytically studied would permit such an adaptive setting of α. Moreover, if in this example we choose to select the gradient-level, one could also think about integrating a selectivity upon the grey-level to diffuse or not. This can be achieved by considering a variant of Eq. (3.11) given by

$$\frac{\partial \psi}{\partial t} = c_{DW_1} div(c_{DW_2}(||\mathbf{A}.\nabla\psi||)\nabla\psi) \; . \tag{3.12}$$

In this equation, c_{DW_2}, as previously shown, permits a selectivity regarding gradient-level, and c_{DW_1} could permit a selectivity in terms of grey-level intensity. Considering the fact that the gey-level intensity of the myocardium is different from the grey-level intensity of the tags, this approach could be a good alternative for enhancement of tagged cardiac MRI, but also for MR images in general.

3.2 Useful Noise Effect for Nonlinear-PDE-Based Image Restoration of Scalar Images

It is progressively realized that noise can play a constructive role in the domain of nonlinear information processing. The starting point of the investigation of such useful noise effect has been the study of stochastic resonance [Benzi *et al.*, 1981; Benzi *et al.*, 1982; Wiesenfeld and Moss, 1995]. Originally introduced to describe the mechanism of a constructive action of a white Gaussian noise in the transmission of a sinusoid by a nonlinear dynamic system governed by a double well potential [Gammaitoni *et al.*, 1989; McNamara and Wiesenfeld, 1989], the phenomenon of stochastic resonance has experienced large varieties of extensions with variations concerning the type of noise, the type of information carrying signal or the type of nonlinear system interacting with the signal-noise mixture (see [Gammaitoni *et al.*, 1998] for a review in physics, [Harmer *et al.*, 2002] for an overview in electrical engineering and [Chapeau-Blondeau, 2000; Chapeau-Blondeau and Rousseau, 2002] for the domain of signal processing). All these extensions of the original setup preserve the possibility of improving the processing of a signal by means of an increase in the level of the noise coupled to this signal. New forms of useful-noise effect, related to stochastic resonance or not, continue to be demonstrated [Ye *et al.*, 2003; Ye *et al.*, 2004; Blanchard *et al.*, 2008; Morfu *et al.*, 2008; Morfu, 2009; V.P. and Kumar Roy, 2010; Rousseau *et al.*, 2010]. A current domain of interest is the study of nontrivial transposition of stochastic resonance to image processing [Bohou *et al.*, 2007b; Bohou *et al.*, 2007a; Renbin *et al.*, 2007; Yang *et al.*, 2009; Jha *et al.*, 2012] and more particularly to nonlinear image restoration.

3.2.1 Global Framework of Stochastic Resonance

From an informational point of view [Chapeau-Blondeau, 2000], stochastic resonance (SR) can be described with the general scheme of Fig. 3.14 which involves four essential elements: (i) an information-carrying or coherent signal s: it can be deterministic, periodic or non, or random; (ii) a noise η, whose statistical properties can be of various kinds (white or colored, Gaussian or non,...); (iii) a process, which generally is nonlinear, receiving s and η as inputs under the influence of which it produces the output signal y; (iv) a measure of performance, which quantifies the input–output information transmission (it may be a signal-to-noise ratio, a correlation coefficient, a Shannon mutual information, ...). By contrast with the informational scheme of Shannon, the noise in Fig. 3.14 is considered as an input with a tunable level. A useful-noise effect occurs when the input–output information transmission, assessed with the chosen measure of performance, is enhanced from an increase of the level of the noise.

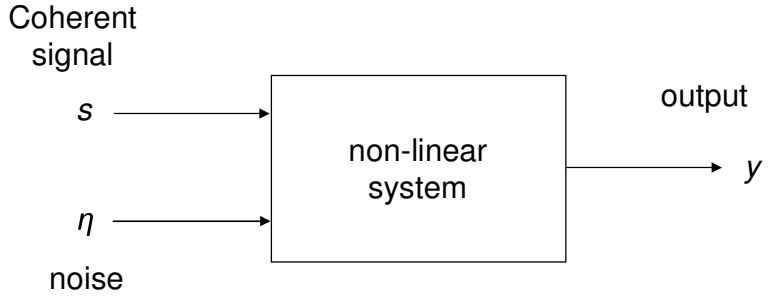

Figure 3.14: Stochastic resonance consists in the possibility of increasing the transmission of information between the input signal s and the output signal y by means of an increase of the level of the noise η.

Historically, the developments of SR have proceeded through variations and extensions over these four basic elements. From the origin, SR studies have concentrated on a periodic coherent signal s, transmitted by nonlinear systems of a dynamic and bistable type. This form of SR now appears simply as a special form of useful-noise effect. This primary form of SR will not be entirely described here but a complete description can be found in [Gammaitoni *et al.*, 1989; McNamara and Wiesenfeld, 1989] for instance. For illustration, we propose to illustrate phenomenon of SR in the framework of image transmission as it was formerly proposed in [Chapeau-Blondeau, 2000]. This example has the advantage of its simplicity which makes both theoretical and experimental analysis possible. Leaning again on the general scheme of SR phenomenon, author considers this time that the coherent information-carrying signal s is a bidimensional image where the pixels are indexed by integer coordinates (i, j) and have intensity $s(i, j)$. For a simple illustration, a binary image with $s(i, j) \in \{0, 1\}$ is considered for experiment. A noise $\eta(i, j)$, statistically independent of $s(i, j)$, linearly corrupts each pixel of image $s(i, j)$. The noise values are independent from pixel to pixel, and are identically distributed with the cumulative distribution function $F_\eta(u) = Pr\{\eta(i, j) \leq u\}$. A nonlinear detector, that it is taken as a simple hard limiter with threshold θ, receives the sum $s(i, j) + \eta(i, j)$ and produces the output image $y(i, j)$ according to:

$$\begin{array}{lll} \text{If } s(i,j)+\eta(i,j) > \theta & \text{then} & y(i,j) = 1, \\ & \text{else} & y(i,j) = 0. \end{array} \tag{3.13}$$

When the intensity of the input image $s(i, j)$ is low relative to the threshold θ of the detector, i.e. when $\theta > 1$, then $s(i, j)$ (in the absence of noise) remains undetected as the output image $y(i, j)$ remains a dark image. Addition of the noise $\eta(i, j)$ will then allow a cooperation between the intensities of images $s(i, j)$ and $\eta(i, j)$ to overcome the detection threshold. The result of this cooperative effect can be visually appreciated on Fig. 3.15, where an optimal nonzero noise level maximizes the visual perception.

Figure 3.15: The image $y(i, j)$ at the output of the detector of Eq. (3.13) with threshold $\theta = 1.2$, when $\eta(i, j)$ is a zero-mean Gaussian noise with rms amplitude 0.1 (left), 0.5 (center) and 2 (right).

To quantitatively characterize the effect visually perceived in Fig. 3.15, an appropriate quantitative measure of the similarity between input image $s(i, j)$ and output image $y(i, j)$, is provided by the normalized cross-covariance defined in [Vaudelle *et al.*, 1998] and given by:

$$C_{sy} = \frac{\langle (s - \langle s \rangle)(y - \langle y \rangle) \rangle}{\sqrt{\langle (s - \langle s \rangle)^2 \rangle \langle (y - \langle y \rangle)^2 \rangle}} , \tag{3.14}$$

where $\langle . \rangle$ denotes an average over the images.

C_{sy} can be experimentally evaluated through pixels counting on images similar to those of Fig. 3.15. Also, for the simple transmission system of Eq. (3.13), C_{sy} can receive explicit

theoretical expressions, as a function of $p_1 = Prs(i,j) = 1$ the probabilty of a pixel at 1 in the binary input image $s(i,j)$, and as a function of the properties of the noise conveyed by $F_\eta(u)$ as mentioned in [Vaudelle *et al.*, 1998].

Considering the above scenario, Fig. 3.16 shows variations of C_{sy} function of rms amplitude of the input noise η.

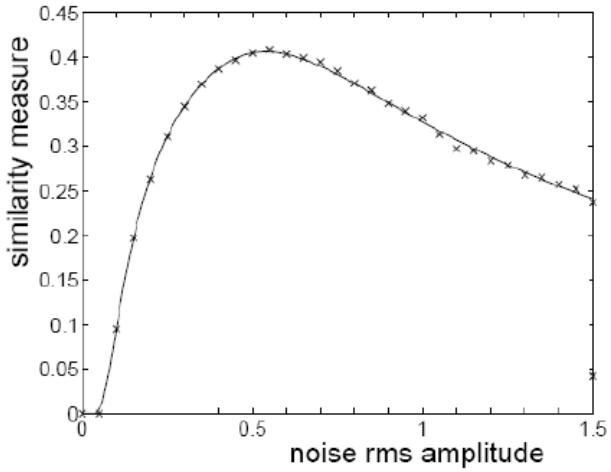

Figure 3.16: Input-output cross-covariance of Eq. (3.14) between input image $s(i,j)$ and output image $y(i,j)$, as a function of the rms amplitude of the noise $\eta(i,j)$ chosen zero-mean Gaussian. The crosses are experimental evaluations through pixels counting on images, the solid lines are the theoretical predictions ($p_1 = 0.6$) calculated by Chapeau *et al.*.

As one can see on Fig. 3.16, measure of cross-covariance as defined Eq. (3.14) identify a maximum efficacy in image transmission for an optimal nonzero noise level. This simple example is interpreted here as the first formalized instance of SR for aperiodic bidimensionnal input signal s (even if it is not clearly an image processing application).

We are now going to show that this kind of approach can be successfully transposed in the framework of nonlinear-PDE-based image restoration approach.

3.2.2 A Stochastic Variant of The Perona–Malik Process for Image Restoration

In the original Perona–Malik process the observable noisy image ψ_0 is restored by considering the solution of the partial differential equation given by

$$\frac{\partial \psi}{\partial t} = div(g(\|\nabla\psi\|)\nabla\psi), \qquad \psi(x,y,t=0) = \psi_0 \ , \tag{3.15}$$

where the anisotropy of this diffusion process is governed by $g(\cdot)$ a nonlinear decreasing function of the norm of the gradient $\nabla\psi$. In this study, we consider a variant of the standard Perona–Malik's process of Eq. (3.15) introduced in [Histace and Rousseau, 2006], where the anisotropic diffusion process, given by

$$\frac{\partial \psi}{\partial t} = div(g_\eta(\|\nabla\psi\|)\nabla\psi) \ , \tag{3.16}$$

which is of a form similar to Eq. (3.15) except for the nonlinear function $g_\eta(\cdot)$ which is given by

$$g_\eta(u) = g(u + \eta(x,y)) \ , \tag{3.17}$$

where η is a noise assumed independent and identically distributed with probability density function $f_\eta(u)$ and rms amplitude σ_η. The noise η, which is distinct from the native noise component ξ to be removed, is a purposely added noise applied to influence the operation of $g(\cdot)$. In [Histace and Rousseau, 2006], we have shown that the injection of a Gaussian noise in Eq. (3.17) can improve the restoration process by comparison with standard Perona-Malik process of Eq. (3.15) when the native noise component ξ is a Gaussian, impulsive or multiplicative noise and with $g(\cdot)$ given by

$$g(u) = e^{-\frac{\|u\|^2}{k^2}} \ . \tag{3.18}$$

In this expression, parameter k can be seen as a soft threshold controlling the decrease of $g(\cdot)$ and the amplitude of the gradients to be preserved from the diffusion process. Our previous works [Histace and Rousseau, 2006] and [Histace and Rousseau, 2007] have shown, as a proof of feasability, that an injection of a non zero amount of noise could help the restoration process when the threshold k is ill-positioned.

3.2.2.1 Preliminary Results

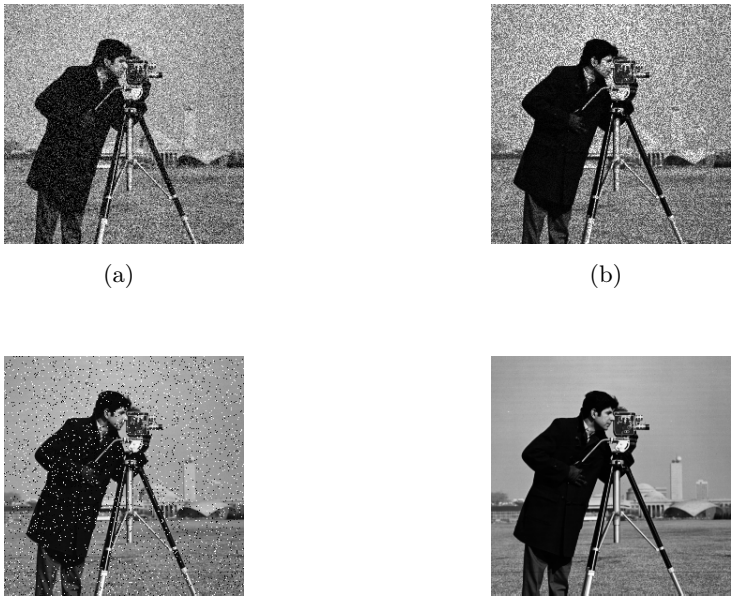

(a) (b) (c) (d)

Figure 3.17: The original image ψ_{ori} cameraman (d) corrupted by three different native noises ξ: (a) additive zero-mean Gaussian noise with $\psi_0 = \psi_{ori} + \xi$, (b) multiplicative Gaussian noise of mean unity with $\psi_0 = \psi_{ori} + \xi.\psi_{ori}$, (c) impulsive noise.The rms amplitude of these noises are separately adjusted in order to have each of the images (a,b,c) characterized by the same normalized crosscovariance (given in Eq. (3.19)) with the original image equal to 0.87.

For illustration, the image "cameraman" (see image (d) in Fig. 3.17), is chosen as reference for the original image ψ_{ori}. Noisy versions of this original image are presented as the observable images ψ_0 of our restoration task in Fig. 3.17 for various image–noise coupling.

A visual appreciation of the performance of the stochastic version of Perona–Malik process of Eq. (3.16) and the original Perona–Malik process of Eq. (3.15) is shown in Fig. 3.18.

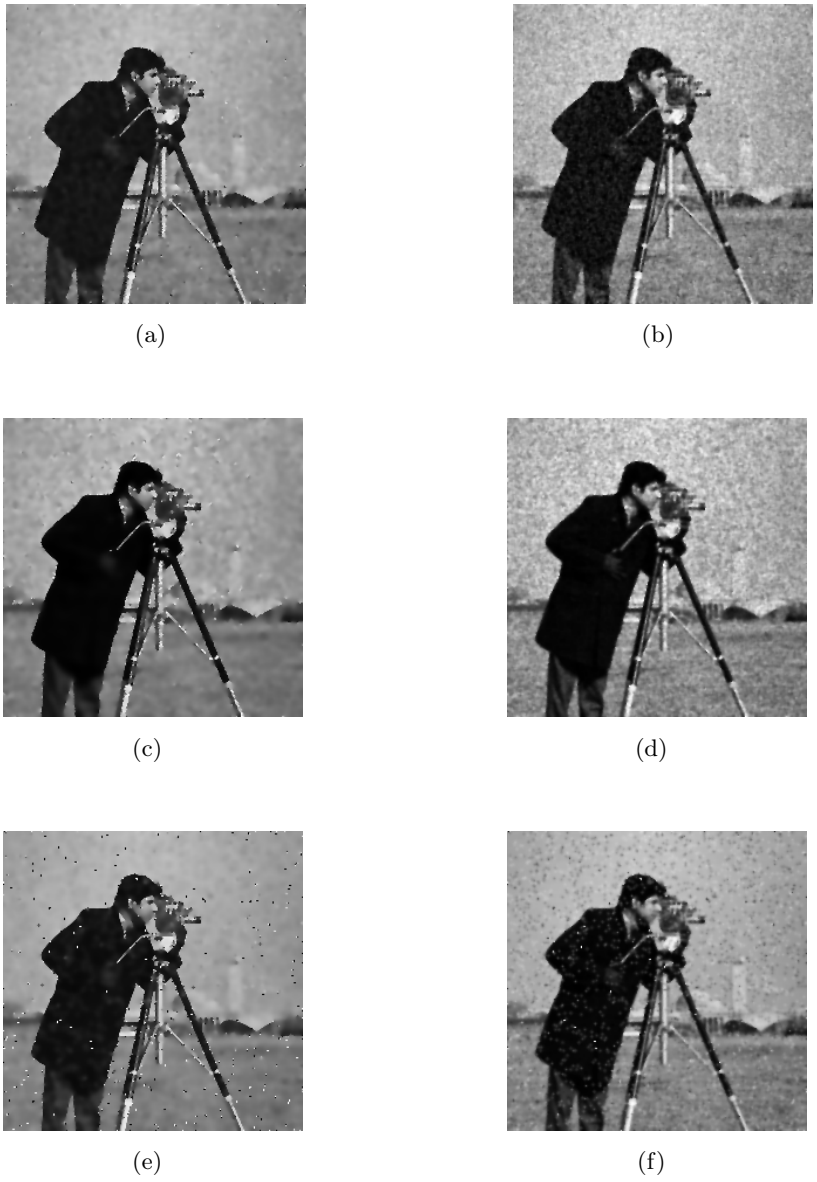

(a) (b) (c) (d) (e) (f)

Figure 3.18: Visual comparison of the performance of the original restoration Perona–Malik process and the corresponding stochastic version. The left column shows the results obtained with usual Perona-Malik restoration process and the right column with our stochastic version of the Perona–Malik process. Each image is obtained with the iteration number n corresponding to the highest value of the normalized crosscovariance. The top (a,b), middle (c,d) and bottom (e,f) lines are respectively standing for the additive, multiplicative and impulsive noise component described in Fig. 3.17.

The images restored by the stochastic process appear to be of better visual interest than those obtained with the usual Perona–Malik process for all the three types of noise component tested. This is especially visible, in Fig. 3.18, in areas of the "cameraman" image characterized by small gradients (face, buildings in the background, or textured area like grass) which are preserved from the diffusion process and better restored with the presented stochastic approach than with the usual Perona–Malik process.

A quantitative analysis is presented in Fig. 3.19 where the number of iteration n of the diffusion processes is fixed. For our purpose, the normalized crosscovariance is adapted to the framework of image restoration by iterative process considering the following equation:

$$C_{\psi_{ori}\psi(t_n)} = \frac{\langle(\psi_{ori} - \langle\psi_{ori}\rangle)(\psi(t_n) - \langle\psi(t_n)\rangle)\rangle}{\sqrt{\langle(\psi_{ori} - \langle\psi_{ori}\rangle)^2\rangle\langle(\psi(t_n) - \langle\psi(t_n)\rangle)^2\rangle}} \quad , \tag{3.19}$$

with $\langle..\rangle$ a spatial average, $\psi(t_n)$ the different restored steps calculated with Eq. (3.16), for (i) g_{eff} and (ii) g_η, at discrete instants $t_n = n\tau$.

Variation of this similarity measure is then presented as a function of the rms amplitude σ_η of the Gaussian noise purposely injected. As visible in Fig. 3.19, the normalized crosscovariance of Eq. (3.19) experiences, for all the 3 tested noise components, a nonmonotonic evolution and culminates at a maximum for an optimal nonzero level of the injected Gaussian noise. These results are in good accordance with the direct visual inspection of the images and demonstrate the possibility of improving the performance of the Perona–Malik process by injecting a non zero amount of the noise η with various image–noise coupling.

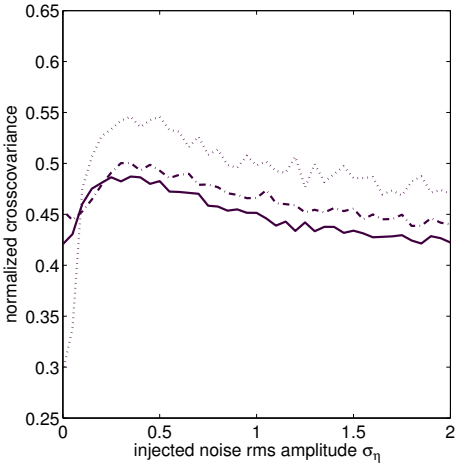

Figure 3.19: Normalized crosscovariance of Eq. (3.19) as a function of the rms amplitude σ_η of the Gaussian noise η purposely injected with the number of iteration n which is fixed to $n = 15$. Solid, dash-dotted and dotted lines are respectively standing for the additive, multiplicative and impulsive noise components described in Fig. 3.17

We now propose to investigate the inner mechanism of the useful-noise effect shown in [Histace and Rousseau, 2006; Histace and Rousseau, 2007]. To this purpose, we propose to simplify the nonlinear function $g(\cdot)$. The diffusive function of Eq. (3.18) was chosen in [Histace and Rousseau, 2006] because it corresponds to the historical function proposed in [Perona and Malik, 1990]. This choice nevertheless presents some drawbacks for the complete understanding of the useful-noise effect since the presence in the analytical definition of $g(\cdot)$ function of a L_2 norm of the purposely

noised gradient of the image leads to an offset shifting that makes the interpretation of the impact of the noise uneasy.

3.2.2.2 A Simple Set of Parameters

In this section, we choose to simplify the shape of $g(\cdot)$ into a hard threshold non-linearity given by

$$g(s) = \begin{cases} 1 \text{ if } s \geq k \\ 0 \text{ if } s < k \end{cases}, \tag{3.20}$$

where parameter k is now a hard threshold. This function integrates a hard non-linearity in order to set in a binary way the diffusion threshold. Moreover, this non-linearity is only function of the norm of the gradient in order to only emphasis the effect of the purposely injection of noise and to avoid the shifting effect described above. One can note that despite this methodological choice regarding $g(\cdot)$ function, this latter is just a simplified version of the former function proposed in [Perona and Malik, 1990] and still embed the fundamental elements of the usual anisotropic diffusion.

For illustration, the data to be restored is also chosen in its most simplest form. We consider a monodimmensional signal ψ_{ori} taken as a unit step function modeling an edge within a noisy image. ψ_0 will denote the noisy version of ψ_{ori}. The goal is now to restore the noisy step version

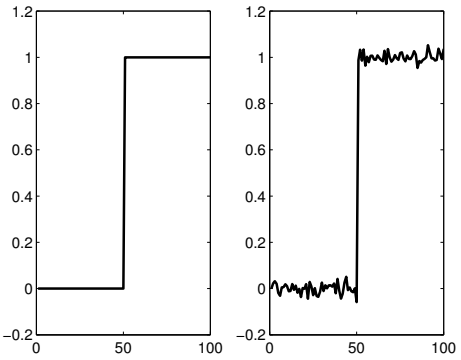

Figure 3.20: Illustration of the monodimensional function used for the study. On the left, the original ψ_{ori} function. On the right, the corrupted version ψ_0 (ξ is chosen gaussian).

without altering the hard discontinuity of ψ_{ori}. More, we want to show that injection of noise within the restoration process can lead to overpass the usual weak point of Perona-Malik process: a lack of robustness regarding k parameter.

Parameter k of Eq. (3.20) plays a very important role in the study as far as little variations of its value can lead to completely different results of restoration. For instance, let us consider ψ_{ori} as defined Fig. 3.20.

To apply usual Perona-Malik process of Eq. (3.15) to ψ_{ori}, Eq. (3.15) is discretized with a time step τ such as $t_n = n\tau$ where n is the number of iterations in the process and t_n the corresponding scale.

Fig. 3.21 shows that the usual Perona-Malik process of Eq. (3.15) with $g(\cdot)$ given by Eq. (3.20) presents a lack of robustness regarding parameter k as far as for different values of this parameter ($k \in \{0; 0.2; 0.4; 0.6; 0.8; 1\}$) final result of each corresponding diffusion process is quite different.

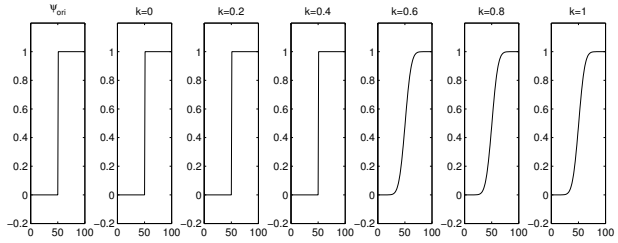

(a)

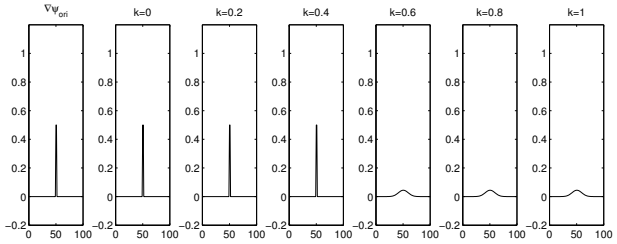

(b)

Figure 3.21: Illustration of the lack of robustness of classic Perona-Malik's process of Eq. (3.15) regarding parameter k. $g(.)$ is given by Eq. (3.20), iteration number n is fixed to 200, and time step τ to 0.2. (a) shows for each value of k the obtained diffused step, and (b) the corresponding gradient function. This Figure shows that the possibility to remove noise without smoothing the discontinuity of ψ_0 strongly depend on the value of k.

More precisely, one can notice in Fig. (3.21) that for $k < 0.5$ ψ_{ori} is not altered by the diffusion process of Eq. (3.15), whereas for $k > 0.5$ ψ_{ori} is diffused as far as a smoothing is introduced which tends to attenuate the maximum value of the corresponding gradient and to spread its width along x-axis. This can be interpreted as an alteration of boundaries within images for a bad tuning of k.

This drawback is all the more embarrassing as the smoothing discrimination between noise and boundaries also depends on the value of k as one can notice on Fig. 3.21.

In [Histace and Rousseau, 2006] we have shown that the stochastic variant of Perona-Malik process of Eq. (3.16) has a stronger robustness toward the tuning of parameter k. We provide an interpretation of the mechanism for this useful-noise effect.

3.2.3 Stochastic Restoration: Theoretical Study

3.2.3.1 Preliminary Calculations

The non-linearity of Eq. (3.16) can be classified as a static or memoryless non-linearity. Possibility of useful-noise effect in static non-linearity has been intensively studied (see [Chapeau-Blondeau and Rousseau, 2002] for a review). The action of the additive noise $\eta(x, y)$ can be understood as a shaping by noise of the input–output characteristic which on average becomes equivalent to

$$g_{eff}(s) = E[g(s + \eta(x, y))] = \int_{-\infty}^{+\infty} g(u) f_\eta(u - s) du \ , \tag{3.21}$$

with $f_\eta(u)$ the probability density function of the purposely injected noise η. In the case of the hard quantizer of Eq. (3.20) with threshold k, Eq. (3.21) becomes

$$g_{eff}(s) = F_\eta(k - s) \ , \tag{3.22}$$

where F_η is the cumulative distribution function of the probability density function of $f_\eta(u)$. If we consider the case where $f_\eta(u)$ is uniform we have

$$g_{eff}(s) = \begin{cases} 0 \text{ for } k - s \leq -\sqrt{3}\sigma_\eta \\ \dfrac{1}{2}\left(1 + \dfrac{k-s}{\sqrt{3}\sigma_\eta}\right) \text{ for } |k - s| < \sqrt{3}\sigma_\eta \\ 1 \text{ for } k - s \geq \sqrt{3}\sigma_\eta \end{cases} . \tag{3.23}$$

$g_{eff}(\cdot)$ function corresponds to the average theoretical equivalent characteristic of $g_\eta(\cdot)$ in presence of a purposely added noise with standard deviation σ_η.

3.2.3.2 Experiments

We now propose to compare the behavior of the numerical diffusion process of Eqs. (3.17) and (3.20) with the equivalent theoretical input–output characteristic of Eq. (3.21). We choose the noisy step ψ_0 of Fig. 3.22.(a), and we assess the efficacy of the restoration process with the normalized cross-covariance as previously defined (Eq. 3.19).

As noticeable in Figs. 3.22.(b) and 3.22.(c), restoration results are in good accordance between numerical simulation and theoretical relation (standard deviation of ξ noise is set to 0.05 for illustration).

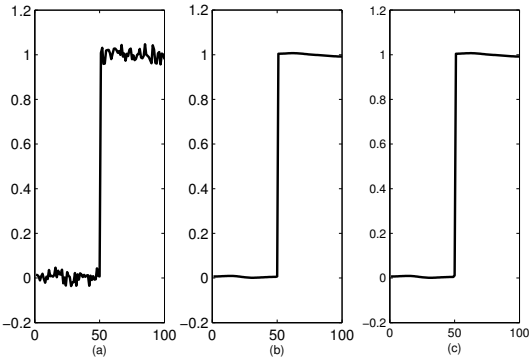

Figure 3.22: Comparison between the numerical implementation of the stochastic diffusion process (Eqs. (3.17) and (3.20) and the theoretical one (Eq. (3.21)) on noisy step ψ_0.ξ noise is gaussian of standard deviation fixed to 0.05. iteration number n is fixed to 150. (a) ψ_0, (b) noise-enhanced diffusion process, (c) diffusion process with $g(\cdot) = g_{eff}(\cdot)$.

This agreement is also valid in Fig. 3.23 which shows average evolution of normalized cross-covariance (Eq. (3.19)) in terms of iteration number n calculated for 1000 diffusion processes.

Fig. 3.23.(c) shows again a perfect matching between both average evolution curves.

These results establish the link between the useful-noise effect shown in [Histace and Rousseau, 2006] and the mechanism at work in static nonlinear systems as described in [Chapeau-Blondeau and Rousseau, 2002].

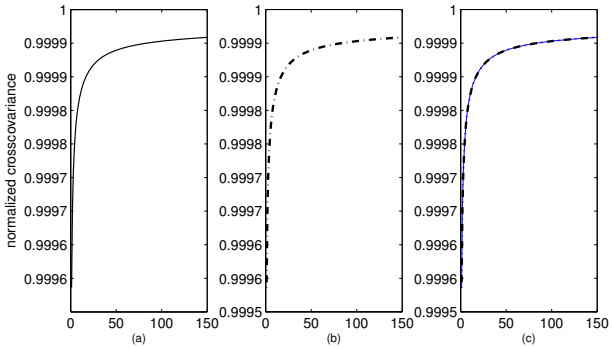

Figure 3.23: Comparison of evolution of normalized cross-covariance for 1000 diffusion processes (Eq. (3.19) between the numerical implementation stochastic diffusion process (Eqs. (3.17) and (3.20) and theoretical one (Eq. (3.21)) on noisy step ψ_0. n is fixed to 150. (a) noise-enhanced diffusion process, (b) diffusion process with $g(\cdot) = g_{eff}(\cdot)$, (c) superposition of both. One can notice that the scale for normalized crosscovariance is very tiny: this can be easily explained by the fact that even corrupted, the noisy version of the step function remains characterized by a high value of this parameter. Global variations still remain of primary importance and must be only considered for this study.

3.2.4 Study of The Stochastic Resonance Effect

In order to further study the influence of an injection of noise in usual Perona-Malik process, we consider in this section that k (Eq. (3.20)) is badly tuned (i.e. $k > 0.5$).

Considering the stochastic version of Perona-Malik process (Eq. (3.16)) with $g(\cdot)$ given by Eq. (3.20), the purposely injected noise η is a zero-mean Gaussian noise characterized by a tunable rms amplitude σ_η. For a visual appreciation of the noise-enhanced process, we consider the noisy step ψ_0 of Fig. 3.20 and k is set to 0.6, which corresponds to a badly tuned value regarding Fig. 3.21. In these conditions, as shown in Fig. 3.24.(b), Perona-Malik process fails in denoising ψ_0 without altering its integrity. If we now consider the stochastic Perona-Malik process of Eq. (3.16) with same parametrization of k, addition of noise η acts as a random resetting of parameter k, and, as shown in Fig. 3.24.(c), sometimes makes the preservation of the discontinuity of ψ_0 possible whereas k was badly tuned. It is important to notice, that this positive effect does not occur systematically, because of the random nature of the noise η.

Although the positive effect of injection of η noise is not systematic, this clearly demonstrates that an increase of the robustness of usual Perona-Malik process regarding parameter k is possible with the function $g_\eta(\cdot)$ proposed. Concerning the optimal amount of noise η to inject and the possibility to estimate the probability to have an averaged positive effect, we propose to quantitatively characterize the noise-enhanced effect shown Fig. 3.24 in the following way. We compute the percentage of well-restored steps (no alteration of the discontinuity) among a large number N of restoration attempts and for different values of σ_η, k being set up to a non optimal value. This ratio can be interpreted as a measure of the gain of robustness compare to the usual Perona-Malik process of Eq. (3.15) toward threshold k. Fig. 3.26 shows the evolution of the percentage of well restored steps for $k = 0.6$.

One can notice in Fig. 3.26 that the variations of the ratio of well restored steps is typical of the existence of a stochastic resonance effect related to a static ity where a maximum of the measure of performance is reached for a non zero amount of injected noise. Same experiments can be made for other badly-tuned values of k. Results are presented Fig. 3.27.

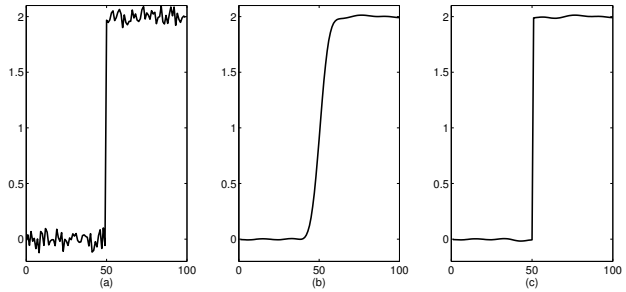

Figure 3.24: (a) Noisy step $\psi_0 = \psi_{ori} + \xi$ (rms amplitude of ξ is fixed to 0.05), (b) Perona-Malik restoration of ψ_0 ($n = 50$), (c) Stochastic Perona-Malik restoration of ψ_0 ($n = 50$ and $\sigma_\eta = 0.3$. For (b) and (c), k is fixed to 0.6 (badly tuned). Injection of η noise makes possible to obtain a better restoration of the noisy step regarding the fact that noise is suppressed and step discontinuity is preserved.

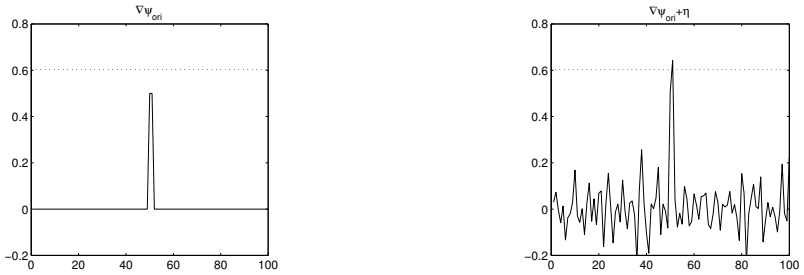

(a) (b)

Figure 3.25: (a) Solid line stands for variations of $\nabla\psi_{ori}$. Maximum value (0.5) is reached at the discontinuity of the studied step. Dotted line represents hard threshold k (fixed to 0.6 and considered as badly tuned) leading the diffusion process (Eq. (3.20)). (b) Solid line stands for variations of $\nabla\psi_{ori} + \eta$ (η is chosen gaussian) and dotted line still represents k-threshold. As one can notice in (b), sometimes the purposely injected noise η makes it possible to cross k-threshold, that is to say to locally tuned diffusion process in order to increase its robustness regarding k.

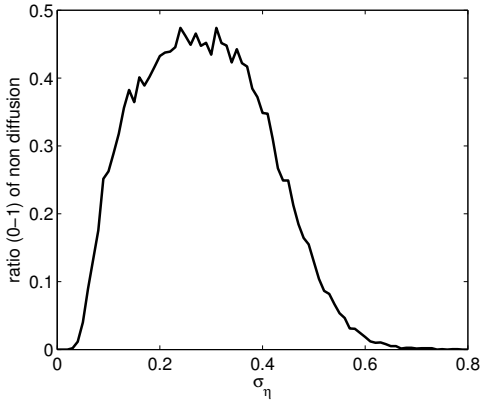

Figure 3.26: Variation of the ratio of well restored steps (no alteration of the discontinuity) thanks to the purposely injection of η (Eq. (3.16)) function of rms amplitude σ_η. k is fixed to 0.6 and N, the total amount of restoration attempts, to 1000.

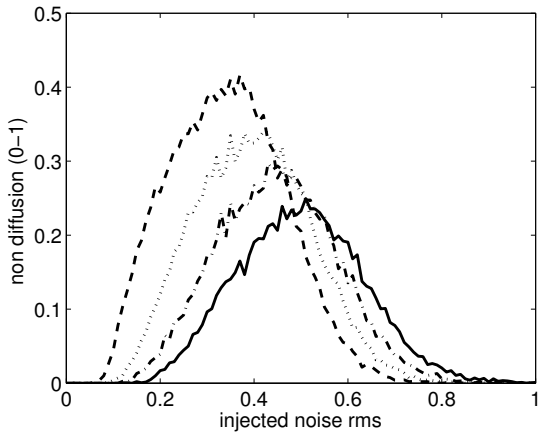

Figure 3.27: Ratio of non-diffused steps function of rms amplitude σ_η. N is fixed to 1000. Dashed line stands for $k = 0.65$, dotted one for $k = 0.7$, dash-dotted one for $k = 0.75$ and solid one for $k = 0.8$. For each value of k, same stochastic effect as before (Fig. 3.26) can be observed : the non-diffusion ratio is maximum for a non zero amount of purposely injected noise.

As visible in Fig. 3.27, even if the maximum value of the ratio decreases, the useful-noise effect can be observed. This decrease can be easily explained by the fact the farer parameter k is from 0.5, the more important is the necessary amount of noise to inject to finally make an interesting retuning of k. As a consequence positive effect of purposely injected noise η is less important and presents a maximum for a value of σ_η also increasing (which can also be noticed on Fig. 3.27). Moreover, that type of curves also makes possible an evaluation of the optimal amount of noise to add regarding k values. For instance, it appears that for $k = 0.6$ (Fig. 3.26), a maximum probability of 46% of non diffusion of the discontinuity of ψ_{ori} can be reached for $\sigma_\eta = 0.3$ thanks to the stochastic Perona-Malik process.

3.2.5 Conclusion and Perspectives

This work has permitted to establish a link between noised-enhanced anisotropic diffusion and stochastic resonance in static nonlinearities. This shows the way to non trivial transposition of stochastic resonance effect previously dedicated to monodimensional signal to images. Further investigations in the continuity of this report could deal with extensions to more complex nonlinear partial differential equation of the literature.

More precisely, in some recent publications ([Morfu, 2009; Histace and Rousseau, 2010; Jha *et al.*, 2012]) dealing with diffusion processes for image restoration, particular nonlinear anisotropic PDE, integrating a double-well potential function of the form $f(\psi) = \psi(\psi - a)(\psi - 1)$, have been proposed. One of the obtained PDE [Morfu, 2009] is an extension of the Fisher equation, derived from the Perona–Malik process, and given by

$$\frac{\partial \psi}{\partial t} = div(g(\|\nabla\psi\|)\nabla\psi) + f(\psi)\,. \tag{3.24}$$

Such an equation has proved to be efficient for image enhancement. Nevertheless, sharpness preservation of the edge profiles remains a real challenge.

Moreover, Eq. (3.25) can be related to the evolution equation of dynamic systems as described in [Chapeau-Blondeau, 2000] for instance, for which SR phenomenon have been clearly identified,

a complete theoretical and practical study of those type of PDE could be of real interest for image restoration. For such a study, the considered image restoration PDE could be of the form

$$\frac{\partial \psi}{\partial t} = div(g(\|\nabla \psi\|)\nabla \psi) + f(\psi) + \eta(x, y)\,. \tag{3.25}$$

Establishment of a link between Fisher equation and stochastic resonance in dynamic nonlinearities could be of real interest to propose original restoration processes based on SR PDE and would extend the study proposed here but restricted to static nonlinearities.

Finally, an other objective will be now to experiments proposed approach on medical data to take into account the particular noise coupling that can be encountered in the different imaging techniques like MRI (Rayleigh) or Ultrasound Images (Speckle).

Chapter 4

Contribution to Active-Contour-Based Image Segmentation Approaches

This chapter focuses on image segmentation using active contour technics. The scientific aspect of this chapter is situated in the same area than Chapter 4, since we still are considering PDE-based approaches and more precisely, variationnal approaches. Nevertheless, the constituting PDE are somehow different in the particular context of active contour segmentation.

Two main contributions are presented: first of all, a general framework for shape prior constrains in active contour segmentation is introduced, and second, contributions to statistical-region-based approaches are proposed. In the latter case, we focus our attention on the proposal of statistical-region-based descriptor: a fractional entropy inspired from Rényi's one, and a study of a particular divergence family called the alpha-divergence.

The work on shape constraints was jointly developed with Prof. Bogdan Matuszewski (ADSIP Research Center, University of Central Lancashire, UK), Dr Yan Zhang (Post-Doc student at ADSIP), and Prof. Frédéric Precioso formerly Associate Professor at ETIS.

The fractional entropy descriptor was studied during the MSc internship of Mickael Garnier. The alpha-divergence contribution was studied during the PhD of Dr Leila Meziou (2010-2013) for which I was cosupervisor (70%) with Prof. Frédéric Precioso.

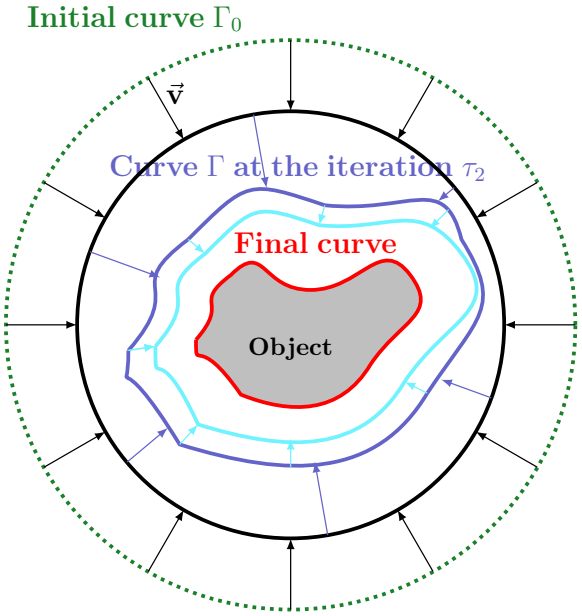

Figure 4.1: Illustration of active contour segmentation: $\Gamma = \Gamma(p, \tau)$ denotes the coordinate of the point p of the curve at iteration τ of the segmentation process.

Originally proposed in [Kass *et al.*, 1988], the basic idea of the active contour is to iteratively evolve an initial curve towards the boundaries of target objects driven by the combination of internal forces, determined by the geometry of the evolving curve, and external forces, induced from the image. Image segmentation methods using active contour are often derived from a variational principle in which a functional defined on contours encodes our knowledge about desirable solutions. The functional minimization leads to a partial differential equation (PDE), constructed as the Gateaux derivative gradient flow which steers the evolution of the active contour. Fig. 4.1 shows an illustration of the main principle that is active contour segmentation.

It is commonly accepted that, depending on the functional (or energy) related to the segmentation problem, two main kind of approaches are to be considered: The gradient-based approach formerly introduced in [Osher and Setian, 1988] and [Kass *et al.*, 1988], and the region-based approaches with the most known Chan and Vese's [Chan and Vese, 2001] approach.

For the last 8 years, in the particular segmentation framework of region-based active contour, through the collaborations with ADSIP research centre, we mainly focus our attention on two main scientific objectives:

- How to efficiently integrate shape prior into the classic scheme of active contour?
- How to take benefit of recent advances in information theory into the particular framework of statistical-region-based active contour?

As it has been already said, the main targeted application area is medical image analysis for CAD and the different studies presented in this Chapter were supported by ETIS lab and UK government thanks to the obtaining of EPSRC fundings (ECSON, TERAFS projects). The following sections give an overview of the work achieved until now on the two aforementioned point of interest.

4.1 Statistical Model of Shape Moments with Active Contour Evolution for Shape Detection and Segmentation

Introduction of a prior shape constraint into the image segmentation functional has recently become the focus of intensive research in Computer Vision and Image Processing communities [Lecellier, *et al.*, 2006; Kim, *et al.*, 2007; Etyngier *et al.*, 2007; Houhou, *et al.*, 2008; Thiruvenkadam *et al.*, 2007; Erdem *et al.*, 2009; Prisacariu and Reid, 2011]. In the particular context of medical image segmentation, the work of Dahdou et al. has shown the real interest for such prior constraints [Dahdouh *et al.*, 2013] with an application to fetal envelop segmentation in ultrasonic images.

The early work on this problem has been done by Cootes *et al.* [Cootes *et al.*, 1995]. Their method is based on principal component analysis (PCA) calculated for landmarks selected for a training set of shapes which are assumed to be representatives of the shape variations. The method is implemented in the parametric active contour framework, with results strongly depending on the quality of the selected landmarks.

Leventon *et al.* [Leventon, *et al.*, 2000] considered introduction of prior shape information using level set based representation, where landmarks are replaced by signed distance functions calculated for the contours in the training data set, providing hence an intrinsic and parametrization free shape model. However, it was demonstrated that, linear combinations of signed distance functions do not necessarily result in a signed distance function, and therefore possibly compromise the quality of the solution. Furthermore, all these methods effectively assume that the shape prior has a Gaussian distribution. As a result, these methods cannot handle multi-modal shape distributions and thus are restricted to the segmentation of target objects with limited shape variabilities.

Instead of using evolution of active contour to search optimum in the image space, Tsai *et al.* [Tsai, *et al.*, 2003] proposed a method to directly search solution in the shape space which is built by the signed distance functions of aligned training images and reduced by PCA. In their paper, a few cost functions are proposed and their derivatives with respect to eigen-shape weights and to pose parameters are given, so that the steepest descent algorithm can be applied. In [Fussenegger *et al.*, 2009], Fussenegger *et al.* apply a robust and incremental PCA algorithm on binary training masks of the object(s) to define an active shape model which is then "embedded" in a level set implementation. Segmentation (or tracking) is computed using pre-trained shape model, then PCA representation is updated using this result in order to improve next iteration of segmentation process. Although this self-improving "looping process" between the image space and the shape space is interesting, PCA of binary training masks requires that these training examples are aligned before learning the implicit shape model. The major limitation of all these methods is the implicit assumption of uniform distribution in the shape space.

Recently, it has been proposed to construct nonparametric shape prior by extending the Parzen density estimator to the space of shapes. For instance, in [Cremers *et al.*, 2006; Rousson,, and Cremers, 2005; Rousson,, and Paragios, 2002; Rousson and Paragios, 2008], authors proposed a nonlinear statistical shape model for level set segmentation which can be efficiently implemented. Given a set of training shapes, they performed kernel density estimation in the low dimensional subspace. In this way, they are able to combine an accurate model of the statistical shape distribution with efficient optimization in a finite-dimensional subspace. In a Bayesian inference framework, they integrated the nonlinear shape model with a nonparametric intensity model and a set of pose parameters which are estimated in a more direct data-driven manner than in previously proposed level set methods. Kim *et al.* [Kim, *et al.*, 2007] proposed a non-

parametric shape prior model for image segmentation problems. Given example training shapes, they estimate the underlying shape distribution by extending a Parzen density estimator to the space of shapes. Such density estimates are expressed in terms of distances between shapes. The learned shape prior distribution is then incorporated into a maximum a posteriori estimation framework which is solved using active contours.

Recently, Foulonneau *et al.* [Foulonneau, *et al.*, 2009] proposed an alternative approach for shape prior integration within the framework of parametric snakes. They combined a compact, parametric representation of shapes within curve evolution theory. More specifically, they proposed to define a *geometric* shape prior based on a description of the target object shape using Legendre moments. A new shape energy term, defined as the distance between moments calculated for the evolving active contour and the moments calculated for a fixed reference shape prior, is proposed and derived in the mathematical framework of [Aubert *et al.*, 2003] in order to obtain the evolution equation. Initially, the method was designed for a single reference shape prior [Foulonneau, *et al.*, 2003], but in the most recent version is able to take into account multi-reference shape priors. As a result, the authors have defined a new efficient method for region-based active contours integrating static shape prior information. Nevertheless, one of the main drawbacks of such an approach lies in its strong dependence to the shape alphabet used as reference. Indeed, as stated by the authors themselves in [Foulonneau, *et al.*, 2009], this method is more related to *template matching* than to *shape learning*.

Inspired by the aforementioned results and especially by the approach proposed by Foulonneau *et al.*, the method proposed here optimizes, within the level sets framework, model consisting of a prior shape probability model and image likelihood function conditioned on shapes. The statistical shape model results from a learning process based on nonparametric estimation of the posterior probability, in a low dimensional shape space of Legendre moments built from training silhouette images. Such approach tends to combine most of the advantages of the aforementioned methods, that is to say, it can handle multi-modal shape distributions, preserve a consistent framework for shape modeling and is free from any explicit shape distribution model.

Currently, no direct application to medical image segmentation is proposed in order to keep the generality of the proposed framework. Nevertheless, some elements for application to Prostate MRI segmentation are given in the "Conclusion and Perspectives" section.

4.1.1 Segmentation Framework

The proposed segmentation framework can be seen as constrained contour evolution, with the evolution driven by an iterative optimization of the posterior probability model that combines a prior shape probability and an image likelihood function linked with a coupling prior imposing constraints on the contour evolution in the image domain. The method can be implemented with any combination of the shape descriptors and dimensionality reduction techniques as long as the shape reconstruction is possible from the selected low dimensional representation. Although for the clarity of the presentation and due to analysis in the experimental section comparing the proposed method against [Foulonneau, *et al.*, 2009], Legendre moments are used in the paper other shape descriptors such as Zernike moments [Teague, 1980] could be equally used.

In this section all the elements of the proposed model along with the proposed optimization procedure are described in detail.

4.1.1.1 Shape representation using Legendre moments

The method proposed here can utilize any shape descriptor as long as it enables shape reconstruction [Teague, 1980]. However, in order to simplify description of the method and comparison with other approaches [Chan and Vese, 2001; Foulonneau, *et al.*, 2009] shapes are encoded, as in [Foulonneau, *et al.*, 2009], by central-normalized Legendre moments $\boldsymbol{\lambda} = \{\lambda_{pq}, p+q \leq N_o\}$ of order N_o where p and q are non-negative integers, and therefore $\boldsymbol{\lambda} \in \mathbf{R}^{N_f}$ with $N_f = (N_o+1)(N_o+2)/2$.

The central-normalized Legendre moments are attractive for shape representation as they can be used for objects in arbitrary dimensional spaces and having different topology. They are also invariant to shape scaling and translation and provide compact shape representation where a tradeoff between feature space dimension and shape representation accuracy can be simply controlled by the single parameter N_o. Figure 4.2 shows an example of shape reconstruction when different values of N_o are used.

For a given shape Ω the moments are defined by:

$$\lambda_{pq} = \frac{1}{|\Omega|} \int_{\Omega} L_{pq}(x, y, \Omega)\, dxdy \tag{4.1}$$

where the 2D central-normalized Legendre polynomials L_{pq} are the tensor product of two 1D central-normalized Legendre polynomials L_p and L_q:

$$L_{pq}(x, y, \Omega) = L_p\left(\frac{x-\bar{x}}{|\Omega|^{1/2}}\right) L_q\left(\frac{y-\bar{y}}{|\Omega|^{1/2}}\right) \tag{4.2}$$

with Legendre polynomials defined on the interval $[-1, 1]$ as:

$$L_n(x) = \sqrt{\frac{2n+1}{2}} \frac{1}{2^n n!} \frac{d^n}{dx^n}[(x^2-1)^n] \tag{4.3}$$

The area $|\Omega|$ and the center of gravity coordinates $(\bar{x}, \bar{y})$ are calculated from:

$$|\Omega| = \int_{\Omega} dxdy, \tag{4.4}$$

$$\bar{x} = \frac{1}{|\Omega|} \int_{\Omega} x\, dxdy, \quad \bar{y} = \frac{1}{|\Omega|} \int_{\Omega} y\, dxdy \tag{4.5}$$

The Legendre polynomials form the orthonormal basis:

$$\int_{-1}^{1} L_m(x) L_n(x)\, dx = \delta_{mn} \tag{4.6}$$

and therefore are very effective for shape representation. Although the central-normalized Legendre moments provide only scale and translation invariance, the theory presented in this section can be further extended to provide similarity or affine transformation invariance of the moments. Such extension has been well exposed in [Foulonneau, *et al.*, 2009].

In the following sections the scale and translation invariant moments are used but the method would remain the same if similarity or affine invariant moments were used instead.

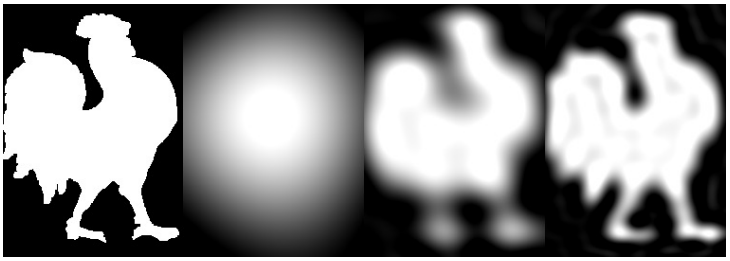

Figure 4.2: Images reconstructed from the Legendre moments with different orders. From left to right: original image and reconstruction images with orders $N_o = 5, 20, 40$.

4.1.1.2 Statistical Shape Model of Legendre Moments

In the method proposed here the prior shape constraint is introduced into the segmentation process in the form of probability density function defined on the low dimensional shape space [Cootes *et al.*, 1995] and estimated using Parzen window method. The shape space is constructed using PCA method on a training set consisting of N_s binary silhouette images with foreground and background represented respectively by ones and zeros. The training data can be obtained from previously segmented images or generated from computer models of the objects of interest. In the first instance the central-normalized Legendre moments $\{\boldsymbol{\lambda}_i\}_{i=1}^{N_s}$ are calculated for the shapes $\{\Omega_i\}_{i=1}^{N_s}$ from the training database. Following the methodology proposed in [Cootes *et al.*, 1995] the mean vector $\bar{\boldsymbol{\lambda}}$ and the $N_f \times N_f$ covariance matrix $\mathbf{Q}$ are estimated using:

$$\bar{\boldsymbol{\lambda}} = \frac{1}{N_s} \sum_{i=1}^{N_s} \boldsymbol{\lambda}_i \tag{4.7}$$

$$\mathbf{Q} = \frac{1}{N_s} \sum_{i=1}^{N_s} (\boldsymbol{\lambda}_i - \bar{\boldsymbol{\lambda}})(\boldsymbol{\lambda}_i - \bar{\boldsymbol{\lambda}})^T \tag{4.8}$$

Subsequently the $N_f \times N_c$ projection matrix $\mathbf{P}$ is formed by the eigenvectors of the covariance matrix $\mathbf{Q}$ that correspond to the largest N_c ($N_c \leq \min\{N_s, N_f\}$) eigenvalues. The projection of feature vectors $\{\boldsymbol{\lambda}_i\}_{i=1}^{N_s}$ onto the shape space, spanned by the selected eigenvectors, forms the feature vectors $\{\boldsymbol{\lambda}_{r,i}\}_{i=1}^{N_s}$:

$$\boldsymbol{\lambda}_{r,i} = \mathbf{P}^T(\boldsymbol{\lambda}_i - \bar{\boldsymbol{\lambda}}) \tag{4.9}$$

The density estimation $P(\boldsymbol{\lambda}_r)$, with $\boldsymbol{\lambda}_r$ defined in the shape space, is performed up to a scale, using $\boldsymbol{\lambda}_{r,i}$ as samples from the population of shapes and with the isotropic Gaussian function as the Parzen window:

$$P(\boldsymbol{\lambda}_r) = \sum_{i=1}^{N_s} \mathcal{N}(\boldsymbol{\lambda}_r; \boldsymbol{\lambda}_{r,i}, \sigma^2) \tag{4.10}$$

where $\mathcal{N}(\boldsymbol{\lambda}_r; \boldsymbol{\lambda}_{r,i}, \sigma^2) = \exp(-||\boldsymbol{\lambda}_r - \boldsymbol{\lambda}_{r,i}||^2/2\sigma^2)$

4.1.1.3 Level Set Active Contour Model

Introduced in the previous section, density function $P(\boldsymbol{\lambda}_r)$ is defined on the shape space of Legendre moments and represents a prior knowledge learned from the training shape examples.

To detect and segment shapes present in an observed image, a mechanism for taking into consideration the evidence about shape needs to be included. Due to the way the final objective function is optimized, any energy-based level-set contour evolution schemes can be used. In this paper, it is proposed to consider for this purpose active contours implemented in the level set framework. The region competition scheme proposed by [Chan and Vese, 2001] will be used for the illustration purposes. In this case, it is assumed that the image I is formed by regions of approximatively constant intensity values and the segmentation is defined as energy minimization problem, with the energy given by:

$$\begin{aligned} E_{cv}(\Omega, \mu_\Omega, \mu_{\Omega^c}|I) &= \int_\Omega (I-\mu_\Omega)^2\, dxdy \\ &+ \int_{\Omega^c} (I-\mu_{\Omega^c})^2\, dxdy + \gamma|\partial\Omega| \end{aligned} \tag{4.11}$$

where Ω^c represents the complement of Ω in the image domain and $|\partial\Omega|$ represents the length of the boundary $\partial\Omega$ of the region Ω. The above defined energy minimization problem can be equivalently expressed as maximization of the likelihood function:

$$P(I|\Omega) \propto \exp(-E_{cv}(\Omega, \mu_\Omega, \mu_{\Omega^c}|I)) \tag{4.12}$$

where $P(I|\Omega)$ could also be interpreted as a probability of observing image I when shape Ω is assumed to be present in the image. Introducing level set (embedding) function ϕ such that the Ω can be expressed in terms of ϕ as $\Omega = \{(x,y) : \phi(x,y) \geq 0\}$, as well as $\Omega^c = \{(x,y) : \phi(x,y) < 0\}$ and $\partial\Omega = \{(x,y) : \phi(x,y) = 0\}$, the foregoing functional is equivalent to

$$\begin{aligned} E_{cv}(\phi, \mu_\Omega, \mu_{\Omega^c}|I) &= \int (I-\mu_\Omega)^2 H(\phi)\, dxdy \\ &+ \int (I-\mu_{\Omega^c})^2 (1-H(\phi))\, dxdy \\ &+ \gamma \int |\nabla H(\phi)|\, dxdy \end{aligned} \tag{4.13}$$

with H representing Heaviside function. Calculating Gateaux derivative [Aubert *et al.*, 2003] it can be shown that such energy function is minimized by function ϕ given as a solution of the following PDE equation

$$\begin{aligned} \frac{\partial\phi}{\partial t} &= \left((I-\mu_{\Omega^c})^2 - (I-\mu_\Omega)^2\right)|\nabla\phi| \\ &+ \gamma\nabla\left(\frac{\nabla\phi}{|\nabla\phi|}\right)|\nabla\phi| \end{aligned} \tag{4.14}$$

with $\mu_\Omega = \int_\Omega I\, dxdy$ and $\mu_{\Omega^c} = \int_{\Omega^c} I\, dxdy$ representing respectively the average intensities inside and outside the evolving curve.

4.1.1.4 MAP Framework

Introduced in the previous two sections, distributions representing shape prior information and image intensity can be combined using Bayes rule:

$$P(\boldsymbol{\lambda}_r|I) \propto P(\boldsymbol{\lambda}_r)P(I|\boldsymbol{\lambda}_r) \tag{4.15}$$

where $P(\boldsymbol{\lambda}_r)$ and $P(I|\boldsymbol{\lambda}_r)$ represent respectively shape and intensity based information. In [Zhang *et al.*, 2011] it was proposed to optimize $P(\boldsymbol{\lambda}_r|I)$ by restricting the shape evolution in the estimated shape space, by imposing following constraint: $P(I|\boldsymbol{\lambda}_r) = P(I|\Omega)|_{\Omega=\Omega(\boldsymbol{\lambda}_r)}$. As maximizing $P(\boldsymbol{\lambda}_r|I)$ is equivalent to minimizing $-\ln(P(\boldsymbol{\lambda}_r|I))$, Zhang *et al.* [Zhang *et al.*, 2011] suggested minimizing an energy function:

$$E(\boldsymbol{\lambda}_r) = E_{prior}(\boldsymbol{\lambda}_r) + E_{image}(\boldsymbol{\lambda}_r) \tag{4.16}$$

where the shape prior term is defined as:

$$E_{prior}(\boldsymbol{\lambda}_r) = -\ln\left(\sum_{i=1}^{N_s}\mathcal{N}(\boldsymbol{\lambda}_r;\boldsymbol{\lambda}_{r,i},\sigma^2)\right) \tag{4.17}$$

and is built based on the shape samples Ω_i as explained in section 2.2. The image term is defined as:

$$E_{image}(\boldsymbol{\lambda}_r) = E_{cv}(\Omega,\mu_\Omega,\mu_{\Omega^c}|I)|_{\Omega=\Omega(\boldsymbol{\lambda}_r)} \tag{4.18}$$

where optimization of E_{cv} is constraint to shapes Ω from the estimated shape space $\Omega = \Omega(\boldsymbol{\lambda}_r)$ where $\Omega(\boldsymbol{\lambda}_r)$ denotes a shape from the shape space represented by the Legendre moments $\boldsymbol{\lambda} = \mathbf{P}\boldsymbol{\lambda}_r + \bar{\boldsymbol{\lambda}}$.

As it was indicated in [Zhang *et al.*, 2011] such approach provides a very robust segmentation. Unfortunately the solution which minimizes $E(\boldsymbol{\lambda}_r)$ belongs to the shape space and as such may not accurately represent object of interest. To resolve this the Eq.(4.15) can be redefined as:

$$P(\Omega,\boldsymbol{\lambda}_r|I) \propto P(\boldsymbol{\lambda}_r)P(\Omega|\boldsymbol{\lambda}_r)P(I|\Omega,\boldsymbol{\lambda}_r) \tag{4.19}$$

Eq.(4.19) is now optimized jointly with respect to shape Ω defined in the image space and vector $\boldsymbol{\lambda}_r$ defined in the shape space. The coupling between these two is achieved by $P(\Omega|\boldsymbol{\lambda}_r)$ defined as:

$$P(\Omega|\boldsymbol{\lambda}_r) \propto \exp(-E_c(\Omega|\boldsymbol{\lambda}_r)) \tag{4.20}$$

with:

$$E_c(\Omega|\boldsymbol{\lambda}_r) = \alpha\int\left(H(\phi) - H(\phi_r)\right)^2 dxdy \tag{4.21}$$

where α is a weighting factor defining the strength of coupling between Ω and ϕ_r is a signed distance function representing the shape defined by the $\boldsymbol{\lambda}_r$ in the image domain. The overall energy to be minimized is now given by:

$$E(\Omega,\boldsymbol{\lambda}_r) = E_{prior}(\boldsymbol{\lambda}_r) + E_{image}(\Omega,\boldsymbol{\lambda}_r) \tag{4.22}$$

with the image energy:

$$E_{image}(\Omega,\boldsymbol{\lambda}_r) = E_{cv}(\Omega,\mu_\Omega,\mu_{\Omega^c}|I)| + E_c(\Omega|\boldsymbol{\lambda}_r) \tag{4.23}$$

It can be shown that the corresponding PDE describing the solution of this new image energy is given by:

$$\begin{aligned}\frac{\partial\phi}{\partial t} &= \left((I-\mu_{\Omega^c})^2 - (I-\mu_\Omega)^2\right)|\nabla\phi| \\ &+ \alpha\left(2H(\phi_r)-1\right)|\nabla\phi| + \gamma\nabla\left(\frac{\nabla\phi}{|\nabla\phi|}\right)|\nabla\phi|\end{aligned} \tag{4.24}$$

The details of the optimization procedure for energy $E(\Omega,\boldsymbol{\lambda}_r)$ are given in the next section.

4.1.1.5 Optimization

In the implementation of the proposed method the energy given in Eq.(4.22) is minimized using a greedy method where each of the two energy components E_{prior} and E_{image} is minimized in turn. The optimization of the image based energy E_{image} is implemented through evolution of the level set ϕ defined by Eq.(4.24) with $\boldsymbol{\lambda}_r$ fixed. Subsequently the E_{prior} is minimized in the shape space with respect to the $\boldsymbol{\lambda}_r$. In this approach active contour evolution can be interpreted as a method for transferring the evidence about the shape present in the image into the shape space where it is combined with the shape information derived from the training shape samples.

The overall optimization procedure is summarized in the following steps:

- Projection of the current shape $\Omega^{(k)}$ into the shape space:

$$\Omega^{(k)} \rightarrow \boldsymbol{\lambda}_r^{(k)} \tag{4.25}$$

where $\boldsymbol{\lambda}_r^{(k)} = \mathbf{P}^T(\boldsymbol{\lambda}^{(k)} - \bar{\boldsymbol{\lambda}})$, and the central-normalized Legendre moments in vector $\boldsymbol{\lambda}^{(k)}$ are calculated using:

$$\lambda_{pq}^{(k)} = \frac{1}{|\Omega^{(k)}|} \int_{\Omega^{(k)}} L_{pq}\left(x, y, \Omega^{(k)}\right) dxdy \tag{4.26}$$

where $\Omega^{(k)}$, comes from the previous algorithm iteration;

- Shape space vector update:

$$\boldsymbol{\lambda}_r^{(k)} \rightarrow \boldsymbol{\lambda}_r^{\prime(k)} \tag{4.27}$$

This step reduces the value of E_{prior} by moving $\boldsymbol{\lambda}_r^{(k)}$ in the steepest descent direction:

$$\boldsymbol{\lambda}_r^{\prime(k)} = \boldsymbol{\lambda}_r^{(k)} - \beta \left.\frac{\partial E_{prior}}{\partial \boldsymbol{\lambda}_r}\right|_{\boldsymbol{\lambda}_r = \boldsymbol{\lambda}_r^{(k)}} \tag{4.28}$$

where

$$\frac{\partial E_{prior}}{\partial \boldsymbol{\lambda}_r} = \frac{1}{2\sigma^2} \sum_{i=1}^{N_s} w_i(\boldsymbol{\lambda}_r - \boldsymbol{\lambda}_{r,i}) \tag{4.29}$$

with

$$w_i = \frac{\mathcal{N}(\boldsymbol{\lambda}_r; \boldsymbol{\lambda}_{r,i}, \sigma^2)}{\sum_{k=1}^{N_s} \mathcal{N}(\boldsymbol{\lambda}_r; \boldsymbol{\lambda}_{r,k}, \sigma^2)} \tag{4.30}$$

- Shape reconstruction from Legendre moments:

$$\boldsymbol{\lambda}_r^{\prime(k)} \rightarrow \Omega^{\prime(k)} \tag{4.31}$$

where shape $\Omega^{\prime(k)}$ is reconstructed using:

$$\Omega^{\prime(k)} = \left\{(x, y) : \left(\sum_{p,q}^{p+q \leq N_o} \lambda_{pq}^{\prime(k)} L_{pq}\left(x, y, \Omega^{(k)}\right)\right) > 0.5\right\} \tag{4.32}$$

with the Legendre moments $\lambda_{pq}^{\prime(k)}$ in vector $\boldsymbol{\lambda}^{\prime(k)}$ calculated from the shape space vector $\boldsymbol{\lambda}_r^{\prime(k)}$ using: $\boldsymbol{\lambda}^{\prime(k)} = \mathbf{P}\boldsymbol{\lambda}_r^{\prime(k)} + \bar{\boldsymbol{\lambda}}$

- Evolution of $\Omega^{'(k)}$ according to Eq.(4.24):

$$\Omega^{'(k)} \rightarrow \Omega^{(k+1)} \tag{4.33}$$

  shape $\Omega^{'(k)}$, is a shape represented in the shape space and $\Omega^{(k+1)}$ is the result of shape evolution in the image domain;

These steps are iterated until no shape change occurs in two consecutive iterations: $\Omega^{(k+1)} = \Omega^{(k)}$.

The proposed strategy provides the maximum flexibility by making the optimizations in image space and shape space two independent processes bridged by shape projection and reconstruction. Thus, changing the curve evolution model in the image space or probability estimation model in the shape space will not affect other procedures. Although Legendre moments and PCA are selected to build the shape space in this paper, other shape descriptors and dimensionality reduction techniques can be easily 'plugged' into the optimization framework as long as the shape reconstruction from the shape space is possible. It should be pointed out that, unlike derivative based optimization methods such as [Foulonneau, *et al.*, 2003] and [Foulonneau, *et al.*, 2009], the shape descriptors need *not* be differentiable in the proposed method.

To guarantee convergence of the algorithm the parameter α in equation Eq.(4.24) should be non-decreasing function of the iteration index. In that case the convergence is guaranteed as for large enough value of α the algorithm, if not terminated beforehand, is equivalent to the steepest descent in the reduced shape space. In practical implementation the value of α is periodically increased after predefined number of iterations lapses. With this in mind the proposed algorithm can be interpreted as a mode seeking shape detection procedure. With small value of α the algorithm can relatively easily make long "unconstrained" jumps in the shape space following the shape evidence in the image domain. With the gradually increasing value of α the algorithm will be restricted to make gradually smaller steps to maintain similarity of the evolving shape in the image domain to the current shape defined in the shape space. It should be noted that in the practical experiments the algorithm converged in just a few iterations without increasing α for the vast majority of cases. To further improve segmentation results after the algorithm terminates the image energy can be minimized independently through the contour propagation defined by formula Eq.(4.24). In this case the value of the parameter α should correspond to the level of noise present in the image, with small values of α corresponding to low level of noise. This is further explained in the experimental section.

4.1.2 Experimental Results

To evaluate the proposed method, experiments were carried out using binary silhouette and real gray scale images. The main reason behind using the silhouette images was to investigate robustness of the proposed technique against severe random and structural noise present in data. The segmentation of such images without any noise is straightforward, as it could be achieved by simple thresholding, proving ready ground truth data. Additionally any incorrect segmentation of the noisy images can be directly associated with the noise rather than with a specific "non-optimal" type of image intensity descriptor used to compute the external energy in the active contour model. As it was explained in the previous sections, the proposed method can be used with any contour evolution equation and as such can be used with color or even tensor valued data. Here for illustration purposes results showing segmentation of real gray scale images were included.

4.1.2.1 Silhouette Data

A first set of experiments were carried out using a chicken image set consisting of 20 binary silhouette images of different shapes, orientations and sizes from the *MPEG7 CE shape-1 Part B* database. The first 19 of them were used as training shapes for building the statistical prior model and the remaining image was used for testing (see Figure 4.3). The diversity of the training shapes can be clearly noted — rotations in the images were not removed on purpose to test robustness of the proposed method against large shape variability.

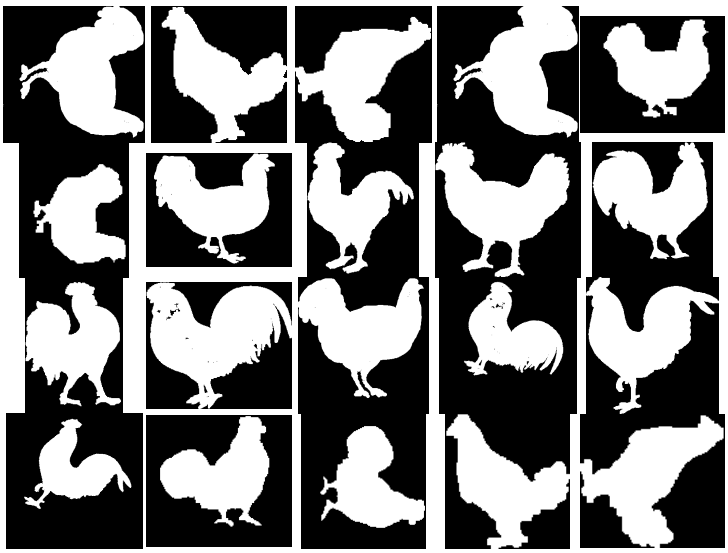

Figure 4.3: The chicken image set.

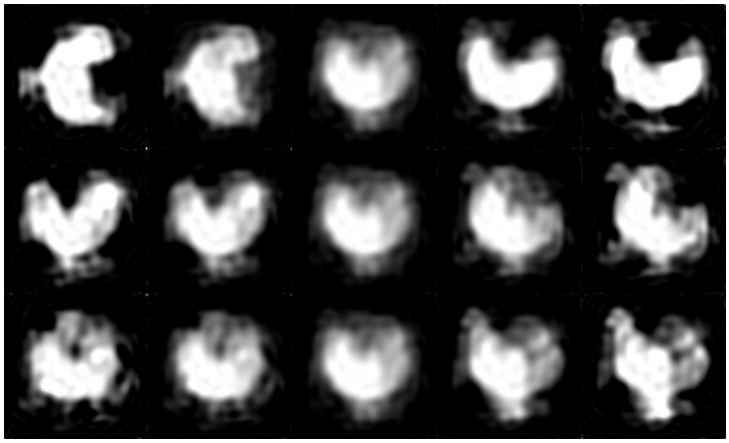

Figure 4.4: PCA results on the chicken images. From top to bottom, the three rows represent the shapes reconstructed from the Legendre moments sampled along the three most dominant principal axes (eigenvectors) in the feature space. From left to right, each column corresponds to different magnitude (-2, -1, 0, 1, 2 times the squared root of the eigenvalue associated with the corresponding eigenvector) of shape variations from the mean shape.

Shape variations represented by the sample points along the three most dominant principal axes in the feature space are shown in Figure 4.4, from which it can be observed that the three principal axes respectively capture the shape variabilities of rotation (vertical position v.s. horizontal position), trend (V-shape v.s. L-shape) and reflection (right headed v.s. left headed).

The selected chicken's silhouette image (Figure 4.5(a)) was corrupted by a combination of two different types of noise, namely, the additive white Gaussian noise for the simulation of a sensor noise and a structural noise simulating occlusions and defects.

The test image with Gaussian noise is shown in Figure 4.5(b) where the noise level is so high that even with a prior knowledge of the shape it is difficult to find the original silhouette in the noisy image. For the structural noise (Figure 4.5(c)), hard alterations are made on the original image in order to emphasis the need for shape constraints. Finally, the last test image is corrupted by both Gaussian and structural noise (Figure 4.5(d)).

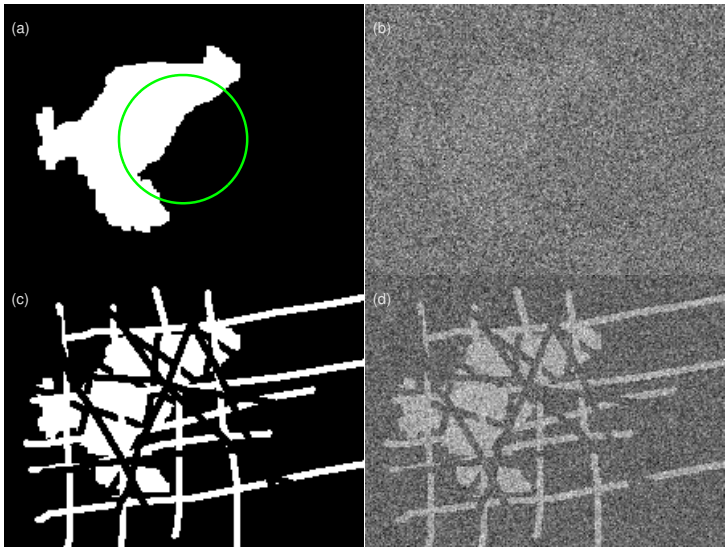

Figure 4.5: Test images, (a) original binary silhouette image with initial active contour used in the experiments, shown as a circle at the center of the image, (b) test image corrupted by Gaussian noise, (c) test image with structural noise, (d) test image with hybrid (Gaussian and structural) noise

All the experimental results shown in Figure 4.6 were based on the test images as shown in Figure 4.5 and with the same parameters $N_o = 40$ and $N_c = 10$, used to calculate Legendre moments and the shape space.

As it can be seen in Figure 4.6 for each corrupted image, the proposed method makes a satisfactory shape segmentation even though this shape was not included in the database of the shapes used to calculate the shape space. Figure 4.6(d) shows the final segmentation results for the image corrupted by both Gaussian and structural noise. It can be seen that in the solution, following Eq.(4.15), defined in the shape space (shown in green) detailed shape variabilities are normally missing. This is most prominent in the noiseless image. Whereas the solution defined in the image space, Eq.(4.19), the corresponding Ω (shown in red), closely follows edges of the silhouette. For the noisy images, particularly with the severe random noise, quality of the segmentation in the image domain slightly deteriorates. This can be understood as manifestation a basic tradeoff between fidelity and robustness to noise. In the proposed method this tradeoff

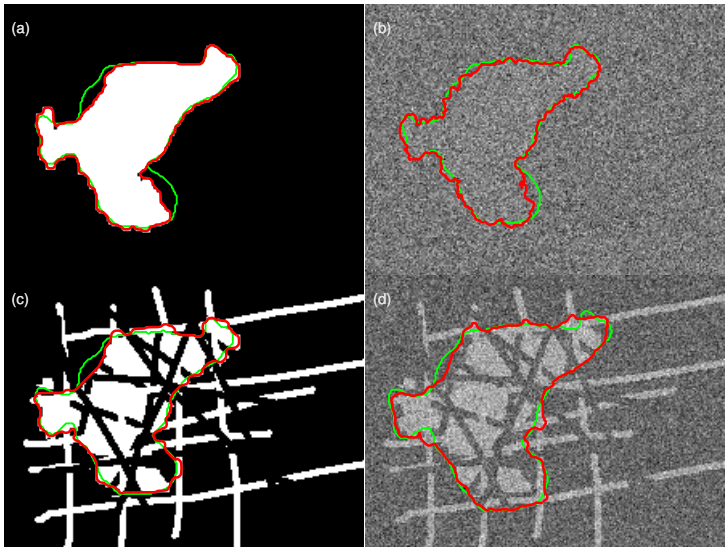

Figure 4.6: Results obtained by the proposed method for: (a) noise-free test image; (b) test image corrupted by the Gaussian noise; (c) test image with the structural noise; (d) test image corrupted by the hybrid noise. Whereas the green line represents the solutions defined in the shape space corresponding to $\alpha = \infty$ in the final algorithm iteration, the red line shows solutions obtained for α chosen based on the level of noise present in the images, e.g. for noise free image shown in (a) $\alpha = 0$.

is controlled by the α parameter, Eq.(4.24), where small value of α encourages fidelity whereas larger values improve robustness of the solution. Samples of the evolving shape for this specific test image are shown in Figure 4.7.

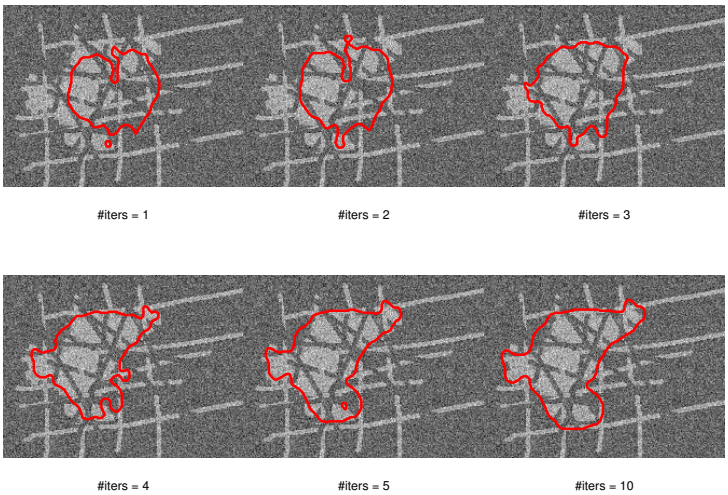

Figure 4.7: Intermediate contour evolution in the shape space obtained for the result shown in Figure 4.6(d).

Figure 4.8 shows the shape evolution trajectories in the feature space, spanned by the first

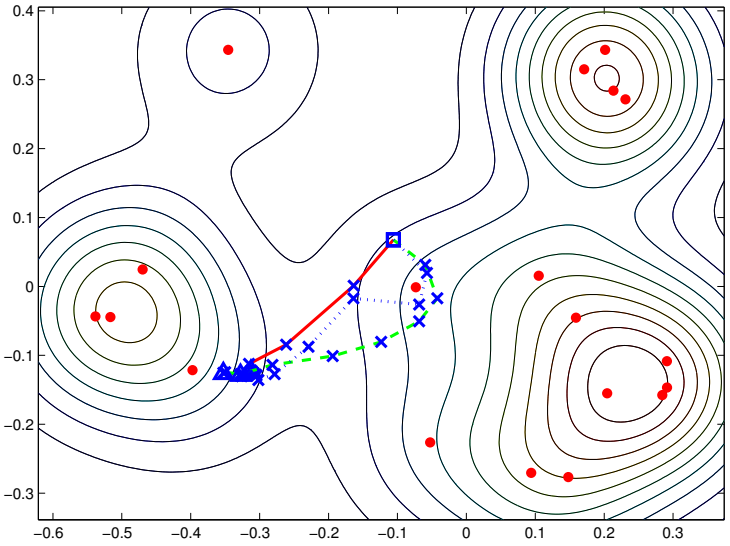

Figure 4.8: Shape evolution trajectories shown in the feature space spanned by the first two principal axes.

two principal axes, corresponding to the results shown in Figure 4.6. The iso-contours shown in this figure illustrate the probability density function (pdf) estimated using isotropic Gaussian function as the Parzen window with $\sigma^2 = 0.02$. The dots represent the projections of the 19 training shapes.

The three curves in Figure 4.8, shown in solid, dash and dotted lines, respectively demonstrate the trajectories formed by the optimization processes of the proposed method based on the test images with Gaussian, structural and hybrid noise. As the same initial circular shape was used for all three test images all the trajectories start at the same point marked by a square. All trajectories converge to points scattered nearby the dot representing the shape included in the image shown in the first row and third column in Figure 4.3, which is the most similar to the shape present in the test images. Focusing on the dotted trajectory within the feature space, one can match trajectory steps with the intermediate results shown in Figure 4.7. The fact that the convergent points are close but not exactly on the dot indicates that the proposed approach is not a template matching. Although the method is designed to search for shapes similar to shapes seen during the training process it can recover some unseen shape variations.

To assess the performance of the proposed method, the results obtained were compared against the segmentation results generated by the usual Chan-Vese model (without shape constraint) shown in Figure 4.9 and with the result obtained using the multi-reference method proposed in [Foulonneau, *et al.*, 2009] shown in Figure 4.10.

The segmentation result for the additive Gaussian noise from the Chan-Vese model, which is well-known for its robustness to Gaussian noise, is shown in Figure 4.9(b). Inaccurate as it is, the result does provide some reasonable indications about the shape and position of the desired object, shown as a dash line, which is one of the major reasons why region-based active contour approaches such as Chan-Vese model are good choices for the image term in the proposed method. Figure 4.10(b) shows the segmentation result using the multi-reference method from [Foulonneau, *et al.*, 2009], where all the 20 training shapes were used as references. The result demonstrates a dilemma for the methods with 'soft' shape constraints – How to or is it possible

to select an appropriate weight to balance the image term and shape term? For a noisy image like this, a strong image force could lead to the inaccurate result as shown in Figure 4.9(b), whereas a strong shape force could result in the convergence to a wrong shape at a wrong location due to the lack of guidance from image force. In this case, a range of different weights were tried, but none of them converged to the right result. Much better result was achieved using the proposed method as shown in Figure 4.6(b). As expected, the resulting shape living in the reduced feature space tends to have more regular appearance.

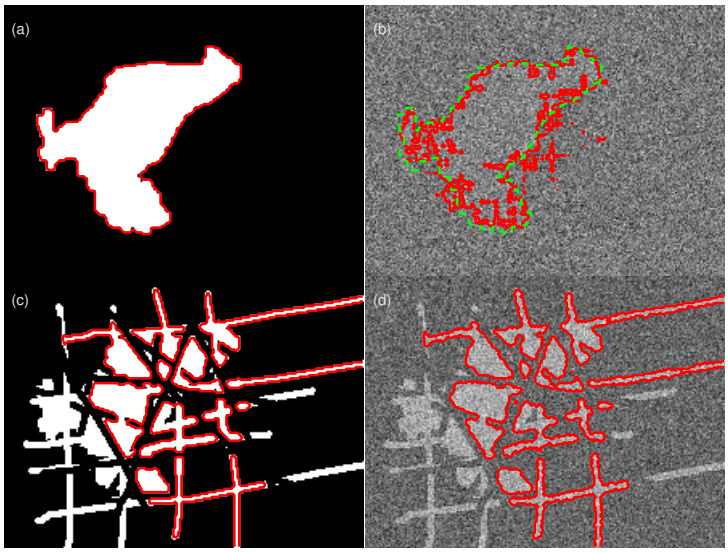

Figure 4.9: Segmentation results obtained for the corresponding test images from Figure 4.5 using Chan-Vese model.

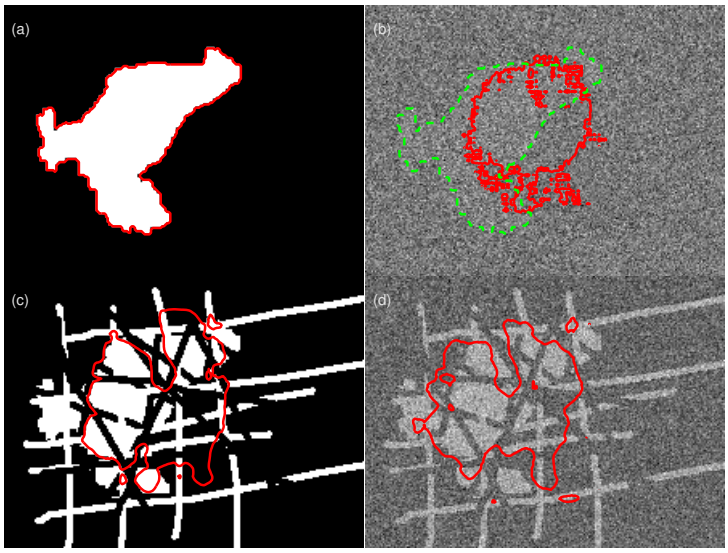

Figure 4.10: Segmentation results obtained for the corresponding test images from Figure 4.5 using multi-reference method proposed by Foulonneau *et al.*.

For images with a large amount of structural noise Chan-Vese model without shape constraint completely failed, as shown in Figure 4.9(c-d), by following the false structures. Although increasing the weight associated with the length term (γ in Eq.(4.11)) can avoid some of the false structures, it cannot properly locate the desired shape. Again, the multi-reference method failed to converge to the right result as evident from Figure 4.10(c-d).

Figure 4.11 collocates the results obtained for a different test images generated from the different chicken silhouette. As before the selected image was removed from the training set prior to construction of the shape space.

Once again, the proposed method leads to the most satisfying results. Figure 4.12 demonstrates the trajectories formed by the optimization processes of the proposed method applied to the data with Gaussian, structural and hybrid noise. It can be noticed that the local pdf maxima are "better defined" in comparison to the pdf shown in Figure 4.8 as in this case a smaller value of σ^2=0.002 was used within the Gaussian kernel. Regarding convergence of the different trajectories, the same conclusions as in the first set of experiments can be made.

Although the main objective of the described experiment was to demonstrate a superior robustness of the proposed methods with respect to severe random and structural noise, the accuracy of the method was also tested on repeated experiments with different combination of the target image and structural noise pattern. It transpired that the proposed method was able to localize object boundary with an average accuracy of 1.2, 1.7 and 2 pixels when operating respectively on images with Gaussian, structural and hybrid noise.

4.1.2.2 Gray Scale Images

Finally experiments were carried out using a gray scale images to test performance of the proposed methodology on real images. The first test image used in these experiments is shown in Figure 4.14(a) where the objective was to segment the cup. The shape space was constructed from the image set shown in Figure 4.13, with a subset of the *MPEG7 CE shape-1 Part B* database used. It can be clearly seen that the training shapes integrate a large shape variability, and that different positions of the handle are taken into account (left and right). Results of segmentation using the Chan-Vese, multi-reference and the proposed method are shown in Figure 4.14.

Assuming that the goal of the segmentation was to recover the shape of the cup, the proposed method leads to more accurate result with the final shape segmentation not altered by the drawing on the cup or by books and a pen in the background. The corresponding trajectory of the optimization process can be seen in Figure 4.15.

This demonstrates that the proposed method is more robust than the other two tested methods with respect to "shape distractions" present in the data. The final result can be seen as a good compromise between image information and the prior shape constraints imposed by the training data set used.

4.1.3 Conclusion and perspectives

Previous sections describe a novel method for shape detection and image segmentation. The proposed method can be seen as constrained contour evolution, with the evolution driven by an iterative optimization of the posterior probability function that combines a prior shape probability, the coupling distribution, and the image likelihood function . The prior shape probability function is defined on the subspace of Legendre moments and is estimated, using Parzen window method, on the training shape samples given in the estimated beforehand shape space. The

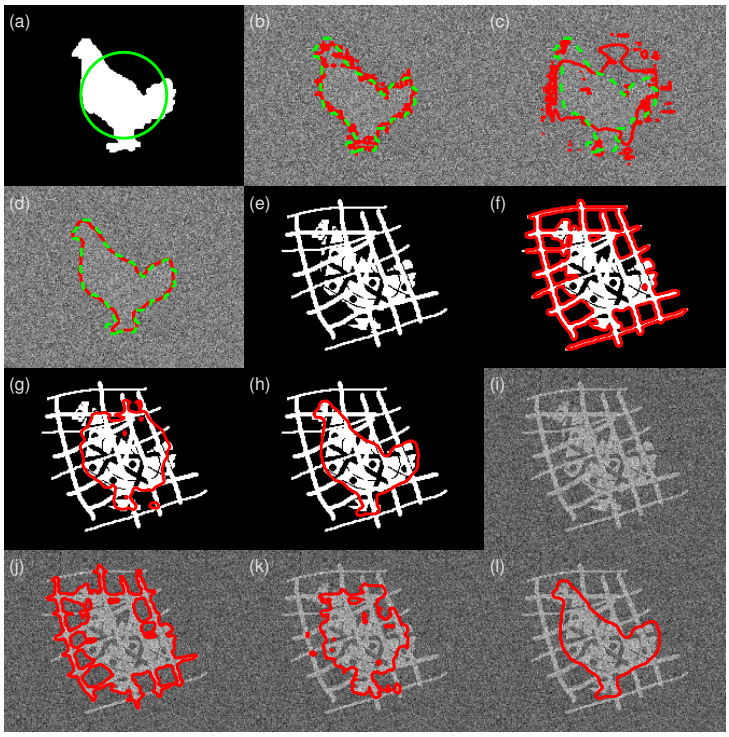

Figure 4.11: Results for a second set of experiments using different chicken's silhouette image. This specific image has been removed from the database before building the shape space subsequently used in the iterations. The segmentation results are shown as red solid curves, whereas the desired results are shown as green dash lines. (a) Original noise-free test image with initial active contour shown as a circle at the center of the image; (b) Segmentation of the test image with severe Gaussian noise using Chan-Vese method; (c) Segmentation of the same test image as in (b) using the multi-reference method proposed by Foulonneau *et al.*; (d) Segmentation of the same test image as in (b) using the proposed method; (e) Test image with structural noise; (f) Segmentation of (e) using Chan-Vese model; (g) Segmentation of (e) using the multi-reference method; (h) Segmentation of (e) using the proposed method; (i) Test image with hybrid noise; (j) Segmentation of (i) using Chan-Vese method; (k) Segmentation of (i) using the multi-reference method; (l) Segmentation of (i) using the proposed method.

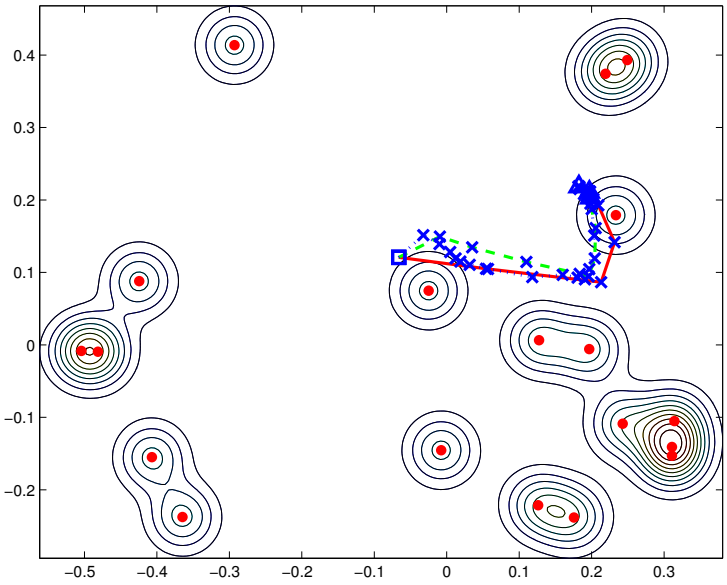

Figure 4.12: Trajectories in the first two principal axes of the shape space: (i)solid for data with Gaussian noise; (ii)dash for data with structural noise; (iii)dotted for data with hybrid noise.

Figure 4.13: Training set used to build the shape space for the cup object.

Figure 4.14: Segmentation results for the cup image (a) an image to be segmented, (b) result of segmentation using Chan-Vese model, (c) result of the segmentation using the multi-reference method from Foulonneau *et al.*, (d) result of the segmentation using the proposed method.

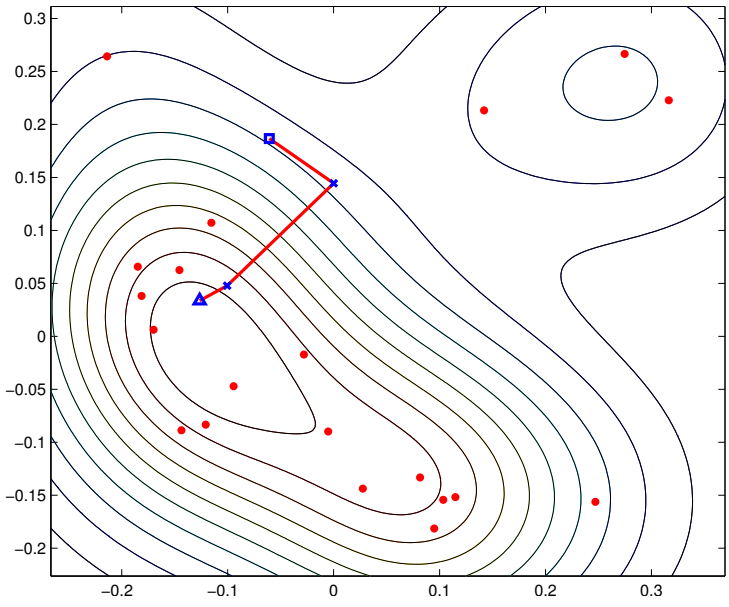

Figure 4.15: Trajectory in the space of the first two principal directions of the cup shape space corresponding to result shown in Figure 4.14. The square represents the starting point, the triangle the projection of the final detected shape.

likelihood function is constructed from conditional image probability distribution, with the image modeled to have regions of approximately constant intensities. The coupling distribution is defined as the prior distribution on the image likelihood function which imposes feasible shapes changes based on the current shape parametrization in the shape space. The resulting constrained optimization problem is solved using combinations of level set active contour evolution in the image space and steepest descent iterations in the shape space. The decoupling of the optimization processes into image and shape spaces provides an extremely flexible optimization framework for general statistical shape based active contour where evolution function, statistical model, shape representation all become configurable. The presented experimental results demonstrate very strong resilience of the proposed method to the random as well as structural noise present in the image.

The recent work introduced in [Dahdouh *et al.*, 2013], shows the real interest for that kind of approaches in the particular area of medical image segmentation. In our case, in the context of ECSON project, a particular focus to Prostate MRI segmentation in on the run. More precisely, main objective is to segment bladder, rectum and prostate using a statistical shape model appearance model in order to help clinicians to draw an efficient radiotherapy planning for Prostate Cancer treatment. In [Zhang *et al.*, 2010] can be found previous results we achieved on that particular application area and that were presented in a dedicated workshop, in conjunction with MICCAI conference.

4.2 Contribution to Statistical-Region-Based Active Contour

4.2.1 Introduction

Formerly introduced in [Aubert *et al.*, 2003], statistical region based active contour methods are derived from traditional region-based approaches [Jehan-Besson *et al.*, 2003] by utilizing integral statistics as descriptors of the inner (Ω_{in}) and outer (Ω_{out}) regions delimited by the active curve Γ at a given iteration τ of the segmentation process (Fig. 4.1). This last approach aims at improving usual region-based descriptors, like mean or variance of pixels, that fail to segment regions in image that can not be easily discriminated by their first order statistics. Main principle is to use probability density function (PDF), computed from histograms of the luminance of the pixels, as region features in order to make evolve the active curve. That kind of approaches leads to energy of two possible forms:

- In the first case, the energy is defined so as to compete inner and outer regions of the active curve using an entropy measurement as the descriptors related to the Density Probability Function (PDF) of considered regions ; Shannon's entropy is usually considered [Herbulot *et al.*, 2006].

- An other option is to define the energy as a divergence between the PDF of inner and outer regions so as to a maximization process of this similarity measure leads to the object to segment. In this case the Kullback-Leibler divergence remains the most used [Lecellier *et al.*, 2010].

The two major issues related to statistical-region-based active contour approach are:

(i) The PDF modelling function that has to be of class C^1 in order to be integrated into a variational approach.

(ii) The choice of a statistical descriptor of the PDF p_{in} and p_{out} describing respectively the inner and outer region delimited by the active curve.

Regarding the first point, a classic choice [Lecellier *et al.*, 2009; Herbulot *et al.*, 2006] is to model current PDFs p_{in} and p_{out} non parametrically using kernel methods like Parzen approach [Parzen, 1962]. In that case, a PDF p_i is estimated the following way:

$$p_i(\lambda) = \frac{1}{|\Omega_i|} \int_{\Omega_i} G_\sigma(\mathbf{I}(\mathbf{x}) - \lambda)\, d\mathbf{x}, \tag{4.34}$$

where $i = \{in, out\}$, λ the luminance intensity value at a pixel $\mathbf{x}$ of the image and g_σ the Gaussian kernel with standard deviation σ used to define the related Parzen estimator. Main advantage of this modelling is in the related abilities to estimate a very large range of PDF with no restriction on peculiar statistical family [Herbulot *et al.*, 2006].

In the last 4 years, we have had a particular interest on the second issue consisting in proposing original statistical descriptors of the PDF that would lead to flexible segmentation approach, able to cop with different kind of segmentation scenarios in the area of CAD. Theoretical elements as well as examples of applications are presented in the following sections. Most precisely, we first introduce an original entropic-based descriptor related to Rényi entropy, and in a second time, we focus our attention on a particular family of divergences between PDF: the alpha-divergences.

4.2.2 A Fractional-Entropy-Based Descriptor

4.2.2.1 Theoretical framework

Let $H(\Omega_i)$ denote an integral entropy estimation associated to a particular region Ω_i within image such as

$$H(\Omega_i) = \int_{\Omega_i} \varphi\left(p(\mathbf{I}(\mathbf{x}), \Omega_i)\right) \, d\mathbf{x} \, , \tag{4.35}$$

with φ a monotonically increasing function, $\mathbf{I}(\mathbf{x})$ the luminance of pixel $\mathbf{x} = (x, y)$ and p the non-parametrically estimated Probability Density Function (PDF) of region Ω_i, estimated using Parzen window described above.

$$p(\mathbf{I}(\mathbf{x}), \Omega_i) = \frac{1}{|\Omega_i|} \int_{\Omega_i} G_\sigma(\mathbf{I}(\mathbf{x}) - I(\lambda)) \, d\lambda, \tag{4.36}$$

where $\lambda \in [0...2^n - 1]$, n is the quantization level of image intensity function, and G_σ is the Gaussian kernel of standard deviation σ. In the framework of statistical region based active contour segmentation, corresponding functional H_T to be minimized is defined as a competition between inner and outer regions characterized by the introduced, in Eq (1), entropy descriptor H:

$$H_T = H(\Omega_{in}) + H(\Omega_{out}) + g \int_\Gamma ds, \tag{4.37}$$

where g is a positive real value and s standard arclength of the curve. This functional combines measures of the considered entropy descriptor of inner Ω_{in} and outer Ω_{out} regions of the curve with an additional regularization term minimizing the curve length. The Euler derivative of Eq. (4.37) and usual minimization scheme leads to the Partial Differential Equation (PDE) steering the evolution in the orthogonal direction $\mathbf{N}$ of the active curve Γ [Herbulot *et al.*, 2006]:

$$\frac{\partial \Gamma}{\partial \tau} = \big(A(s, \Omega_{in}) + \varphi(p(\mathbf{I}(s), \Omega_{in})) - A(s, \Omega_{out}) + \varphi(p(\mathbf{I}(s), \Omega_{out})) + g\big)\mathbf{N} \tag{4.38}$$

where $s = \Gamma(p, \tau)$ and A is related to the proposed descriptor and is defined by:

$$A(s, \Omega_i) = -\frac{1}{|\Omega_i|} \int_{\Omega_i} \varphi'(p(\mathbf{I}(\mathbf{x}), \Omega_i))[p(\mathbf{I}(\mathbf{x}), \Omega_i) - G_\sigma(\mathbf{I}(\mathbf{x}) - \mathbf{I}(s))] \, d\mathbf{x} \, . \tag{4.39}$$

For illustration, let's consider the particular case of Shannon's entropy: φ function is given by

$$\varphi(r) = -r \times log(r) \, , \tag{4.40}$$

and then

$$H(\Omega_i) = -\int_{\Omega_i} p(\mathbf{I}(\mathbf{x}), \Omega_i) log(p(\mathbf{I}(\mathbf{x}), \Omega_i)) d\mathbf{x}. \tag{4.41}$$

As it will be shown in the "Experiments and Results" section, standard Shannon's entropy has some limitations in terms of segmentation performance: more specifically, this measure makes segmentation of corrupted (with Gaussian or Poissan noises) textured images challenging [Herbulot *et al.*, 2006], and in the case of high level of structural noise, the segmentation results are not that satisfactory.

First of all, as shown in [Jehan-Besson *et al.*, 2003], this can be explained by the fact that Shannon's criterion is equivalent to a region based approach depending only on variance difference

in p_{in} and p_{out} regions. As a consequence if the corresponding PDFs cannot be discriminated by their first order statistics, this criterion is not applicable. In this particular context, fractional entropy like the Rényi's entropy [Rényi, 1960] defined such as:

$$H_R(\Omega_i) = \frac{1}{1-\alpha} log \int_{\Omega_i} p(\mathbf{I}(\mathbf{x}), \Omega_i)^\alpha \, d\mathbf{x} \; . \tag{4.42}$$

can be of primary interest.

It can be shown [Bromiley *et al.*, 2004], using L'Hôpital, in the limit $\alpha \to 1$ Renyi's entropy converges to the Shannon's entropy. For any value of $\alpha \geq 0$, Rényi's entropy is nonnegative and for $\alpha \in [0, 1]$, Rényi's entropy is concave and shows an additional parameter α which can be used to make it more or less sensitive to the shape of PDF p. For illustration, Fig. 4.16 shows the Rényi's entropy of Eq. (4.42) considering the usual Bernoulli's distribution for input variable.

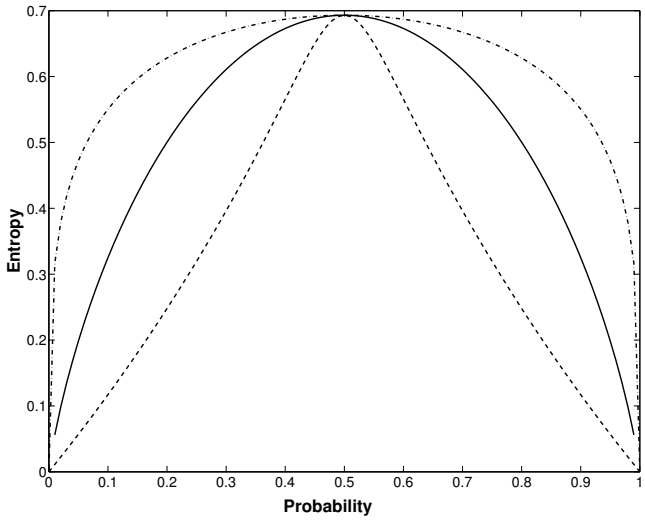

Figure 4.16: Rényi entropy H_R of Eq. (4.42) as a function of the probability p of a binary source $(p, 1-p)$ (Bernoulli's distribution), for three values of the order $\alpha = 0.4$ (dash-dotted line), $\alpha = 10$ (dashed line), and $\alpha = 1$ identified by plain line corresponding to the Shannon's entropy.

This relaxation property (see $\alpha = 0.4$ in Fig. 4.16) is the starting point of the following study. Unfortunately, Rényi's entropy as expressed in Eq. (4.42) is part of the non-integral entropy family that can not be easily associated to a region-based criterion in a classic active contour based segmentation. Nevertheless, taking benefits of the possible sensibility tuning of the Rényi's entropy using α parameter, we propose to define a fractional entropy measure adapted to the framework of statistical region-based active contour segmentation. For this, let consider Eq. (4.35) with φ function and its derivative given by:

$$\varphi(r) = \varphi_\alpha(r) = -log\,(r^\alpha) \;\; \text{and} \;\; \varphi'_\alpha(r) = -\frac{\alpha}{r} \; . \tag{4.43}$$

with $\alpha \in [0, 1]$. Considering φ_α function of Eq. (4.43), we obtain an integral entropic measure[8] integrating a fractional parameter allowing some relaxation properties as shown Fig. 4.17.

[8]It should be noticed that as for the Renyi's entropy, the proposed entropy fulfills only two out of three conditions for the measure of amount of information as postulated by Shannon, and therefore the proposed entropy should not be confused with the Shannon entropy

Moreover, let's note that at the limit $\alpha = 1$, we obtain $\varphi_\alpha(r) = -ln(p)$ which is the Ahmad-Lin estimator of Shannon's entropy [Ahmad and Lin, 1976].

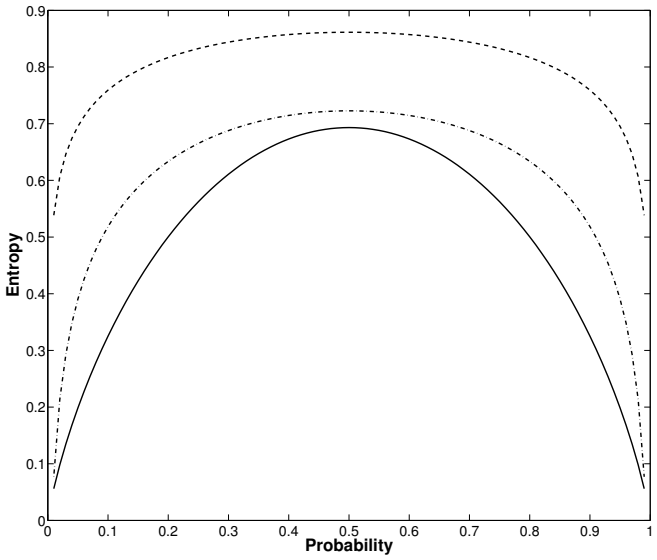

Figure 4.17: fractional entropy measure of Eq. (4.43) as a function of the probability p of a binary source $(p, 1-p)$ (Bernoulli's law), for two values of the order $\alpha = 0.1$ (dash-dotted line), $\alpha = 0.2$ (dashed line). Plain line corresponds to the Shannon's entropy.

4.2.2.2 Experiments and Results on Synthetic and Natural Images

In order to be able to cop with segmentation scenario where Ω_{in} is defined by more than one region, we propose to implement the aforementioned PDEs using level-set method, formerly introduced by Osher and Sethian [Osher and Setian, 1988], where the active contour Γ is a zero level of a function defined such as $\phi : \Re^2 \times \Re^+ \rightarrow \Re$. For all experiments, except when precise, the initialization of the active contour function ϕ is a set of small circles uniformly distributed all over the image. This choice allows an easy initialization of the algorithm with no need of manual intervention. Classic AOS (Additive Operator Splitting) scheme [Weickert, 1998] is used for implementation in order to obtain a reasonably fast convergence.

Synthetic Data

In order to compare performances of both Shannon's entropy and the proposed fractional entropy measure inspired by Rényi's entropy, tests were carried out first on synthetic images.

For the first experiments, the main idea is to compare performances of the two aforementioned criteria with respect to the type of corrupting noise. Zero-mean Gaussian and Poisson were considered with a related PSNR equal to 3 dB corresponding to significant level of image distortion. In order to also test capabilities of the proposed approach in terms of adaptation to topological changes, the considered synthetic images presents two disjoint objects to be segmented (see Fig. 4.18 for illustration).

Fig. 4.18 shows comparative segmentation results between the Rényi-like entropic measure and the standard Shannon's entropy. When Gaussian noise is considered, one can notice in

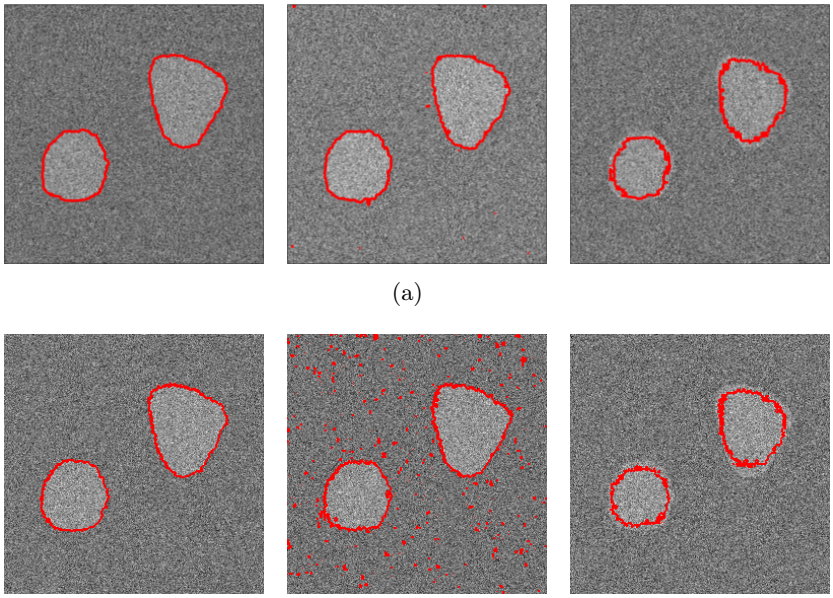

(a)

(b)

Figure 4.18: Segmentation of synthetic images (PSNR = 3dB) corrupted with different type of noise, and for different value of α parameter. (a) Zero-Mean Gaussian noise, (b) Poissan noise. From left to right : (a) $\alpha = 0.5$, $\alpha = 0.7$ and Shannon's entropy. For these experiments, the regularization term g is set to 5 ; (b) $\alpha = 0.1$, $\alpha = 0.5$ and Shannon's entropy. For these experiments, the regularization term g is set to 0.1.

Fig. 4.18.(a) that the proposed Renyi like entropic region descriptor leads to good segmentation results, whereas the Shannon criteria is less accurate even if the main structure is captured. This can be explained by the fact that Shannon's criterion is not statistically discriminative enough for high level of noise in the considered PDF when foreground and background have the same variance. Having in focus the proposed application to microscopic images corrupted by Poissan noise, Fig. 4.18.(b) shows results obtained for that kind of corrupting noise. Same global results are obtained than with Gaussian noise, even if it can be noticed that the α value leading to the satisfying segmentation is lower than for Gaussian noise.

Considering the proposed criterion, the robustness to the level of corrupting noise can be explained by the use of logarithm function combined with fractional values of α (α between 0 and 1) which can be interpreted here as a smoothing term on the shape of the PDF. As one can seen in Fig. 4.18, the more α tends to the asymtotic value of 1, the more the segmentation method is sensitive to the level of corrupting noise which is not that surprising considering the fact that for $\alpha = 1$ the corresponding entropy is the Shannon's entropy.

The second experiment proposed consists in estimating the capability of the proposed method to discriminate between two regions having statistically similar characteristics. To illustrate this, we propose to segment the peanut shape in Fig. 4.19 which is characterized by a challenging statistical texture discrimination between p_{in} and p_{out} because of the similarity in the statistical distribution extracted from histograms of corresponding regions ((variance and mean of each PDF are very close even if visually each texture is quite different).

Fig. 4.19 shows results obtained with the Rényi-like criterion (for two different values of α) and the segmentation obtained with the standard Shannon's entropy. This latter descriptor completely failed in the segmentation task, whereas the proposed fractional entropy criterion

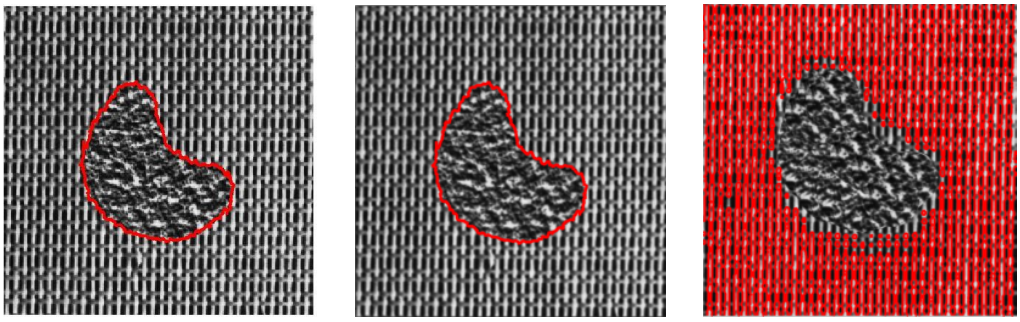

Figure 4.19: Segmentation of synthetic textured images with $\alpha = 0.5$ (left), 0.7 (middle) and Shannon entropy based segmentation.

leads to satisfying segmentation results for the two proposed values of α: it seems that the opportunity to take into account not only first order statistics of the PDF via α parameter tuning makes possible to dissociate similar distribution p_{in} and p_{out}.

Natural Image Segmentations

In this section, we present some segmentation results obtained on natural images. Fig. 4.20 shows comparative results for a flower image. This segmentation task is not the most challenging since the main part of the flower is statistically quite different from the background. Nevertheless, it remains a good reference in order to study the influence of parameter α related to the proposed fractional entropy descriptor. As it can be noticed in Fig. 4.20, Shannon's entropy criterion, for a same tuning of the regularization term g, leads to a global shape segmentation, whereas the proposed fractional entropy descriptor offers an additional flexibility of segmentation related to the α value: For instance, Fig. 4.20.(a) shows that for $\alpha = 0.1$, a better recall can be achieved than in Fig. 4.20.(d). Figs. 4.20.(b) and (c) show that a more detailed segmentation could also be obtained depending on the objective of the segmentation task.

Considering now a more challenging problem, we propose to tackle the segmentation of the "Cheetah" image. Fig. 4.21 shows comparative results obtained for different values of α parameter and for Shannon's entropy.

Obtained segmentation with Shannon's entropy criterion appears quite sensitive to noise and if the whole body of the animal is segmented, some background area are also included within the final result which is not that satisfying. When utilizing the proposed fractional entropy criterion, it can be noticed that better results are obtained. Once again, depending on the value of α parameter, different level of segmentation details are obtained: For $\alpha = 0.1$, only the main textured body of the cheetah is segmented whereas for upper values, the whole shape (including head and tail) is delineated. As illustrated with synthetic images, it also appears that the closer α is to one, the segmentation is sensitive to the background noise. This is not surprising since, as we have already mentioned it, for $\alpha = 1$, the proposed fractional entropy is related to the Ahmad-Lin estimator of Shannon's entropy.

4.2.2.3 Nuclei Segmentation In Confocal Microscopy Images

Fluorescence Confocal Microscopy Images

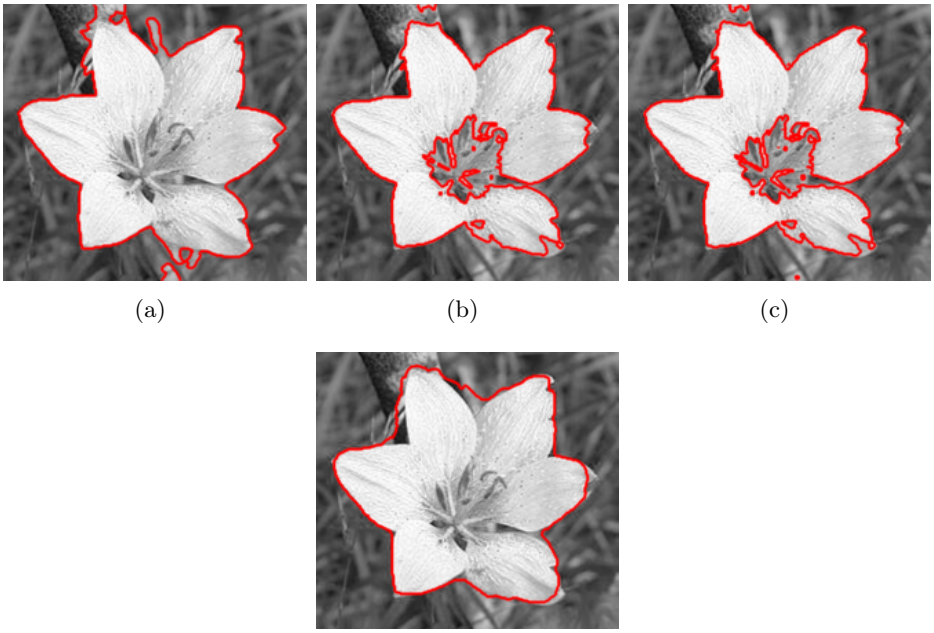

(a) (b) (c)

(d)

Figure 4.20: Different segmentation results of the "Flower image" using the proposed fractional entropy criterium: (a) $\alpha = 0.2$, (b) $\alpha = 0.4$, (c) $\alpha = 0.6$. (d) Shannon entropy based segmentation. For each experiment, g is set to 0.1.

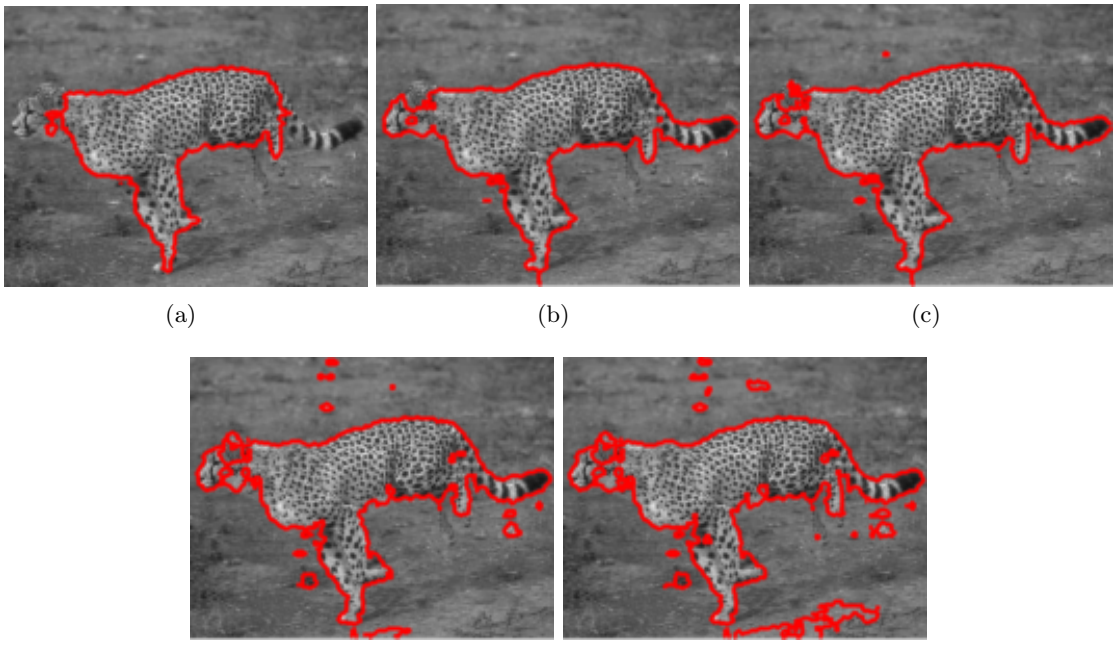

(a) (b) (c)

(d) (e)

Figure 4.21: Different segmentation results of the "Cheetah image" using the proposed fractional entropy criterium: (a) $\alpha = 0.1$, (b) $\alpha = 0.2$, (c) $\alpha = 0.3$. (d) Shannon entropy based segmentation. For each experiment, g is set to 0.3.

The data used in this paper were obtained from human prostate cells (PNT2). Actin were labelled with phalloidin-FITC and all imaging was carried out using a Zeiss LSM510 confocal microscope. Fig. 4.22 shows different slices from the microconfocal acquisition of the monolayer PNT2 cell culture. The stack volume is defined on the $512 \times 512 \times 98$ grid of pixels each $0.21\mu m \times 0.21\mu m \times 0.11\mu m$ in size [Matuszewski *et al.*, 2011].

The choice of filamentous marker actin (F-actin) is motivated by the fact that F-actin is known to play a vital role in in cell structure and mechanics [Hall, 2009]. As Actin is one of the main existing proteins in human cytoskeleton, studying its changes and properties could help to understand better cell bio-mechanical properties. As actin is mostly present in the cytoplasm, we can notice that high intensities in slices of Fig. 4.22 show areas of high concentration of actin in proximity of cell membrane which allows us to find approximate location of cell boundaries whereas darkest areas represent nuclei. Due to the high level of Poisson noise corrupting these images and their particular textured structures, it is difficult to propose a parametric model of this. Moreover, due to the particular texture of actin, classic region based active contour approach, like the Chan and Vese one [Chan and Vese, 2001], fails even in segmenting properly the boundaries of nuclei corresponding to each cell [Meziou *et al.*, 2011a]: We then propose to tackle this segmentation using statistical based active contour (see [Lecellier *et al.*, 2010] for an overview on the work on this area) more adapted to this particular context than classic region based ones.

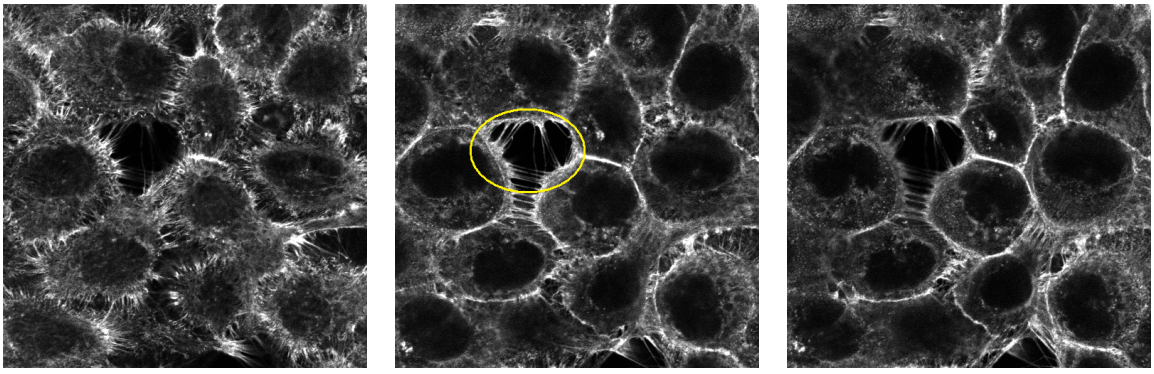

(a) (b) (c)

Figure 4.22: Examples of actin tagged fluorescence confocal microscopy images extracted from a 3D microconfocal acquisition of the monolayer PNT2 cell culture. (a) Lower slice (with low z-stack index), (b) Mid-slice with the lowest level of structural noise (a "hole" is highlighted in yellow which should not to be confused with a nucleus), (c) Upper slice with non-homogeneity of the fluorescent marker on the left hand side.

In this section, comparative segmentation results obtained are first described for the unsupervised nuclei segmentation within the mid-slice of the considered single channel confocal microscopy acquisition (Fig. 4.22(b)).

Fig. 4.23 shows results obtained with the standard Shannon's entropy criterion and the proposed fractional entropy descriptor. Considering experiments based on Shannon's entropy (Fig. 4.23 (left)), as one can notice, the method does not lead to satisfying results . Fig. 4.23 (middle and right) shows results of nuclei segmentation on the same slice, but with the proposed fractional entropy criterion: the nuclei segmentation is definitely improved. As one can notice, as actin is a complex structure, some artifacts could appear. It is possible to overcome this drawback with an adapted choice of α parameter. As one can see in Fig. 4.23, for $\alpha = 0.5$,

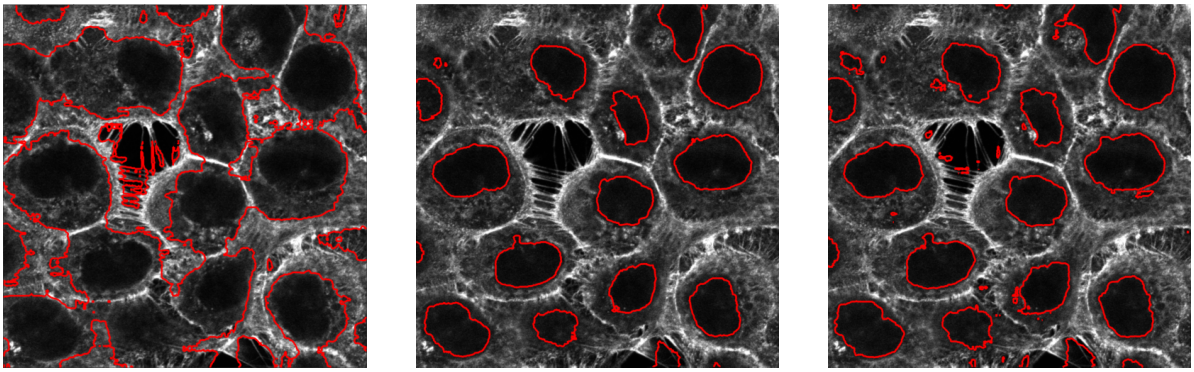

Figure 4.23: Comparative results of nuclei segmentation. Left: Shannon's entropy ; Middle and Right: Fractional entropy descriptor with $\alpha = 0.5$ (middle) and $\alpha = 0.7$ (right) ; for all experiments $g = 10$.

smaller number of artifacts related to α value and those results show that this parameter plays an important role in the sensitivity of the criterion to the level of corrupting noise. Moreover, it is important to notice that the proposed fractional entropy measure can also distinguish a hole from a nucleus (which method based on Shannon's criterion was not able to achieve), whereas the associate PDFs are statistically very similar. This is in accordance with the results obtained on the highly corrupted synthetic images: When looking at the histogram of one of the considered microcopy images (see Fig. 4.24), it appears that the modes corresponding to the hole and to the nucleus class of the pixels are very close one to each other. As a consequence, as seen before, the Shannon's entropy is not able to discriminate both and finally, nuclei and hole are merged into a single class. Considering the fractional entropy descriptor, the related ability to separate very close PDF, makes possible the discrimination between both modes.

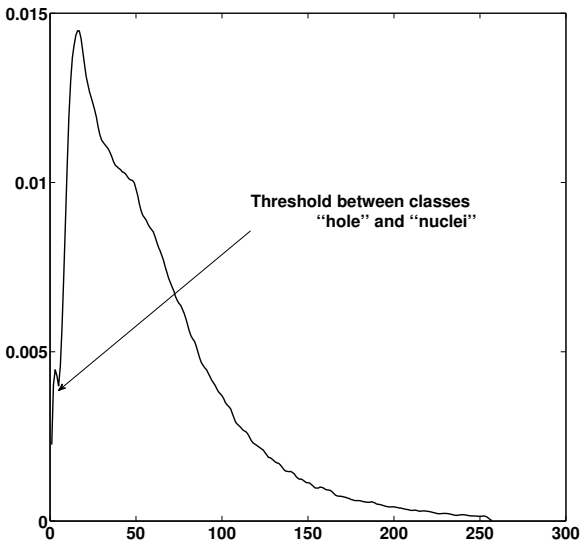

Figure 4.24: PDF of the mid-slice microscopy acquisition sequence.

Fig. 4.25 shows some segmentation results obtained on the whole stack of acquired images.

Results shown are obtained with $\alpha = 0.5$, and $g = 10$. To obtain these results, a propagation initialization strategy, starting on middle slice is used which makes integration of some spatial coherence within the segmentation scheme to avoid propagation of false detection due to complex appearance of actin.

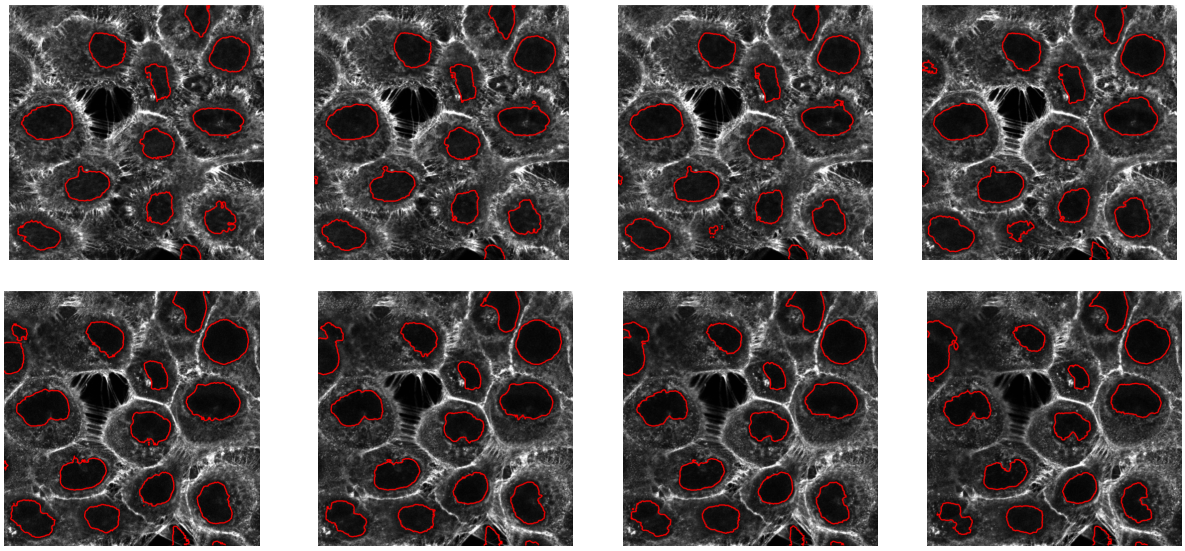

Figure 4.25: Segmentation of nuclei made on upper (upper row) and lower (bottom row) slices of the stack, mid-slice of Fig. 4.23 being the initialization level). $\alpha = 0.5$ and $g = 10$.

These results have been qualitatively considered as very satisfactory from an expert point of view and a very good start for further investigations on that particular data.

Finally, Fig. 4.26, shows results obtained on other images extracted from different acquisitions in order to illustrate the adaptability of the proposed process.

Results obtained remain satisfactory considering the fact that the non-homogeneity of the fluorescent actin marker significantly different than in previous images.

4.2.2.4 Conclusion and Perspectives

The contribution of the segmentation approach presented here is twofold: (i) Whereas in the framework of statistical based active contour methods standard Shannon's entropy is most often considered as the region descriptor, we proposed an original fractional entropy measure inspired from Rényi's entropy making possible a relaxation of the sensibility of the descriptors to strong variations of the shapes of the non parametrically estimated related PDF. The main motivation was to overcome the limitations of Shannon's entropy which appeared not adapted to our segmentation problem; (ii) An unsupervised cell nuclei segmentation method is proposed for single channel actin tagged acquisitions without any enhancement or denoising preprocessing of the considered images. First obtained results are very encouraging.

On the theoretical aspect of this work, the possibility to locally relate the optimal choice of α parameter with the level of noise and/or the type of texture characterizing the image to segment remains a real challenge. From an application point of view, membrane segmentations will be the next step in order to have a complete segmentation of the cell structure.

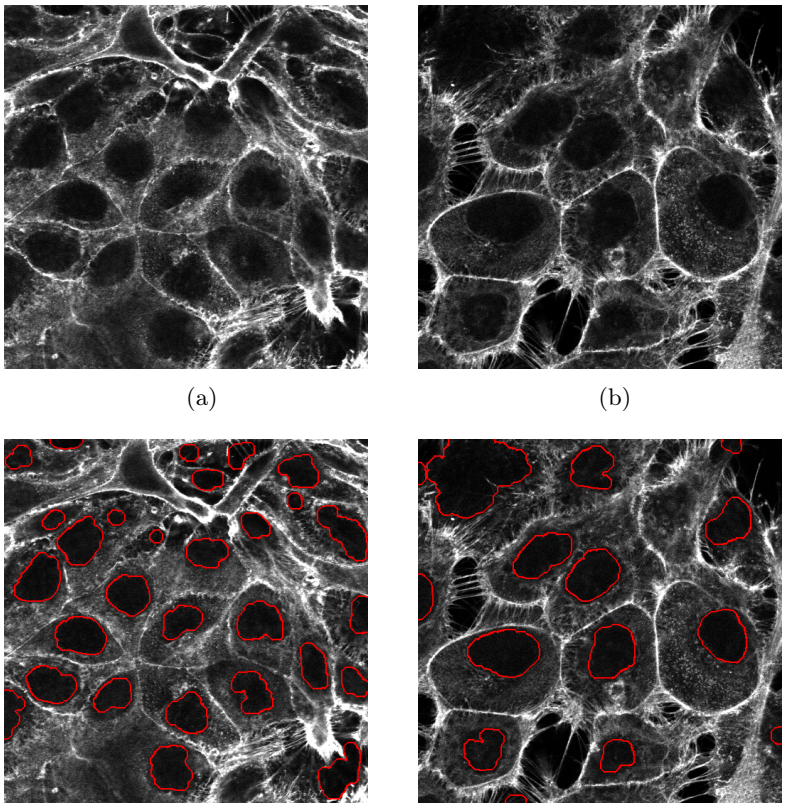

(a) (b)

(c) (d)

Figure 4.26: Segmentation of nuclei made on images extracted from different acquisitions. Up: original images, below: segmentation results with $\alpha = 0.5$ and $g = 1$.

4.2.3 Alpha-Divergence Joint Optimization For Statistical-Region-Based Active Contour Segmentation With Non-Parametric PDF Estimations

As said in introduction of this section, statistical-region-based active contour approach aims at improving usual region-based descriptors, like mean or variance of pixels, that fail to segment regions in image that can not be easily discriminated by their first order statistics. A different strategy than from the one presented in previous section consists in deriving the related steering PDE through maximization of an energy J defined as a statistical distance between the PDFs of inner (Ω_{in}) and outer (Ω_{out}) regions of the active curve Γ [Lecellier *et al.*, 2009; Michailovich *et al.*, 2007; Heiler and Schnörr, 2005; Freedman *et al.*, 2005]. Considering two PDF p_{in} and p_{out} such a distance is defined as follows:

$$D(p_{in} \| p_{out}, \Omega) = \int_{\Re^m} \varphi(p_{in}, p_{out}, \lambda)\, d\lambda \,, \tag{4.44}$$

where φ is a cost function related to the maximized distance D and Ω the image domain. $p_i(\lambda) : \Re^m \rightarrow [0, 1]$ represents probability distribution of pixel intensity λ in the image. In the particular case of this study, $m = 1$ since we will only consider grayscale images. Finally, as in the previous section, PDF are *non-parametrically* estimated at each iteration of the segmentation process using Parzen Window 4.34.

Considering the maximization of Eq. (4.44), the corresponding general PDE is usually de-

duced from the Euler derivative of D given by :

$$< D'(\Omega), \mathbf{V} >= -\int_{\partial\Omega} \mathbf{v}(\mathbf{x}, \Omega) < \mathbf{V} \cdot \mathbf{N} > \, da(\mathbf{x}), \tag{4.45}$$

where $\partial\Omega$ is the boundary of the region Ω and da an area element of Ω, with $\mathbf{N}$ the inner normal vector of the curve and $\mathbf{v}$ the velocity of the curve.

The contribution of this work is twofold: First, in the framework of the divergence maximization between non-parametrically-estimated PDF, we propose to derive the corresponding PDE, and second, we particularize to the case of alpha-divergence family, a flexible statistical similarity measure between PDF whose inner metric (φ function) can be adapted to the statistics of the data.

4.2.3.1 PDE Derivation

Considering Eq. (4.44), a first rewriting of D' of Eq. (4.45) is

$$\begin{aligned} < D'(\Omega), \mathbf{V} > &= dD(p_{in} \| p_{out}, \Omega, \mathbf{V}) \\ &= \int_{\Re} d\varphi(p_{in}, p_{out}, \lambda, \mathbf{V}) \, d\lambda. \end{aligned} \tag{4.46}$$

The problem is now then shifted to the calculation of the Euler derivative of the φ function. To achieve this, let us introduce f the function such as:

$$\begin{aligned} \varphi(p_{in}, p_{out}, \lambda) &= \varphi\Big(\frac{G_{1,in}}{G_{2,in}}, \frac{G_{1,out}}{G_{2,out}}, \lambda\Big) \\ &= f(G_{1,in}, G_{2,in}, G_{1,out}, G_{2,out}, \lambda), \end{aligned} \tag{4.47}$$

$$\begin{aligned} \text{with } G_{1,i}(\lambda, \Omega_i) &= \int_{\Omega_i} g_\sigma(\mathbf{I}(\mathbf{x}) - \lambda) \, d\mathbf{x} \\ \text{and } G_{2,i}(\Omega_i) &= |\Omega_i| = \int_{\Omega_i} d\mathbf{x}. \end{aligned} \tag{4.48}$$

From Eq. (4.47) and Eq. (4.48), we can then deduce that:

$$\begin{aligned} d\varphi(p_{in}, p_{out}, \lambda, \mathbf{V}) &= df(p_{in}, p_{out}, \lambda, \mathbf{V}) \\ &= \sum_{i=\{in,out\}} \frac{\partial f}{\partial G_{1,i}} dG_{1,i}(\lambda, \Omega_i, \mathbf{V}) \\ &+ \sum_{i=\{in,out\}} \frac{\partial f}{\partial G_{2,i}} dG_{2,i}(\Omega_i, \mathbf{V}). \end{aligned}$$

Since the function $g_\sigma(\mathbf{I}(\mathbf{x}) - \lambda)$ does not depend on the region Ω_i, we have:

$$\begin{aligned} dG_{1,i}(\lambda, \Omega_i, \mathbf{V}) &= -\int_{\partial\Omega_i} g_\sigma(\mathbf{I}(\mathbf{x}) - \lambda) \, < \mathbf{V} \cdot \mathbf{N} > \, da(\mathbf{x}), \\ dG_{2,i}(\Omega_i, \mathbf{V}) &= -\int_{\partial\Omega_i} < \mathbf{V} \cdot \mathbf{N} > \, da(\mathbf{x}), \end{aligned}$$

and partial derivatives of f are given by:

$$\begin{aligned}\frac{\partial f}{\partial G_{1,i}} &= \frac{1}{|\Omega_i|}\partial_k\varphi(p_{in}, p_{out}, \lambda)\\ \frac{\partial f}{\partial G_{2,i}} &= -\frac{p_i}{|\Omega_i|}\partial_k\varphi(p_{in}, p_{out}, \lambda),\\ \text{where } \{i,k\} &= \{\{in,1\},\{out,2\}\}.\end{aligned}$$

where $\partial_1\varphi$ and $\partial_2\varphi$ are the derivatives of φ with respect to the first (p_{in}) and the second (p_{out}) variables.

Merging all those intermediate calculations and noticing that by convention, the curve $\Gamma = \partial\Omega_{in} = -\partial\Omega_{out}$, the Euler derivative of the maximized functional D becomes :

$$\begin{aligned}dD(p_{in}\|p_{out}, \Omega, \mathbf{V}) &= \int_\Gamma \Big(\frac{-1}{|\Omega_{in}|}(A_1 - C_1)\\ &+ \frac{1}{|\Omega_{out}|}(A_2 - C_2)\Big) < \mathbf{V}\cdot\mathbf{N} > da(\mathbf{x}),\end{aligned} \tag{4.49}$$

$$\begin{aligned}\text{with} \quad A_k &= \partial_k\varphi(p_{in}, p_{out}, \lambda) * g_\sigma(\mathbf{I}(\mathbf{x}))\\ C_k &= \int_\Re \partial_k\varphi(p_{in}, p_{out}, \lambda)\, p_i\, d\lambda,\\ \text{where} \quad \{i,k\} &= \{\{in,1\},\{out,2\}\}.\end{aligned}$$

Finally, the PDE corresponding to the maximization of a distance D between two non-parametrically-estimated PDFs is obtained thanks to the Gateaux derivative gradient flow:

$$\frac{\partial\Gamma}{\partial t} = \Big[\frac{1}{|\Omega_{in}|}(A_1 - C_1) - \frac{1}{|\Omega_{out}|}(A_2 - C_2)\Big]\mathbf{N}. \tag{4.50}$$

4.2.3.2 Alpha-Divergence Family

About the choice of the statistical distance between PDFs, usually, literature focuses on classic distances like the Kullback- Leibler divergence (KL), the Hellinger distance or the χ_2 divergence [Lecellier *et al.*, 2009; Aubert *et al.*, 2003]. Nevertheless, those distances does not always lead to satisfying results of segmentation for strongly corrupted images or textured ones, as shown in [Meziou *et al.*, 2011b]. In a recent paper [Meziou *et al.*, 2012], we proposed a flexible family of divergences named alpha-divergences as similarity criterion. Introduced in information theory by Amari *et al.* [Amari, 1985], this divergence family is characterized by a tunable statistical metric (via α parameter), allowing its adaptation to the particularity of the data statistics as opposed to classic distances. The alpha-divergence between two PDF p_{in} and p_{out} is defined as follows [Cichocki and Amari, 2010]:

$$D_\alpha(p_{in}\|p_{out}, \Omega) = \int_{\chi^m} \varphi_\alpha(p_{in}, p_{out}, \lambda)\, d\lambda \tag{4.51}$$

with $\varphi_\alpha(p_{in}, p_{out}, \lambda) =$

$$\begin{cases} \dfrac{\alpha p_{in} + (1-\alpha)p_{out} - {p_{in}}^{\alpha}{p_{out}}^{1-\alpha}}{\alpha(1-\alpha)}\ , & \alpha \in \mathbb{R} \setminus \{0,1\} \\ p_{out}\ log\left(\dfrac{p_{out}}{p_{in}}\right) + p_{in} - p_{out}\ , & \alpha = 0 \\ p_{in}\ log\left(\dfrac{p_{in}}{p_{out}}\right) - p_{in} + p_{out}\ , & \alpha = 1 \end{cases} \tag{4.52}$$

It can be noticed here that at the limits α tends to 1 and 0, the corresponding divergence is the classic KL divergence (L'Hôpital Theorem): A complete study about the mathematical properties of alpha-divergences can be found in [Beirami *et al.*, 2008], but more than KL particular case, let us highlight that for specific values of α, some aforementioned standard distances can also be connected to alpha-divergences. For instance: $D_2(\Omega) = \frac{1}{2}D_{\chi^2}(\Omega)$, $D_{\frac{1}{2}}(\Omega) = 2D_{Hellinger}(\Omega)$. This makes alpha-divergence a generic distance estimation, with multiple tuning possibilities via α parameter and as a consequence, a very flexible measure.

In the context of active contour segmentation, in order to properly define the corresponding PDE, first and second derivatives of corresponding φ_α function with respect to p_{in} and p_{out} are then given by:

$$\begin{aligned} \partial_1\varphi_\alpha(p_{in}, p_{out}, \lambda) &= \frac{1}{1-\alpha}\Big(1 - \Big[\frac{p_{out}}{p_{in}}(\lambda)\Big]^{1-\alpha}\Big) \\ \partial_2\varphi_\alpha(p_{in}, p_{out}, \lambda) &= \frac{1}{\alpha}\Big(1 - \Big[\frac{p_{in}}{p_{out}}(\lambda)\Big]^{\alpha}\Big), \end{aligned} \tag{4.53}$$

which completely defines the iterative process of segmentation.

4.2.3.3 Experiments and Results: Part 1

Again, In order to be able to segment images presenting more than one target object, we propose to embed the alpha-divergence maximization within the now usual level-set framework. In this framework, considering the standard level-set embedding function $\phi : \Re^2 \times \Re^+ \to \Re$ and preliminary calculations given by Eq. (4.50), the following evolution PDE is obtained:

$$\begin{aligned} \frac{\partial\phi}{\partial t} =& \delta\phi\Big(\beta\nabla\cdot\left(\frac{\nabla\phi}{|\nabla\phi|}\right) \\ & - \xi(\frac{1}{|\Omega_{in}|}(A_1 - C_1) + \frac{1}{|\Omega_{out}|}(A_2 - C_2))\Big), \end{aligned} \tag{4.54}$$

where A_1, A_2, C_1 and C_2 are taken from Eq. (4.50) and Eq. (4.53), β and ξ positive weighting parameters and ∇ the gradient operator. The first term of Eq. (4.54) consists in a regularization constrain on the total length of the final segmentation and second and third terms are related to the iterative maximization of the alpha-divergences between p_{in} and p_{out} (see Eq. (4.50) for corresponding general PDE).

Segmentation of noisy synthetic images

In order to evaluate the performance of the proposed method based on maximization of alpha-divergences, we first propose to achieve the segmentation of synthetic images corrupted by various types of noises (see Fig. 4.27 for illustation). Mainly, corrupting noises considered here are

zero-mean Gaussian and Poisson ones: The Gaussian noise is a standard one in the majority of acquisition systems, and the Poisson distribution will model the corrupting process of X-Ray imaging system that will be studied in next section. Moreover, in order to highlight the benefit from the level-set implementation of Eq. (4.54), the synthetic image presents two objects to segment. Finally, the initialization of the active curve is a set of little circles regularly dispatched on the whole image which allows not to consider a too specific initialization process (too close to the boundaries of the objects to segment for example). Some results of segmentation are shown in Fig. 4.27. The first row shows results obtained with the Gaussian noise and the second row with the Poisson distribution. In both cases, we purposely chose to highly corrupt the original image ($PSNR = 10\ dB$) and to set the regularization parameter β of Eq. (4.54) to 10 whereas the weigthing parameter for distance maximization is fixed to $\xi = 0.01$. As one can notice, regarding the value of α parameter (restricted to $[0 \cdot \cdot 1]$ in this study), the segmentation results is very different: considering the Gaussian noise, best results are obtained with non-standard values of α parameter like $\alpha = 0.4$ (Fig. 4.27.(a)). Usual distances like Hellinger and KL do not lead to satisfying segmentations: In the first case, the main object is not finally well-segmented (Fig. 4.27.(b)) and in the second, the segmentation process does not even really starts owing to unsuficient generated forces in terms of magnitude by the alpha-divergence measure. This can not be balanced by a more important regularization: In this case, the active contour can not even stop to the boundaries of the two objects. For Poisson noise, same kinds of results are obtained: best segmentation is achieved thanks to 0.3-divergence (which remains a non-standard value), whereas Hellinger and KL do not lead to proper segmentations (Fig. 4.27.(e) and 4.27.(f)).

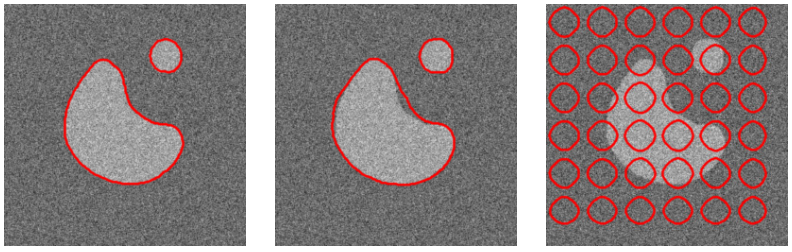

(a) $\alpha = 0.4$ (b) Hellinger (c) KL

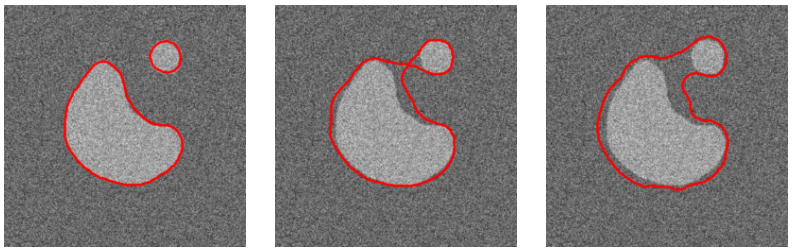

(d) $\alpha = 0.3$ (e) Hellinger (f) KL

Figure 4.27: Some results of segmentation using distance maximization between PDF of inner and outer regions of the synthetic peanut corrupted by Gaussian (a, b, c) and Poisson (d, e, f) noises of $PSNR = 10\ dB$.

Segmentation of Texture Images

In order to evaluate the performance of alpha divergence on texture images, we generate

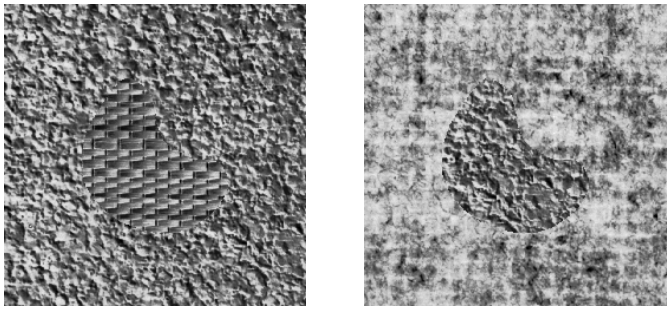

(a) (b)

Figure 4.28: Synthetic texture images

synthetic images with different textures taken from the Brodatz database, Fig. 4.28 shows two examples of these images.

Due to the difficulty related to the manual tuning of the alpha value in those particular cases, iFigure 4.29 shows alpha divergence measure plotted with respect to α value used in segmentation process and iteration number. The first textured image appears to be hardly segmented if the α parameter isn't next to 0.5. In the case of the second image, we can see the evolution of alpha divergence across iterations until maximum stage.

As last plots show that some α comparing to others, we apply segmentation process directly on the best value of this parameter for the two considered images. Results are shown in Fig. 4.30.

This first study shows that in the context of distance maximization for statistical region based active contour, alpha-divergence measure brings a very interesting flexibility, allowing obtaining of improved segmentation results that usual distances does not make possible. We now propose in the next section, results of segmentation obtained on real clinical images.

Segmentation of X-ray Images

X-Ray imaging remains of primary interest for diagnosis and follow-up of pathologies related to bones. More precisely, segmentations of some bone structures are required to quantify gold standard parameters (as density, curvature, spacement...) that lead clinicians to a precise diagnosis and follow-up of the considered pathology. Segmentation of that kind of images is challenging for two main reasons: First, these acquisitions are corrupted by a strong Poisson noise that makes its segmentation not always that easy with standard approaches like Chan and Vese [Chan and Vese, 2001] one (which is known to be unadapted to clinical image analysis); Second, bones area are characterized by a trabecular texture that can not be easily parametrically-estimated.

In this clinical context, we propose to tackle the segmentation problem of hip bone in X-Ray images . Fig. 4.31 shows the particular structure to highlight (see green circles) for the achievement of a quantification of the severity of the pathology. Moreover, we also show on Fig. 4.31 a classic result of segmentation (in red) obtained thanks to standard active contour segmentation based on the minimization of the mean and the variance of the inner and the outer regions of the curve. As one can notice, the segmentation results are not satisfying since the important structures of the bone are not preserved due to the presence of some areas of less density. Calculations of quantitative parameters like curvature of the bone are then biased. Fig. 4.32 shows now segmentation obtained with the proposed approach and for different distances.

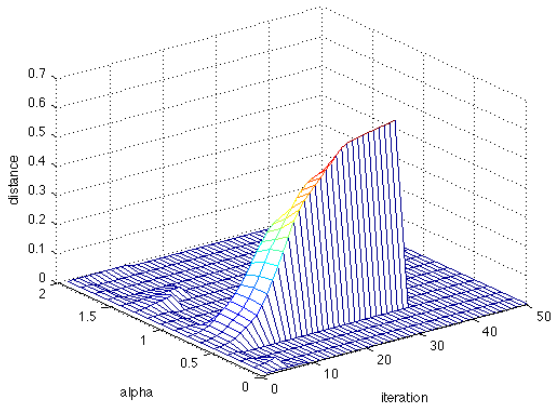

(a)

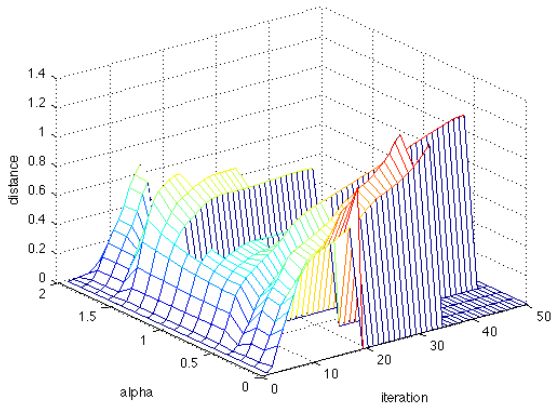

(b)

Figure 4.29: Study of Distance evolution with respect to α value and process iterations. (a) First textured image (b) Second textured image

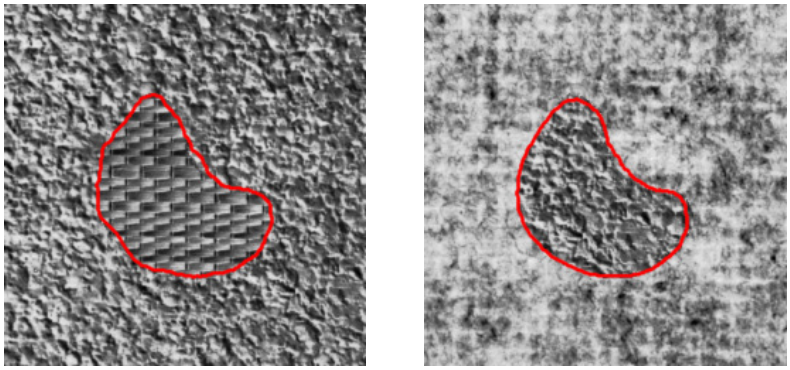

(a) (b)

Figure 4.30: Segmentation of textured images with best α value. (a) First texture image (0.65) (b) Second texture image (0.5)

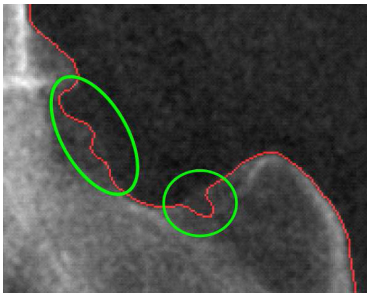

Figure 4.31: In green, typical structures of the bones related to osteoporosis pathology. In red, usual segmentation result using a parametric Chan et Vese like method.

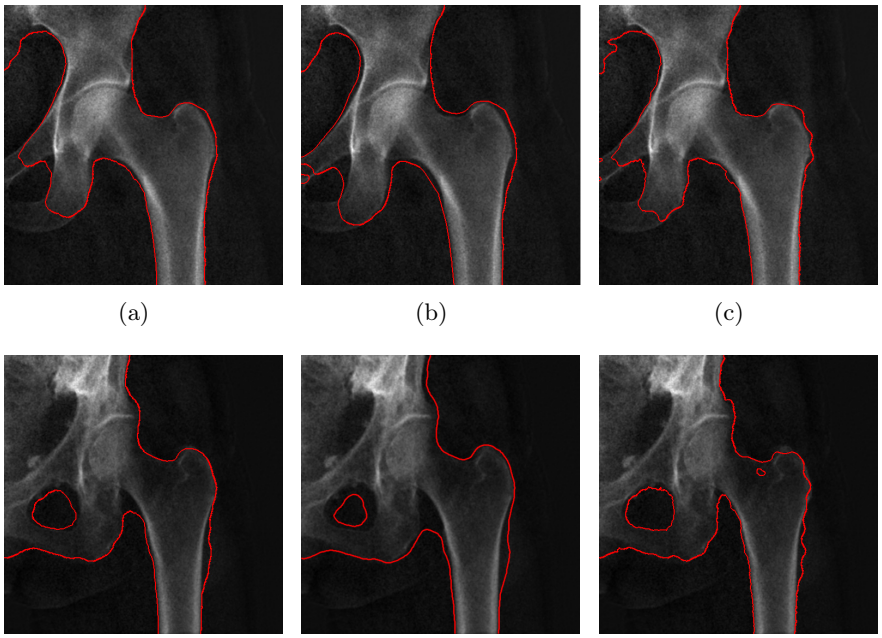

(a) (b) (c)

(d) (e) (f)

Figure 4.32: Hip segmentations from X-ray acquisition for different α value (to each row corresponds a different acquisition): (a, d) $\alpha = 0.75$, (b, e) $\alpha = 0.5$ (Hellinger/Bhattacharaya distance), (c, f) $\alpha \to 1$ (Kullback-Leibler divergence)

As one can notice on Fig. 4.32, usual distances do not make possible a satisfying segmentations: The Hellinger distance provides a segmentation result (Fig. 4.32.(b) and 4.32.(e)) too smooth that leads to an oversegmentation of the whole bone, and the KL divergence definitely do not fit to this segmentation task (Fig. 4.32.(c) and 4.32.(f)). Finally, this is a non-standard value of α (0.75) that leads to the most satisfying segmentation results (Fig. 4.32.a and 4.32.(d)).

Intermediate Conclusion

These first set of experiments shows the capabilities of alpha-divergence with different kind of segmentation context. Nevertheless, until now, α parameter is a constant that is tuned at the beginning of the segmentation process and does not evolve during the iterative optimization of the energy related to the segmentation framework. This could be seen as a real limitation, and we then propose in the following section a joint optimization process of this energy and α parameter to increase the flexibility of proposed divergence.

4.2.3.4 Alpha Optimization Strategy

If in recent contributions on statistical-based active contour ([Lecellier, *et al.*, 2006] among others), authors propose to model the statistics of the imaging techniques using parametric family like the exponential family for instance, associated to KL-divergence, to our knowledge, it appears that there is no study on how to find the analytical form of the most appropriate divergence to particular unknown distributions.

However, in the context of non-rigid image registration using the generalized f-divergences, formerly introduced in [Csiszár, 1967], as similarity measure, Rougon *et al.* [Rougon *et al.*, 2003] propose an optimal joint optimization of the related PDE and the metric of the aforementioned f-divergence. Inspired by this work, we propose a similar optimization process of the φ_α metric associated to alpha-divergences.

More precisely, in the particular case of alpha-divergence maximization between PDFs p_{in} and p_{out} at an iteration τ, optimal parameter α , "fitting" the most the statistics of the inner and outer regions (i.e. the most efficient to discriminate two PDF of unknown shape), is obtained through the maximization of D_α such as:

$$\alpha_{opt} = argmax_\alpha \left(D_\alpha(p_{in} \| p_{out})\right) \tag{4.55}$$

Taking into account the whole segmentation framework that is active contour, the joint optimization of the divergence and α parameter is obtained by the following PDE systems:

$$\begin{cases} \dfrac{\partial \alpha}{\partial \tau} = & -\partial_\alpha D_\alpha(p_{in}, p_{out}, \alpha) \\ \dfrac{\partial \Gamma}{\partial \tau} = & -\partial_{p_{in}, p_{out}} D_\alpha(p_{in}, p_{out}, \alpha). \end{cases} \tag{4.56}$$

Numerically, Eq. (4.55) is solved using a usual gradient descent strategy:

$$\alpha^{n+1} = \alpha^n - \delta\tau * \frac{\partial \alpha}{\partial \tau} \tag{4.57}$$

where α^i is the value of alpha at iteration i of the gradient-descent, and:

$$\frac{\partial \alpha}{\partial \tau} = -\int_{\chi^m} \frac{1}{\alpha^2\,(1-\alpha)^2}\Bigg[\alpha^2\, p_{in} - (\alpha-1)^2\, p_{out} - {p_{in}}^{\alpha}\, {p_{out}}^{1-\alpha}\left(2\alpha - 1 + (\alpha-\alpha^2)\, ln\left(\frac{p_{in}}{p_{out}}\right)\right)\Bigg]\, d\lambda\ . \tag{4.58}$$

A major issue of the proposed strategy is the initialization of α : More precisely, two initialization strategies can be considered.

- A first one, $\alpha_0 \gg 1$ or $\ll 1$, avoids possible falling into local minimum as the joint optimization process starts. Nevertheless, because being far from the Shannon case where $\alpha = 1$, such initialization need prior information on the statistics of the data to be efficient.
- The second one, $\alpha \to 1$, proposes to take as a starting point the most general divergence as defined by Shannon, corresponding to the maximization of p_{in}, with respect to p_{out} to fit with the usual active contour segmentation framework.

We naturally chose the second strategy that fit the most to the considered segmentation task, for which no prior is given on the inner and outer PDFs.

4.2.3.5 Experiments and Results: Part 2

In the particular framework of the joint process of the α parameter optimization and the usual active curve evolution, the entire algorithm is described above:

1. **Initialization**
   - $\tau = 0$
   - p_{in} and p_{out} (depends on active contour initialization)
   - $\alpha_{opti} \leftarrow \alpha_0$
2. **Optimization**
   While $\phi(\tau) \neq \phi(\tau - 1)$, do :
   (a) For $\alpha = \alpha_{opti}$:
   Iteration of convergence process of the curve ϕ
   p_{in} and p_{out} update
   (b) For fixed p_{in} and p_{out} :
   Iteration of optimization process for α
   α_{opti} value update
   (c) $\tau \leftarrow \tau + 1$

   End while

In the following section, results of segmentation are showed first on synthetic images and then on real images for illustration.

Synthetic Images

First we propose a two-objects segmentation task on a synthetic image corrupted by different kinds and different levels of noise. Main idea is to show that the proposed method is flexible and can be used for very different scenarios corresponding to classic imaging technique as X-Ray imaging or MRI for instance.

In Fig. 4.33, the segmented images are corrupted by two different types of noise (Gaussian or Poisson) with a similar $PSNR = 2dB$ and $10dB$. Initialization of the active contour is a set of small circles uniformly dispatched and the obtained results are averaging on 100 realizations of the noise to show the robustness of the proposed approach.

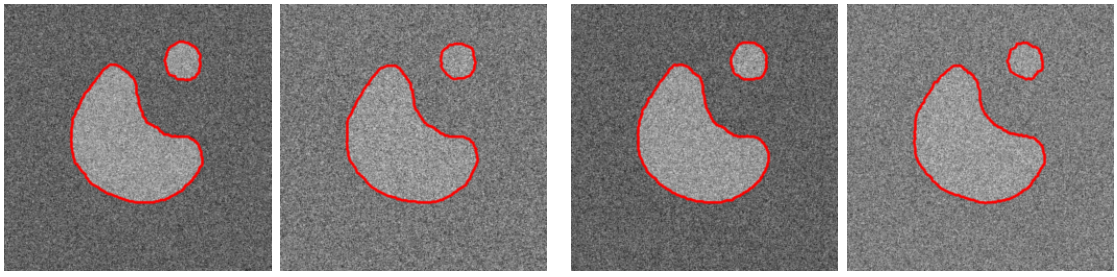

(a) optimized α

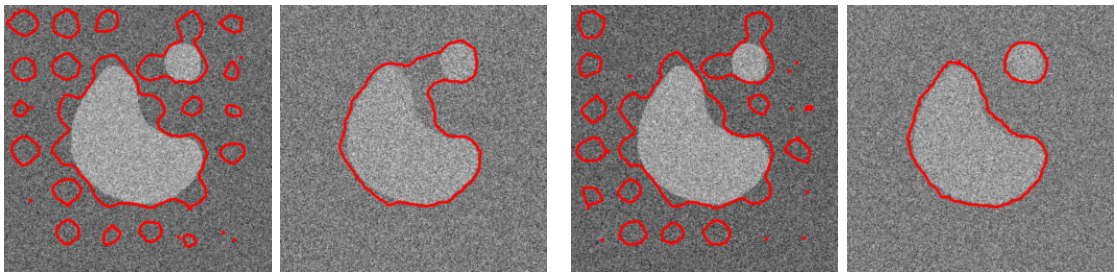

(b) KL

Figure 4.33: Segmentation of images corrupted by different kinds and levels of noise: On two first columns a Gaussian noise ($PSNR = 10dB$ and $PSNR = 2dB$) is considered and on two last columns a Poisson noise (same PSNR). Upper row shows segmentation with optimization of α, lower row shows segmentation with classic KL-divergence.

First of all, Fig. 4.33 shows satisfying segmentation result using joint PDE strategy of Eq. (4.56) (less than 1% of misclassified pixels) when compared to Kullback-Leibler divergence (13% of the pixels are finally misclassified).

In addition, the shape evolution of the active contour and the corresponding PDFs could be observed in Fig. 4.34 using joint PDE strategy when image is corrupted by a Gaussian noise ($PSNR = 10dB$). We can see here that even if final PDFs have a strong overlap, the algorithm succeeds in separating them.

These experiments also show that the initialization strategy of α is in accordance with the segmentation task, since the segmentation process finally succeeded in converging to the right segmentation without any prior on the statistics of the luminance distribution, that strongly overlapped at the beginning of the process.

Secondly, to demonstrate the real interest of proposed joint optimization, Fig. 4.35. (a,b) shows the evolution of α and the related divergence when images are corrupted by a Gaussian

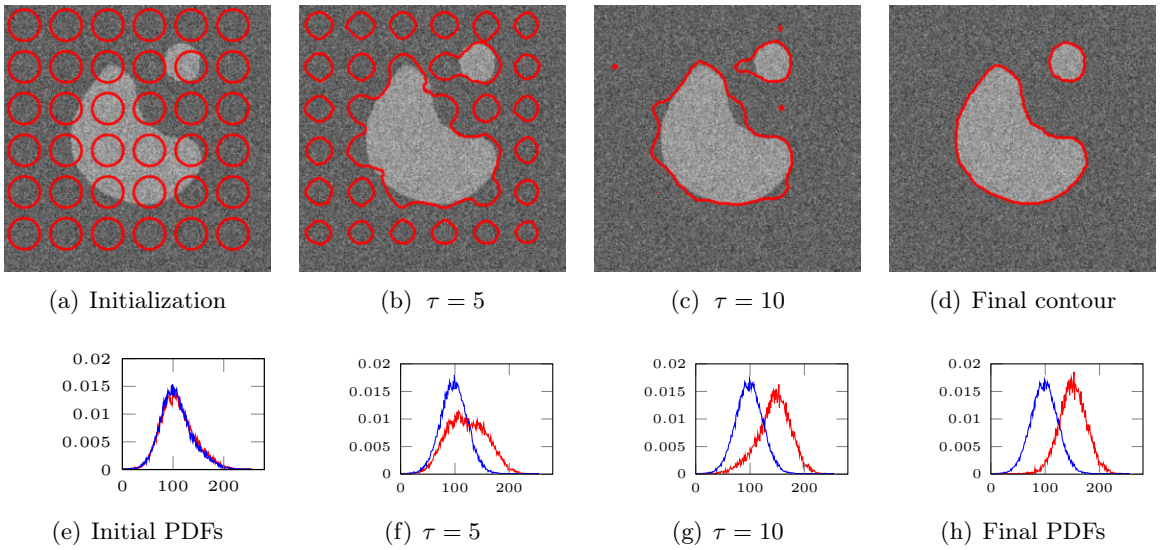

(a) Initialization (b) $\tau = 5$ (c) $\tau = 10$ (d) Final contour

(e) Initial PDFs (f) $\tau = 5$ (g) $\tau = 10$ (h) Final PDFs

Figure 4.34: Some steps of the active contour Γ and related PDFs (p_{in} (red) and p_{out} (blue)) evolutions for the Gaussian noise with PSNR= $10dB$.

noise with a PSNR of 20 dB and 10dB. In both cases, α evolve from 1 to a global minimum before settling down to 0.5 (Hellinger divergence). First, one can notice that this final value is in accordance with literature [Hero *et al.*, 2002] in which authors show that Hellinger divergence give a better accuracy than KL-divergence for strongly overlapping PDF.

It also appears, as it could be expected, that the segmentation of highly corrupted images is slower than less corrupted ones. But more than this, these curves emphasis a particular effect of the α -optimization process that is of primary interest: Let focus on the evolution of the segmentation when Gaussian noise of 10 dB is considered (blue plots in Fig. 4.35.(a, b, c) and Fig. 4.34). Starting from 1, the alpha-divergence rapidly grows until a first stationary step in the maximization of associated divergence at iteration 5. This particular iteration corresponds to a local maximum of the divergence that does not lead to an optimal final contour (see iteration 5^{th} in Fig. 4.34. (b) for illustration). Indeed, if the segmentation process is proceeded with a constant value $\alpha = 1$, divergence maximization converges at this local maximum and the segmentation process, corresponding to KL divergence, stops as shown by the green plot in Fig. 4.35.(c).

It appears here, that optimization of α parameter pulls out segmentation process from a stationary step in order to get a more satisfactory final contour (Fig. 4.34.(d)): This can be interpreted as a constant optimization of α parameter to the statistics of the inner and outer regions of the active curve all along the iterations of the segmentation process. This is all the more interesting since the optimization of α does not require any tuning of the parameter even for highly corrupted images.

Texture Images

In addition to noise phenomenon, the segmentation of images with complex texture is a real challenge. We then provide results obtained on a synthetic image where object and background corresponds to two different texture taken from the Brodatz database [Brodatz, 1999].

Tests were performed with the same initializations than with noisy images: a set of small circles uniformly dispatched for level set dunction and $\alpha = 1$. Some steps of the active contour

evolution are shown in Fig. 4.36 from the initialization to the convergence of the active contour toward the target-object.

Visually speaking, the performance of the joint optimization process proposed is satisfying: we can notice, as for corrupted image of previous section, that the optimization of α allows to avoid a local maximum of the divergence which evolution with respect to the iteration number is showed in Fig. 4.36. More precisely, it can be noticed that the segmentation using KL-divergence maximization in Fig. 4.37. (b) is outperformed: The iteration 5 of the optimized process is the result obtained when segmentation is performed using the usual distance.

Tests on synthetic images presented above allow us to emphasis the performance of alpha-divergence segmentation associated with the α parameter optimization. Indeed, using this approach, we obtain a good robustness not only considering strongly corrupted images but also textured image.

Natural Images

Finally, to illustrate the segmentation capabilities of the proposed approach, some examples obtained on real images (natural and medical ones) are proposed .

First of all, in Fig. we show Fig. 4.38 an example of segmentation obtained on simple image where the object to segment could be easily be identified by first order statistics.

It can be seen in that example that the segmentation task is easily achieved. In addition, Fig. 4.39 shows the evolution of alpha parameter and related divergence during the joint maximization process.

Despite the fact that α value first increase above 1 to finally decrease until 0.4 value, one can notice, that the related divergence is well maximized all along the segmentation process. This first decrease is probably due to the fact that the initialization curve proposed here is a circle centered on the flower that leads to a necessary stronger value of the related alpha-divergence to the PDF outside the curve that is the most informative in this case, contrary to previous examples.

In Fig. 4.40, a more challenging examples is shown, since the task consists in segmenting the "Cheetah" image. In that case, as it can be noticed in Fig. 4.40, the two PDF p_in and p_out have a strong overlap right from the beginning that could make things far more difficult than with previous example in the "Flower" example.

As for the "Flower" experiment, Fig. 4.41 shows the evolution of α parameter and the related divergence during the maximization process.

In this case, it can be noticed that again without the joint optimization of α parameter, the segmentation process would have stuck into a local maximum that corres ponds to a non-satysfying segmentation (around iteration 16).

X-Ray Radiographs

In order to show the abilities of the proposed approach for medical image segmentation, we propose here to tackle again the task consisting in segmenting the hip bones in X-Ray images that are corrupted by a strong level of Poisson noise (Fig. 4.32).

Fig. 4.42 shows the obtained results on a first patient utilizing the joint maximization of α and the related divergence. Initialization curve is here a set of small circles dispatched on the all image domain.

As it can be noticed on Fig. 4.42, the final segmentation is very satisfying when compared with previous results using a manual tuning of α Fig. 4.32. Particular regions are even more precisely segmented than with the value of α equal to 0.75. The convergence is also relatively fast in terms of number of iterations, since only 8 iterations are needed to reach convergence. In addition to this visual results, as for previous experiments, Fig. 4.43 shows the evolutions of α parameter and related divergence during the segmentation process.

The global behavior of the evolution of α and related divergence remains the same as in previous experiments. However, it can be noticed in Fig. 4.43 a kind of instability in the α optimization. We think that this phenomenon may be due to an instability of the numerical optimization scheme proposed and, more precisely, that it is related to the choice of the temporal step parameter. This should be investigated in further work.

Finally, Fig. 4.44 shows results of segmentation for an other acquisition with comparison to the previous one.

4.2.3.6 Conclusion and Perspectives

In this section, we presented a statistical-based active contour segmentation method using alpha-divergence family as similarity measure. More precisely, following recent publications on that topic, a strategy to optimize the α parameter related to the divergence metric is proposed. This optimization iteratively adapts the metric of the divergence to the image statistics during contour evolution process. Satisfying results of segmentation were provided for synthetic images corrupted by different type and level of noise and it can be noticed that, for each more realistic example, without any prior on the PDF p_{in} and p_{out}, proposed method leads to satisfying results of segmentation: the flexibility of the method is shown for different kinds of images from textured one ("Cheetah") to medical ones (X-Ray imaging) with strong level of Poisson noise.

From now on, it could be interesting to extend considered image features for characterization from 1D PDF (related to the image intensity only) to 2D PDF: Most precisely, the method presented here uses neither information about pixels location in the image nor possible statistical properties of its neighborhood. 2D PDF computed from cooccurrence matrices [Haralick *et al.*, 1973], could definitely improve the textured image segmentation task for instance.

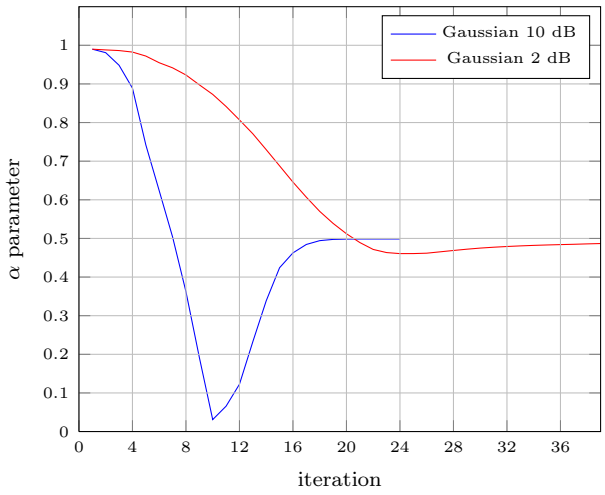

(a)

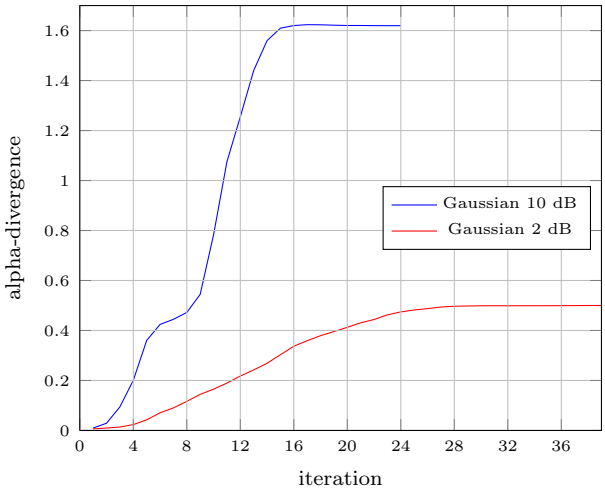

(b)

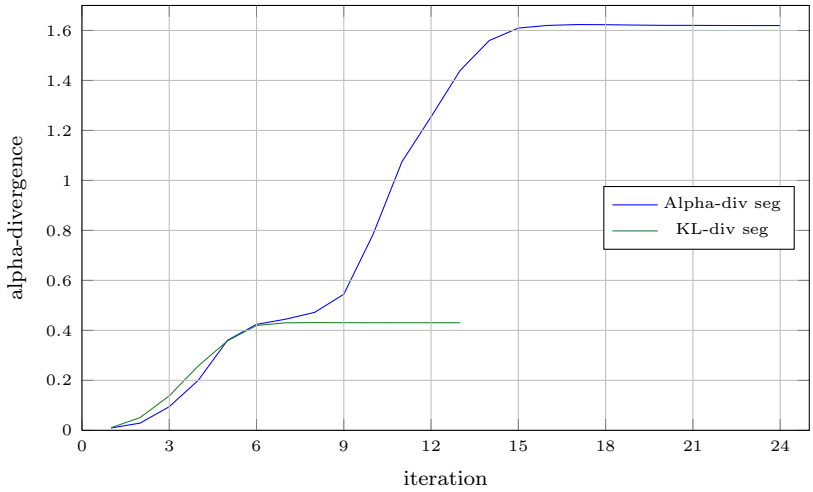

(c)

Figure 4.35: Segmentation of images corrupted by a Gaussian noise: (a) α value evolution according to iterations of convergence process, (b) Evolution of alpha-divergences according to iterations of the same process, (c) Comparison of alpha-divergence evolution when of $\alpha = 1$ (KL, green) and optimized α (blue).

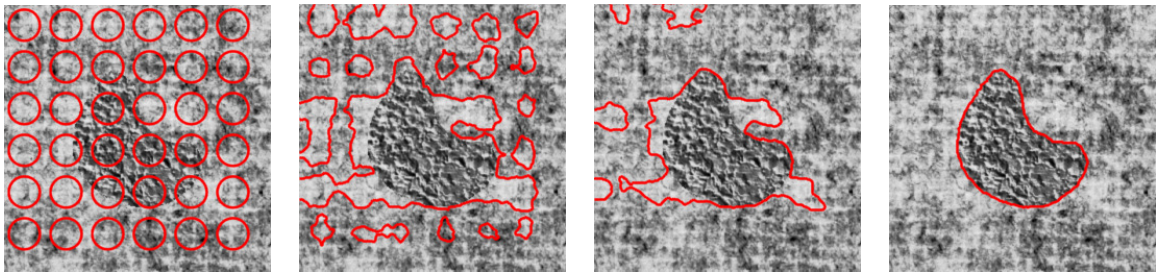

(a) Initialization (b) $\tau = 5$, KL (c) $\tau = 50$ (d) Final contour

Figure 4.36: Some steps of the active contour evolution for segmentation of proposed textured image with optimization of α parameter.

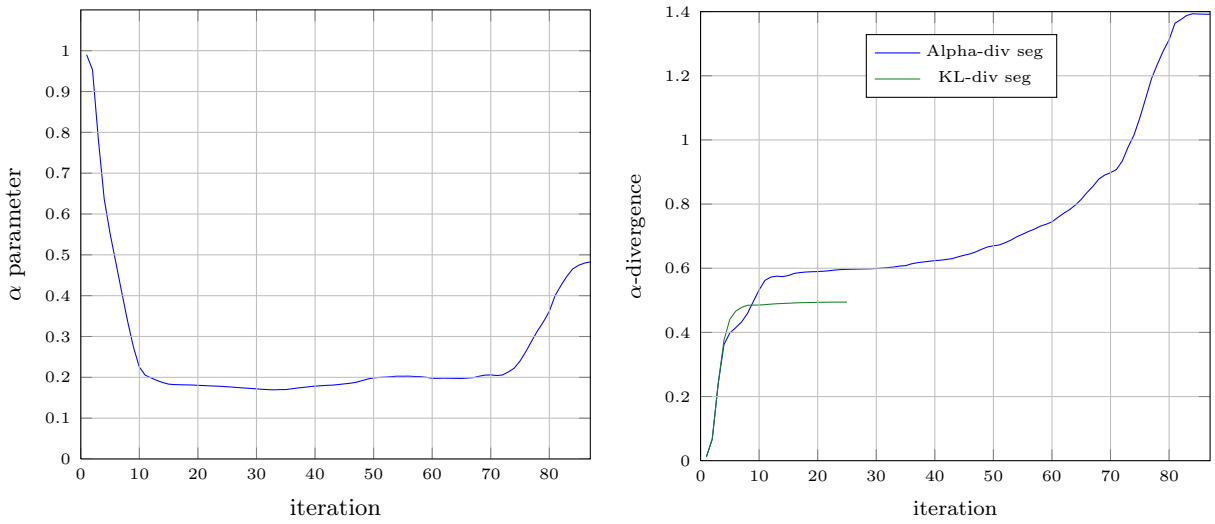

Figure 4.37: Segmentation of textured image with optimization : Evolution of α parameter and the related divergence during segmentation process.

(a) Initialization

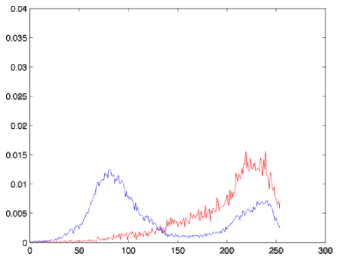

(b) Initial PDF

(c) $\tau = 3$

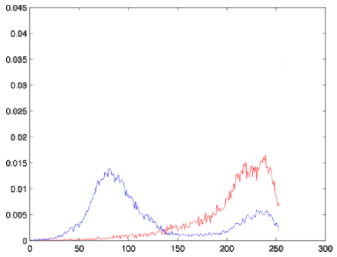

(d) Corresponding PDF, $\tau = 3$

(e) $\tau = 8$

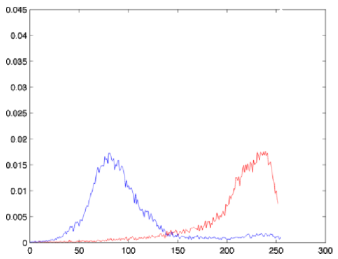

(f) Corresponding PDF, $\tau = 8$

(g) $\tau = 12$

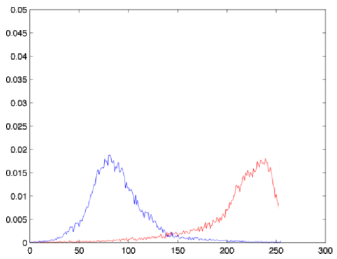

(h) Corresponding PDF, $\tau = 12$

(i) Final Segmentation

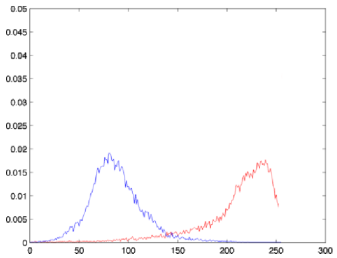

(j) Final PDF

Figure 4.38: Evolution of the active contour and related PDF p_{in} (red) and p_{out} (blue) along the joint maximization process. $\alpha_{init} \to 1$.

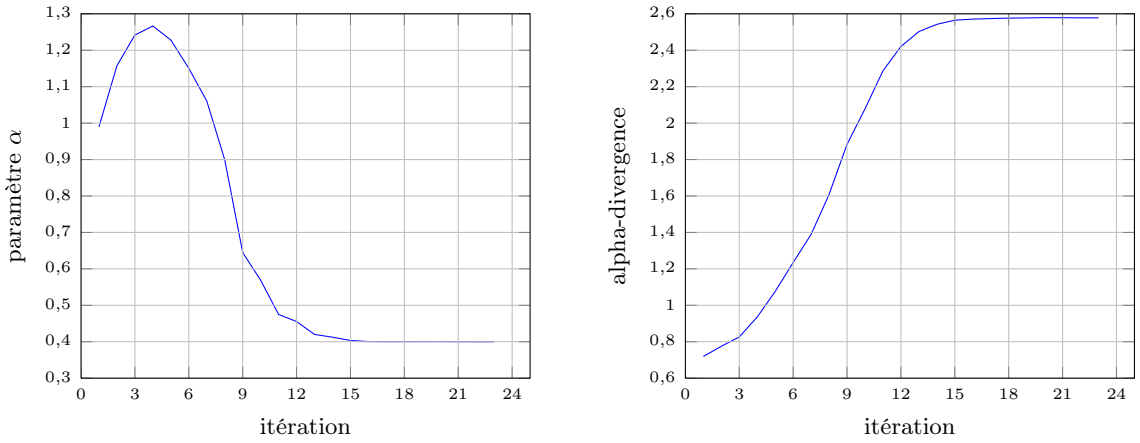

(a) (b)

Figure 4.39: (a) Alpha value function of the iteration of the maximization process, and (b) corresponding divergence evolution.

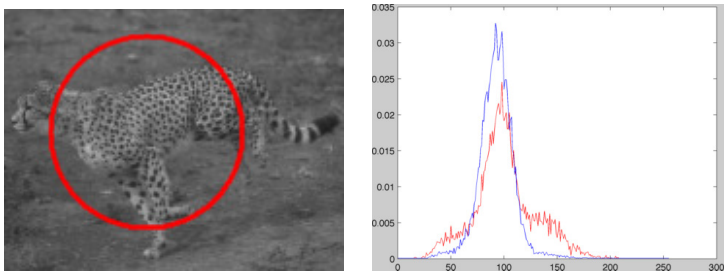

(a) Initialisation (b) Initial PDF

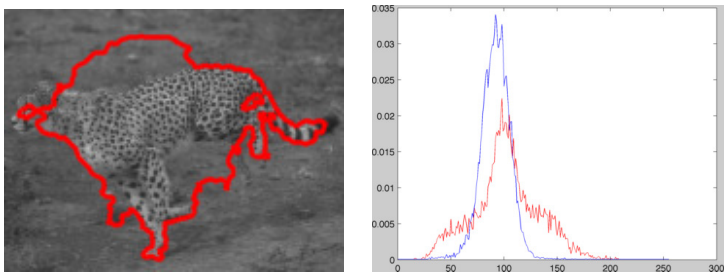

(c) I$\tau = 25$ (d) Related PDF $\tau = 25$

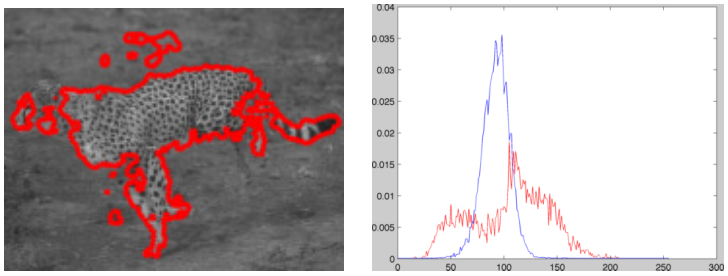

(e) $\tau = 35$ (f) Related PDF $\tau = 35$

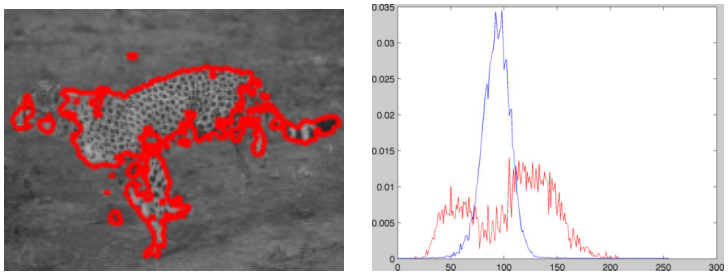

(g) Final Segmentation (h) Final PDF

Figure 4.40: Evolution of the active contour and related PDF p_{in} (red) and p_{out} (blue) along the joint maximization process. $\alpha_{init} \to 1$.

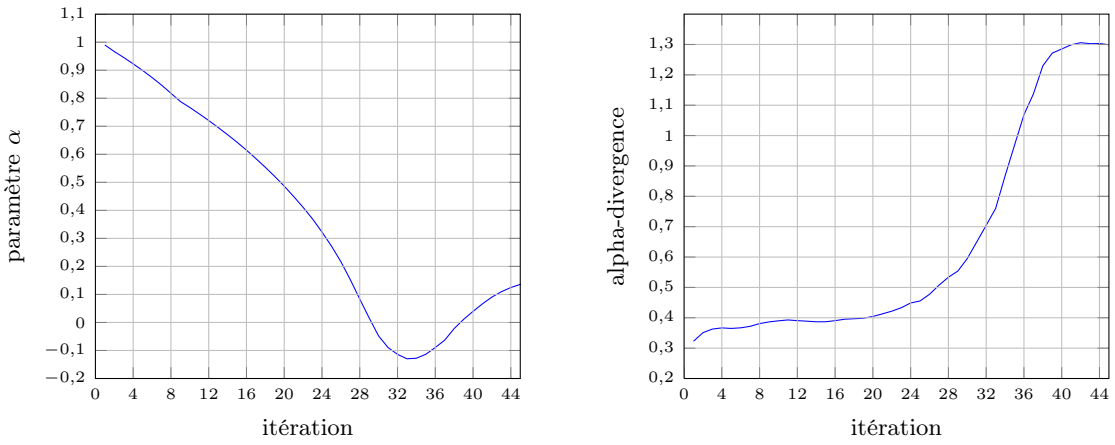

(a) (b)

Figure 4.41: (a) Alpha value function of the iteration of the maximization process, and (b) corresponding divergence evolution.

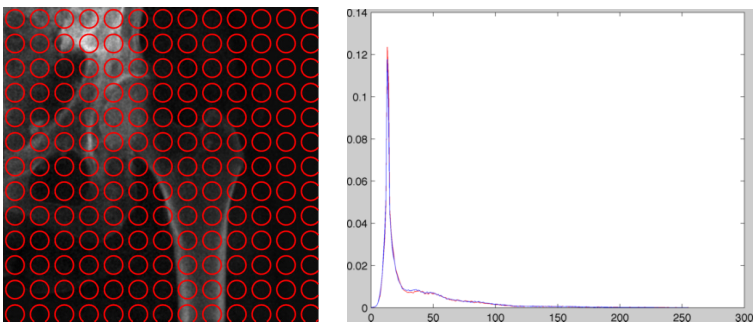

(a) Initialization (b) Initial PDF

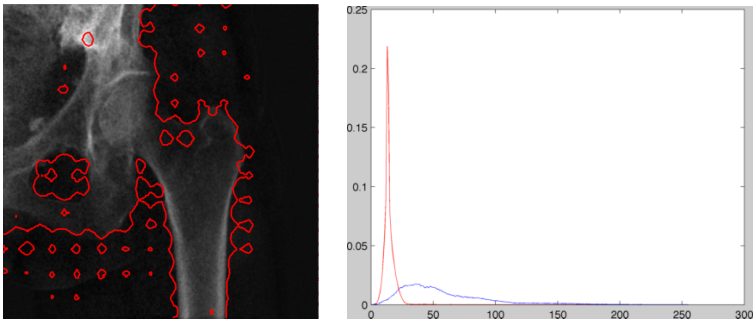

(c) $\tau = 3$ (d) Related PDF $\tau = 3$

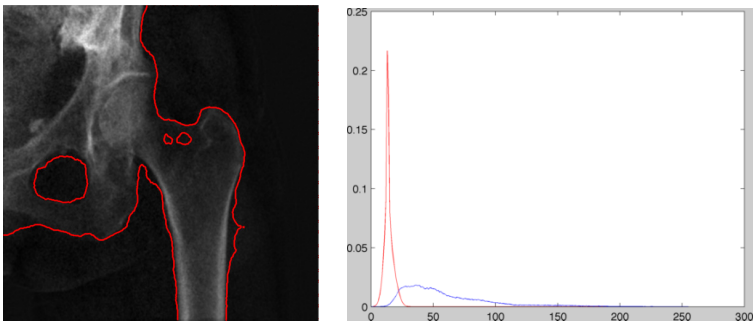

(e) $\tau = 5$ (f) Related PDF $\tau = 5$

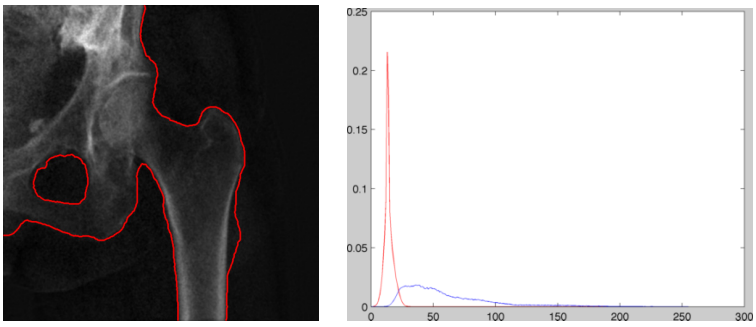

(g) Final Contour (h) Final PDF

Figure 4.42: Evolution of the active contour and related PDF p_{in} (red) and p_{out} (blue) along the joint maximization process. $\alpha_{init} \to 1$.

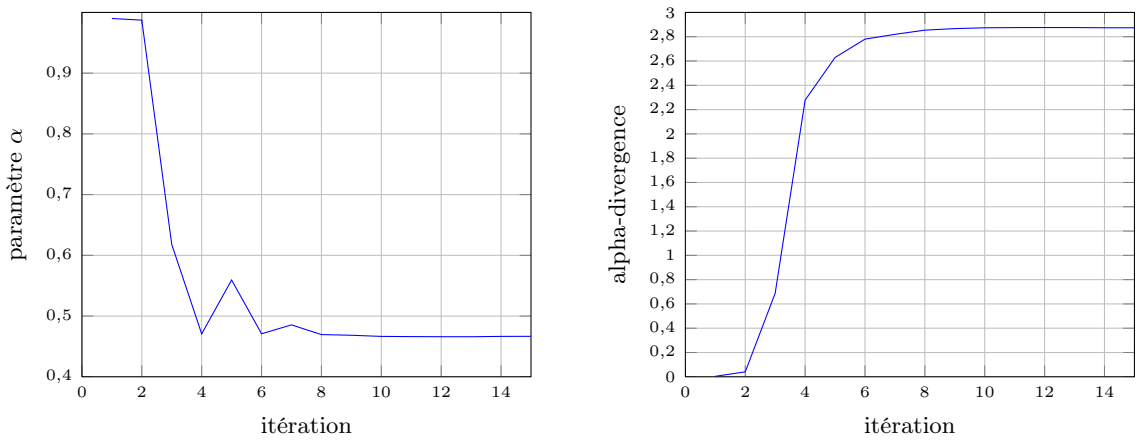

(a) (b)

Figure 4.43: (a) Alpha value function of the iteration of the maximization process, and (b) corresponding divergence evolution.

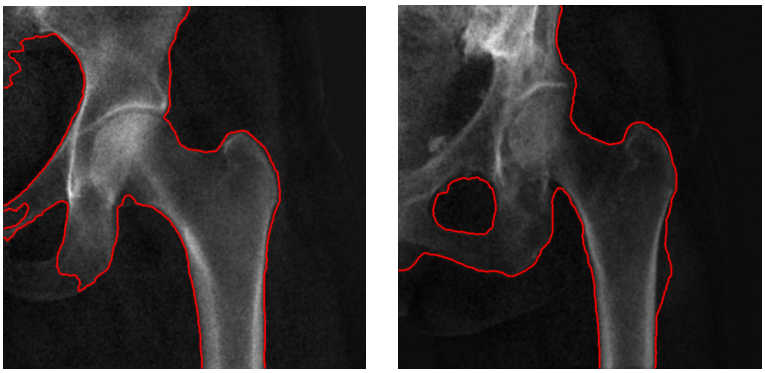

Figure 4.44: Segmentation of X-Ray images using proposed joint optimization of α and related divergence.

Chapter 5

Contribution to Embeddable Pattern Detection Methods: Application to In Situ Diagnosis of Colorectal Cancer Using Wireless Videocapsule

Finally Chapter 6 is dedicated to a more recent research activity related to "Embedded Systems for Health" in which I have been involved for more than 2 years now with Prof. Olivier Romain (Head of ASTRE team of ETIS).

This Chapter is quite different from Chapters 4 and 5 since the global framework is definitely more constrained in terms of technology capabilities (energy, small amount of memory, real-time process...) when comparing with classic Computer-Aided-Diagnosis area. From an applicative point of view, this Chapter focuses on a particular project named "Cyclope" which objective is to design and develop a new generation of wireless videocapsule for early diagnosis of colorectal cancer (polyp detection and identification) and more generally for detection and recognition of gastrointestinal abnormal structures.

This project is developed in collaboration with Prof. Bertrand Granado (LIP6, University Pierre et Marie Curie), Prof. Xavier Dray and Prof Philippe Marteau (Gastroenterologists (PU-PH), Hôpital Lariboisière, APHP). Part of the presented study was made during the MSc internship of Juan-Silva Quintero in the second half of 2012. A PhD will begin next October in the following of the current achieved work.

This chapter is somehow different from the two previous ones. More precisely the work I am going to present here is definitely more technology oriented and corresponds to a "younger" (at least from my perspective) research activity started in 2011 with Prof. Olivier Romain in charge of the ASTRE team of ETIS and Prof. Bertrand Granado (LIP6, University Pierre et Marie Curie).

"Cyclope" project is a multidisciplinary project at the frontier of Signal and Image Processing, Electronics, Circuit Design and of course Medicine (Gastroenterology). From the Image Processing angle, this project is strongly different from the other applications I was used to, since the technological constraints are a great challenge to reach the goal of a small medical device, with autonomous diagnosis capabilities and small energy consumption.

In the following, the general medical context is first presented as well as the existing technological solution available on the market for the wireless imaging of the intestinal tract and the early diagnosis of colorectal cancer, since this is everything about "Cyclope project". A synthesis of the most recent work achieved on the project is then proposed.

5.1 Introduction

5.1.1 Colorectal Cancer and Videocapsule

Colorectal cancer (CRC) is the first cause of death by cancer in developed countries, with an estimated incidence of 728.550 cases worldwide in 2008, with fatal outcome in 43% of cases. Overall, CRC is the third more frequent cancer after lung cancer and breast cancer [F.J. Shin, 2008]. Prevention of CRC by detection and removal of preneoplastic lesions (colorectal adenomas) is therefore of paramount importance and has become a worldwide public health priority. Currently, colonoscopy is the the "gold standard" technique for diagnosis of colorectal adenoma and cancer. Using a videoendoscope, gastroenterologists can perform and record a complete examination of the colon in order to detect and to remove suspicious tissular structures like adenomas which degenerescence could lead to cancer. Because colonoscopy is performed under general anesthesia, mini-invasive techniques such as computed-tomography-based colonography and wireless capsule endoscopy (WCE) have been developed. Both techniques are currently considered valid alternative options to videocolonoscopy in patients with contra-indication or low compliance to general anesthesia. WCE takes form of a pill equipped with a CCD or CMOS sensor, two batteries, and a RF (radiofrequency) transmitter, that enables the wireless identification of gastrointestinal abnormalities such as ulcers, blood and polyps [Moglia *et al.*, 2009] with no need for hospitalization or sedation. In the last decade, WCE has become a breakthrough technology for diagnosis of small bowel pathologies [Spada *et al.*, 2011]. Many fabricants such as Given Imaging, IntroMedic, and Olympus [Bergwerk *et al.*, 2007] have developed a variety of capsules for the complete examination of the gastrointestinal tract.

Practically speaking, after ingestion of the capsule, about 50,000 images are captured along the digestive tract and each of them are wirelessly transmitted to a wearable receiver and saved for a postponed physician's reading. Off-line image processing enables the identification of gastrointestinal abnormalities (like the aforementioned polyps and adenoma) by the gastroenterologist.

Current main issues of WCE are:

- The complete analysis of the 50,000+ images is time-consuming for physicians, and even for experienced ones, WCE diagnoses are sometimes challenging.

- The transmission of the 50,000+ images, that represents 80% of the overall energy consumption of the embedded batteries, limits to 8 hours the autonomy of the classic WCE, whereas 12 hours are necessary to scan the complete intestinal tract.

- A recent study comparing diagnostic capabilities of videoendoscopy and of WCE shows that the average detection rate is around 80% polyps per patient [Spada *et al.*, 2011; Eliakim, 2009]. Thus, the improvement of polyp detection and classification capabilities of WCE is expected from gastroenterologists.

- Processing capabilities of WCE are limited to transmit raw images. No "intelligence" is currently embedded into the imaging device itself.

In the context of early diagnosis of colorectal adenoma and cancer, the "Cyclope" project proposes a new generation of WCE [Kolar *et al.*, 2010] (see Fig. 5.3 for illustration) that will permit an in situ detection of the polyps and, consequently, to only emit the images which are important for the final diagnosis. The expected benefits are twofold:

1. An increase of the battery lifetime up to 12 hours considering the fact that, except for particular pathologies, only a small percentage of the 50,000 images would contain polyps and will be consequently transmitted (see Fig. 5.1).

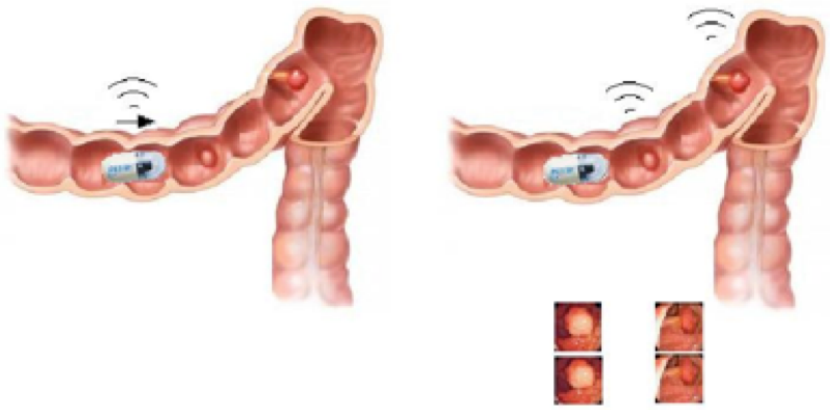

Figure 5.1: Comparison between continuous transmission (left) and intelligent one (right).

2. A facilitated off-line final diagnosis for the clinician considering the law amount of transmitted data after in situ hardware processing and the possibility to highlight particular regions of interest within the images that possibly contain a polyp.

In Fig. 5.2, a comparison between the usual clinical workflow and the expected one with Cyclope WCE is proposed.

In [Kolar *et al.*, 2010] and [Ayoub *et al.*, 2010], a first prototype demonstrator equipped with an active stereo vision sensor was proposed to detect protuberating polyps within the colon. The proposed embedded detection algorithm used a SVM classifier trained on robust 3D feature descriptors. The overall detection performance was very promising with a global classification

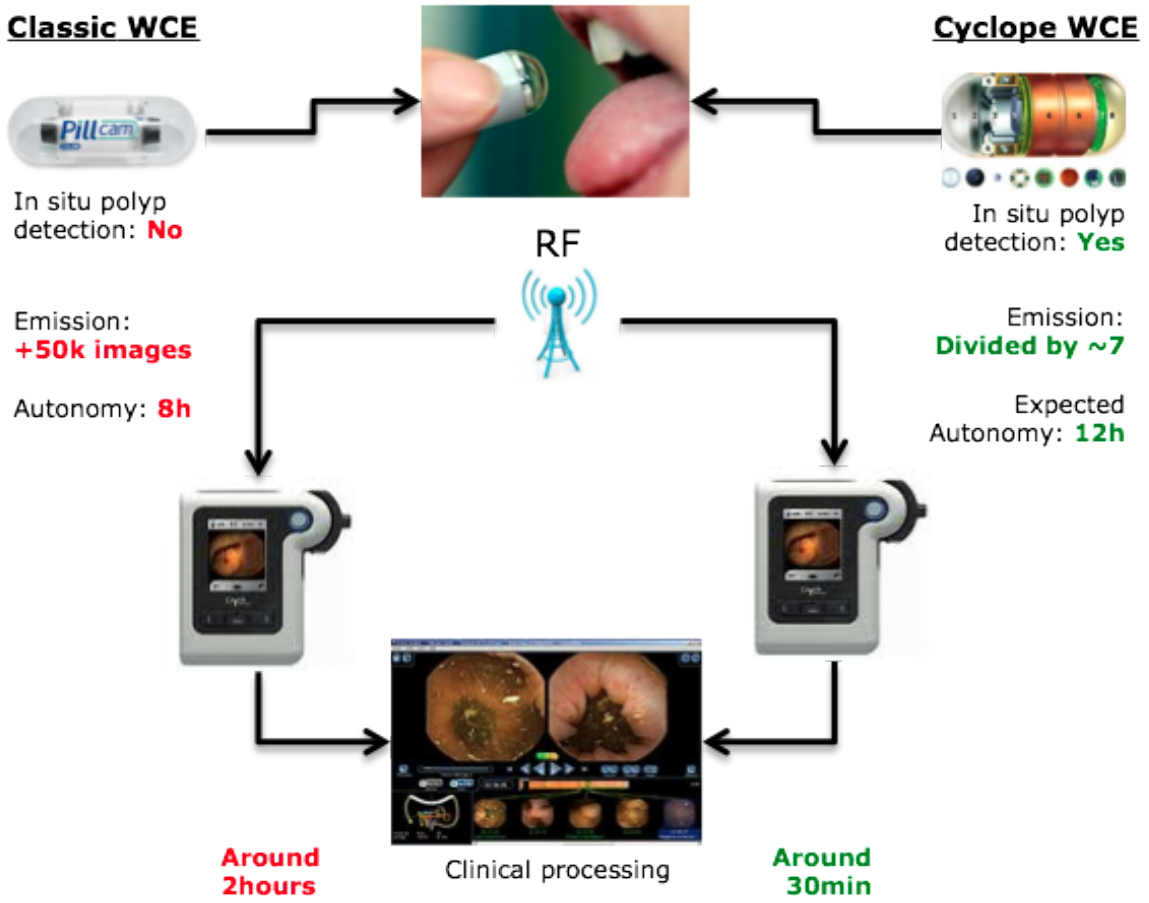

Figure 5.2: Comparison of the classic clinical workflow (left) and the expected one using Cyclope WCE (right), with corresponding improvement in green.

rate of 97% on an in vitro dataset consisting of 111 polyps (40 adenomas and 81 hyperplasias) made in silicon. Nevertheless, it appears that for real case examinations, 3D features are not sufficient to detect the large variety of polyp shapes that can be very flat at an early evolution stage.

In this research work, we focus on the 2D analysis of the videoendoscopy images in order to investigate other possibilities than 3D shape characterization of polyps to improve capabilities of WCE. As in [Ayoub *et al.*, 2010], a particular attention is given to propose a global detection/classification scheme that can be integrated into the "Cyclope"-WCE architecture shown in Fig. 5.3 and more precisely, by taking benefits of the FPGA block.

The remainder of this chapter is organized as follows: a state-of-the-art on detection of polyps in videocolonoscopy using 2D features is proposed in Section 2. In Section 3, the proposed approach is detailed. Experimental results are given in Section 4. Discussion, with a particular focus on hardware implementation, and conclusion are given in the last two sections.

5.1.2 Related Works

Several previous references have considered the detection of intestinal polyps in videocolonoscopy images in the last few years ([Liu *et al.*, 2011a; Bernal *et al.*, 2012; Figueiredo *et al.*, 2011;

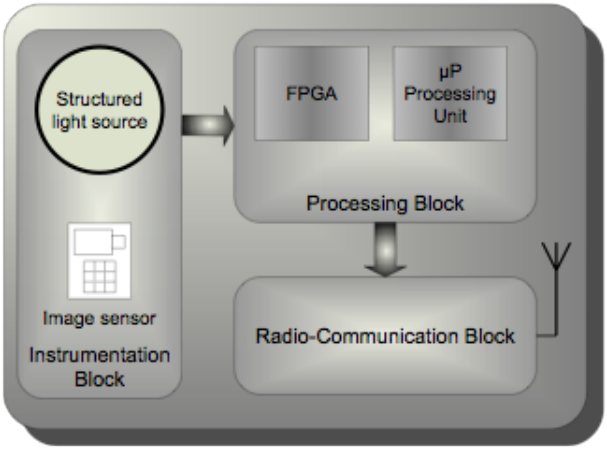

Figure 5.3: Block Diagram of the "Cyclope WCE"

Karargyris and Bourbakis, 2009; Kodogiannis and Boulougoura, 2007] among recent ones). They are mainly divided into two categories: those based on geometric features of the polyps (size and shape) and those based on textural features.

In the framework of "Cyclope project", we focused our attention on four particular recent contributions.

In [Bernal *et al.*, 2012], authors propose a study made on videoendoscopy images. They developed a region descriptor based on the depth of valleys (SA-DOVA). Resulting algorithm, divided into several steps, including region segmentation, region description and region classification, is characterized by promising detection performance (see Tab. 5.1).

In [Figueiredo *et al.*, 2011], authors assume that polyps show up as protrusions that can be detected using the local curvature of the image. Consequently, a method based on the mean and geometric curvature of the WCE image is proposed. The main drawback of the proposed approach is the strong dependance on the protrusion measure of the polyp to identify potential candidates. The consequence is that if a polyp is not protruding "enough" from the surrounding mucosal folds, it may be missed.

In [Karargyris and Bourbakis, 2009], Karargyris and Bourbakis propose an algorithm for WCE images mainly based on Log Gabor filters and Susan edge detector. Based on the geometric information of the resulting detected ROI, a level-set segmentation is then initialized for an accurate delineation of the polyps. On the considered WCE image database (10 polyps and 40 non-polyps), the method gives satisfying results but authors highlight that the taking into account of texture or color-based features within the detection/classification scheme would significantly increase related performance.

Finally, Kodogioannis and Boulougoura [Kodogiannis and Boulougoura, 2007] propose a texture-based approach. Authors introduce new texture-based features computed from the chromatic and achromatic spectra of the Region of Interest (ROI) that may contain a polyp. For classification, a neurofuzzy scheme is proposed. Main result is that the textural information is of first importance for the discrimination between polyps and non-polyps.

Table 5.1 summarizes the main principle and the obtained performance of these four main contributions.

All four presented approaches for polyp detection and classification are definitely of primary interest but may not fully compel to the hardware constraints of Cyclope architecture (the detection algorithm is to be embedded in the FPGA block of limited resources) since all

Authors	**Main principle**	**Classification performance**	**Database**
[Bernal *et al.*, 2012]	Geometry	Sensitivity 89% Specificity 98%	300 video-colonoscopy images containing a polyp (**freely available**)
[Figueiredo *et al.*, 2011]	Geometry	No indicated performance	17 WCE videos of 100 images each, containing example of polyps (10), flat lesions, diverticula, bubbles, and trash liquids
[Karargyris and Bourbakis, 2009]	Geometry	Sensitivity 100% Specificity 67.5%	50 WCE images (10 polyps and 40 non-polyps)
[Kodogiannis and Boulougoura, 2007]	Texture	Sensitivity 97% Specificity 94%	140 WCE images (70 polyps and 70 non-polyps)

Table 5.1: Main characteristics of 4 of the most recent references of the literature.

developed methods were designed mainly for an off-line use by the clinician and can fully benefit from the high computing capabilities of the last-generation processors: As a consequence, the related processing schemes include possible demanding algorithms like active contour segmentation [Karargyris and Bourbakis, 2009], blob detector [Bernal *et al.*, 2012] or local curvature estimation [Figueiredo *et al.*, 2011], that have not been proved yet to be easily embedded on a "low" resource hardware like FPGA. Moreover, it also appears that image databases used for performance estimation are size-limited and/or not freely available for possible comparison, except in the case of [Bernal *et al.*, 2012], more particularly when considering WCE images.

Taking benefits of the aforementioned reference, and taking into account the heavy hardware constraints of "Cyclope" WCE, we propose here a learning-based polyp detection approach using texture-based descriptors. In order to compare related performance to the most recent literature, we will use for illustration the database freely provided by [Bernal *et al.*, 2012].

5.2 Methods

The proposed method is inspired from the psychovisual methodology used by the physician when doing an endoscopic examination: First, a detection of the Regions of Interests (ROI) that may contain a polyp is performed using shape and size features extracted from the image. This first pre-selection allows a first fast scanning of the image. Once the ROI are detected, a second analysis, based on texture (homogeneity, granularity, coarseness...) is achieved. Practically speaking, we propose a global scheme for the detection/classification of possible polyps divided into two steps:

1. Considering the geometric step of the proposed approach, simple image processing tools

make possible the detection of circular/elliptical shape like the Hough transform for instance.

2. The texture-based classification is the main keypoint of the global scheme since the rejection of most of the false positive preselected ROI have to be performed at this stage. To achieve this, we propose to design an ad hoc classifier based on a boosting-based learning process using textural features.

The global scheme of this approach is summarized in Fig. 5.4. Each step is detailed in the following sections.

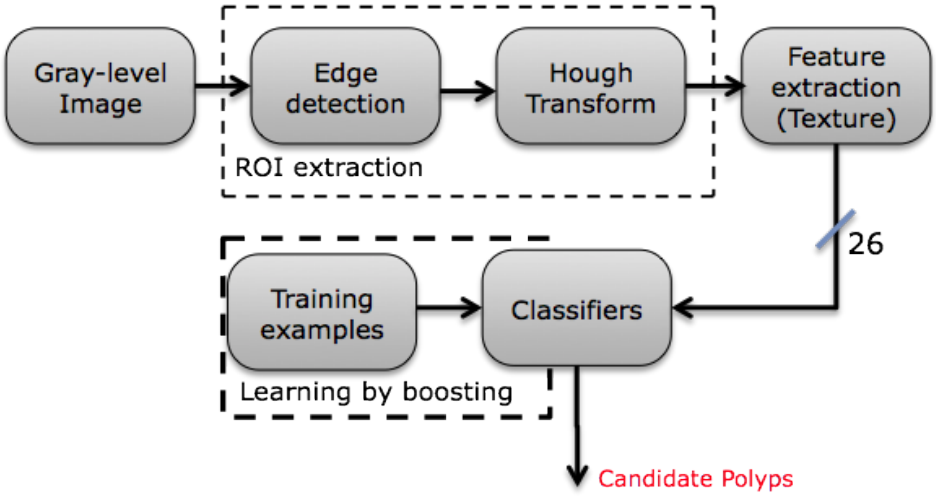

Figure 5.4: Proposed scheme for the detection of polyps within videoendoscopy images.

5.2.1 Geometric And Texture-Based Features

As mentioned before, the first useful characteristics for detection are size and shape of candidate structures. More precisely, a detection algorithm based on the circular form of the polyps is considered. Instead of considering a local curvature estimation or the Log-Gabor filtering, as suggested in [Karargyris and Bourbakis, 2009], the circular Hough transform is used for three reasons; firstly, processing remains simple and efficient; secondly, all polyps must be detected even if numerous false positive ROI are also considered; thirdly, the Hough transform can be FPGA embedded like shown in [Tagzout *et al.*, 2001] for an *in situ* and real-time detection. A discussion on that particular point is provided in the related section. In order to handle with different polyp sizes, we consider a research interval for the radii of the extracted circle.

For the texture-based analysis of pre-detected ROI, the co-occurrence matrix [Davis *et al.*, 1979] is used to discriminate textural patterns of polyps and non-polyps. Main advantage of co-occurrence matrix is in their fixed dimensions only depending on the grey-scale resolution of images: as a consequence whatever is the dimensions of the candidate ROI, the size of the matrix remains the same, which is of first interest when considering the hardware implementation constraints (mainly memory) we have to deal with. Moreover, the textural discrimination capabilities of co-occurrence matrices remain of high efficiency even on grey-scale images [Haralick,

1979] and could be implemented on FPGA [Iakovidis *et al.*, 2007] with possible limited memory resource, the 3 color channels being not necessary.

Basically, the cooccurence matrix $\mathcal{MC}_{\Delta x,\Delta y}(i,j)$ shows how often a pixel of grey-level value i occurs either horizontally, vertically, or diagonally to adjacent pixels of value j:

$$\mathcal{MC}_{\Delta x,\Delta y}(i,j) = \sum_{p=1}^{n}\sum_{q=1}^{m}\begin{cases}1, \text{if } I(p,q)=i \text{ and } I(p+\Delta x, q+\Delta y)=j\\ 0, \text{otherwise}\end{cases} \tag{5.1}$$

Twenty-six features (known as the Haralick's features [Haralick, 1979]) are then extracted from each of the computed matrices. Are included : Contrast, Correlation, Entropy, Cluster Prominence, Cluster Shade, Dissimilarity, Homogeneity, Autocorrelation, Maximum probability, among other parameters (see Eqs. (5.2), (5.3), (5.4) for illustration of the first three parameters).

$$Contrast = \frac{1}{K}\sum_{k=0}^{N-1} k^2 \sum_{|i-j|=k} \mathcal{MC}(i,j) \quad , \tag{5.2}$$

$$Correlation = \frac{1}{K\sigma_x\sigma_y}\sum_{i,j} ijMC(i,j) - \mu_x\mu_y \quad , \tag{5.3}$$

$$Entropy = -\frac{1}{K}\sum_{i,j}\mathcal{MC}(i,j)\log\left(\frac{\mathcal{MC}(i,j)}{K}\right) \quad , \tag{5.4}$$

with K the number of elements of $\mathcal{MC}(i,j)$ and

$$\mu_x = \frac{1}{K}\sum_{i,j} i * \mathcal{MC}(i,j) \quad ,$$

$$\mu_y = \frac{1}{K}\sum_{i,j} j * \mathcal{MC}(i,j) \quad ,$$

$$\sigma_x^2 = \frac{1}{K}\sum_{i,j}(i-\mu_x)^2\mathcal{MC}(i,j) \quad ,$$

$$\sigma_y^2 = \frac{1}{K}\sum_{i,j}(j-\mu_y)^2\mathcal{MC}(i,j) \quad .$$

Since the texture-based classification is performed using a boosting-based algorithm, no limitations about the number of parameters is considered, main idea being to let the learning process converge to the best classification solution without any prior information.

5.2.2 Classification

"Boosting" is a machine learning algorithm for supervised learning (see [Schapire and Singer, 1999] among other publications of the same authors). It consists of the accumulation and constant learning of weak classifiers (a weak classifier is considered slightly correlated (a little better than chance) with the true classification), that once combined together generate a strong classifier, well-correlated with the ground truth provided by the expert. In the framework of our proposed approach, we use the boosting-based method of [Viola and Jones, 2001] set-up in attentional cascade (Cascade Adaboost). This configuration allows us to create a strong classifier which

performance can be priorly set-up in order to optimize the sensibility of the classification along with the specificity. For illustration of the overall learning algorithm, see Fig. 5.8 in which F_i and D_i stand for the maximum authorized False Positive Rate and the minimum acceptable detection rate, respectively, computed for each iteration of the process using the given f and d performance ratio, and F_{target} the global false positive rate.

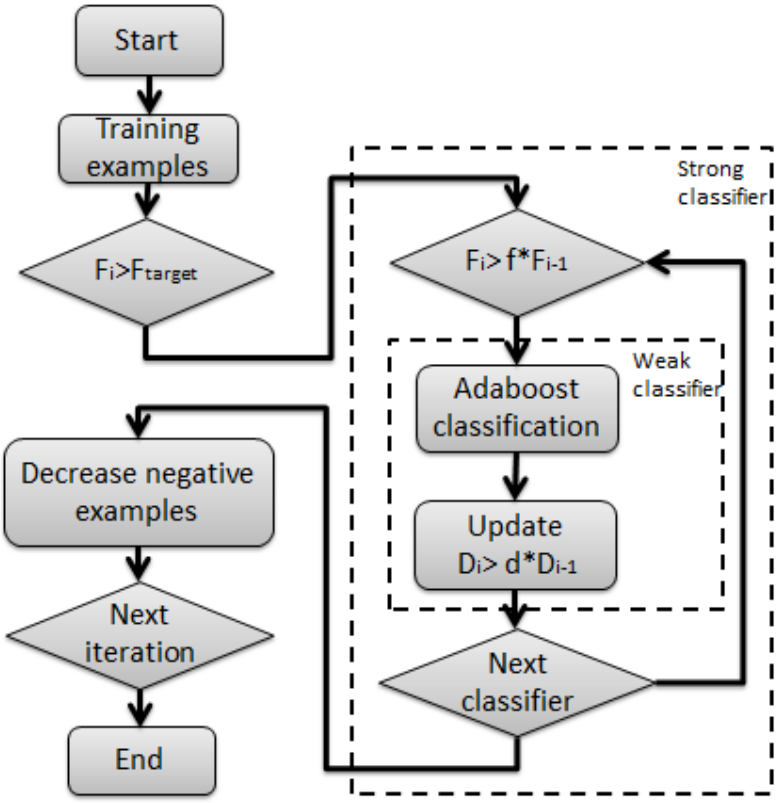

Figure 5.5: Flow diagram that shows how the Cascade Adaboost is performed

If the learning process related to boosting-based algorithms is time consuming, it is important to note that, once the optimal classifier is computed off-line, the classification step is very fast and fully compatible with a hardware implementation as shown by application to real-time face detection [Viola and Jones, 2001] embedded in cameras.

In our particular case, the considered weak classifiers are based on a set of truncated binary decision trees (bootstrapping) built from the 24 textural parameters on the dedicated learning database.

5.2.3 Data

Tests were performed on the database proposed by J. Bernal from the Universitat Autonoma de Barcelona [Bernal *et al.*, 2012], which consists of 300 videoendoscopy images presenting with one single polyp each, identified and segmented by a specialist. The data are courtesy made available by authors. To our knowledge, in the particular framework of colorectal polyp detections, this is currently the only existing on-line database with a sufficient amount of examples to be statistically meaningful. Fig. 5.6 shows some example of polyps extracted from the database.

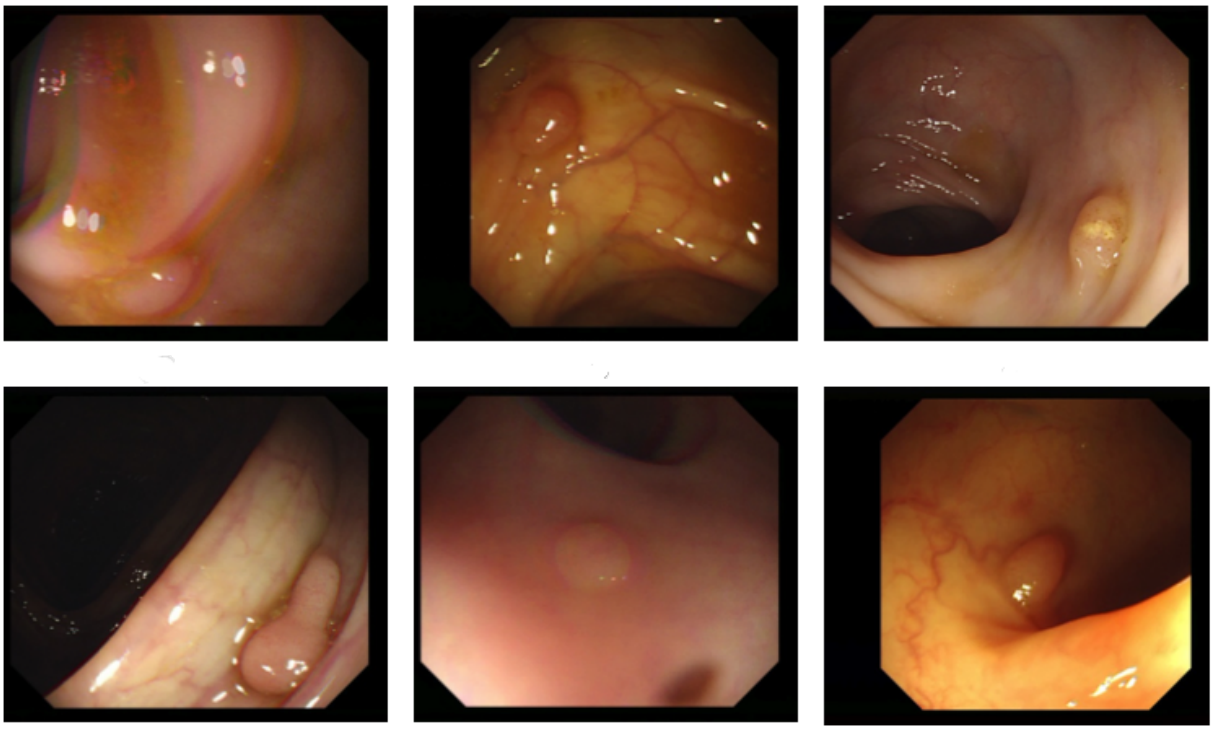

Figure 5.6: Example of polyps extracted from the database of Bernal *et al.*.

To build the learning database each image of the main dataset was sub-divided into five thumbnails by the gastroenterologist, as shown in Fig. 5.7. A first ROI corresponds to the polyp (a), and the other four to non-polyps (b-e). The resulting learning/testing database is then composed of a total of 1500 images, with 300 images of polyps and 1200 images of non-polyps, the labeling being performed,once again, by a specialist.

5.2.4 Performance Evaluation

To proceed to performance evaluation of the proposed boosting-based method, three measures are usually considered meaningful and complementary: the sensitivity, the specificity and the false positive rate (FPR) respectively defined by:

$$Sensitivity = \frac{TP}{TP + FN} , \tag{5.5}$$

$$Specificity = \frac{TN}{TN + FP} , \tag{5.6}$$

$$FPR = \frac{FP}{FP + TN} , \tag{5.7}$$

with TP, FN, TN, FP standing for true positive, false negative, true negative and false positive.

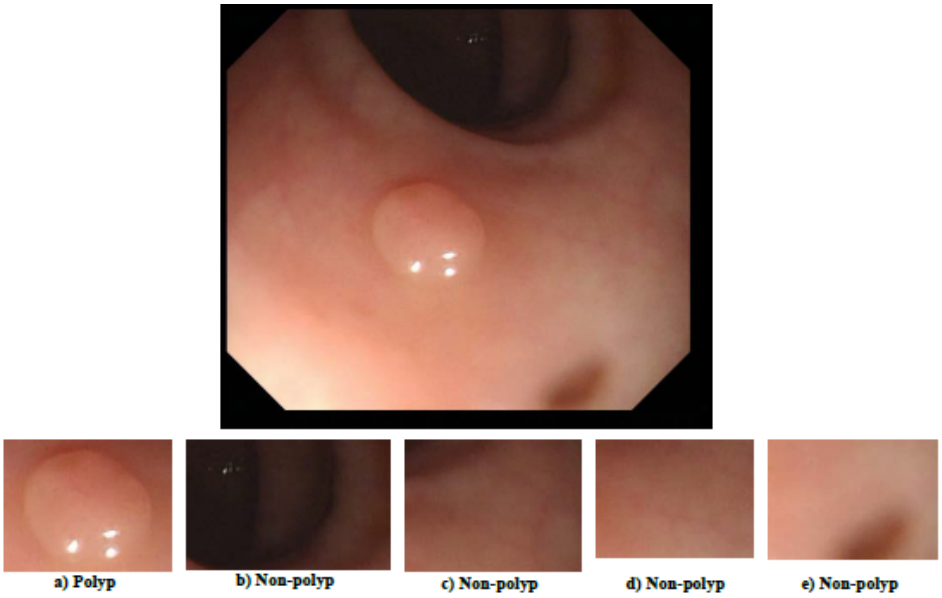

Figure 5.7: Example on how the learning/testing database is generated from the original data of Bernal *et al.*.

5.3 Experiments

5.3.1 Hough Transform-Based Step

In table 5.2 the detection performance of the Hough transform on the aforementioned original database of [Bernal *et al.*, 2012] are shown and compared to the Log Gabor filtering proposed by [Karargyris and Bourbakis, 2009].

	Sensitivity	Specificity
Hough transform	94%	15%
Log-Gabor	42%	89%

Table 5.2: Comparison of the detection sensitivity and specificity of the Hough transform and the Log Gabor filtering approach of Bourbakis *et al.*on the original database of Bernal *et al.*

We provide here the best obtained results considering the sensibility rate for an ad hoc set-up of the Hough transform circle detection threshold and for a research interval of the radii between 40 and 80 pixels.

We do not provide here usual Receiving Operating Curve (ROC) since we do not control the number of detected FP for a given threshold: Depending on the quality of the original image, number of FP can be very important (see Fig. 5.9.(c) for illustration).

At this stage, it can be noticed that the simple Hough transform allows a good detection of ROI containing a polyp even if the assumption made on the shape could be consider as restrictive since polyps are more elliptical than circular most of the times.

Moreover, if the value of specificity is low, the next classifying step will allow to improve the overall method performance.

5.3.2 Learning-Based Classification Performance Using Texture-Based Features.

For these experiments, the ad hoc generated polyp/non-polyp database was divided into two subgroups: A first one composed of 1000 images (200 images of polyps and 800 of non-polyps) for the learning process and a second group for testing composed of the remaining 500 images. In order to obtain classification performance statistically meaningful, the drawing of the elements of both learning and testing databases were randomly made, and presented quantitative results correspond to the average value obtained on 100 different configurations.

In a first experiment, different kinds of methods for classification were compared: Learning Vector Quantization technic (LVQ) [Kohonen, 1995], classic Adaboost and finally Attentional Boosting (cascade adaboost). In terms of performance, as long as, contrary to cascade adaboost, it is not possible to set the obtained performance for LVQ or classic Adaboost, we privileged the balance between "Sensibility" and "Specificity". The results of this experimentation are shown in Fig. 5.8.

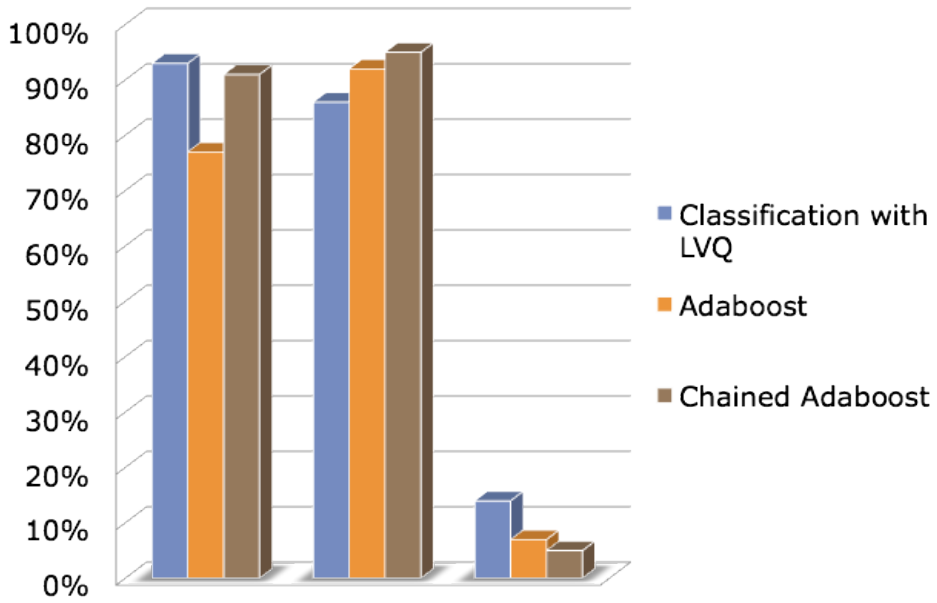

Figure 5.8: Performance comparisons among different types of classification approaches, including adaboost and Cascade Adaboost. From left to right : Sensitivity, Specificity, False Positive Rate.

As it can be noticed, among the different classification techniques used, Cascade Adaboost provides the best compromise between "Sensibility" and "Specificity". If LVQ leads to a good classification of True Positive examples, the total amount of FPR remains too important considering the fact that 10% of the polyps are misclassified.

In a second experiment, only Cascade Adaboost is considered with a setting of the performance parameters (F_i and D_i of Fig. 5.8) chosen in order to have a "Sensibility" the closer to 100%, whatever "Specificity" will be. This scenario fits better the expectations of radiologists who do not wish to miss possible polyps. Performance are shown in Table 5.3.

Tab. 5.3 shows that a high"Sensibility" is an objective that can be reached with a cascade adaboost setting of the learning process. Of course the "FPR" rate increases, but finally not that much considering the fact that for 100 polyps detected, only 14 more will be showed as possible

Cascade Adaboost	Sensibility	Specificity	FPR
Mean	99,5%	86.1%	13.9%
Standard deviation	0.00	0.07	0.07

Table 5.3: Average performance of the Cascade Adaboost learning process with a “Sensibility" set to a minimum of 99%.

candidates to the radiologist.

5.3.3 Examples of Detection And Classification Results

In Fig. 5.9 some examples of detection/classification are shown. ROI that are skirted by a non-bolded plain rectangle are the ROI candidate issued from the Hough transform step of the proposed approach. ROI skirted by a bold plain rectangle are those which are effectively identified as a polyp after the texture-based classification.

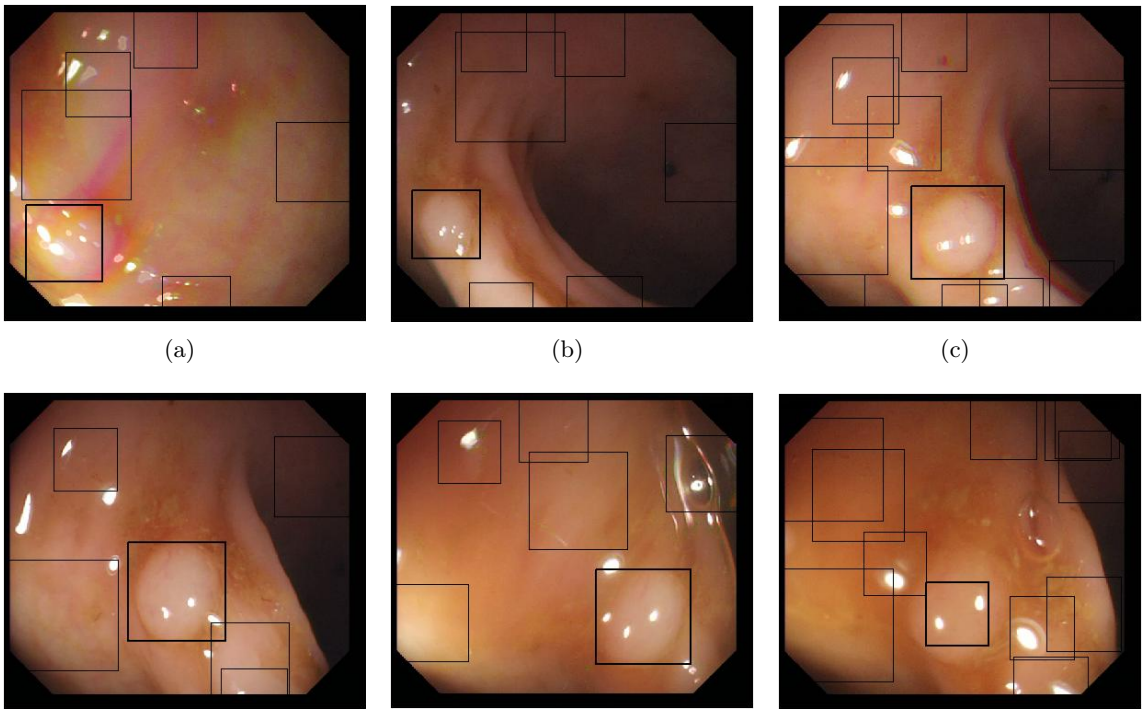

(a) (b) (c)

(d) (e) (f)

Figure 5.9: Detection examples

In two first cases (a) and (b) of Fig. 5.9, the single polyp is detected and well classified. In the third image, where the polyp is even visually not that easy to detect due to the surroundings “noise”, from nine ROI detected using the circular Hough transform, three are finally identified as polyp after the classification step, including the one containing the real polyp, generating two false positives.

5.3.4 Simulation and Time Processing

Up to now, all the developments have been performed under Matlab environment in order firstly to establish the feasibility of this new approach and to reduce the time development hardware. No optimization of the code has been realized. Currently, the time processing per image is about 2.05 seconds on a iCore7 at 2.8GHz. A multithreading version is under development both to accelerate by a factor 50 the time processing and to test first this approach in real time with the video output of a colonoscope before considering dedicated hardware implementation for WCE.

5.4 Discussion

5.4.1 Classification and Detection Performance

A boosting-based approach for polyp detection in videoendoscopy images has been proposed. Obtained results show interesting performance of the classification step in terms of selectivity and specificity, the most efficient learning method being the Cascade Adaboost one as shown in Fig. 5.8: As it can be noticed in Fig. 5.10, the boosting-based approach performed a classification which performance are close to Bernal et al's method. However, this latter comparison must be considered with cares since their proposed method and our are not exactly based on the same fundamental idea.

Moreover, detection results could be improved since currently the global detection rate of the overall processing scheme is only of 68% of the polyps: In Fig. 5.9.(c), it appears that when original image is corrupted by a strong acquisition noise, misclassifications can occur even if many FP ROI are discarded after the textural classification step. The remaining detected false polyps are errors probably made by the insufficient number of examples inside the database used for the learning step of the boosting method. Two main improvement will be considered in a close future: A first one consists in using a less sensitive detector than the circular Hough transform: the LoG (Laplacian of Gaussian) detector could be an alternative for instance even if the hardware implementation will need particular attention. A second point consists in improving the classification performance by integrating other features of interest (color, shape...), but also more training examples in the dataset to ensure a better representativity of the examples. This latter point could be achieved by proposing an off-line interactive process to the clinician that can add possible misclassified polyps to the learning database once the classification has been performed. Although such an approach could be time-consuming because of the iteration of the learning process (boosting) each time a new example is added, such an effort should lead to an active extending of the available training database as well as an increase of the performance in terms of FPR [Liu *et al.*, 2011b].

Moreover, if presented results focus on classic videocolonoscopy, it appears necessary to build a training database dedicated to WCE images which characteristics (resolution, quality, etc.) can be quite different from the data used in this study. Nevertheless, we showed here that the learning-based approach can adapt to the particularity of used data by designing a proper learning database.

5.4.2 Towards an Integrated Hardware Implementation

Currently, the Cyclope project only implements in hardware the SVM-based classification of 3D object with an FPGA Virtex II-pro [Kolar *et al.*, 2010]. Nevertheless, the algorithms proposed here can be also implemented on this platform considering the recent literature. Elhossini [Elhossini and Moussa, 2012] proposed a memory efficient architecture for implementing Hough

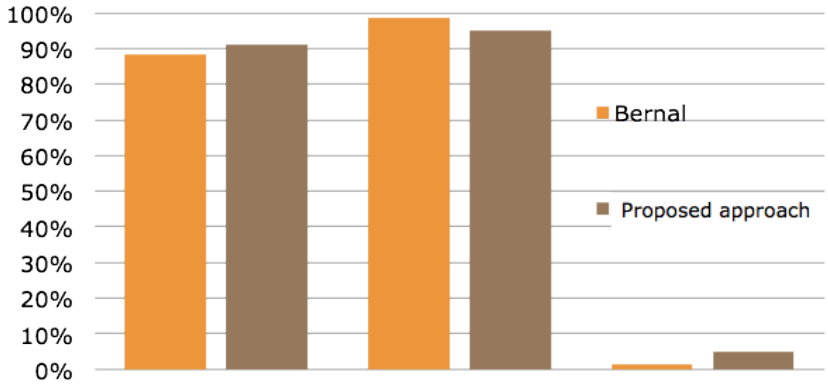

Figure 5.10: Comparison between the method exposed by Bernal *et al.*and the attentional boosting based classification method proposed: from left to right: Sensitivity, Specificity and FPR

Transform on FPGAs. The proposed architecture enables storing the Hough Transform space on the FPGA's memory blocks with no need for accessing external memory while processing large size images in real-time with a 30 frame per second rate. Others hardware implementation allow to optimize the computation of angle by using Cordic algorithms, the time processing, the type (circle and/or line), etc. The main issue, is to develop a Hough Transform architecture that minimize the memory space with a great precision and a high parallelism. Table 5.4 summarizes the technical aspects of the five main contributions in the field.

Authors	Frame Size	Memory	Rate (FPS)	FPGA
[Ruen *et al.*, 2006]	256x256	Ext. 1.6Mb	0.2	Altera Stratix 1
[Souki *et al.*, 2008]	320x240	Ext. 4Mb	0.3	Altera Cyclone 2
[Geninatti *et al.*, 2009]	44x46	Ext. 8Mb	30	Xilinx Spartan 3
[Hardzeyeu and Klefenz, 2008]	500x400	Ext.	800	Xilinx Virtex 2
[Elhossini and Moussa, 2012]	800x600	Int. 250kb	30	Xilinx Virtex 2

Table 5.4: Main characteristics of 5 of the most recent references of the literature.

Optimized embedded architecture based FPGA for an efficient and fast computation of grey level co-occurrence matrices (GLCM) and Haralick textures features for use in high throughput image analysis applications where time performance is critical have been already studied. The three main contributions [Sieler *et al.*, 2010] [Iakovidis *et al.*, 2007] [Tahir *et al.*, 2004] focus on the design of hardware processor that make possible to compute four distances (1, 2, 3 and 4 pixels) and four angles (0°, 45°, 90° and 135°) in parallel. The main difference among these approaches lies in the strategy to address the neighboring pixel. Table 5.5 summarizes the performance of the three main recent contributions obtained on Virtex-II and Virtex-5 FPGA.

Boosting classification has been also implemented in hardware on FPGA [Mitéran *et al.*, 2005]. According to the related work on the hardware implementation of Hough Transform, co-occurence matrices computation and boosting classification, it is feasible to embed our approach on FPGA circuit.

This first step is a pre-required one towards an ASIC design embedded in the WCE, but also to be able to precisely estimate the energy consumption related to the hardware implemented

Feature	[Sieler *et al.*, 2010]	[Iakovidis *et al.*, 2007]	[Tahir *et al.*, 2004]
Year	2010	2007	2004
FPGA	Virtex-5	Virtex II	Virtex II
ref	XC5VLX50T	XCV2000E	XCV2000E
Frequency	56.3MHz	38.2MHz	50MHz
Area (FPGA used)	21.9%	45%	59%
Time processing (128x128)	2.4ms	x	1.756ms
Ext. Mem	x	800kb	327kb
Int. Mem	327kb	83.2kb	81.9kb

Table 5.5: Main characteristics of related work.

detection/classification algorithms. In a previous work, we demonstrated that 75% of the power consumption of a smart RF sensor are due to the RF power budget [Suissa *et al.*, 2010]. Moreover, [Wang and Sodini, 2006] showed the transmitter power consumption is a non linear function of the data rate and concluded that to increase the battery life of a smart sensor, the amount of data should be reduced. The overall gain of an intelligent transmission versus a continuous transmission in a standard WCE (see Fig. 5.1) depends on the one hand on the estimation of the number of images (polyps and false positives) that will be transmitted and on the other hand, on the power consumption due to their processing.

Currently, we can make only an estimation of this overall gain based on hypothesis, because of the integrated circuit has not been yet designed and the in vivo experiments not achieved. We are working on the hardware implementation of the 2D classification on a FPGA-based platform. By considering the above state of the art, the fact that an FPGA also consumes 12 times more dynamic power than an equivalent ASIC on average [Kuon and Rose, 2007] and the power consumption of Virtex 5, we can estimate that the power consumption due to the processing will be approximatively under the hundred of μW. This feature is less than the power consumption of the usual eight white LED used for illumination and the RF transceiver.

Moreover, during a standard examination, around 50 000 images are sent to the data logger with a frame rate of 4 fps up to 35 fps. By considering the same examination with the possible presence of ten polyps and a FPR of 13.9%, only 6960 images will be sent and a 7 factor can been won on the overall power consumption of the transmission RF.

5.5 Conclusion and Perspectives

In this chapter, we introduced a new embeddable method for polyp detection in videoendoscopic examinations. The entire detection chain combines geometric and textural features for polyp characterization: if the first geometric step remains simple with the use of the Hough transform, the textural features computed from co-occurrence matrices are integrated within a boosting-based approach making possible to achieve good classification performance similar to those of the most recent state-of-the-art article. At last, the complete developed detection/classification scheme is in accordance with a hardware implementation which is of primary importance for possible in situ application using WCE.

Conclusion and Future Work

All along this document, I gave a detailed overview of the research work I have been involved in for the last 8 years in order to demonstrate my abilities to animate/supervise research activities (including the supervisions of MSc and PhD students, the writing of proposals for project funding, the sustaining of national and international collaborations, publications, etc.).

It is now time to think about the future and give concrete elements about my scientific project for the years to come. In the following sections, I give scientific elements as well as details about the funding strategy.

From Computer-Aided-Diagnosis...

PDF Modeling in Statistical Region-Based Active Contour

In the framework of histogram-based active contour approach, the modeling of the PDF computed from the histograms extracted from particular regions of interest within the image, and between which the divergence is estimated during the segmentation process, remains a challenging question. Currently, the Parzen-window technique is classically used and this is actually the solution we chose to obtain a continuous and derivable expression from which can be derived a general Partial Differential Equation (PDE) steering the segmentation process. Major weak point of kernel approaches like the Parzen-Window one, is the sensibility related to the parameterization of the related Gaussian kernel.

This challenging problem will be addressed through a "new" fruitful collaboration with Prof. David Rousseau from CREATIS lab on this particular aspect of the proposed approach. Recent publications of Prof. Rousseau[9], as well as recent discussions we had about the work of Leila Meziou (Prof. David Rousseau was external reviewer of the PhD), showed us the real benefits of a joint effort: Objective will be to propose an adaptive solution for the modeling of the PDF based on the minimum description length principle. The underlying idea is to optimally described the considered PDF from a "disorder" measure perspective in such a way that the modeling would not be dependent from any parameterization. Main scientific challenge is to embed such a modeling in the active contour framework which has not been done yet to our knowledge.

Alpha-Divergence Family and Information Theory

An other point of interest is also to have a better understanding of the parameter α of alpha-divergence family. During the PhD of Leila Meziou, we focused on the advantages of this family of divergence and we shown through different experiments the benefits of the tunable inner metric compare for instance, with the classic KL divergence. A step further consists now to be able to propose an interpretation of this parameter α first from an Information Theory angle, and then

[9] Physical Review A 2009, and Optics Letters 2011

in the particular context of image segmentation. To achieve this, a joint work with Prof. David Rousseau has also started since January 2014 with the main objective of being able to show what can brings alpha-divergence in terms of pattern recognition and detection tasks: most precisely, the idea is to evaluate how such divergence like the Rényi's one can be used as a contrast function for pattern detection.

In terms of scientific strategy, at this time, we need to strengthen the first obtained results before being able to go for a PhD funding proposal for instance. In that objective, I apply for a one-year sabbatical with CNRS, next year. If obtained, a significant part of my time will be dedicated to this scientific work including work on PDF modeling and the information theory aspect described here. Depending on the obtained results, a MSc internship would be proposed for next spring.

Actin-Tagged Confocal Microscopy and 3D segmentation

Jointly and beneficially to the national perspective, at an international level, a strong objective for the years to come is to actively strengthen the on going 6-year collaboration with Prof. Bogdan Matuszewski on active-contour based segmentation approaches. First of all, following the work already achieved on the characterization of cell cytoskeleton using actin-tagged confocal microscopy images[10] a European project is to be submitted to next H2020 call. Aims of this project, co-investigated by Liverpool John Moore University and ADSIP Research Centre of University of Central Lancashire, is to study and model the behavior of living cells when submitted to the insult of a ionizing beam. Primary hope is to have a better understanding of the non-desired effect of radiotherapy effects. Biocellular skills as well as Computer Vision and Image Processing ones are necessary to the achievement of this work: Segmentation of the cytoskeleton of living cells for shape and texture characterization is a mandatory step to further investigations.

On this particular topic, plus the already existing joint publications (see the detailed list of references in Annex) a first prospective work on the use of approximate entropy for membrane segmentation in microconfocal microscopy images will be presented at next Biosignals conference in 2014[11]. Finally, we will also concentrate on the following step of the full analysis: The extraction of features closely related to cell adhesion and proliferation rates which are well-known clinical indicators of abnormal alterations of the structure of the cells, above all in oncology.

In parallel and beneficially to the "Cells" activity, a particular research work focusing on 3D modeling of Right Ventricle contraction will also be continued on the basis of a recent joint-MSc internship (Spring-Summer 2012) between ETIS and ADSIP. This project, coming from the early collaborations between our two institutions on the quantitative analysis of the Left Ventricle function using tagged cardiac Magnetic Resonance Images will benefit from the already existing activity on 3D active contour segmentation: the segmentation of such data can not be achieved without prior knowledge on the shape of the organ to segment because of the lack of boundary evidences on the apex level of the heart. As it was presented in Chapter 4, we have recently proposed[12] a 2D segmentation method in which a prior knowledge on the shape can be statistically learnt using a strategy combining a classic level-set region-based approach (Chan and Vese for instance) with a shape prior term taking form of a vector of normalized moments (Legendre or Zernick) expressed in the related shape-space computed using Principal Component

[10] TERAFS, BIOMICMAC 3DCELL projects

[11] "Geodesic Active contour based on Approximate entropy: application to cell membrane segmentation in microscopy images", Proceedings of Biosignals Conference, 3-6 March 2014, Angers, France.

[12] Journal of Mathematical Imaging and Vision, 2013, A.1.1

Analysis on various “ground truth” examples. 3D extension of this approach is not trivial and remains a real challenge to remain accurate, robust and in accordance with a clinical use in terms of computation time.

This project will also be an opportunity to develop a new fruitful collaboration with Dr Luis Garrido from Universitat de Barcelona on 3D segmentation of medical images that will be an invited Professor of ETIS lab for a one-month period in 2014. The “Cage-Active-Contour" approach he recently proposed with researchers of the Imaging Processing Group of UB will be of first interest to the “Right Ventricle” project.

Currently, in order to ensure the viability of these projects for the next 3 years-period, a project called “Modelling the Effects of Ionising Radiation on the Structural, Mechanical & Migratory Properties of Cancer Cells” is being submitting jointly to EPSRC and the Medical Research Council (UK). If accepted, a PhD and a post-doc fundings will start at the latest in early 2015.

.

Industrial Transfer

Finally, a third objective is to strengthen a new collaboration with a private company called EVOLUCARE which activity is focused on CAD interface design for radiologists used. More precisely, some recent joint internships of MSc students from Master SIC showed the possible interactions between the SIMBAD activity and their own R&D objectives: a CIFRE agreement is currently being discussed. The related project proposes to tackle early-diagnosis of prostate cancer from a multi-scale perspective: from micro scales (microscopy cell images) to macro scales (Prostate MRI) to draw some possible correlations of clinical indicators between both visualization levels of the same pathology. Main scientific challenge of the project is in the multiscale approach proposed for which particular segmentation and analysis tools must be developed to cop with the different type of imaging conditions. This collaboration will strongly benefit from the on going link with the University of Central Lancashire that is already endorsing the project.

Training Through Research part 1

Complementary to those scientific objectives, a secondary objective for 2014 is to finalize an on going proposal for a European PhD student program of exchanges in the framework of a dedicated UK-government call. Main objective is to obtained the fundings of 4 PhD, during next 5 years, that will be officially co-supervised by our two institutions. The already existing collaboration between Prof. Matuszewski and I, plus the different projects we were both of us involved in during the last 6 years are strong arguments that will help us in the obtaining of this funding. Both our institution would benefit from such a program in terms of scientific activity. If selected, this program will start in September 2014 with a first joint PhD supervising on active-contour-based image segmentation.

... To In Situ Diagnosis

Cyclope Project

Scientific aspects

As mentioned in Chapter 2, in 2011, with the arrival as a Full Professor of Olivier Romain (formerly Associate Professor at LIP6 lab from Paris 6 University) a transverse research activity between ICI and ASTRE teams with a particular focus on "Embedded System for Health" (ESH) was started. This joint effort currently takes form of three main projects: Cyclope, SmartEEG, and FibroSES.

Cyclope project, in which I am the more involved, aims at developing an original wireless videocapsule for colorectal cancer early-diagnosis with embedded image processing abilities like explained in previous Chapters. A necessary balance must be found between the performance of the detection/segmentation algorithms and their complexity in order to make their embedding possible.

As mentioned in the introduction of this document, this project is in close relationship with two gastoroenterologists (Prof. Xavier Dray, and Prof. Philippe Marteau) of Lariboisière Hospital (APHP, Paris), who are since september 2013 associated researchers of ETIS lab and that "Cyclope" project will benefit from the attribution of a PhD funding next September[13].

In a close future, we will concentrate on two particular objectives:

1. First of all, the recent obtained results[14] permitted us to attract the attention of several European researchers (Greece-University of Lamia, Spain-University of Gran Canarias, Switzerland-EPFL) that we met during a dedicated special session that took place in conjunction with IEEE Bioinformatics and Bioengineering conference 2013 (Chania, Greece). From those discussions, two projects arose:

   - The organization of a challenge in early 2015 dedicated to real-time colorectal polyp detection/segmentation in videocolonoscopy (in conjunction with a major biomedical conference like MICCAI);
   - The submission of a project in the framework of the forthcoming H2020 call (2015).

2. Second, a particular focus will be given on the embedding of active contour segmentation capabilities within the WCE. This objective is a very challenging one since that kind of approaches are iterative and, as a consequence, not that in accordance with classic strategy of embedding with strong parallelism of the tasks. Nevertheless, we have recently shown in a preliminary study (presented in 2012 at the Computer-Assited Radiology and Surgery Conference) that active contour segmentation approach are of real interest for the delineation of multiple type of structure (polyps, lypomas, ulcers, metastasis) in images extracted from a WCE acquisition. If level-set approaches does not intuitively seems to fit the embedding objective, a particular focus on parametric version (using B-spline function for the modeling of the active curve) will be given.

[13] More generally, the ESH activity of ETIS has been identified as a priority research activity for the next 5-years period during last AERES expertise.

[14] International Journal of Computer Assisted Radiology and Surgery, 2013

Industrial Transfer

Recent contacts with the KarlStorz company[15] (videoendoscopy imaging device, Germany) have shown the interest of private companies for Cyclope project. A meeting with their R&D department (Tutlingen, Germany) already took place last January and it definitely appears that joint project focusing on the development of CAD tools for real-time analysis of videocolonoscopy would be of great benefits for both sides. We are now waiting for some official feedbacks on such possible collaborations (CIFRE agreement mainly).

The "Embedded System for Health" (ESH) Activity

Scientific perspectives

As mentioned in the CV Chapter, since September 2013, I am the co-scientific animator with Prof. Olivier Romain of the ESH Activity of ASTRE team. Main aim of this research activity is to imagine original and wireless medical devices , of low consumption and with embedded diagnosis capabilities. If Cyclope project is one of the current on going project, I am also involved in other activities, more related to Signal Processing, as the two already cited FibroSES and SmartEEG projects

- FibroSES project is funded by CNRS (DEFISENS Call 2013-2014) and involved 14 French lab. Main scientific objective is to propose an original approach on how non invasively quantifying the fibrosis process in response to the embedding of sensors inside the human body. This natural phenomenon is still under understood, especially regarding the effect on the measurement capability of a particular sensors.

  In this context, I am involved in a subpart of this project consisting in the designing of an In Vitro test bench with imaging capabilities for the quantitative estimation of the fibrosis phenomenon using impedance measurement. This work is in collaboration with ERRMECE lab for the biocellular aspect of this project.

- SmartEEG is a project funded by the Region Ile de France (FUI programs) and that involves 5 different companies (SME) and two academical partner (University of Cergy, and University of Pierre et Marie Curie). Main aim of this project is to design a complete EEG acquisition device with CAD capabilities.

  In this project, I am involved in the Signal Processing aspect and more precisely on the possibility to use tools from the data learning framework in order to design 'intelligent" algorithms for the different EEG signal analysis (detection of myoclony, epilepsy evidences, etc.).

My involvement in the ESH activity is also a way to have a better overview of the technological needs of the clinical community and allows me to enlarge the research perspective for the next 5 years from a scientific point of view as well as from a funding opportunity one.

In addition to this two on going projects, we are also working on other submissions (FUI, private funding) in collaboration with local companies (2CSI, Digital Simulation to name a few) mainly focusing on smart telemedecine. The main interest here is to find the adapted synergy among different scientific area (electronics, informatics, signal and image processing, data mining) to finally end up with a complete project with a straightforward impact on the every-day life.

The one-year sabbatical already mentioned earlier in this Chapter would help to concentrate on the reinforcement of the ESH activity management.

[15] www.karlstorz.com

Training Through Research Part 2

An other aspect of the ESH Activity is the strong existing link with the "Cursus Master Ingénieur" *BioSan* of the University of Cergy-Pontoise, recently labelled by the French FIGURE Network. More precisely, Olivier Romain and I are deeply involved in the Electronics Lecture, Labs and Project that will take place right from the Licence degree. The different projects of the ESH Activity will strongly support the training of the students of the forthcoming years, and will also create some positive emulation between different research domains (Biocells, Chemistry, Physics, Electronics, Image and Signal Processing) as the on going projects have already made it possible.

Final Words

I want to conclude this document by the list of the students (in alphabetical order) that were involved in the different activities I have described here and that have their own contribution (whatever it is) to the achievement of the related projects.

C. Azib (2013), E. Bonnefoye (2012), M. Breuilly (2009), N. Cazin (2014), M. Degaudez (2007), M.-C. Desseroit (2013), H. Diouane (2014), C. Fouquet (2011-2014), M. Garnier (2009, 2011), C. Georgel (2013), A. Izard (2013), T. Longret (2013), L. Meziou (2010-2013), S. Mouzay (2014), G. Pardeschi (2014), M. Rémignon (2014), A. Riaz (2013), J. Silva-Quintero (2012), Y. Zhang (2009-2010).

Appendix A

Full List of Publications (2006-2014)

A.1 Article in peer-reviewed journal

1. Silva J. S., Histace A., Romain O., Dray X., Granado B., "***Towards embedded detection of polyps in WCE images for early diagnosis of colorectal cancer***", *International Journal of Computer Assisted Radiology and Surgery* In press, (2014)

   10.1007/s11548-013-0926-3

2. Zhang Y., Matuszewski B., Histace A., Precioso F., "***Statistical Model of Shape Moments with Active Contour Evolution for Shape Detection and Segmentation***", *Journal of Mathematical Imaging and Vision* **47**, **1**, 35-47, (2013)

   10.1007/s10851-013-0416-9

3. Histace A., Meziou L., Matuszewski B., Precioso F., Murphy M., Carreiras F., "***Statistical region based active contour using a fractional entropy descriptor: Application to nuclei cell segmentation in confocal microscopy images***", *Annals of British Machine Vision Association* **2013**, **5**, 1-15, (2013)

4. Histace A., Rousseau D., "***Useful Noise effect for nonlinear PDE based restoration of scalar images***", *International Journal of Computer Information Systems and Industrial Management* **4**, 411-420, (2012)

5. Histace A., Portefaix C., Matuszewski B., "***Comparison of Different Grid of Tags Detection Methods in Tagged Cardiac MR Imaging (Journal Version)***", *International Journal of Computer Assisted Radiology and Surgery* **6**, **2**, pp. 153-161, (2011)

   10.1007/s11548-010-0495-7

6. Histace A., Ménard M., Cavaro-Ménard C., "***Selective Diffusion for Oriented Pattern Extraction: Application to Tagged Cardiac MRI Enhancement***", *Pattern Recognition Letters* **30**, **15**, 1356-1365, (2009)

   10.1016/j.patrec.2009.07.012

7. Histace A., Matuszewski B., Zhang Y., "***Segmentation of myocardial boundaries in tagged cardiac MRI using active contours: a gradient-based approach integrating texture analysis***", *International Journal of Biomedical Imaging* **2009**, 8 pages, (2009)

10.1155/2009/983794

8. Histace A., Rousseau D., "***Constructive Action of Noise for Impulsive Noise Removal in Scalar Images***", *Electronics Letters* **42**, **7**, 393-395, (2006)
   10.1049/el:20060180

9. Histace A., Courboulay V., Cavaro-Ménard C., Ménard M., "***Traitement et analyse quantitative de séquences IRM cardiaques marquées***", *Traitement du Signal* **23**, **2**, 125-143, (2006)

A.2 Invited conference talk

1. Garda P., Romain O., Histace A., Granado B., Pinna A., Dray X., Leprince P., "***Endocom and Cyclope: Two smart biomedical sensors for cardio-vascular surgery and gastro-enterology***", 3rd International Conference on Wireless Mobile Communication and Healthcare **61**, 286-294 (2012-11-21) (2012) Paris France Springer

A.3 Conference proceedings

1. Meziou L., Histace A., Precioso F., "***Statistical Region-Based Active Contour Using Optimization of Alpha-Divergence Family For Image Segmentation***", 21st IEEE International Conference on Image Processing, (2014-10-27), (2014) In press Paris France

2. Fouquet C., Histace A., Duvaut P., "***Automated Detection Of Defects Signature in Pipelines Using Ultra Sonic Thickness Images***", European Conference on Non-Destructive Testing, (2014-11-06) Pragues In press Czech Republic

3. Iakovidis D., Sarmiento R., Silva, J., Histace A., Romain O., Koulaouzidis A.,Dehollain C., Pinna A., Granado B., Dray, X., "***Towards Intelligent Capsules for Robust Wireless Endoscopic Imaging of the Gut***", IEEE International Conference on Imaging Systems and Techniques, (2014-11-03), (2014) In press Santorini Greece

4. Histace A., Bonnefoye E., Garrido L., Matuszewski B. J., Murphy M. J., "***Active contour based on approximate entropy: application to cell membrane segmentation in confocal microscopy***", International Conference on Bio-inspired systems and signal processing in press (2014-03-03) (2014) Angers France Scitepress

5. Romain O., Histace A., Silva J., Ayoub J., Granado B., Pinna A., Dray X., Marteau P., "***Towards a multimodal wireless video capsule for detection of colonic polyps as prevention of colorectal cancer.***", IEEE BIBE'13 1-6 (2013-11-10) (2013) Chania Greece IEEE 10.1109/BIBE.2013.6701670

6. Fouquet C., Histace A., Meziou L., Duvaut P., "***Automated Detection and Fine Segmentation of Defects Signature in Pipelines using US Thickness Images***", The 12th International Conference for Non-Destructive Testing : "Application of Contemporary Non-Destructive Testing in Engineering" in press (2013-09-04) (2013) Ljubljana Slovenia

7. Silva J. S., Histace A., Romain O., Dray X., Granado B., Pinna A., "***Cyclope : vers une vidéocapsule intelligente pour la détection in situ des polypes colorectaux***", GRETSI 2013 accepté (2013-09-03) (2013) Brest France

8. Silva J., Histace A., Romain O., Dray X., Granado B., Pinna A., "***Towards real-time in situ polyp detection in WCE images using a boosting-based approach***", International conference of the IEEE Engineering in Medecine and Biology Society 5711-5714 (2013-07-03) (2013) Osaka Japan 10.1109/EMBC.2013.6610847

9. Silva J., Histace A., Romain O., Dray X., Granado B., Marteau P., "***Towards embedded detection of polyps in videocolonoscopy and WCE images for early diagnosis of colorectal cancer***", *International Journal of Computer Assisted Radiology and Surgery* Computer Assisted Radiology and Surgery in Press (2013-06-26) (2013) Heidelberg Germany

10. Silva J. S., Histace A., Romain O., Dray X., Granado B., Marteau P., "***Développement et validation d'un algorithme de reconnaissance automatique de polypes coliques***", JFHOD'13 Abstract (2013-03-21) (2013) Paris France

11. Picard D., Histace A., Desseroit M.-C., "***Joint MAS-PDE Modeling of Forest Pest Insect Dynamics: Analysis of the Bark Beetle's Behavior***", VISIGRAPP (Workshop GEODIFF) In Press (2013-02-21) (2013) Barcelone Spain

12. Silva J., Histace A., Romain O., Dray X., Granado B., "***Embeddable automatic polyp detection for videoendoscopy and WCE image analysis***", 27th Conference on Design of Circuits and Integrated Systems (DCIS), Special Session on Biomedical Systems 177 (2012-11-28) (2012) Avignon France

13. Meziou L., Histace A., Precioso F., Matuszewski B., Carreiras F., "***Fractional Entropy Based Active Contour Segmentation of Cell Nuclei in Actin-Tagged Confocal Microscopy Images***", Conference on Medical Image Understanding and Analysis 117-123 (2012-07-09) (2012) Swansea United Kingdom

14. Meziou L., Histace A., Dray X., Romain O., Granado B., "***Segmentation of video capsule endoscopic images using alpha-divergence based active contour method***", *International Journal of Computer Assisted Radiology and Surgery* Computer Assisted Radiology and Surgery (CARS) S325–S326 (2012-06-27) (2012) Pisa Italy Springer

15. Meziou L., Histace A., Precioso F., "***Alpha-divergence maximization for statistical region based active contour segmentation with non-parametric PDF estimations***", International Conference on Acoustic Speech and Signal Processing 861-864 (2012-03-25) (2012) Kyoto Japan IEEE

16. Meziou L., Histace A., Precioso F., Matuszewski B., Carreiras F., "***3D Confocal Microscopy data analysis using level-set segmentation with alpha-divergence similarity measure***", International Conference on Computer Vision Theory and Applications 861-864 (2012-02-24) (2012) Rome Italy

17. Matuszewski B., Murphy M., Burton D.R., Marchant T., Moore C., Histace A., Precioso F., "***Segmentation of Cellular Structures in Actin Tagged Fluorescence Confocal Microscopy Images***", IEEE ICIP 2011 pp. 3081-3084 (2011-09-11) (2011) Bruxelles Belgium

18. Meziou L., Histace A., Precioso F., Matuszewski B., Murphy M., "***Confocal Microscopy Segmentation Using Active Contour Based on Alpha-Divergence***", IEEE ICIP 2011 pp. 3077-3080 (2011-09-11) (2011) Bruxelles Belgium

19. Meziou L., Histace A., Precioso F., Matuszewski B., "***Alpha-divergences pour la segmentation par contours actifs basés histogramme : application à la segmentation d'images cellulaires en microscopie confocale tridimensionnelle***", GRETSI'11 Accepté (2011-09-05) (2011) Bordeaux France

20. Zhang Y., Matuszewski B., Histace A., Precioso F., "***Statistical Shape Model of Legendre Moments with Active Contour Evolution for Shape Detection and Segmentation***", Computer Analysis of Images and Patterns **6854**, **1**, 51-58 (2011-08-29) (2011) Sevilla Spain Springer

21. Meziou L., Histace A., Precioso F., Matuszewski B., "***MRI segmentation using histogram based active contour method: application to prostate MR image analysis***", CARS'11 **6**, **Supplement 1**, S50-S51 (2011-06-22) (2011) Berlin Germany Springer

22. Histace A., "***Nonlinear low-level image processing improvement by a purposely injection of noise***", International Conference on Computer Vision Theory and Applications 226-229 (2011-03-05) (2011) Algarve Portugal

23. Histace A., Rousseau D., "***Noise-enhanced Nonlinear PDE for Edge Restoration in Scalar Images***", SOft Computing and PAttern Recognition 458-461 (2010-12-07) (2010) Cergy France IEEE

24. Zhang Y., Matuszewski B., Histace A., Precioso F., Killgalon J., Moore C., "***Boundary Delineation in Prostate Imaging using Active Contour Segmentation Method with Interactively Defined Object Regions***", MICCAI (Workshop on Prostate Cancer Imaging) **LNCS 6367**, 131-142 (2010-09-20) (2010) Beijing China Springer

25. Histace A., Portefaix C., "***Comparison of different detection and tracking of the grid of tags methods in tagged cardiac MR imaging (Conference version)***", CARS'10 (Computer Assisted Radiology and Surgery) Accepté (2010-06-23) (2010) Genève Switzerland

26. Lamard L., Histace A., Matuszewski B., "***Contours actifs paramétriques fondés sur le calcul de distances inter histogrammes pour la segmentation d'images médicales***", CNRIUT 2010 Accepté (2010-06-09) (2010) Angers France

27. Histace A., Ménard M., "***MR Image enhancement: a PDE based approach integrating a double well potential function for thin structure preservation***", VISAPP'10-International conferences on computer vision theory and applications 501-508 (2010-05-17) (2010) Angers France

28. Portefaix C., Histace A., Breuilly M., Matuszewski B., "***Segmentation semi-automatique en IRM3T des muscles oculomoteurs dans le suivi de la maladie de Grave-Basedow***", JFR'09 www.sfrnet.org (2009-10-16) (2009) Paris France

29. Breuilly M., Histace A., Portefaix C., Matuszewski B., Precioso F., "***Segmentation des muscles oculomoteurs en IRM cérébro-orbitaire pour l'aide au diagnostic de l'exophtalmie***", GRETSI'09 http://hdl.handle.net/2042/29110 (2009-09-08) (2009) Dijon France

30. Histace A., Portefaix C., Matuszewski B., Zhang Y., "***Level set segmentation of extraocular muscles in MR images for thyroïd-associated-ophtalmopathy diagnosis***", Computer Assisted Radiology and Surgery (CARS) **4**, **Supplement 1**, S325-S326 (2009-06-23) (2009) Berlin Germany

31. Zhang Y., Matuszewski B., Histace A., "***A fully automatic segmentation method for myocardial boundaries of left ventricle in tagged MR images***", CARS 2010 **4**, **Supplement 1**, S43-S44 (2009-06-23) (2009) Berlin Germany

32. Histace A., Ménard M., "***Double well potential as diffusive function for PDE-based scalar image restoration method***", ICINCO 2009. 6th International Conference on Informatics in Control Automation and Robotics. 401-404 (2009-07-02) (2009) Milan Italy

33. Histace A., Courboulay V., Ménard M., "***Selective Image Diffusion for Oriented Pattern Extraction***", ICINCO'07 270-274 (2007-05-09) (2007) Angers France

34. Histace A., Rousseau D., "***Noise Enhanced Anisotropic Diffusion for Scalar image Restoration***", PSIP'07 5 pages (2007-01-31) (2007) Mulhouse France

A.4 Scientific Book chapter

1. Histace A., Ménard M., "***Gradient Intensity Selectivity for Scalar Image Restoration using PDE***", Chap. 9

   S. Yokota and D. Chugo 978-1463789442

2. Histace A., Menard M., Cavaro-Menard C., "***Chapter 11 : PDE Based Approach for Segmentation of Oriented Patterns (pp 207-218)***", 450

   Aleksandar Lazinica 978-953-7619-20-6 10.5772/6283

A.5 Edition of book or proceedings

1. Histace A., "***Proceedings of First GEODIFF Workshop***", 64

   978-989-8565-49-5

2. Histace A., "***Image Restoration - Recent Advances and Applications***", 372

   978-953-51-0388-2

A.6 Research report

1. Meziou L., Histace A., Precioso F., "***Alpha-divergences pour la segmentation d'images par contours actifs basés histogrammes : Application à l'analyse d'images médicales et biomédicales***",

Bibliography

[Ahmad and Lin, 1976] I. A. Ahmad and P. E. Lin. A nonparametric estimation of the entropy for absolutely continuous distributions. *IEEE Trans. Information Theory*, 1976. 94

[Alvarez *et al.*, 1992] L. Alvarez, F. Guichard, P.L. Lions, and J.M. Morel. Image selective smoothing and edge detection by nonlinear diffusion (ii). *Arch. Rationnal Mech. Anal.*, 29(3):845–866, 1992. 44

[Amari, 1985] S.-I. Amari. *Differential-Geometrical Methods in Statistics (Lecture Notes in Statistics 28)*. Springer, 1985. 103

[Aubert *et al.*, 2003] G. Aubert, M. Barlaud, O. Faugeras, and S. Jehan-Besson. Image segmentation using active contours: Calculus of variations or shape gradients? *SIAM J. Appl. Math.*, 63:2128–2154, 2003. 31, 74, 77, 91, 103

[Axel *et al.*, 2007] L. Axel, Sohae Chung, and Ting Chen. Tagged mri analysis using gabor filters. In *Biomedical Imaging: From Nano to Macro, 2007. ISBI 2007. 4th IEEE International Symposium on*, pages 684–687, 2007. 46

[Ayoub *et al.*, 2010] J. Ayoub, B. Granado, Y. Mhanna, and O. Romain. SVM based colon polyps classifier in a wireless active stereo endoscope. In *2010 IEEE EMBC*, pages 5585 –5588, 2010. 125, 126

[Beirami *et al.*, 2008] A. Beirami, V. Cevher, B. Bower, and K. Tsianos. Proofs of alpha divergence properties. Rapport Technique STAT 631 / ELEC 639, Rice University, September 2008. 34, 104

[Benzi *et al.*, 1981] R. Benzi, A. Sutera, and A. Vulpiani. The mechanism of stochastic resonance. *Journal of Physics A*, 14:L453–L458, 1981. 58

[Benzi *et al.*, 1982] R. Benzi, G. Parisi, A. Sutera, and A. Vulpiani. Stochastic resonance in climatic changes. *Tellus*, 34:10–16, 1982. 58

[Bergwerk *et al.*, 2007] A. Bergwerk, D. Fleischer, and J. Gerber. A capsule endoscopy guide for the practising clinician: technology and troubleshooting. *Medline*, 66(6):1188–1195, Décembre 2007. 124

[Bernal *et al.*, 2012] J. Bernal, J. Sanchez, and F. Vilariño. Towards automatic polyp detection with a polyp appearance model. *Pattern Recognition*, 45(9):3166 – 3182, 2012. 39, 127, 128, 131, 133

[Blanchard *et al.*, 2008] S. Blanchard, D. Rousseau, D. Gindre, and F. Chapeau-Blondeau. Benefits from a speckle noise family on a coherent imaging transmission. *Optics Communications*, 281:4173–4179, 2008. 58

[Bohou *et al.*, 2007a] X. Bohou, J. Zhong-Ping, W. Xingxing, and D.W. Repperger. Nonlinear bistable stochastic resonance filters for image processing. In *Proceedings of IEEE International Conference on Acoustics, Speech and Signal Processing*, volume 1, pages 717–720, 2007. 58

[Bohou *et al.*, 2007b] X. Bohou, J. Zhong-Ping, W. Xingxing, and D.W. Repperger. Theoretical analysis of image processing using parameter-tuning stochastic resonance technique. In *Proceedings of American Control Conference*, pages 1747–1752, 2007. 58

[Brodatz, 1999] Phil Brodatz. *Textures: A Photographic Album for Artists and Designers*. Dover Publications, Aôut 1999. 112

[Bromiley *et al.*, 2004] P.A. Bromiley, N.A. Thacker, and E. Bouhova-Thacker. Shannon entropy, renyi entropy, and information. Rapport technique, School of Cancer and Imaging Sciences, University of Manchester, 2004. 93

[Catté *et al.*, 1992] F. Catté, T. Coll, P. Lions, and J. Morel. Image selective smoothing and edge detection by nonlinear diffusion. *SIAM Journal of Applied Mathematics*, 29(1):182–193, 1992. 24, 44, 45, 50

[Chan and Vese, 2001] T. F. Chan and L. A. Vese. Active contours without edges. *IEEE Trans. on Image Processing*, 10(2):266–277, 2001. 72, 75, 77, 98, 106

[Chapeau-Blondeau and Rousseau, 2002] F. Chapeau-Blondeau and D. Rousseau. Noise improvements in stochastic resonance: From signal amplification to optimal detection. *Fluctuation and noise letters*, 2:221–233, 2002. 58, 65, 66

[Chapeau-Blondeau, 2000] F. Chapeau-Blondeau. *Noise, Oscillators and Algebraic Randomness-From Noise in Communication Systems to Number Theory*, volume 550 de *Lecture Notes in Physics*, chapitre Stochastic resonance and the benefit of noise in nonlinear systems, pages 137–155. Springer (Berlin), 2000. 27, 58, 59, 69

[Cichocki and Amari, 2010] A. Cichocki and S.-I. Amari. Families of alpha- beta- and gamma-divergences: Flexible and robust measures of similarities. *Entropy*, 12(6):1532–1568, 2010. 103

[Cootes *et al.*, 1995] T. F. Cootes, C. J. Taylor, D. H. Cooper, and J. Graham. Active shape models — their training and application. *Comput. Vis. Image Underst.*, 61(1):38–59, 1995. 73, 76

[Cremers *et al.*, 2006] Daniel Cremers, Stanley J. Osher, and Stefano Soatto. Kernel density estimation and intrinsic alignment for shape priors in level set segmentation. *Int. J. Comput. Vision*, 69(3):335–351, 2006. 73

[Csiszár, 1967] I. Csiszár. Information-type measures of difference of probability distributions and indirect observations. *Studia Scientiarum Mathematicarum Hungarica*, 2:299–318, 1967. 109

[Dahdouh *et al.*, 2013] S. Dahdouh, A. Serrurier, G. Grange, E.D. Angelini, and I. Bloch. Segmentation of fetal envelope from 3d ultrasound images based on pixel intensity statistical distribution and shape priors. In *Biomedical Imaging (ISBI), 2013 IEEE 10th International Symposium on*, pages 1026–1029, April 2013. 73, 90

[Davis *et al.*, 1979] Larry S. Davis, Steven A. Johns, and J. K. Aggarwal. Texture analysis using generalized co-occurrence matrices. *Pattern Analysis and Machine Intelligence, IEEE Transactions on*, PAMI-1(3):251 –259, july 1979. 129

[Denney, 1999] T. Denney. Estimation and detection of myocardial tags in MR images without user-defined myocardial contours. *IEEE Transactions on Medical Imaging*, 18(4):330–344, 1999. 47, 55

[Deriche and Faugeras, 1996] R. Deriche and O. Faugeras. Les edp en traitements des images et visions par ordinateur. *Traitement du Signal*, 13(6):551–578, 1996. 44, 45

[El Hamidi *et al.*, 2009] Abdallah El Hamidi, Michel Menard, Mathieu Lugiez, and Ghannam Clara. Weighted and Extended total variation for image restoration and decomposition. *Pattern Recognition*, page Received 2 April 2009; revised 15 October 2009; accepted 17 October 2009. Available online 1 Novembe, Novembre 2009. 44

[Elhossini and Moussa, 2012] A. Elhossini and M. Moussa. Memory efficient fpga implementation of Hough transform for line and circle detection. In *CCECE*, pages 1–5, 2012. 136, 137

[Eliakim, 2009] R. et al. Eliakim. Prospective multi center performance evaluation of the second generation colon capsule compared with colonoscopy. *Endoscopy*, 41:1026–1031, 2009. 125

[Erdem *et al.*, 2009] Erkut Erdem, Sibel Tari, and Luminita Vese. Segmentation using the edge strength function as a shape prior within a local deformation model. In *Proceedings of the 16th IEEE International Conference on Image Processing*, ICIP'09, pages 2953–2956, Piscataway, NJ, USA, 2009. IEEE Press. 73

[Etyngier *et al.*, 2007] P. Etyngier, R. Keriven, and F Ségonne. Projection onto a shape manifold for image segmentation with prior. In *14th IEEE International Conference on Image Processing*, San Antonio, Texas, US, Sep 2007. 73

[Figueiredo *et al.*, 2011] P. N. Figueiredo, I. N. Figueiredo, S. Prasath, and R. Tsai. Automatic polyp detection in pillcam colon 2 capsule images and videos: Preliminary feasibility report. *Diagnostic and Therapeutic Endoscopy*, (182435):7 pages, 2011. 127, 128

[F.J. Shin, 2008] M. C. Parkin F.J. Shin, B.F. Forman. Globocan 2008 v1.2, cancer incidence and mortality worldwide: Iarc cancerbase no. 10. *International Agency for Research on Cancer*, 2008. 124

[Foulonneau, *et al.*, 2003] Alban Foulonneau,, Pierre Charbonnier, and Fabrice Heitz. Geometric shape priors for region-based active contours. In *ICIP*, volume 3, pages 413–416, 2003. 74, 80

[Foulonneau, *et al.*, 2009] Alban Foulonneau,, Pierre Charbonnier, and Fabrice Heitz. Multi-reference shape priors for active contours. *Int. J. Comput. Vision*, 81(1):68–81, 2009. 74, 75, 80, 84

[Freedman *et al.*, 2005] D. Freedman, R. J. Radke, T. Zhang, Y. Jeong, Student Member, D. M. Lovelock, and G. T. Y. Chen. Model-Based Segmentation of Medical Imagery by Matching Distributions. *IEEE Trans. Med. Imaging*, 24:281–292, 2005. 101

[Fussenegger *et al.*, 2009] Michael Fussenegger, Peter Roth, Horst Bischof, Rachid Deriche, and Axel Pinz. A level set framework using a new incremental, robust active shape model for object segmentation and tracking. *Image Vision Comput.*, 27(8):1157–1168, 2009. 73

[Gammaitoni *et al.*, 1989] L. Gammaitoni, F. Marchesoni, E. Menichella-Saetta, and S. Santucci. Stochastic resonance in bistable systems. *Physical Review Letters*, 62:349–352, 1989. 58, 59

[Gammaitoni *et al.*, 1998] L. Gammaitoni, P. Hangi, P. Jung, and F. Marchesoni. Stochastic resonance. *Reviews of Modern Physics*, 70:223–287, 1998. 58

[Geman and Reynolds, 1992] S. Geman and G. Reynolds. Constrained restoration and the recovery of discontinuities. *IEEE Transactions on Pattern Analysis and Machine Intelligence*, 14(3):367–383, 1992. 44

[Geninatti *et al.*, 2009] S.R. Geninatti, S.R. Benavidez-Benitez, M. Hernandez-Calvino, N. Guil-Mata, and J. Gomez-Luna. Fpga implementation of the generalized hough transform. In *Proceedings - 2009, International Conference ReConFigurable Computing and FPGAs*, pages 172 – 177, 2009. 137

[Guidotti *et al.*, 2013] P. Guidotti, Y. Kim, and J. Lambers. Image restoration with a new class of forward-backward-forward diffusion equations of perona–malik type with applications to satellite image enhancement. *SIAM Journal on Imaging Sciences*, 6(3):1416–1444, 2013. 44

[Hall, 2009] A. Hall. *The cytoskeleton and cancer*, volume 28. Springer Netherlands, Philadelphia, PA, USA, 06 2009. 98

[Haralick *et al.*, 1973] R.M. Haralick, K. Shanmugam, and Its'Hak Dinstein. Textural features for image classification. *IEEE Transactions on Systems, Man and Cybernetics*, SMC-3(6):610–621, Novembre 1973. 114

[Haralick, 1979] R.M. Haralick. Statistical and structural approaches to texture. *Proceedings of the IEEE*, 67(5):786–804, 1979. 130

[Hardzeyeu and Klefenz, 2008] V. Hardzeyeu and F. Klefenz. On using the hough transform for driving assistance applications. In *2008 International Conference on Intelligent Computer Communication and Processing*, pages 91 – 98, 2008. 137

[Harmer *et al.*, 2002] G.P. Harmer, B.R. Davis, and D. Abott. A review of stochastic resonance: Circuits and measurement. *IEEE Transactions on Instrumentation and Measurement*, 51:299–309, 2002. 58

[Heiler and Schnörr, 2005] M. Heiler and C. Schnörr. Natural Image Statistics for Natural Image Segmentation. *Int. J. Comput. Vision*, 63:5–19, 2005. 101

[Herbulot *et al.*, 2006] A. Herbulot, S. Jehan-Besson, S. Duffner, M. Barlaud, and G. Aubert. Segmentation of vectorial image features using shape gradients and information measures. *Journal of Mathematical Imaging and Vision*, 25(3):365–386, 2006. 32, 91, 92

[Hero *et al.*, 2002] A.O Hero, B. Ma, O. Michel, and J.D. Gorman. Alpha-divergence for classification, indexing and retrieval. Rapport Technique CSPL-328, University of Michigan, June 2002. 112

[Histace and Rousseau, 2006] A. Histace and D. Rousseau. Constructive action of noise for scalar image restoration. *Electronics Letters*, 42(7):393–395, 2006. 60, 61, 63, 65, 66

[Histace and Rousseau, 2007] A. Histace and D. Rousseau. Noise-enhanced anisotropic diffusion for image scalar restoration. In *Proceedings of the fifth PSIP congress (Physics in Signal and Image Processing*, 2007. 61, 63

[Histace and Rousseau, 2010] A. Histace and D. Rousseau. Noise-enhanced Nonlinear PDE for Edge Restoration in Scalar Images. In *Proceedings of SOCPAR 2010 SOft Computing and PAttern Recognition*, éditeur IEEE, pages 458–461, Cergy France, 12 2010. 44, 69

[Histace *et al.*, 2005] A. Histace, C. Cavaro-Ménard, V. Courboulay, and M. Ménard. Analysis of tagged cardiac MRI sequences. *Lecture Notes on Computer Science (Proceedings of the 3rd Functional Imaging and Modelling of the Heart (FIMH) Workshop)*, 3504:404–413, June 2005. 44

[Histace *et al.*, 2009] A. Histace, M. Ménard, and C. Cavaro-Ménard. Selective diffusion for oriented pattern extraction: Application to tagged cardiac mri enhancement. *Pattern Recognition Letters*, 30(15):1356–1365, November 2009. 44, 55

[Houhou, *et al.*, 2008] Nawal Houhou,, Alia Lemkaddem, ValÃ©rie Duay, Allal, Abdelkarim, and Jean-Philippe Thiran. Shape prior based on statistical MAP for active contour segmentation. In *ICIP*, 2008. 73

[Iakovidis *et al.*, 2007] D. K. Iakovidis, D. E. Maroulis, and D. G. Bariamis. Fpga architecture for fast parallel computation of co-occurrence matrices. *Microprocess. Microsyst.*, 31(2):160–165, Mars 2007. 130, 137, 138

[Jehan-Besson *et al.*, 2003] S. Jehan-Besson, M. Barlaud, and G. Aubert. Deformable regions driven by an eulerian accurate minimization method for image and video segmentation. *Int. J. Comput. Vision*, 53:45–70, June 2003. 91, 92

[Jha *et al.*, 2012] R.K. Jha, P.K. Biswas, and B.N. Chatterji. Contrast enhancement of dark images using stochastic resonance. *Image Processing, IET*, 6(3):230–237, April 2012. 58, 69

[Karargyris and Bourbakis, 2009] A. Karargyris and N. Bourbakis. Identification of polyps in wireless capsule endoscopy videos using log gabor filters. In *IEEE Workshop LiSSA*, pages 143 –147, april 2009. 127, 128, 129, 133

[Kass *et al.*, 1988] M. Kass, A. Witkin, and D. Terzopoulos. Snakes: Active contour models. *International Journal of Computer Vision*, 1:321–331, 1988. 30, 72

[Kim, *et al.*, 2007] Junmo Kim,, Müjdat Çetin, and Alan S. Willsky. Nonparametric shape priors for active contour-based image segmentation. *Signal Process.*, 87(12):3021–3044, 2007. 73

[Kodogiannis and Boulougoura, 2007] V. Kodogiannis and M. Boulougoura. An adaptive neuro-fuzzy approach for the diagnosis in wireless capsule endoscopy imaging. *Int. J. of Information Technology*, 13:46 – 56, 2007. 127, 128

[Kohonen, 1995] T. Kohonen. *The Handbook of Brain Theory and Neural Networks*, chapitre Learning vector quantization. MIT Press, Cambridge, MA, 1995. 134

[Kolar *et al.*, 2010] A. Kolar, O. Romain, J. Ayoub, S. Viateur, and B. Granado. Prototype of Video Endoscopic Capsule With 3-D Imaging Capabilities. *Biomedical Circuits and Systems, IEEE Transactions on*, 4(4):239 –249, 2010. 125, 136

[Kuon and Rose, 2007] I. Kuon and J. Rose. Measuring the gap between fpgas and asics. *Trans. Comp.-Aided Des. Integ. Cir. Sys.*, 26(2):203–215, Février 2007. 138

[Lecellier, *et al.*, 2006] F. Lecellier,, S. Jehan-Besson, J. Fadili, G. Aubert, M. Revenu, and E. Saloux. Region-based active contour with noise and shape priors. In *ICIP*, pages 1649–1652, 2006. 73, 109

[Lecellier *et al.*, 2009] F. Lecellier, S. Jehan-Besson, J. Fadili, G. Aubert, and M. Revenu. Optimization of divergences within the exponential family for image segmentation. In *Proceedings of the Second International Conference on Scale Space and Variational Methods in Computer Vision (SSVM'09)*, pages 137–149, Berlin, Heidelberg, 2009. Springer-Verlag. 91, 101, 103

[Lecellier *et al.*, 2010] F. Lecellier, M.J. Fadili, S. Jehan-Besson, G. Aubert, M. Revenu, and E. Saloux. Region-based active contours with exponential family observations. *Journal of Mathematical Imaging and Vision*, 36(1):28–45, January 2010. 32, 91, 98

[Leventon, *et al.*, 2000] M. Leventon,, W. Grimson, and O. Faugeras. Statistical shape influence in geodesic active contours. In *CVPR*, pages 316–323, 2000. 73

[Liu *et al.*, 2011a] M. Liu, L. Lu, J. Bi, V. Raykar, M. Wolf, and M. Salganicoff. Robust large scale prone-supine polyp matching using local features: A metric learning approach. In *Medical Image Computing and Computer-Assisted Intervention, MICCAI 2011*, éditeurs Gabor Fichtinger, Anne Martel, and Terry Peters, volume 6893 de *Lecture Notes in Computer Science*, pages 75–82. Springer Berlin Heidelberg, 2011. 127

[Liu *et al.*, 2011b] M. Liu, L. Lu, X. Ye, S. Yu, and M. Salganicoff. Sparse classification for computer aided diagnosis using learned dictionaries. In *Medical Image Computing and Computer-Assisted Intervention, MICCAI 2011*, éditeurs Gabor Fichtinger, Anne Martel, and Terry Peters, volume 6893 de *Lecture Notes in Computer Science*, pages 41–48. Springer Berlin Heidelberg, 2011. 136

[Matuszewski *et al.*, 2011] B. Matuszewski, M. Murphy, D.R. Burton, T. Marchant, C. Moore, A. Histace, and F. Precioso. Segmentation of Cellular Structures in Actin Tagged Fluorescence Confocal Microscopy Images. In *Proceedings of IEEE International Conference on Image Processing*, pages 3142–3145, Brussels, Belgium, September 2011. 98

[McNamara and Wiesenfeld, 1989] B. McNamara and K. Wiesenfeld. Theory of stochastic resonance. *Physical Review A*, 39:4854–4869, 1989. 58, 59

[Meziou *et al.*, 2011a] L. Meziou, A. Histace, F. Precioso, B. Matuszewski, and M. Murphy. Confocal Microscopy Segmentation Using Active Contour Based on Alpha-Divergence. In *Proceedings of IEEE ICIP conference*, pages 3138–3141, 09 2011. 98

[Meziou *et al.*, 2011b] Leila Meziou, Aymeric Histace, Frédéric Precioso, and Bogdan Matuszewski. MRI segmentation using histogram based active contour method: application to prostate MR image analysis. In *International Journal of Computer Assisted Radiology and Surgery*, éditeur Springer, page accepted, Berlin, Allemagne, Juillet 2011. 103

[Meziou *et al.*, 2012] L. Meziou, A. Histace, and F. Precioso. Alpha-divergence maximization for statistical region-based active contour segmentation with non-parametric PDF estimations. In *Proceedings of 37th IEEE International Conference on Accoustics, Speech and Signal Processing (ICASSP'12)*, pages 861–864, Kyoto, Japan, March 2012. 103

[Michailovich *et al.*, 2007] O.V. Michailovich, Y. Rathi, and A. Tannenbaum. Image segmentation using active contours driven by the bhattacharyya gradient flow. 16(11):2787–2801, 11 2007. 101

[Mitéran *et al.*, 2005] J. Mitéran, J. Matas, E. Bourennane, M. Paindavoine, and J. Dubois. Automatic hardware implementation tool for a discrete adaboost-based decision algorithm. *EURASIP Journal on Applied Signal Processing*, 2005:1035–1046, 2005. 137

[Moglia *et al.*, 2009] A. Moglia, , A. Menciassi, A. Dario, and A. Cuschieri. Capsule endoscopy: progress update and challenges ahead. *Nature reviews. Gastroenterology & hepatology*, (6):352–362, Juin 2009. 124

[Morfu *et al.*, 2008] S. Morfu, P. Marquié, B. Nofiélé, and D. Ginhac. Nonlinear systems for image processing. *Advances in imaging and electron. physics*, 2008. 58

[Morfu, 2009] S. Morfu. On some applications of diffusion processes for image processing. *Physics Letters A*, 373:2438–2444, 2009. 58, 69

[Nitzberg and Shiota, 1992] M. Nitzberg and T. Shiota. Nonlinear image filtering with edge and corner enhancement. *IEEE Transactions on Pattern Analysis and Machine Intelligence*, 14(8):826–833, 1992. 44

[Osher and Setian, 1988] S. Osher and J. Setian. Fronts propagating with curvature dependant speed: algorithms based on the hamilton-jacobi formulation. *Journal of Computational Physics*, 79:12–49, 1988. 72, 94

[Parzen, 1962] E. Parzen. On Estimation of a Probability Density Function and Mode. *The Annals of Mathematical Statistics*, 33(3):1065–1076, 1962. 91

[Perona and Malik, 1990] P. Perona and J. Malik. Scale-space and edge detection using anistropic diffusion. *IEEE Transcations on Pattern Analysis and Machine Intelligence*, 12(7):629–639, 1990. 23, 44, 45, 46, 63, 64

[Petitjean and Dacher, 2011] Caroline Petitjean and Jean-Nicolas Dacher. A review of segmentation methods in short axis cardiac MR images. *Medical Image Analysis*, pages 169–84, 2011. 44

[Petitjean *et al.*, 2005] C. Petitjean, N. Rougon, and P. Cluzel. Assessment of myocardial function: A review of quantification methods and results using tagged MRI. *Journal of Cardiovascular Magnetic Resonance*, 7(2):501–516, 2005. 46

[Prisacariu and Reid, 2011] V. A. Prisacariu and I. Reid. Nonlinear shape manifolds as shape priors in level set segmentation and tracking. In *Proceedings of the 2011 IEEE Conference on Computer Vision and Pattern Recognition*, CVPR '11, pages 2185–2192, Washington, DC, USA, 2011. IEEE Computer Society. 73

[Rao and Jain, 1992] A. Rao and R.C. Jain. Computerized flow field analysis: Oriented texture fields. *Transactions on pattern analysis and machine intelligence*, 14(7), 1992. 55

[Renbin *et al.*, 2007] P. Renbin, C. Hao, P.K. Varshney, and J.H. Michels. Stochastic resonance: An approach for enhanced medical image processing. In *Proceedings of Life Science Systems and Applications Workshop*, pages 253–256, 2007. 58

[Rényi, 1960] A. Rényi. On measures of entropy and information. *4th Berkeley Symposium on Mathematical Statistics and Probability.*, 1:547–561, 1960. 93

[Rougon *et al.*, 2003] N. Rougon, C. Petitjean, and F. J. PrÃªteux. Variational non rigid image registration using exclusive f-information. In *Proceedings of IEEE International Conference on Image Processing (ICIP)*, pages 703–706, 2003. 109

[Rousseau *et al.*, 2010] D Rousseau, A. Delahaies, and F. Chapeau-Blondeau. Structural similarity measure to assess improvement by noise in nonlinear image transmission. *IEEE Signal Processing Letters*, 17:36–39, 2010. 58

[Rousson,, and Cremers, 2005] Mikael Rousson,, and Daniel Cremers. Efficient kernel density estimation of shape and intensity priors for level set segmentation. In *MICCAI*, pages 757–764, 2005. 73

[Rousson,, and Paragios, 2002] M. Rousson,, and N. Paragios. Shape priors for level set representations. In *ECCV*, pages 78–92, 2002. 73

[Rousson and Paragios, 2008] Mikael Rousson and Nikos Paragios. Prior knowledge, level set representations & visual grouping. *Int. J. Comput. Vision*, 76(3):231–243, Mars 2008. 73

[Ruen *et al.*, 2006] J. J. Ruen, M. S. Shie, and C. Chen. A circular hough transform hardware for industrial circle detection applications. In *Industrial Electronics and Applications, 2006 1ST IEEE Conference on*, pages 1–6, 2006. 137

[Schapire and Singer, 1999] R.E. Schapire and Y. Singer. Improved boosting algorithms using confidence-rated predictions. *Mach. Learn.*, 37(3):297–336, Décembre 1999. 130

[Sieler *et al.*, 2010] L. Sieler, C. Tanougast, and A. Bouridane. A scalable and embedded FPGA architecture for efficient computation of grey level co-occurrence matrices and haralick textures features. *Microproc. and Microsys.*, 34(1):14 – 24, 2010. 137, 138

[Souki *et al.*, 2008] M.A. Souki, L. Boussaid, and M. Abid. An embedded system for real-time traffic sign recognizing. In *Proceedings - 2008 3rd International Design and Test Workshop, IDT 2008*, pages 273 – 276, 2008. 137

[Spada *et al.*, 2011] Cristiano Spada, Cesare Hassan, Miguel Munoz-Navas, Horst Neuhaus, Jacques Deviere, Paul Fockens, Emmanuel Coron, Gerard Gay, Ervin Toth, Maria Elena Riccioni, Cristina Carretero, Jean P. Charton, AndrÃ¨ Van Gossum, Carolien A. Wientjes, Sylvie Sacher-Huvelin, Michel Delvaux, Artur Nemeth, Lucio Petruzziello, Cesar Prieto de Frias, Rupert Mayershofer, Leila Aminejab, Evelien Dekker, Jean-Paul Galmiche, Muriel Frederic, Gabriele Wurm Johansson, Paola Cesaro, and Guido Costamagna. Second-generation colon capsule endoscopy compared with colonoscopy. *Gastrointestinal Endoscopy*, 74(3):581 – 589, 2011. 124, 125

[Suissa *et al.*, 2010] A. Suissa, O. Romain, J. Denoulet, K. Hachicha, and P. Garda. Empirical method based on neural networks for analog power modeling. *Trans. Comp.-Aided Des. Integ. Cir. Sys.*, 29(5):839–844, Mai 2010. 138

[Tagzout *et al.*, 2001] S. Tagzout, K. Achour, and O. Djekoune. Hough transform algorithm for fpga implementation. *Signal Processing*, 81(6):1295 – 1301, 2001. 129

[Tahir *et al.*, 2004] M.A. Tahir, A. Bouridane, and F. Kurugollu. *An FPGA Based Coprocessor for the Classification of Tissue Patterns in Prostatic Cancer*, volume 3203 de *Lecture Notes in Computer Science*, pages 771–780. Springer Berlin Heidelberg, 2004. 137, 138

[Teague, 1980] Michael Reed Teague. Image analysis via the general theory of moments∗. *J. Opt. Soc. Am.*, 70(8):920–930, Aug 1980. 74, 75

[Terebes *et al.*, 2002] R. Terebes, O. Lavialle, P. Baylou, and M. Borda. Mixed anisotropic diffusion. In *Proceedings of the 16th International Conference on Pattern Recognition*, volume 3, pages 1051–4651, 2002. 44, 55

[Thiruvenkadam *et al.*, 2007] SheshadriR. Thiruvenkadam, TonyF. Chan, and Byung-Woo Hong. Segmentation under occlusions using selective shape prior. In *Scale Space and Variational Methods in Computer Vision*, éditeurs Fiorella Sgallari, Almerico Murli, and Nikos Paragios, volume 4485 de *Lecture Notes in Computer Science*, pages 191–202. Springer Berlin Heidelberg, 2007. 73

[Tsai, *et al.*, 2003] A. Tsai,, A.J. Yezzi, W. M. Wells, C.M. Tempany, D. Tucker, A.C. Fan, W.E.L. Grimson, and A.S. Willsky. A shape-based approach to the segmentation of medical imagery using level sets. *IEEE Trans. Med. Imaging*, 22(2):137–154, 2003. 73

[Tschumperle and Deriche, 2005] D. Tschumperle and R. Deriche. Vector-valued image regularization with pde's: A common framework for different applications. *IEEE Transactions on Pattern Analysis and Machine Intelligence*, 27:506–517, 2005. 44

[Tshumperlé and Deriche, 2002] D. Tshumperlé and R. Deriche. Diffusion PDEs on vector-valued images. *Signal Processing Magazine, IEEE*, 19(5):16–25, September 2002. 44

[Vaudelle *et al.*, 1998] F. Vaudelle, J. Gazengel, G. Rivoire, X. Godivier, and F. Chapeau-blondeau. Stochastic resonance and noise-enhanced transmission of spatial signals in optics: The case of scattering. *Journal of the Optical Society of America B*, 13:2674–2680, 1998. 59, 60

[Viola and Jones, 2001] S. Viola and M. Jones. Rapid object detection using a boosted cascade of simple features. In *Proceedings of the 2001 IEEE CVPR Conference*, pages 511–518, 2001. 130, 131

[V.P. and Kumar Roy, 2010] Subramanyam Rallabandi V.P. and P. Kumar Roy. Magnetic resonance image enhancement using stochastic resonance in fourier domain. *Magnetic Resonance Imaging*, 2010. 58

[Wang and Sodini, 2006] A.Y. Wang and C.G. Sodini. On the energy efficiency of wireless transceivers. In *Communications, 2006. ICC '06. IEEE International Conference on*, volume 8, pages 3783–3788, 2006. 138

[Weickert, 1995] J. Weickert. Multiscale texture enhancement. In *Computer Analysis of Images and Patterns*, pages 230–237, 1995. 44, 53

[Weickert, 1998] J. Weickert. *Anisotropic Diffusion in image processing.* Teubner-Verlag, Stuttgart, 1998. 44, 94

[Whitaker and Pizer, 1993] R. Whitaker and S. Pizer. A multi-scale approac to nonuniform diffusion. *CVGIP:Image Understanding*, 57(1):99–110, 1993. 44

[Wiesenfeld and Moss, 1995] K. Wiesenfeld and F. Moss. Stochastic resonance and the benefits of noise: From ice ages to crayfish and SQUIDs. *Nature*, 373:33–36, 1995. 58

[Yang *et al.*, 2009] Y. Yang, Z.P. Jiang, B. Xu, and D.W. Repperger. Investigation of 2-d psr and applications in nonlinear image processing. *J. Physics A: Math. Theor.*, 2009. 58

[Ye *et al.*, 2003] Q. Ye, H. Huang, X. He, and C. Zhang. A sr-based radon transform to extract weak lines from noise images. In *Proceedings of ICIP*, volume 1, pages 849–852, 2003. 58

[Ye *et al.*, 2004] Q. Ye, H. Huang, and C. Zhang. Image enhancement using stochastic resonance [sonar image processing applications. In *Proceedings of ICIP*, volume 1, pages 263–266, 2004. 58

[Zerhouni *et al.*, 1988] E. Zerhouni, D. Parish, W. Rogers, A. Yang, and E. Shapiro. Human heart : tagging with MR imaging - a method for noninvasive assessment of myocardial motion. *Radiology*, 169(1):59–63, 1988. 22, 46

[Zhang *et al.*, 2010] Y. Zhang, B.J. Matuszewski, A. Histace, F. Precioso, J. Kilgallon, and C. Moore. Boundary delineation in prostate imaging using active contour segmentation method with interactively defined object regions. In *Prostate Cancer Imaging. Computer-Aided Diagnosis, Prognosis, and Intervention*, éditeurs Anant Madabhushi, Jason Dowling, Pingkun Yan, Aaron Fenster, Purang Abolmaesumi, and Nobuhiko Hata, volume 6367 de *Lecture Notes in Computer Science*. 2010. 90

[Zhang *et al.*, 2011] Y. Zhang, B. Matuszewski, A. Histace, and F. Precioso. Statistical Shape Model of Legendre Moments with Active Contour Evolution for Shape Detection and Segmentation. In *Proceedings of the 14th CAIP Conference*, éditeur Springer, volume 6854 de *LNCS*, pages 51–58, Sevilla, Espagne, Aôut 2011. 78

Résumé

Les travaux de recherche que j'ai menés ces dix dernières années sont principalement centrés sur l'analyse d'images médicales pour le diagnostic assisté par ordinateur. Le traitement d'image, discipline à la frontière entre le traitement du signal, l'informatique et les mathématiques appliqués, se présente comme un cadre théorique adapté à la mise en place d'outils permettant la restauration des données (minimisation du bruit d'acquisition), l'extraction automatique ou semi automatique (segmentation) de régions d'intérêt (organes, tumeurs, zones à risque d'une manière générale) et la détection et la reconnaissance de structures pathologiques au sein des séquences d'image et ce quelles que soient les caractéristiques de la modalité utilisée (IRM, Radiographie X, Ultrason, etc.). Depuis mon arrivée au laboratoire ETIS (ENSEA-Université de Cergy-Pontoise, CNRS) en septembre 2006 comme Maîtres de Conférences au sein de l' équipe Information, Communication, Imagerie (ICI), j'ai particulièrement abordé les problématiques associées à la restauration d'image par Equations aux Dérivées Partielles (EDP), la segmentation d'image par contours actifs et depuis plus récemment je développe une activité centrée sur la proposition de chaînes de détection/reconnaissance compatibles avec des contraintes d' Adéquation-Algorithme-Architecture propres à l'intégration matérielle pour des applications en Systèmes embarqués pour la santé (collaboration avec l'équipe ASTRE d'ETIS). Dans ce manuscrit, je présente une sélection des travaux de recherche que j'ai menés ces dernières années dans les trois domaines cités ci-dessus en proposant à chaque fois le contexte applicatif médical qui a impulsé le projet. Je présente également les perspectives des travaux en cours et les choix stratégiques qui permettront d'esquisser les lignes de mon projet de recherche pour les années à venir. Des éléments sur mon trajet professionnel sont également donnés en préambule afin de replacer mes travaux dans leur contexte.

Mots-clés: Approche variationnelle, contours actifs, restauration d'image par diffusion, systèmes embarqués pour la santé

Abstract

For the last decade, Medical Image Analysis for Computer-Aided-Diagnosis (CAD) has been the central motivation of my research activity. With the constant increase of the imaging capabilities of medical devices and the huge amount of produced digital information, physicians are in real need for semi-automatic image processing tools making possible fast, precise and robust analysis, including restoration, segmentation, pattern detection and recognition, quantitative analysis, etc. In this particular application area, from an image processing perspective, my research work has mainly focused for the last 8 years on two main tracks: (i) The study of the variational approach framework for image restoration and segmentation which common point is the formalization of the related optimization problem under the form of a Partial Differential Equation (PDE); (ii) The development of embeddable pattern detection and recognition methods based on statistical learning process for real-time in situ diagnosis.

The main scientific contributions of my research activities have been since 2006: In image restoration: (i) The study of the stochastic resonance phenomenon in non-linear PDE for image restoration and (ii) The study of double-well potential functions for Gradient-Oriented-PDE in image restoration. In image segmentation: (i) An Active contour segmentation approach with learning-based shape prior information; (ii) An Alpha-divergence-based active contour image segmentation approach; (iii) A Fractional-entropy-based active contour image segmentation approach. And finally in pattern recognition: The proposal of a complete embeddable image processing scheme for in situ polyp detection in Wireless Capsule Endoscopy for early colorectal cancer diagnosis.

This manuscript proposes a detailed overview of these contributions as well as elements for my future research activities.

Keywords: Variational Approach, Active Contours, Diffusion-based Image Restoration, Smart Embedded Systems for Health

ETIS UMR CNRS 8051, 6 avenue du Ponceau, 95014 Cergy-Pontoise